WEATHER AND CLIMATE IN THE AMUNDSEN SEA EMBAYMENT, WEST ANTARCTICA: OBSERVATIONS, REANALYSES AND HIGH RESOLUTION MODELLING

A thesis submitted to the School of Environmental Sciences
of the University of East Anglia in partial fulfilment
of the requirements for the degree of Doctor of Philosophy

RICHARD JONES

JANUARY 2018

ABSTRACT

Glaciers within the Amundsen Sea Embayment (ASE) are rapidly retreating and so contributing ~10% of current global sea level rise, primarily through basal melting. Here the focus is atmospheric features that influence the mass balance of these glaciers and their representation in atmospheric models.

New radiosondes and surface-based observations show that global reanalysis products contain relatively large biases in the vicinity of Pine Island Glacier (PIG), e.g. near-surface temperatures 1.8 °C (ERA-I) to 6.8 °C (MERRA) lower than observed. The reanalyses all underestimate wind speed during orographically-forced strong wind events and struggle to reproduce low-level jets. These biases would contribute to errors in surface heat fluxes and thus the simulated supply of ocean heat leading to PIG melting.

Ten new ice cores show that there is no significant trend in accumulation on PIG between 1979 and 2013. RACMO2.3 and four global reanalysis products broadly reproduce the observed time series and the lack of any significant trend. The zonal pressure gradient between the Amundsen Sea and the Antarctic Peninsula is the main driver of variability in accumulation on PIG.

Finally, the meteorological conditions associated with high heat flux events within coastal polynyas in the ASE are investigated. In three case studies high resolution simulations produce turbulent heat fluxes that are 10-20% (up to 100 W m^{-2}) larger than those in coarse resolution simulations. Representation of a hydraulic jump at the base of a slope is the key driver of the increased heat fluxes in a polynya close to PIG, with its presence leading to large differences in surface fluxes in the simulations.

Overall it is shown that moving towards using higher resolution atmospheric products will both reduce the magnitude of coastal biases near PIG in reanalysis products, and allow complex orographic flows, important to coastal polynya processes, to be more adequately resolved.

ACKNOWLEDGEMENTS

Firstly, I want to thank my primary supervisor Prof. Ian Renfrew for his guidance, support and constructive criticism. Also the occasional running hints and tips were much appreciated. To the rest of my supervisory team Ben Webber, Andrew Orr and Karen Heywood thankyou all for your feedback on my work throughout this PhD. Further thanks to Andy Elvidge, Denis Sergeev and Stuart Webster for their invaluable advice on setting up and running the Met Office Unified Model. Thanks also to all those onboard the JCR294 cruise, your enthusiasm for helping with the radiosonde launches was brilliant and helped to make my life easier.

To all of the inhabitants of office 3.17, both past and present, it has been a pleasure to share the office with you over the last four years. Thanks to Tahmeena for sharing the multiple trips up and down the stairs each day to drink life giving tea, and for the useful advice on how to finish a thesis. Rhiannon, thanks for the crosswords and putting up with my boring matlab questions, Karin thanks for for your LaTeX help over the years and for showing me that a work-life balance is important. Umberto and Louise thanks for helping to stop me from going insane and teaching me about Seagliders. Honza, Dave, Laura, Alastair, Matt et al., thanks for putting up with me. My housemates for the last couple of years, Osgur and Barney, 55 Edinburgh Road will not be the same without you, it has been fantastic getting to know you both (too well) and it's been fun to spend weekends concentrating on football and avoiding having to think about the return to the PhD thesis each Monday morning.

To my Mum and Dad, thanks for supporting me throughout my studies at school and then university, without you I would never have gone on this meteorological journey. Thanks also for all your proof reading over the years - many embarrassing typos have been avoided (did I spell that correctly?). Finally my sister, Dr. Lizzy Jones, thanks for blazing the PhD trail in our family, you showed me that PhD life can be fun and that there are many opportunities to explore far away places along the way. Oh and final thanks to Leicester City, for showing us that miracles can happen, and bringing much happiness (though also stress) to the Jones/Wilson household.

CONTENTS

LIST OF FIGURES

LIST OF TABLES

LIST OF SYMBOLS AND ACRONYMS

cm	centimetres
km	kilometres
m	metres
$mslp$	mean sea level pressure
$m.w.e$	metres of water equivalent
q	specific humidity
t	time
u	zonal (eastward) wind
v	meridional (northward) wind
AMRC	Antarctic Meteorological Reseach Centre
ASE	Amundsen Sea Embayment
ASL	Amundsen Sea Low
AWS	Automatic Weather Station
BP	Bear Peninsula (AWS)
CDW	Circumpolar Deep Water
CFSR	Climate Forecast System Reanalysis
CMIP	Coupled Model Intercomparison Project
DJF	December, January, February
ECMWF	European Centre for Medium-Range Weather Forecasts
EK	Evans Knoll (AWS)
ENSO	El Niño-Southern Oscillation
ERA5	ECMWF 5th generation reanalysis
ERA-I	European Centre for Medium Range Weather Forecasts Interim Reanalysis
GPS	Global Positioning System
GTS	Global Telecommunication System
IPCC	Intergovernmental Panel on Climate Change

iSTAR	Ice Sheet Stability Programme
JCR	RRS James Clark Ross
JJA	June, July, August
JMA	Japanese Meteorological Agency
JRA-55	Japanese 55-year reanalysis
LLJ	Low-level jet
MAM	March, April, May
MERRA(2)	Modern-Era Retrospective Analysis for Research and Applications (version 2)
MetUM	Met Office Unified Model
MODIS	Moderate Resolution Imaging Spectroradiometer
NASA	National Aeronautics and Space Administration
NOAA	National Oceanic and Atmospheric Administration
NWP	Numerical Weather Prediction
NYU	New York University (AWS)
OSTIA	Operational Sea Surface Temperature and Sea Ice Analysis
PIG	Pine Island Glacier
PSK	Pope, Smith, Kohler (polynya)
RACMO(2.3)	Regional Atmospheric Climate Model (version 2.3)
RH	Relative Humidity
RMSE	Root Mean Square Error
SAM	Southern Annular Mode
SON	September, October, November
SST	Sea Surface Temperature
TI	Thurston Island (AWS)
UTC	Coordinated Universal Time

1

INTRODUCTION

Globally 2016 and 2015 have been the two warmest years since the industrial revolution; global mean temperatures in 2016 were 0.77 °C above the 1961-1990 average (Met Office, 2017). The global climate is changing and the effects of this are starting to be observed around the world. Global sea levels continue to rise at a rate of ~3.2 mm per year and are now ~20 cm above the level they were in 1900 (Church et al., 2013). Across many parts of the world temperatures are rising; in Antarctica there is a dipole between rapid warming of the Antarctic Peninsula and little to no warming in East Antarctica (Steig et al., 2009). Temperatures at Byrd station in West Antarctica have been shown to be warming at ~0.5 °C per decade since 1957 (Bromwich et al., 2013a). Steig et al. (2009) find that West Antarctica and the Antarctic Peninsula are seeing the most rapid temperature increases in the southern hemisphere, the map in Fig. 1.1 depicts their reconstruction of 1979-2003 decadal temperature trends over Antarctica.

Many of the glaciers and ice shelves in the region have been shown to be retreating and losing mass (Shepherd, 2001; Mouginot et al., 2014; Rignot et al., 2014). The mass balance of a glacier is determined by the difference between the amount of snow accumulating on top of the glacier and the loss of ice through processes such as basal melt, iceberg calving, sublimation, and surface melt (Rignot et al., 2008; Pritchard et al., 2012). In the Amundsen Sea region large increases in the rate of basal melt at the ocean interface are driving rapid glacial retreat (Rignot et al., 2008; Mouginot et al.,

2014). Surface melting events are uncommon but Nicolas et al. (2017) observe a rare, prolonged surface melt event across many low lying parts of the West Antarctic ice sheet, and indicate that such events will become more common as climate changes. More frequent surface melt events combined with a continued increase in basal melt rate will lead to a larger mass balance deficit and the rate of ice loss will accelerate. Atmospheric, oceanographic and glaciological research into the processes driving glacial retreat in West Antarctica is therefore crucial in order to constrain estimates of future sea level rise.

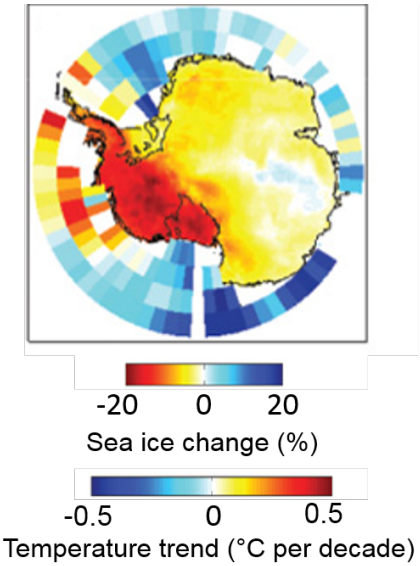

Figure 1.1: The 1979-2003 average decadal temperature change across Antarctica. Over the ocean the colour scale corresponds to sea ice changes over the same period. Taken from Steig et al. (2009).

1.1 GLACIAL RETREAT IN WEST ANTARCTICA

The map in Fig. 1.2 shows West Antarctica and some of the key glaciers which have been rapidly retreating in recent years. Mercer (1978) first hypothesised that anthropogenic climate change could lead to the disintegration of the west Antarctic ice sheet. While, Hughes (1981) described the Amundsen Sea sector (see Fig. 1.2) as the 'weak underbelly of West Antarctica' due to both its glaciers lacking the protection afforded by a large ice sheet or shelf and the sub-glacial topography deepening inland.

The water contained within the west Antarctic ice sheet has the potential to raise

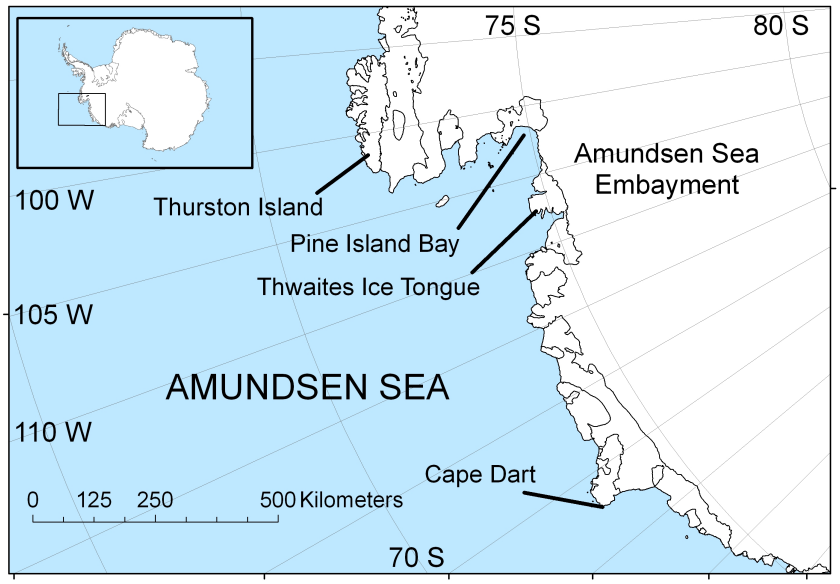

Figure 1.2: The Amundsen Sea Embayment with key locations marked. The inset map shows the location of the Amundsen Sea sector within Antarctica. Source iSTAR website.

global sea levels by up to 3.3 metres (Bamber et al., 2009). In the latter part of the 20th century evidence from satellite observations began to show a thinning of glaciers within the Amundsen Sea Embayment (ASE) (Wingham et al., 1998). Shepherd (2001) showed that the trunk of Pine Island Glacier (PIG) was thinning at a rate of 1.6 metres per year. Alongside these observations were oceanographic measurements showing that relatively warm circumpolar deep water (CDW) was present at the front of PIG, making it susceptible to basal melt (Jacobs and Hellmer, 1996). Pritchard et al. (2012) revealed that the continental shelves of the Amundsen and Bellingshausen Seas are unique around Antarctica, as these are the only regions where warm CDW is persistently and extensively transported on to the continental shelf, resulting in the warm sea floor ocean temperatures seen in Fig. 1.3. The large grey circle in the Pine Island drainage basin and dark red colours of the Amundsen Sea ice shelves in Fig. 1.3 also reveal there has been a rapid thinning and a large loss of grounded ice in recent decades (Pritchard et al., 2012). Rignot et al. (2013) have shown that, due to the intrusion of CDW on to the continental shelves of West Antarctica, ten ice shelves in the region are responsible for ~50% of Antarctic basal melt, despite comprising only 8% of the total ice shelf area. Recent estimates suggest that PIG is thinning at a rate of up to 7 metres per year (Pritchard et al., 2012), and the rate of ice loss has been increasing in recent years (Rignot et al., 2008). The loss of ice from glaciers

within the Amundsen Sea region is thought to contribute towards approximately 10% of global sea level rise (Mouginot et al., 2014), equivalent to an additional ~0.3 mm per year (Shepherd et al., 2012). Further, Rignot et al. (2014) find that, due to the reverse sloping bedrock underlying many of the glaciers in West Antarctica, there is no major obstacle to prevent rapid glacial retreat continuing in the coming decades. Recent modelling work has shown that PIG alone may contribute a further 3.5-10 mm of global sea level rise over the next two decades (Favier et al., 2014).

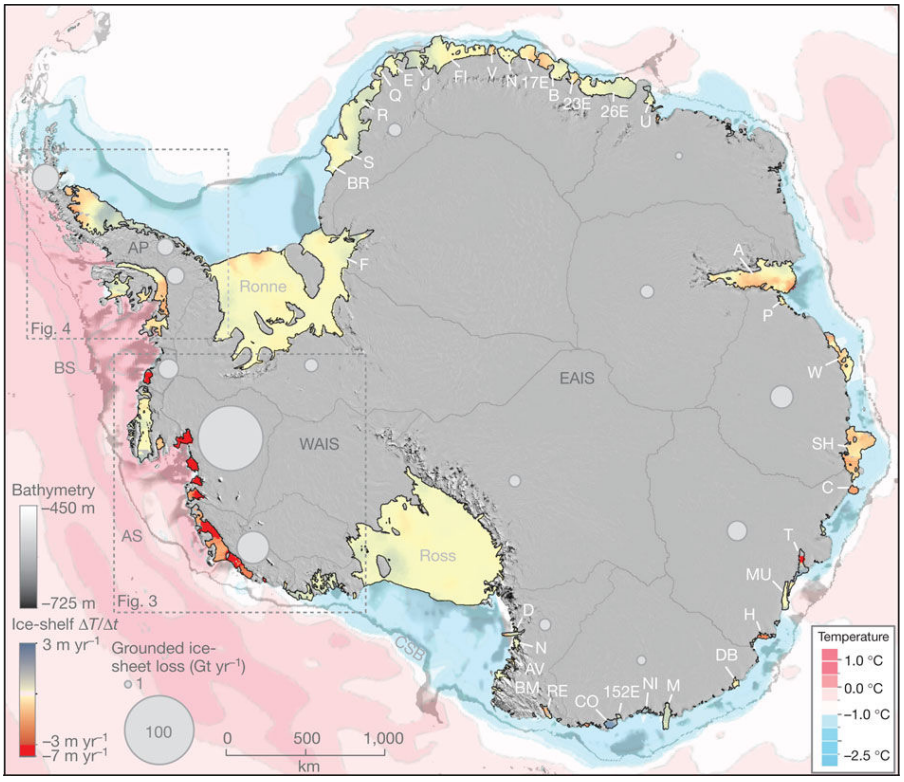

Figure 1.3: A map of Antarctica showing the rate of ice loss and sea floor ocean temperatures. The ocean colour contours show the time-averaged bottom water potential temperature around Antarctica. On the ice shelves the colour contour indicates the thickness change, with red colours indicating thinning and blue thickening. The grey circles show the magnitude of grounded ice loss from drainage basins that lost mass between 1992 and 2006. Taken from Pritchard et al. (2012).

1.2 VARIABILITY OF GLACIAL RETREAT IN THE AMUNDSEN SEA

The glaciers of the Amundsen Sea sector are buttressed and protected by relatively small floating ice shelves (Bamber et al., 2009). In the case of PIG the ice shelf extends approximately 400m below the surface of the ocean and during the 1940s it is thought to have become detached from a bathymetric ridge (Jenkins et al., 2010; Turner et al., 2017) (see Fig. 1.4). Between the ice shelf and the sea bed there is a cavity (which grew following the detachment from the ridge), and the base of the ice shelf (including in this cavity) is exposed to the relatively warm CDW, that is approximately 3 °C above the in-situ freezing temperature (Jenkins et al., 2010). As such, the main driver of glacial retreat in this region is basal melt (Pritchard et al., 2012; Rignot et al., 2014). As shown in Fig. 1.4, since the detachment from the bathymetric ridge PIG has been grounded on bedrock that slopes downwards with distance inland — a retrograde slope. This is an unstable position and has encouraged the recent acceleration of glacial retreat (Favier et al., 2014). Joughin et al. (2014) show that the collapse of Thwaites glacier is likely already underway due to the retrograde slope of the bedrock there, though the rate of retreat is still influenced by ocean temperatures and basal melt rates. Such retrograde slopes are observed beneath many of the glaciers in the Amundsen Sector (Rignot et al., 2014), small perturbations in the gradient of the slope may also be important to the rate of retreat (Nias et al., 2016).

The schematic in Fig. 1.4 shows some of the key processes and bedrock features that are thought to be important in controlling the rate of retreat of ice shelves such as Pine Island ice shelf. The CDW is transported on to the continental shelf and towards the ice shelves within the ASE through glacially carved bathymetric troughs at the continental shelf edge (Wåhlin et al., 2010; Assmann et al., 2013). Thoma et al. (2008) use an ocean model and link the amount of CDW transport to the strength of the zonal winds at the shelf break. When westerly winds are weaker there is less CDW transported on to the shelf and hence less warm water and a lower melt rate within the ice shelf cavity (Thoma et al., 2008). In Fig. 1.5 it is clear that there is significant inter-annual variability in the temperature of ocean water close to PIG. Dutrieux et al. (2014) show that in 2012 when there were anomalously easterly winds at the shelf break there was an associated drop in deep ocean temperatures within

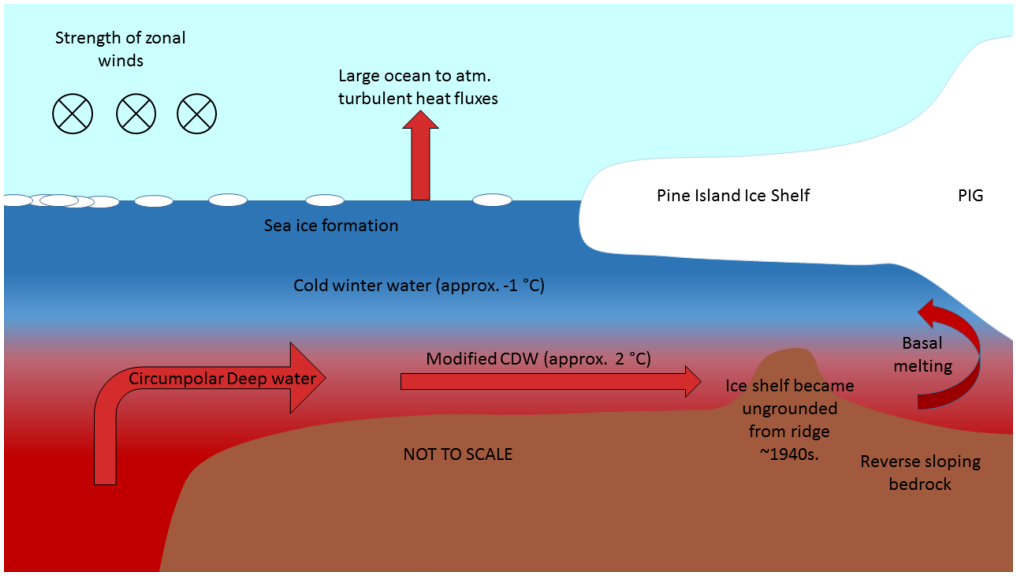

Figure 1.4: A schematic showing the key processes that are thought to be important in controlling the rate of retreat of Pine Island ice shelf. Adapted from Biddle et al. (2017).

Pine Island Bay. However, ocean buoy observations close to PIG reported in Webber et al. (2017) show a cold period between October 2011 and March 2013, and yet there is no evidence of an associated decrease in on-shelf heat transport in observations at the continental shelf edge. Instead, they suggest that there are local processes close to PIG that are important in determining the heat content within the ice shelf cavity. Sea ice formation and changes in the local ocean circulation can generate or advect cooler water towards PIG and its ice shelf (Webber et al., 2017). Christianson et al. (2016) show that the melt rate of Pine Island ice shelf does slow in response to this cool period but only by a small amount.

St-Laurent et al. (2015) use an ocean model to show that local cooling of ocean waters in coastal polynyas in the eastern Amundsen Sea may influence the temperature of water within the ice shelf cavity of PIG and impact the basal melt rate. Features such as coastal polynyas and sea ice formation are strongly linked to the local atmospheric circulation in the vicinity of PIG (e.g. Stammerjohn et al., 2015), but despite this there has been little research investigating the meteorological conditions associated with such events in the Amundsen Sea region. The relative importance of local and remote mechanisms in determining the melt rate remains unclear but it is noteworthy that atmospheric interactions are likely crucial, either through large scale changes at the shelf edge or smaller scale effects and sea ice formation close to PIG.

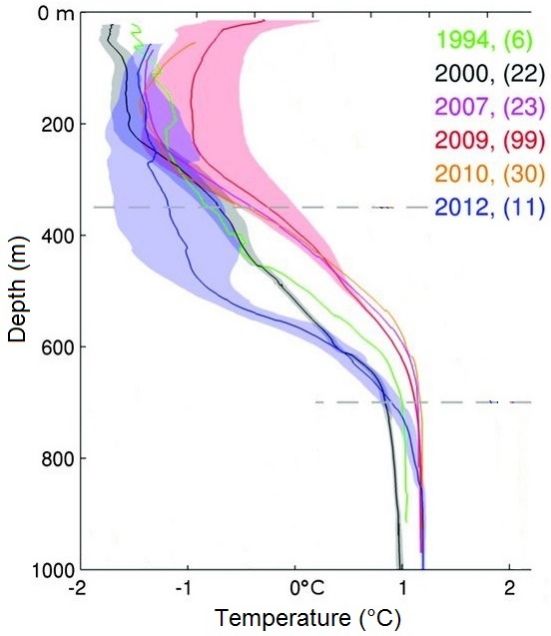

Figure 1.5: Mean ocean temperature profiles within Pine Island Bay for years when research vessel observations are available. The dashed line show the approximate depth of the base of the ice shelf and top of the bathymetric ridge, the water between the two dashed lines is therefore likely to be that which enters the ice shelf cavity. Note the pronounced cooling in 2012 and significant interannual variability within the 400-700 m layer. Adapted from Dutrieux et al. (2014).

1.3 THE CLIMATE OF THE AMUNDSEN SEA EMBAYMENT

In general terms the climate of West Antarctica is cold, average annual air temperatures are approximately -15 to -25 °C (Nicolas and Bromwich, 2011), and it is rare for temperatures to reach 0 °C even in summertime. In winter there is 24 hour darkness over much of the inland portion of the Amundsen Sea sector, with typical conditions being a very stable boundary layer and frequent katabatic winds descending down the complex orography of the ASE. The region is also affected by frequent cyclones, both mesoscale cyclones that form during during cold air outbreaks (Papritz et al., 2015) and synoptic scale storms (Fogt et al., 2012).

1.3.1 THE AMUNDSEN SEA LOW

The West Antarctic region has been described as the 'pole of variability', as it displays the greatest variability in surface pressure in the southern hemisphere (Connolley,

1997). This is primarily due to annual cycles in the dominant mode of synoptic-scale variability in the region, the Amundsen Sea Low (ASL). The ASL is a semi-permanent area of low pressure that is formed due to both the high topography and non-axisymmetric nature of the Antarctic continent (Lachlan-Cope et al., 2001). The location of the ASL influences surface temperatures, surface winds, sea ice extent and precipitation within the ASE (Hosking et al., 2013; Turner et al., 2013; Stammerjohn et al., 2015). We elaborate below and in section 1.3.3 with regards precipitation.

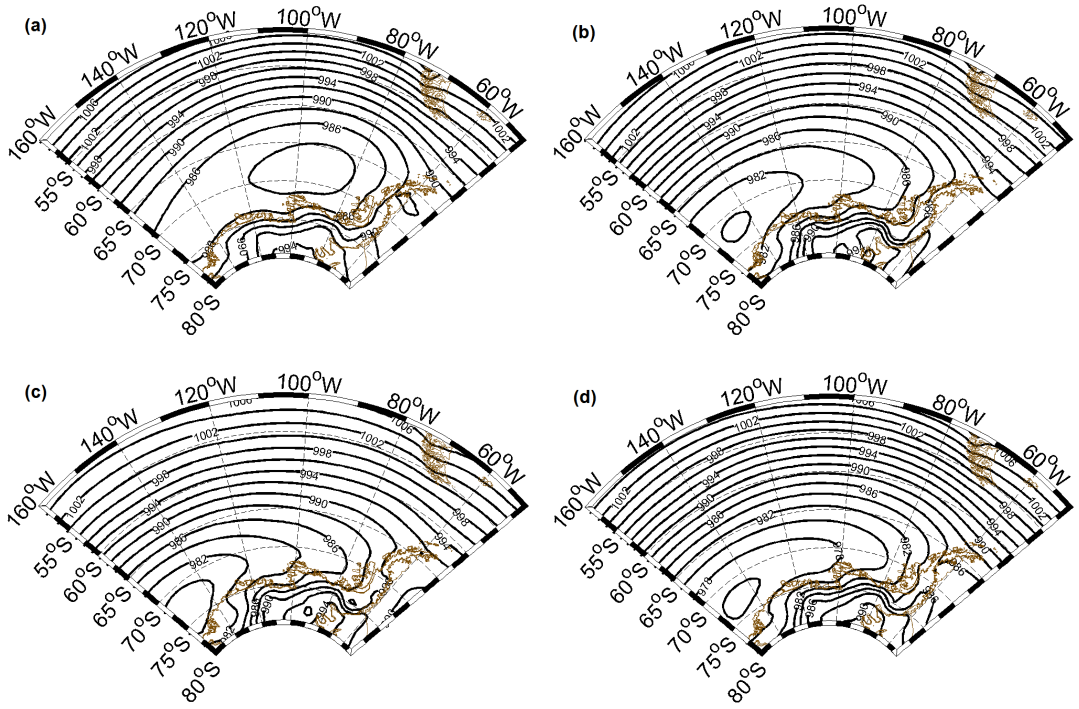

Figure 1.6: ERA-Interim mean sea level pressure data showing the 1979-2012 mean location of the ASL in: (a) summer (DJF), (b) autumn (MAM), (c) winter (JJA), and (d) spring (SON).

The ASL has been shown to undergo an annual cycle in terms of its longitudinal and latitudinal position (Fogt et al., 2012; Hosking et al., 2013; Turner et al., 2013). In austral summer the ASL is located in its most easterly position towards the Amundsen/Bellingshausen Sea boundary at 100°W (Fig. 1.6a). Then in autumn it shifts westwards and is located on the boundary of the Ross and Amundsen Seas at ~150°W (Fig. 1.6b), where it remains through winter and spring (Figs. 1.6c and 1.6d). The most westerly location of the ASL is typically recorded in the winter season (JJA). The latitudinal position of the ASL also varies, it is typically 5°S further south in winter than in summer, the annual mean latitude is approximately 70°S (Fogt et al., 2012; Turner et al., 2013; Hosking et al., 2013). For the ASE, the wintertime

position of the ASL towards the Ross Sea leads to frequent mild, maritime, northerly wind outbreaks on the eastern side of the Amundsen Sea. This gives the ASE what has been described as a 'coreless winter' whereby the average temperatures remain near constant through late autumn and mid-winter (van Loon, 1967; Nicolas and Bromwich, 2011). In summer the easterly position of the ASL means that the ASE is influenced by more frequent southerly winds and cold air outbreaks. These cold air outbreaks are assoicated with mesocyclone formation, and Carrasco et al. (2003) show a summertime peak in the number of mesocyclones observed in the Amundsen/Bellingshausen sector. However, these cold air outbreaks are typically less severe than the wintertime mild air outbreaks as there is less of a difference between the marine and continental air masses (Hosking et al., 2013). The longitudinal cycle also means there is an annual cycle in the strength of zonal winds at the shelf break with stronger westerly winds in winter when the ASL is located west of the ASE (Thoma et al., 2008).

1.3.2 TELECONNECTIONS AND THE INFLUENCE OF LARGE SCALE CLIMATE MODES

Being located at the southern edge of the Pacific Ocean the climate of the ASE can also be influenced by the El Niño Southern Oscillation (ENSO) and the Southern Annular Mode (SAM). ENSO can be in either an El Niño or La Niña phase; the minimum threshold for an El Niño event is a +0.4 °C sea surface temperature anomaly in the central Pacific, whereas La Niña is a -0.4 °C anomaly (Trenberth, 1997). Turner (2004) reviews the influence of ENSO on climate around Antarctica. He shows that in West Antarctica the effects are predominantly seen in wintertime, when through the Pacific-South America teleconnection the region tends to experience higher mean sea level pressure. Kwok and Comiso (2002) show that this pressure pattern is linked to a strengthening of southerly winds over the Bellingshausen Sea sector and associated negative temperature anomalies.

The SAM is the principal mode of variability in Southern Hemisphere atmospheric circulation, it is the leading empirical orthogonal function in a number of atmospheric fields including; zonal wind, surface pressure, geopotential height and surface temperature (see Thompson and Wallace, 2000a, and references therein).

From station observations the SAM is defined as the difference between the mean sea level pressure at 40°S and 65°S (Gong and Wang, 1999). The positive phase of SAM results in a strengthening and poleward shift of the Southern Ocean storm track, with a decrease in surface pressure and stronger westerly winds close to Antarctica (Thompson and Wallace, 2000a; Turner, 2004; Gillett et al., 2006). In recent decades there has been a trend towards the positive phase of SAM with an increase in the strength of westerly winds around Antarctica (Thompson and Wallace, 2000b; Marshall, 2003).

Fogt et al. (2011) show that the phase of both the SAM and ENSO is important in determining whether any impacts are felt in West Antarctica. It is only when the SAM and ENSO are in phase (La Niña and positive SAM or El Niño and negative SAM), or if there is a strong ENSO event during neutral SAM conditions, that significant pressure anomalies are observed in West Antarctica (Fogt et al., 2011). When La Niña and a positive phase of SAM occur together there is lower pressure than usual over much of West Antarctica. Conversely, when El Niño and a negative SAM event occur simultaneously there is a positive pressure anomaly over the region and increased blocking in the south Pacific (Fogt et al., 2011). The perturbation of the sea level pressure field during a strong La Niña event is thought to have caused anomalous easterly winds in the ASE during 2011 (Dutrieux et al., 2014). This reduced the transport of CDW on to the continental shelf and hence, cooler ocean temperatures were observed in the vicinity of PIG (Dutrieux et al., 2014).

1.3.3 PRECIPITATION AND MARINE AIRMASS INTRUSIONS

Accumulation on glaciers in West Antarctica is largely determined by precipitation as processes such as sublimation, wind-blown snow and surface melt are small in comparison (Lenaerts et al., 2012b). Ice cores drilled to measure accumulation across the region are sparse (Medley et al., 2013; Favier et al., 2013), while in-situ observations of precipitation are non-existent, as such there are large uncertainties attached to accumulation estimates in the region. These uncertainties contribute to uncertainties in glacier mass balance and therefore the regions contribution to global sea level rise (Turner et al., 2017). West Antarctic annual accumulation is generally a function of elevation, a recent radar derived accumulation field on PIG found

accumulation varies from approximately 0.3 metres per year on the higher elevation portion of PIG (above 1500 metres) to approximately 0.7 metres per year (below 500 metres elevation) (Medley et al., 2014). However the radar survey of Medley et al. (2014) had relatively sparse coverage of PIG and as such accumulation estimates remain uncertain, particularly at low elevations where both radar observations and ice core estimates are very sparse.

In the absence of reliable observations of accumulation a variety of atmospheric models have been used to generate basin wide accumulation estimates, most commonly the Regional Atmospheric Climate Model (RACMO) (e.g. van de Berg et al., 2006; van den Broeke et al., 2006; Shepherd et al., 2012; Rignot et al., 2013; van Wessem et al., 2014b). Medley et al. (2014) present evidence that RACMO version 2.3 satisfactorily reproduces the radar derived annual accumulation estimates over PIG and Thwaites Glacier. Although at low elevations, (where even radar coverage is extremely sparse), there are relatively large discrepancies between RACMO2.3 and the radar derived estimates. Despite the widespread use of RACMO in Antarctica, there have been relatively few studies that utilise observations of annual accumulation from ice cores to assess the model performance, one example is van de Berg et al. (2006) although this study didn't include observations from coastal West Antarctica.

Marine airmass intrusions are responsible for advecting moisture towards the Antarctic continent and it is mostly during such events that clouds form and precipitation falls within the ASE (Nicolas and Bromwich, 2011). Due to the more frequent maritime air outbreaks in wintertime it is shown that autumn and winter precipitation is greater than summer precipitation across much of coastal west Antarctica (Nicolas and Bromwich, 2011). Fig. 1.7 shows the annual cycle of precipitation (minus evaporation) from global meteorological reanalysis products and RACMO2.3. The austral autumn (MAM) and winter (JJA) seasons each account for ~30% of annual accumulation while summer (DJF) only accounts for 15%. This seasonal cycle has also been shown in seasonally resolved ice core accumulation data at four different locations in West Antarctica (Thomas and Bracegirdle, 2014). The seasonal cycle in precipitation is driven by the changing longitudinal location of the ASL. When the ASL is centred at ~100°W in summer there are fewer marine airmass intrusions with the wind direction tending to be southerly or easterly over PIG, as the climatological cyclone is located to the northeast. While less frequent, summertime

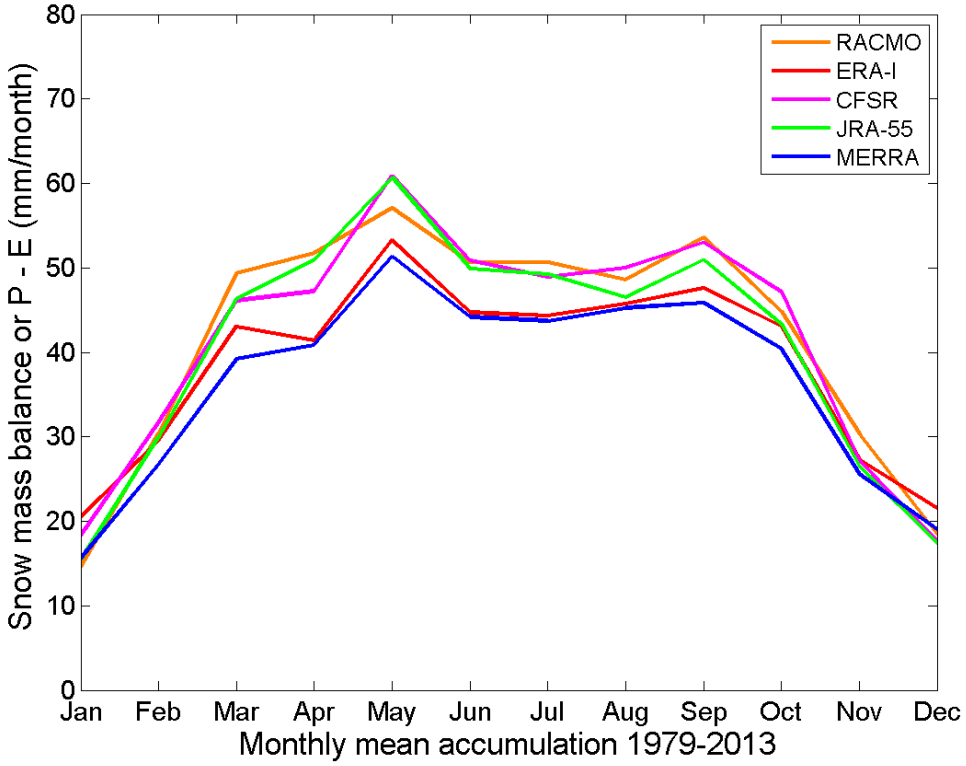

Figure 1.7: The 1979-2013 monthly mean accumulation over PIG (defined as 74°S to 77°S and 102°W to 86°W) from RACMO2.3 and four global reanalysis products.

marine airmass intrusions such as the one that occurred in January 2016 can lead to short periods (~10 days) of surface melt in lower elevation coastal areas of the ASE (Nicolas et al., 2017). During this event a blocking ridge of high pressure disrupted the circumpolar westerly flow and brought mild and moist northerly winds across a large part of West Antarctica.

1.3.4 KATABATIC WINDS AND OROGRAPHIC FLOWS

Over the continental interior of Antarctica the highly reflective ice surface and low sun angle cause a negative radiation budget (King and Turner, 1997). The near-surface air therefore becomes colder than the air above it by as much as ~30 °C and is negatively buoyant (van den Broeke and van Lipzig, 2003). On sloping terrain this results in a buoyancy driven flow that will accelerate as it travels downslope — it is this which is called a katabatic flow or katabatic wind (Renfrew and Anderson, 2006). The surface wind direction over Antarctica is therefore typically downslope from the high continental interior to the low lying coastal regions (Parish and Bromwich, 1987;

Renfrew and Anderson, 2002). The coastline in the Amundsen Sea region has been identified as an area of katabatic wind convergence (Carrasco et al., 2003; Parish and Bromwich, 1987). Convergence of the surface wind field leads to stronger surface winds and so larger surface heat fluxes, often triggering atmospheric convection and this can in turn lead to the generation of mesocyclones, Carrasco et al. (2003) show that mesocyclone formation is common in coastal parts of the Amundsen Sea region.

On the Antarctic Peninsula orographic flows, in particular foehn winds, have been shown to cause widespread surface melt events in areas such as the Larsen-C ice shelf (Elvidge et al., 2015). During a foehn event, air cools at the moist adiabatic lapse rate as it travels up slope and then warms more rapidly, at approximately the dry adiabatic lapse rate, as it descends; alternatively warm air can be drawn down from aloft isentropically (Elvidge and Renfrew, 2016), either way near-surface air temperatures on the downslope side of the barrier are warmer. On the Antarctic Peninsula foehn events are typically associated with westerly winds and as such the warming and melt events impact the eastern side of the Peninsula (Elvidge et al., 2015; Elvidge and Renfrew, 2016). In the Amundsen Sea sector despite the orography being relatively complex and steep, especially around the coastline, there are no significant topographic barriers that produce the type of foehn flows described by Elvidge et al. (2015).

Low-level jets (LLJs) are defined as relative wind speed maxima that are more than 2 $m\ s^{-1}$ faster than the wind speed minima above and below it (Stull, 1988). Stull (1988) outlines how through the thermal wind relationship, mesoscale temperature gradients over sloping terrain can cause a wind speed maxima in the near-surface layer. Such surface temperature gradients are common in the Amundsen Sea sector where, in summer, glaciers and ice shelves are often bordered by open ocean with a surface temperature of approximately -1 °C. LLJs have been reported over Antarctic sea ice, such as those described by Andreas et al. (2000) in the Weddell Sea. Given that Andreas et al. (2000) find LLJs in 132 of 164 tethersonde profiles it is expected they will be observed in the Amundsen Sea sector too.

1.4 SEA ICE AND POLYNYAS IN THE AMUNDSEN SEA

Jacobs and Comiso (1997) describe the seasonal sea ice cycle in the Amundsen Sea.

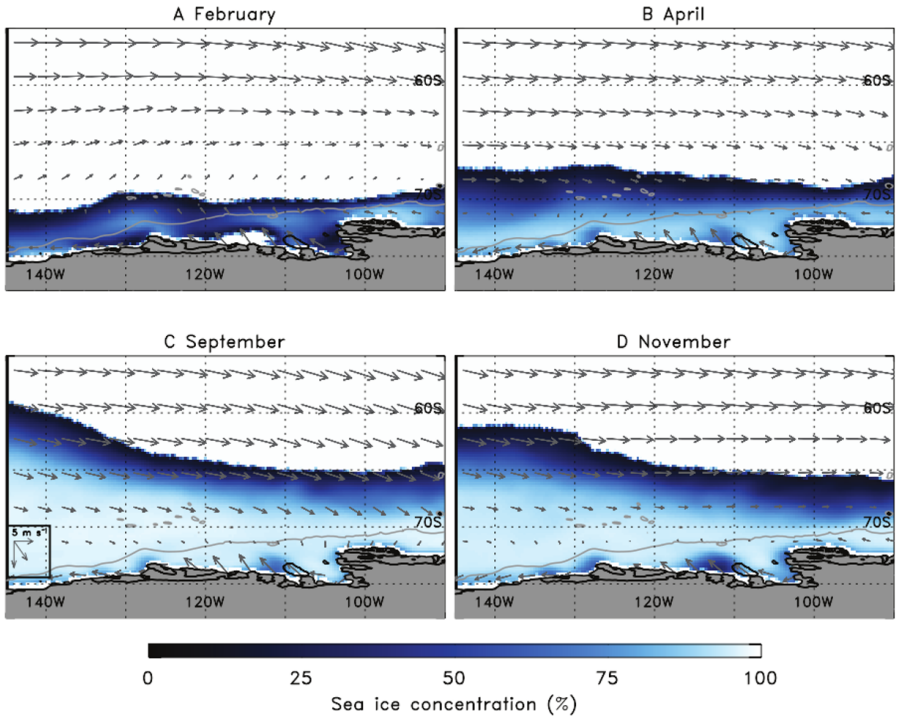

Figure 1.8: The 1979-2012 mean sea ice concentration for February, April, September and November. The sea ice concentration is derived from the Goddard Space Flight Center bootstrap scanning multi-channel radiometer — special sensor microwave / imager. The 1979-2012 monthly mean wind vectors from ERA-Interim are also shown. Note to the north white indicates open ocean. Figure taken from (Stammerjohn et al., 2015).

The sea ice season is long in the near shore region of the ASE with an average of over 300 days of ice cover (Jacobs and Comiso, 1997). The summertime minimum typically occurs in late February or early March with the winter maximum in September. Fig. 1.8 shows the seasonal cycle of sea ice in the Amundsen Sea. In February there is a widespread reduction in sea ice concentration and a more southerly ice edge (~70°S), whereas in September sea ice concentrations are high and the ice edge advances to ~65°S (see Fig. 1.8). In September and November the sea ice is zonally asymmetric with the ice edge further north in the west of the Amundsen Sea sector (Fig. 1.8). This is due to the location of the ASL towards the Ross Sea in winter and spring with more frequent northerly winds in the eastern Amundsen Sea pushing sea ice further south in this region.

Usually some sea ice remains on the continental shelf throughout the summer, although in the summers of 1992, 2003 and 2010 there was very little sea ice remaining in the eastern Amundsen Sea (Stammerjohn et al., 2015). As noted by Jacobs and

Comiso (1997) when summer sea ice concentration falls to a very low minima there is a high proportion of first year ice on the continental shelf in the following season. A large and early summer retreat is linked to a later autumn advance as the ice free ocean water can warm sufficiently to delay the onset of autumn freeze-up (Stammerjohn et al., 2015)

1.4.1 POLYNYAS

As described previously it is thought that coastal polynyas in the Amundsen Sea may be important in determining the heat content of water in the vicinity of PIG (St-Laurent et al., 2015), therefore it is important to outline what polynyas are, how they form, and how they impact both the ocean and the atmosphere in Polar Regions.

The word polynya originates from Russia, it describes an area of open water within sea ice. Polynyas regularly occur in the Polar Regions, they are typically bounded by pack ice, ice shelves or coastlines. They are non-linear in shape, differentiating them from smaller leads in sea ice which are cracks formed through deformation (Renfrew, 2006). Polynyas vary in size, they can be fairly small from 10 km^2, or very large, up to ~100,000 km^2 (Morales-Maqueda et al., 2004). They are often divided into two groups; sensible and latent heat polynyas, depending on the mechanism that forms and maintains the area of open water.

Sensible heat polynyas are most often observed in regions of open ocean away from coastlines and are generated through the upwelling or advection of relatively warm ocean water (Smith et al., 1990; Morales-Maqueda et al., 2004). Typically this occurs in the vicinity of complex bathymetry and the polynya is opened through basal melting of the sea ice, for example in the Cosmonaut Sea and over the Maud Rise in the Weddell Sea (Renfrew, 2006). The warm ocean water also acts to limit the reformation of sea ice and as such sea ice production is limited within sensible heat polynyas (Morales-Maqueda et al., 2004; Renfrew, 2006; Weijer et al., 2017).

Latent heat polynyas, or alternatively coastal polynyas are formed when persistent offshore winds or ocean currents transport sea ice away from the shoreline or a barrier such as fast ice or ice shelves (Morales-Maqueda et al., 2004; Fiedler et al., 2010). They are common in regions of strong offshore katabatic winds such as the Ronne and Ross ice shelves (Renfrew, 2006). Strong winds and large ocean to atmosphere

temperature gradients are the typical meteorological conditions associated with latent heat polynyas and as such sea ice production is often large (Morales-Maqueda et al., 2004; Fiedler et al., 2010). In the Weddell Sea total annual sea ice production within a group of coastal polynyas has been estimated to be 240 km^3 (Drucker et al., 2011). To our knowledge no such estimate has been calculated for Amundsen Sea polynyas, though Webber et al. (2017) show sea ice production rates of up to 20 metres per day close to PIG. Sea ice production cools the near-surface ocean which is often already at or close to its freezing temperature, and so, latent heat polynyas can become covered or partially covered by thin sea ice (e.g. Fiedler et al., 2010). Their name suggests that the latent heat released during sea ice formation is important in the maintenance of these polynyas, however it is the continual export of sea ice away from the coastline or barrier that keeps them open (Renfrew, 2006). Therefore from now onwards we refer to them as coastal polynyas.

Both sensible heat and coastal polynyas have been observed within the ASE. Mankoff et al. (2012) find that relatively warm and buoyant meltwater plumes melt sea ice close to the front of PIG ice shelf can create sensible heat polynyas ~10 km in size. Wind driven coastal polynyas are frequently observed in the ASE, and can be seen regularly in Moderate Resolution Imaging Spectroradiometer (MODIS) satellite imagery. The image from September 2016 in Fig. 1.9 shows open water along the eastern shore of the Amundsen Sea Embayment, strong easterly winds lead to the transport of sea ice away from the coastline and maintained the area of open water.

1.4.2 HOW DO POLYNYAS AFFECT THE ATMOSPHERE?

The areas of open water within polynyas allow efficient exchange of heat and moisture between the atmosphere and the ocean. Heat fluxes can be between 1 and 2 orders of magnitude larger within a polynya than through the surrounding sea ice (Renfrew et al., 2002). When polynyas occur in wintertime very large turbulent heat fluxes are possible due to the large ocean-atmosphere temperature gradient.

The schematic in Fig. 1.10 shows the key processes that produce and maintain a coastal polynya, along with the typical impact they have on the overlying atmosphere. In coastal polynyas, where strong winds transport sea ice away from a barrier, cold near-surface air is advected from the nearby landmass/ice shelf over the relatively

Figure 1.9: A MODIS satellite image showing coastal polynya formation in the eastern Amundsen Sea on 30th September 2016. MODIS visible satellite imagery data from (Scambos et al., 2001).

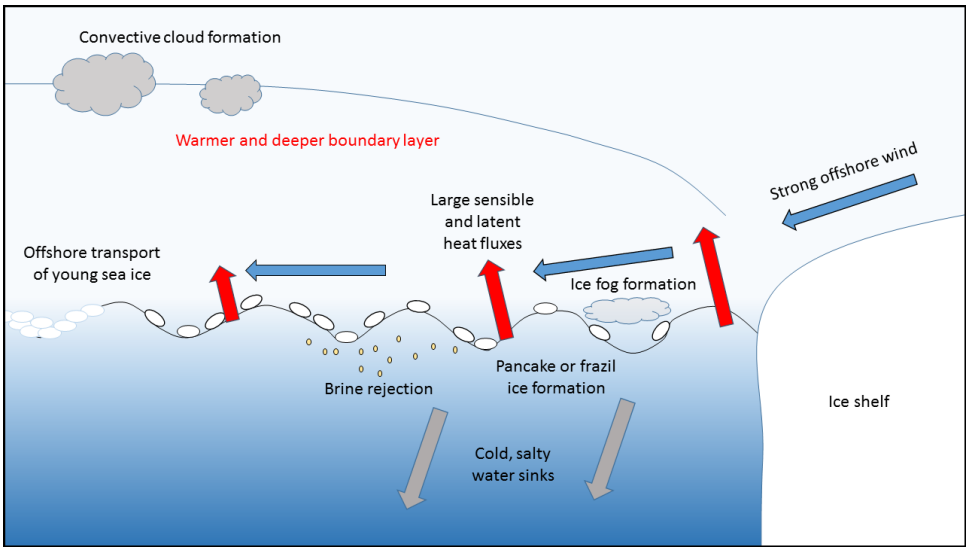

Figure 1.10: A schematic showing the typical processes occuring within a coastal polynya. Adapted from Fiedler (2010).

warm ocean. The combination of strong winds and a large ocean to atmosphere temperature gradient drives large turbulent heat fluxes from the ocean to the atmosphere. These fluxes continue over the width of the polynya, and the input of heat at the surface triggers convective mixing, so gradually the depth of the boundary

layer increases with fetch (Fiedler, 2010). This is known as a convective internal boundary layer, which is typically capped by a dry, stable layer (Renfrew and King, 2000). With increasing fetch over the polynya the ocean-atmosphere temperature gradient gradually reduces (the near-surface air temperature rises) and so the sensible and latent heat fluxes reduce. Over distances of tens of kilometres the reduction in total turbulent heat flux is approximately 20% (Renfrew et al., 2002). The large moisture fluxes over coastal polynyas can also lead to the formation of convective clouds or condensation fog (Smith et al., 1983; Walter, 1989). Larger coastal polynyas can impact the mesoscale atmospheric circulation and initiate processes that result in mesocyclone formation and/or intensification of synoptic scale cyclones (Walter, 1989; Smith et al., 1990; Morales-Maqueda et al., 2004).

In sensible heat polynyas strong winds are not involved in the formation of the polynya and as such the wind speeds and turbulent heat fluxes are often smaller than in coastal polynyas. They do though remain elevated above those through surrounding sea ice and the fluxes of heat and moisture are large enough for fog and cloud to form which can alter the surface radiation budget (Smith et al., 1990).

1.4.3 HOW DO POLYNYAS AFFECT THE OCEAN?

Within coastal polynyas the large fluxes of sensible and latent heat to the atmosphere lead to sea ice formation, initially of grease, frazil, and then pancake ice. The wind and/or ocean currents then transport this ice away from the barrier and the process of sea ice formation is continuous within the coastal polynya. Hence they are sometimes referred to as 'sea ice factories' (e.g. Fiedler et al., 2010). Through the process of brine rejection, the salinity of the surface ocean increases. This increased salinity makes the ocean water denser and if this process continues for a sustained period, this cold, saline water can sink to form high salinity shelf water (e.g. Petty et al., 2014). This then combines with other water masses and is transported off the continental shelf to form Antarctic Bottom Water, for example in the Weddell and Ross Seas (Renfrew, 2006; Kusahara et al., 2010; Mathiot et al., 2012). Coastal polynyas are therefore important locations for ventilation of the deep ocean and in driving the global thermohaline circulation (Renfrew et al., 2002; Morales-Maqueda et al., 2004).

Sensible heat polynyas in the open ocean can also drive the formation of deep

water. The upwelling warm water which melts the sea ice loses heat to the overlying atmosphere. As this water cools it becomes denser and can sink once again to start an overturning process within a convective cell (Morales-Maqueda et al., 2004). It is this convective cell which can help to maintain the polynya through a continuous upwelling of warm water from depth.

1.4.4 COASTAL POLYNYAS AND ICE SHELVES AROUND ANTARCTICA

It has been postulated that the duration and size of coastal polynyas can influence the melt rate of various ice shelves around Antarctica. Khazendar et al. (2013) and Gwyther et al. (2014) have shown that the melt rate of Totten glacier in East Antarctica is influenced by the annually varying size of the coastal polynya that borders the ice shelf. In years when the polynya is large, there is a greater volume of colder winter water generated. In modelling studies this has been transported beneath the ice shelf (after mixing with warmer CDW) and reduces the temperature of the water within the ice shelf cavity (Khazendar et al., 2013; Gwyther et al., 2014). This means there is less energy available to melt the ice shelf and hence the melt rate decreases (Khazendar et al., 2013; Gwyther et al., 2014).

Similarly, in the vicinity of the George VI ice shelf in the Bellingshausen Sea a modelling study by Holland et al. (2010) has shown that sea ice production and ocean-atmosphere interaction tend to dominate in determining the melt rate variability of the ice shelf. The modelled depth of the cold, near-surface water is influenced by the amount of sea ice production (and so atmospheric conditions). It is shown that the years with the largest melt rates are when the cold water is shallower, this increases the exposure of the ice shelf base to warm, CDW (Holland et al., 2010). Elsewhere, the melt rate of Wilkins ice shelf on the western side of the Antarctic Peninsula is also thought to be influenced by local atmospheric variability (Padman et al., 2012). The Wilkins ice shelf is relatively thin (~ 170m) and sits within a layer of cold winter water. The basal melt rate of Wilkins ice shelf was shown to decrease dramatically around the year 2000 when either the base of ice shelf thinned sufficiently to sit within the layer of cold winter water, or the depth of cold water increased (Padman et al., 2012). Padman et al. (2012) go on to explain that accurately resolving wind speed and direction close to the coastline (using a high resolution atmospheric model) is important if we are to

accurately model the melt rate of Wilkins ice shelf.

1.4.5 A CHANGING SEA ICE SEASON IN THE AMUNDSEN SEA

The Amundsen Sea sits between two regions with large but opposing sea ice trends. The ice season to the west in the Ross Sea has increased by 2 months since 1979 whereas in the neighbouring Bellinshausen Sea it has decreased by 3 months (Stammerjohn et al., 2012; Turner et al., 2015). The variability of sea ice extent in the Amundsen Sea is large, and as such trends in sea ice extent since the start of the satellite era can be difficult to detect (Stammerjohn et al., 2015). This variability is largely wind driven but with ocean-feedbacks also involved (Holland and Kwok, 2012; Stammerjohn et al., 2015). Stammerjohn et al. (2015) examine long term changes in sea ice extent within the Amundsen Sea; over the period 1979-2013 they show there has been a reduction in the length of the sea ice season, both north of the continental shelf and within two coastal polynyas. At the shelf edge in both spring and autumn there has been a reduction in the amount of ice advected into the region from the west, this makes the ice cover more vulnerable to summer melting (Stammerjohn et al., 2015). On the continental shelf an increase in the strength of south-easterly winds in springtime reduces ice concentrations within coastal polynyas close to Pine Island ice shelf. The sea ice season within these two areas has reduced by 1-2 months between 1979 and 2013 (Stammerjohn et al., 2015).

1.5 LACK OF IN-SITU OBSERVATIONS

The ASE is a very remote part of Antarctica, without any manned bases, some 1300 km away from Rothera station on the Antarctic Peninsula to the east and 1000 km from McMurdo station to the west, to the north lies the vast Pacific Ocean. As such observations are mainly limited to those obtained from satellites, sporadic research vessel cruises and just a few Automatic Weather Stations (AWS). In terms of meteorological and climatological studies this means there is a heavy reliance on; the AWS record (e.g. O'Donnell et al., 2011; Bromwich et al., 2013a; Deb et al., 2016), global meteorological reanalysis products (Fogt et al., 2012; Turner et al., 2013; Bracegirdle, 2013), and satellite products (Steig et al., 2009). Reanalysis products have also been

used both to force ocean models (Thoma et al., 2008; Assmann et al., 2013; Nakayama et al., 2014) and in order to explain ocean observations (Wåhlin et al., 2013; Dutrieux et al., 2014; Webber et al., 2017). Despite the many uses of reanalyis products in this region, to date there has only been a very limited evaluation of their accuracy.

1.6 THESIS AIMS AND STRUCTURE

This project is funded through the Ice Sheet Stability Research (iSTAR) programme, a major collaborative effort investigating ice, ocean and atmospheric processes in the Amundsen Sea region. Two seasons of fieldwork took place on PIG and a research vessel travelled to the region for a variety of science activities; including making observations of the atmosphere using radiosondes for this PhD. This is the first comprehensive atmospheric sounding programme in this region.

In order to better understand the processes controlling both current and future glacial retreat in the Amundsen Sea region it is important to investigate the variability of winds close to the continental shelf break and the variability of heat fluxes in the vicinity of ice shelves. Both of these processes are important in determining ocean heat content and basal melt rates. To fully understand the mass balance of the glacier, accumulation must also be considered. We identify key uncertainties as being the reliability of global reanalysis products in this data sparse region (chapter 3), and the ability of atmospheric models and by implication reanalysis products to capture small scale processes related to heat loss in coastal polynyas (chapter 5). We also assess the capacity of the extensively used RACMO product and reanalysis products to reproduce ice core observed accumulation on PIG and its tributaries (chapter 4).

The thesis will be laid out as follows:

Chapter 2 is a data and methods chapter. It describes the meteorological observational data collected and used in the project, along with the global reanalysis products that are used in chapters 3 and 4. The Met Office Unified Model (MetUM) set up is also described.

Chapter 3 contains an evaluation of global meteorological reanalysis products using in-situ meteorological observations within the ASE, including the new radiosonde soundings.

Chapter 4 investigates annual accumulation on PIG using observations collected

on the iSTAR traverse and modelled accumulation fields from RACMO and various global reanalysis products.

Chapter 5 examines the meteorological conditions associated with high heat flux events in the ASE. A control case and three high heat flux events are studied to investigate whether these events are more accurately captured using a high resolution model.

Chapter 6 is the concluding chapter highlighting the major results of this project and the likely direction of future work in this region.

2

OBSERVATIONAL DATA, REANALYSES AND NWP MODEL SETUP

2.1 OBSERVATIONS

2.1.1 RADIOSONDES

As part of the iSTAR programme a series of 40 radiosonde launches were planned. These radiosondes were the first launched for research purposes in the Amundsen Sea, although occasional launches have occurred in the area by research vessels such as the *RV Polarstern*. The radiosonde data was withheld from the global telecommunication system to make sure we had an independent data set with which to validate global reanalysis products.

38 radiosondes were successfully launched from the deck of *RRS James Clark Ross* (*JCR*) in February-March 2014. With the ship spending ~30 science days in the study area, the pre-cruise plan was to launch one radiosonde every day with an additional ten used in two or three separate time series to examine any interesting weather events that occurred during the cruise. Radiosonde launch times needed to be flexible as we were restricted by other activities on board the *JCR* but we aimed to launch between 1100 UTC and 1200 UTC each day to allow easy comparison with reanalysis products.

The radiosonde equipment was borrowed from the National Centre for Atmospheric Science. The radiosondes were RS92 Vaisala sondes measuring temperature, humidity and pressure with winds calculated using the Global Positioning System (GPS). The RS92 sondes have been shown to provide more accurate relative humidity observations at low temperatures than previous versions (RS90 and RS80) (Suortti et al., 2008). On board the ship we had a Vaisala GC25 ground check box, prior to each launch the radiosonde sensors were checked and the humidity sensor re-conditioned using the software. The system uses a small box of desiccant to recondition the humidity sensor at ~0% relative humidity. The desiccant was removed and replaced every 7-10 days. There was an AWS on board the *JCR* and this provided the surface conditions for each profile (required by the Vaisala software), the near surface radiosonde observations were in good agreement with the ship's AWS (which was calibrated against national standards before departure to Antarctica). The radiosonde observations were checked for consistency with both surface observations and internal consistency within each profile, no calibration errors were found. Table A.1 notes the launch time, location, maximum altitude reached, and surface conditions for all 38 of the successful radiosonde launches. There is a map displaying the launch locations of the radiosondes in chapter 3. On three days (13th, 18th and 23rd February) we launched multiple radiosondes to examine interesting weather events, i.e. synoptic scale cyclones, off-ice and orographic flows.

Figure 2.1: (a) A typical iSTAR radiosonde launch with three launch assistants helping to stabilise the balloon while moving it from the Helium cylinders to the launch location (a distance of ~5 metres); (b) The launch area at the stern end of the Naval bridge deck marking important equipment and areas.

The photo in Fig. 2.1a shows a typical iSTAR radiosonde launch from the deck of the JCR in fairly windy conditions. The eight 50 litre Helium cylinders used to fill the balloons were already on board the JCR when we arrived. We decided to move the Helium from its original location low down on the ship to the stern end of the Naval bridge deck, higher up on the ship. When the ship is on station for a conductivity, temperature, depth profile or other science activity the nose of the ship is pointed in to the wind. This new location high up on the ship provided some shelter from the wind behind the superstructure of the ship- which helped to make the balloon filling process more straightforward. It also allowed us to launch radiosondes off the stern whenever the ship was stationary for science activities. While the launch location we chose was very good, and allowed us to successfully launch 38 radiosondes, it was also challenging. There was limited space and in order to launch in windy conditions we had to manoeuvre the balloon towards the railings while having three to four people hold the balloon steady to prevent the balloon bursting on sharp surroundings such as the barrels seen in the photo. We had two unsuccessful launches during the cruise, on one occasion we popped the balloon on the railing in front of the barrels (see Fig. 2.1b). On the second occasion in very windy conditions we successfully launched the balloon but it got caught in a downdraught behind the superstructure of the ship and was damaged (and lost communications) after hitting the top of the crane at the stern of the ship.

Overall the radiosonde launch campaign during the iSTAR cruise was very successful and it generated a unique observational data set with which to evaluate meteorological reanalysis products in the ASE.

2.1.2 METEOROLOGICAL CONDITIONS DURING THE JCR CRUISE

In February-March 2014 during the *JCR* cruise the eastern ASE was almost completely free of sea ice (see Fig. 2.2). There was some remaining sea ice both to the west, around Thwaites glacier and to the north, around Thurston Island, which we encountered as we travelled into the area having departed from Punta Arenas in southern Chile. Most of this sea ice was thin and broken, there was also a large tabular iceberg (B-22A formerly part of Pine Island ice shelf) which was in the eastern Amundsen Sea during the cruise. Fig. 2.2 shows the February 2014 ERA-

Interim temperature and wind speed anomalies over the ASE compared to the 1981-2010 February mean. Over much of the eastern ASE it was colder than average for February by 1 to 2 °C, further inland this anomaly increased to 3 to 4 °C. The wind was anomalously southerly over the region close to PIG and this off-ice, cold wind direction was persistent for much of the cruise. This made for challenging conditions in which to launch radiosondes, with near surface temperatures frequently below −10 °C and often strong southeasterly winds, particularly when we were close to Pine Island ice shelf. The largely ice free ocean did mean it was very good conditions for hydrographic measurements, both when deploying autonomous underwater vehicles and when using the conductivity, temperature, depth sensor rosette. However, the cold near surface temperatures did cause some problems for the autonomous underwater vehicles too, there was icing reported on the antennae of both Seagliders and Autosub which affected their communications systems.

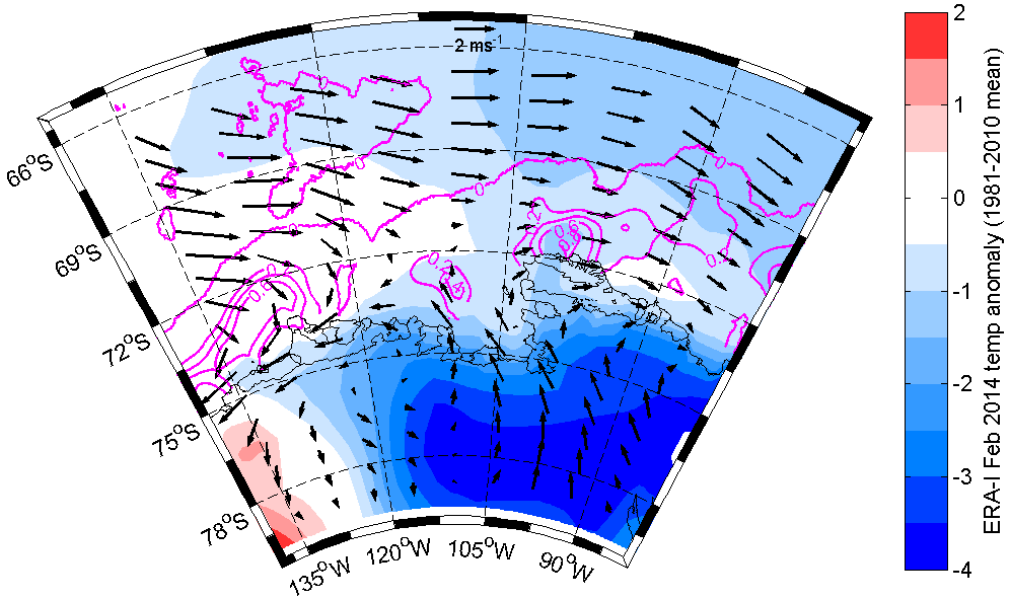

Figure 2.2: Atmosphere and sea ice conditions in the Amundsen Sea Embayment in February 2014. The colour shading shows the ERA-Interim 2-metre temperature anomaly from the February 1981-2010 mean (blue is cooler than average), the wind vectors show 10-metre wind speed and direction anomalies compared with the 1981-2010 mean. The magenta contours show the February 2014 mean sea ice concentration from Operational Sea Surface Temperature and Sea Ice Analysis (OSTIA) 1/20th degree data.

2.1.3 RESEARCH VESSEL OBSERVATIONS

Research vessels have been making relatively frequent visits to the ASE in recent years to try to increase understanding of the complex oceanographic conditions and processes in the region (e.g. see Dutrieux et al., 2014). Many of these research vessels are fitted with AWS (or at least meteorological instruments) and some launch radiosondes each day. To increase the diversity of the in-situ observations in our reanalysis evaluation study (chapter 3) we utilised some of these observations. Along with the *JCR*, the *RV Polarstern* was within the ASE for approximately 1 month in March 2010, and *The Nathaniel B. Palmer* was in the region for a similar length of time in January-February 2009, the tracks of all three research vessel cruises within the Amundsen Sea are shown in Fig. 2.3. It is our understanding that the meteorological instruments on board both of these ships were calibrated and checked in a similar way to those on the *JCR*. The instruments are located at various heights above the sea surface, between 19 metres and 37 metres. In order to compare them to the reanalysis data we use the sea surface temperatures recorded on board the ship and the observed atmospheric temperature to calculate the atmospheric stability and then make a height adjustment based on Monin-Obukhov similarity theory (following, Smith, 1988).

2.1.4 AWS OBSERVATIONS

The sparse AWS network within the Amundsen Sea region provide the only year round, near surface meteorological observations in the region. The AWS at Thurston Island (TI), Bear Peninsula (BP) and Evans Knoll (EK) — see Fig. 2.3 for locations — are part of the Antarctic Meteorological Research Centre's (AMRC) network and were installed in early 2011. Lazzara et al. (2012) provide a history of the AMRC AWS network on the Antarctic continent and how the design of their AWS has changed over the last 30 years. The three AMRC AWS used in both chapter 3 and chapter 5 of this thesis are of the CR1000 type and installed in a similar layout to that shown in Fig. 2.4, however there are no temperature observations at 0.5 metres above the surface at any of the sites.

The data are recorded at 10 minute time resolution and quality controlled before being made available on the AMRC website (http://amrc.ssec.wisc.edu), where a

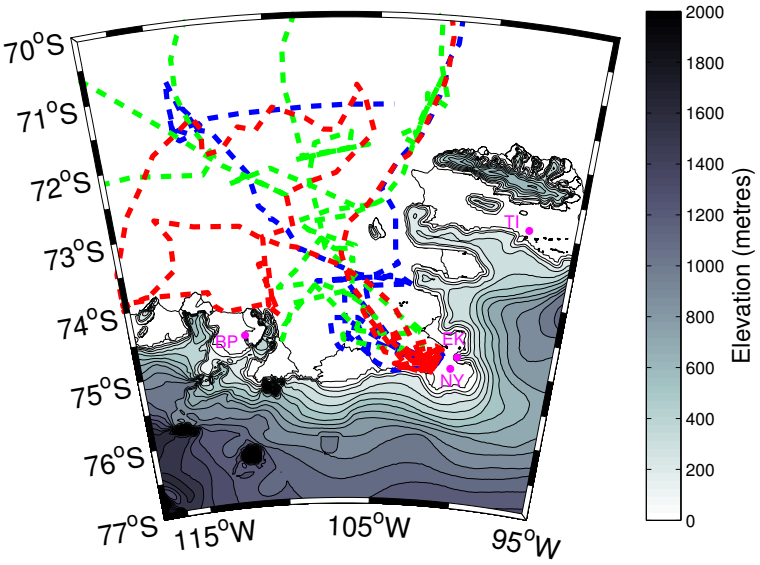

Figure 2.3: The tracks of the three research vessel cruises, meteorological data from each are used in the reanalysis evaluation. The tracks are for the *JCR* (blue), *RV Polarstern* (green) and *The Nathaniel B. Palmer* (red). The locations of the AWS stations are also marked with magenta circles.

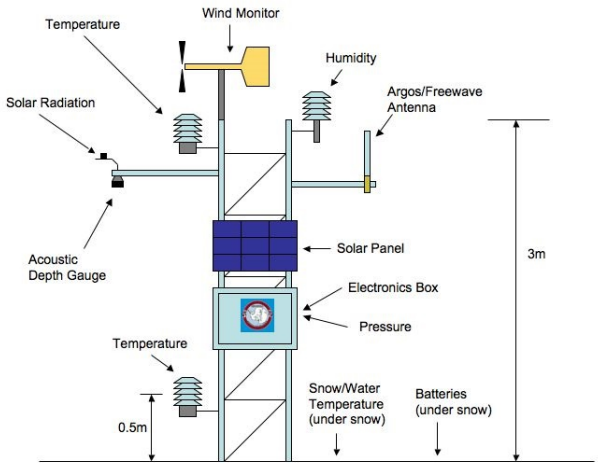

Figure 2.4: A diagram showing the components and layout of a CR1000 latest generation Antarctic Meteorological Research Centre AWS. Note that the 0.5 m temperature sensor is not present on any of three AWS within the ASE. Taken from (Lazzara et al., 2012).

3 hourly data set is also available. The instrumentation used at the three AMRC AWS sites is as follows: the temperature sensor is a Campbell Scientific resistance temperature detector 100-ohm Platinum resistance thermometer (accuracy $\pm$ 0.5 $^{\circ}C$), the pressure sensor is a Paroscientific Model 215A ($\pm$ 0.1 hPa), the humidity sensor

is a Vaisala HMP155 (± 2%), finally the wind sensor is a R.M. Young Model 05103/106 (± 0.2 $m\ s^{-1}$) (Lazzara et al., 2012). A photo of the instrumentation and site at EK AWS is shown in Fig. 2.5. The instruments have all been carefully selected after many years of testing. Renfrew and Anderson (2002) note that humidity observations at low temperatures are notoriously difficult and that the accuracy of these is questionable at low temperatures or when the air is relatively dry. Due to the AWS being located on rocky outcrops (see Fig. 2.5) rather than ice shelves we decided not to re-calibrate the AWS humidity observations as would usually be done over an ice/snow covered surface (Anderson, 1994). These AMRC AWS are typically very reliable and as such there were few data drop outs, one exception was a failure of the wind speed and direction sensor at BP AWS following a strong wind event in 2013.

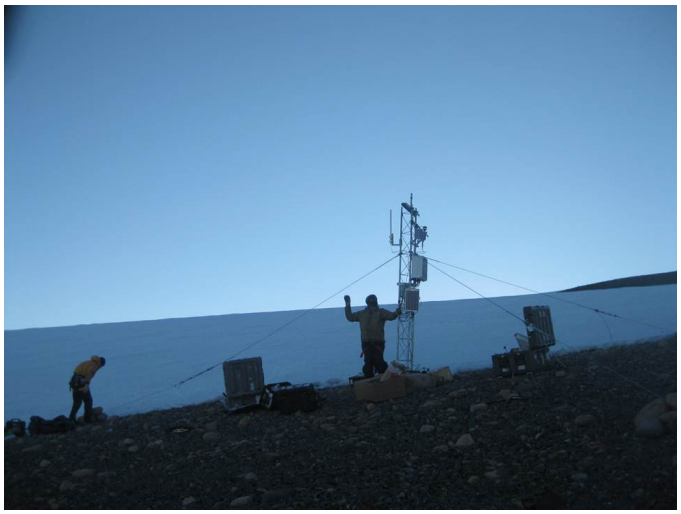

Figure 2.5: A photo showing the site and set up of Evans Knoll AWS, data from which is used in both chapters 3 and 5 of this thesis. Photo from AMRC website.

Observations from a fourth AWS, located on PIG are also used in chapter 3. This site was maintained by scientists from New York University and had to be dug out each field season due to accumulating snow and was sometimes moved to a different location on the glacier. Due to these issues there were some data outages and so we only use one years worth of continuous data covering the period February 2013 to February 2014. The instrumentation on this AWS was as follows: the temperature sensor was a Campbell Scientific 43347 RTD, the pressure sensor was a Campbell Scientific CS100 Barometer, the humidity sensor was a Campbell Scientific HMP45C, the wind speed and direction measured using an R.M Young Model 05103/5.

2.1.5 ICE CORE ACCUMULATION OBSERVATIONS

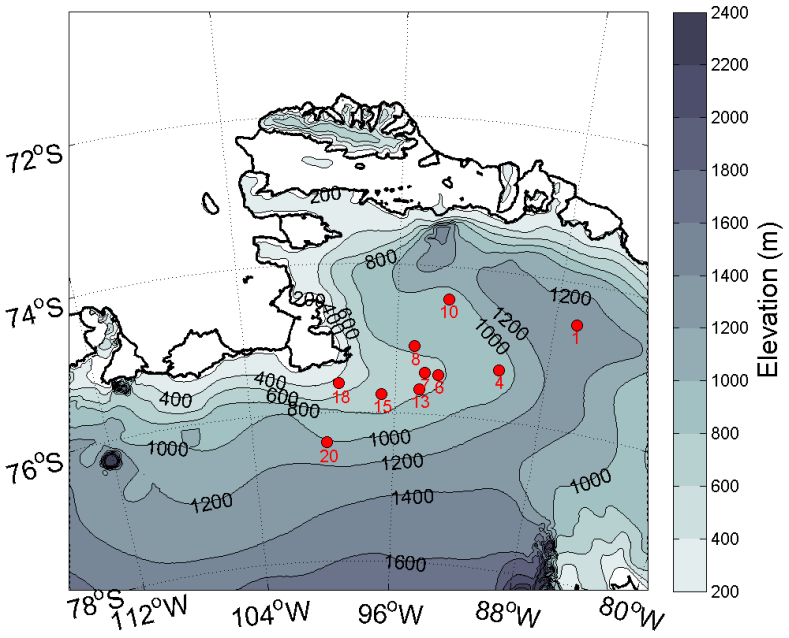

Figure 2.6: The location of iSTAR ice core accumulation sites. The colour contours show the elevation from the etopo2 digital elevation model. The elevation of the sites range from $\sim 1300m$ to $\sim 500m$.

On the 2014 iSTAR traverse ten ice cores were collected and from them a history of annual accumulation at each of the sites was estimated. The collection of the ice cores and subsequent analysis to calculate mean annual accumulation was conducted by Dr. Robert Mulvaney and colleagues at the British Antarctic Survey. The ten sites were chosen so as to give good spatial coverage across PIG and across a range of elevations, the locations of the sites are shown in Fig. 2.6. The cores were recovered to a maximum depth of 50 metres. The length of accumulation history at each site depends on the annual accumulation, as such the records in this study range from almost 100 years in length down to approximately 35 years at low elevation, coastal sites. With increasing depth, the density of ice within the core increases (see Fig. 2.7), as over time what was fresh snow on the surface of the glacier gradually solidifies to become firn ice. This means that what was 50 cm of surface accumulation 30 years ago will be a considerably thinner layer within the ice core. The density profile of each ice core is therefore measured in the field in order to calculate a water equivalent annual accumulation value on return to the UK.

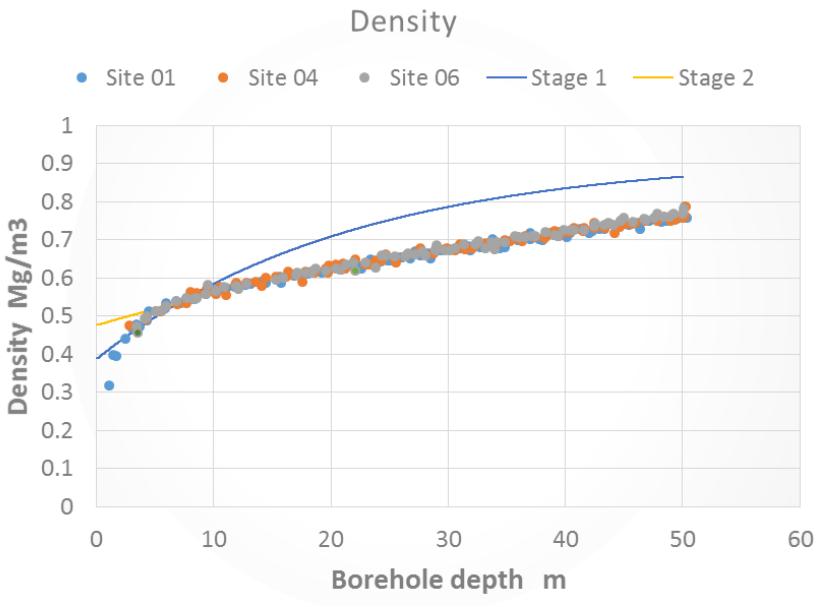

Figure 2.7: Density profiles from iSTAR ice cores. Stage 1 curve- rapid near surface density increase, stage 2 curve- slow transition to firn. Figure provided by Dr. Robert Mulvaney.

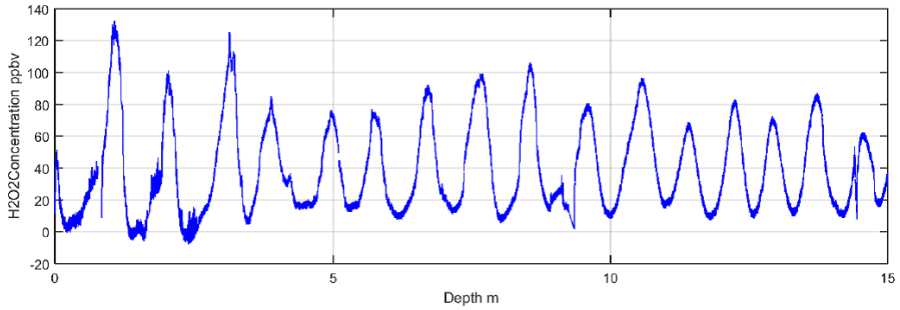

Figure 2.8: A depth profile of the concentration of Hydrogen Peroxide at iSTAR site 6, the peaks indicate summertime maximum concentration, the distance between peaks is used to calculate annual accumulation. Figure provided by Dr. Robert Mulvaney.

The other requirement in order to annually resolve the accumulation profile is to be able to identify the thickness of each annual layer. In the iSTAR ice cores this was achieved using hydrogen peroxide analysis, a chemical species which is only formed photochemically in the atmosphere, therefore only present during the austral summer in Antarctica. A graph of hydrogen peroxide concentration with depth in an iSTAR core is shown in Fig. 2.8. A similar technique was used to identify annual ice core layers in the study of Medley et al. (2013). The annual accumulation rate is corrected for strain rate using the simple Nye model (Nye, 1963) which is typically suitable in the upper 10% of the glacier depth, which all of these cores lie within.

2.2 REANALYSIS PRODUCTS AND RACMO

2.2.1 REANALYSIS PRODUCTS

Global meteorological reanalyses provide a multi-decadal record of climate conditions. They combine a variety of in-situ and satellite observations with forecast model data from a fixed version of a numerical weather prediction model using data assimilation. Through incorporating these observations reanalysis products aim to provide an accurate, gridded, and homogeneous meteorological data set for use in practical applications such as: initial conditions for numerical weather weather prediction models, surface forcing fields for oceanographic models and for studying long-term climatological trends. The main challenge for reanalysis projects is assimilating data from different observational sources. The introduction and rapid increase in the availability of satellite observations in recent decades has provided a huge amount of data for reanalysis projects but trying to prevent observational biases being incorporated requires complex data assimilation techniques. The latest generation of global reanalysis products have improved homogeneity and fewer step changes (that coincide with new observational data sets) (Bromwich et al., 2011). Four global reanalysis products have been produced and released over the last decade; ERA-Interim (ERA-I) (Dee et al., 2011), the Japanese 55-year reanalysis (JRA-55) (Kobayashi et al., 2015), the Climate Forecast System Reanalysis (CFSR) (Saha et al., 2010) and the Modern Era Retrospective Analysis for Research and Applications (MERRA) (Rienecker et al., 2011), more details about these products are shown in Table 2.1. The vertical layers and model top of each reanalysis product is as follows: ERA-I, 60 vertical levels with model top at 0.1 hPa, CFSR, 64 levels with ~0.266 hPa top, JRA-55, 60 levels with 0.1 hPa top, and MERRA, 72 levels with 0.01 hPa top.

In chapter 3 of this thesis we aim to evaluate the performance of global meteorological reanalysis products in the data sparse region of the ASE. We use the 6 hourly output of: screen level temperature, humidity and 10-metre winds from reanalysis products and compare with meteorological observations from AWS and research vessels. For the radiosonde comparison we use vertical profiles on pressure levels from the reanalysis products. In chapter 4 of this thesis we explore how comparable the precipitation fields of reanalysis products are with ice core

Table 2.1: An overview of the latest generation of global reanalysis products.

Met. Centre	Product	Period covered	Grid Res.	Atm. model
European Centre for Medium range Weather Forecasting	ERA-I	1979-present	T255 ~79km	ECMWF-IFS
Japanese Met. Agency	JRA-55	1958-present	TL319 ~60km	JMA-GSM
National Center for Environmental Prediction	CFSR	1979-2010 (brought forward using CFSv2)	T382 ~38km	GFS (2003)
NASA	MERRA	1979-present	0.5° x 0.67° ~50km	GEOS-5

observations from PIG. For this study we use monthly mean total precipitation and evaporation (or sublimation) fields from the reanalyses.

2.2.2 RACMO2.3

The Regional Atmospheric Climate Model (RACMO2.3) has been developed by the Royal Netherlands Meteorological Institute (Noël et al., 2015). RACMO2.3 uses the atmospheric physics schemes from the European Centre for Medium-Range Weather Forecasting's (ECMWF) Integrated Forecast System and the dynamical core of the High Resolution Limited Area Model (Noël et al., 2015). The polar version of RACMO2.3 has been developed by Utrecht University specifically to represent the surface mass balance over the ice shelves of Greenland and Antarctica (van Wessem et al., 2014b). The atmospheric model has been coupled with a multilayer snow model that simulates meltwater, refreezing and runoff. Further, RACMO2.3 also includes a blowing snow routine, meaning the addition or removal of wind blown snow is included in the model, something which is absent in all of the global reanalysis products (Lenaerts et al., 2012b).

RACMO2.3 data cover the 1979-2015 period, the horizontal resolution of RACMO2.3 is 27.5 km, higher than any of the current generation of global reanalysis products (van Wessem et al., 2014a). The model domain of RACMO2.3 covers the entire Antarctic continent (see Fig. 2.9) and is forced at its lateral boundaries by ERA-

Interim. RACMO2.3 is not a reanalysis product, it is free-running within its domain and there is no data assimilation of observations. Sea ice cover and sea surface temperature fields are also derived from ERA-Interim. Within the model domain RACMO2.3 is free-running and has 40 terrain following vertical levels (van Wessem et al., 2014a). The RACMO2.3 model (used here) is a recent upgrade with improved representation of turbulent and radiative fluxes and a new cloud microphysics scheme, full details of the model developments can be found in Noël et al. (2015). RACMO2.3 also uses an upper air relaxation scheme with nudging from ERA-Interim, this has been shown to increase the correlation between interannual accumulation observations and RACMO2.3 (van De Berg and Medley, 2016).

In chapter 4 of this thesis we compare RACMO2.3 and reanalysis products to observations of accumulation from the ice cores on PIG. We do not include RACMO2.3 in the evaluation of global reanalysis products in chapter 3 of this thesis as it is not a reanalysis product and does not assimilate any of the available observational data.

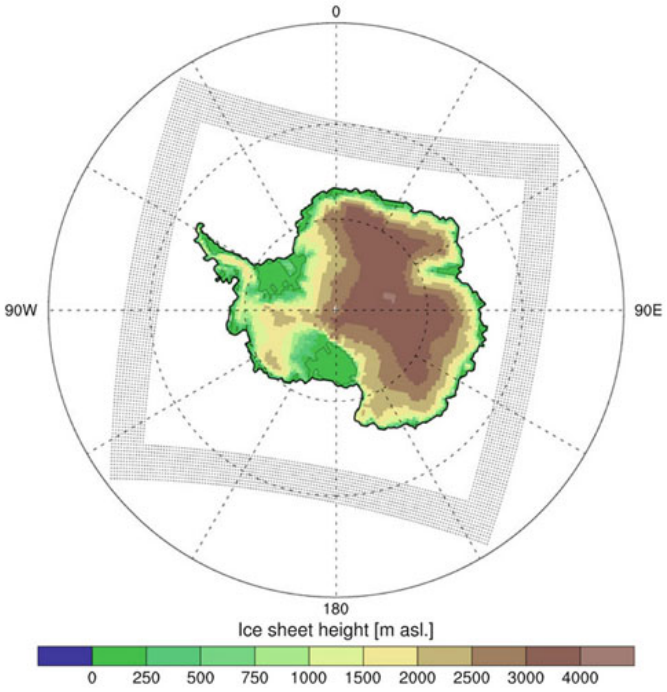

Figure 2.9: The RACMO2.3 Antarctica model domain with colour contours showing the topographic height above sea level.

2.3 MET OFFICE UNIFIED MODEL DETAILS AND CONFIGURATION

In chapter 5 we use new state-of-the-art numerical weather prediction simulations to investigate high surface heat flux events via a number of case studies. The Met Office Unified Model (MetUM) is the numerical weather prediction (NWP) model produced by the UK Met Office for use in operational forecasting, climate modelling and research applications. Here we use version 10.2 (the most recent available) of the atmosphere-only part of the MetUM to investigate high heat flux events in the ASE, their causes and how they are represented, in particular at different horizontal resolutions. The MetUM solves a set of equations in order to resolve the time evolution of the atmosphere. The main prognostic variables are potential temperature, Exner pressure, density, the three components of the wind field (u,v and w), and moisture (vapour, cloud water, cloud ice) (Greed, 2010; Walters et al., 2017). The dynamical core of the MetUM is non-hydrostatic and fully compressible which enables vertical accelerations (making it suitable for high horizontal resolution simulations). It uses a semi implicit, semi-Lagrangian predictor-corrector scheme to solve the equations of motion, this allows the model time step to be slightly longer while maintaining model stability (Walters et al., 2017). In its atmosphere only configuration the MetUM can produce accurate simulations at very high resolutions ~100 metres (e.g. Alexander et al., 2017), here the highest horizontal resolution we use is 2.2 km.

Here our global configuration of the model is on a N768 (1536 by 1152) horizontal grid (~ 17km resolution), with 70 vertical levels and a model top at 40 km. The vertical levels are on a hybrid-height co-ordinate system with Charney-Phillips staggering (Walters et al., 2017). They are terrain following near the surface but higher up they are at a constant height above the surface. The initial conditions for the MetUM are from Met Office operational analysis with sea ice and sea surface temperatures from the Operational Sea Surface Temperature and Sea Ice Analysis (OSTIA) data set. Our limited area high resolution model configuration is 600 (east-west) by 500 (north-south) grid points centred at 74 °S and 100 °W (see Fig. 2.10 for location) and has the same vertical levels as in the global simulation. The high resolution model uses a rotated pole in order to achieve near-uniform horizontal resolution. The boundary

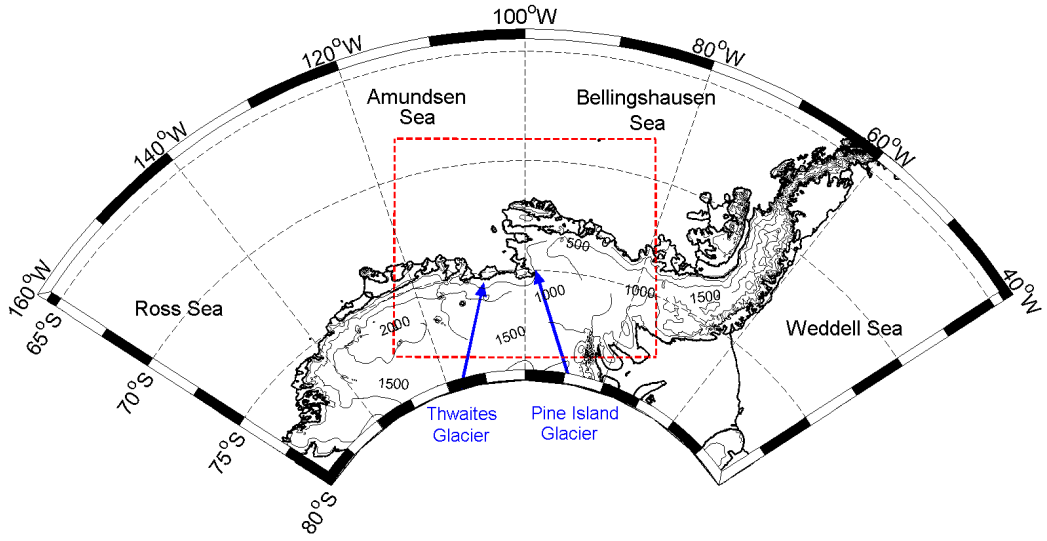

Figure 2.10: A map showing west Antarctica with orography contours labelled, the red dashed box marks the boundaries of the high resolution simulation.

conditions for the nested domain come from the global simulation. We allow a 12 hour spin up time before we start using any of the NWP output from either resolution of the model.

To avoid forecast drift at the end of any of our 48 and 72 hour case studies we use only the forecast period between 12 and 36 hours after model initialisation and concatenate the output. So for a 72 hour case study (such as the October 2011 case in chapter 5) we use three separate MetUM simulations starting 24 hours after one another. This does mean there are some discontinuities at the boundary between simulations but these are typically fairly small, and our decision was that this was better than having unrealistic output towards the end of each case study.

There are a variety of different science settings and physical schemes that can be used in the MetUM. To try to make the two resolutions of the MetUM comparable we maintain the same settings wherever possible. Some of the parameters are altered in the coarse resolution MetUM to make it comparable with the high resolution model. We use the 'sharp' stability function which results in weak turbulent mixing when the stability is high, this is important over Antarctica where stable boundary layers are common. The surface roughness over sea ice and the ocean is the same in both models, it is set to 5 x 10^{-4} m over sea ice and over open sea it is dependent on the wind speed according to the Charnock formula (Smith, 1988). The sea ice surface roughness value was changed from 3 x 10^{-3} m after this was found to give

very large turbulent heat fluxes in test simulations. The value of 5 x 10^{-4} m is in line with observational estimates (Wamser and Martinson, 1993) and with other Antarctic MetUM studies (e.g. Orr et al., 2014). Although note recent work on marginal ice zone roughness length suggests this should be a function of sea ice concentration (Elvidge et al., 2016). In the coarse resolution simulation we also turn off the heating generated through turbulence dissipation, this is to bring the global simulation in line with the with the high resolution model.

There are however some differences between the two resolutions of the model, most notably in the high resolution model convection is resolved so this parametrisation scheme is turned off. In the coarse resolution simulation we also reduce the value of the flow blocking drag coefficient from 4 to 0.5, this has been shown to reduce overnight cooling in the global simulation and reduces the magnitude of overnight temperature biases compared to AWS observations (see chapter 5). Due to the computational expense of doing multiple calls to the radiation scheme during each time step we also only do a single call to the radiation scheme in the coarse resolution simulation.

The focus of much of the work in chapter 5 is investigating the magnitude of turbulent heat fluxes in coastal polynyas using the MetUM. The model is atmosphere only and the turbulent heat fluxes are calculated using bulk formulae simplified here as:

$$\text{Sensible heat flux} = \rho.c_p.C_H.u_{10}.(SST - T_{1.5m}),$$
$$\text{Latent heat flux} = \rho.L.C_q.u_{10}.(q_{sat} - q_{1.5m}),$$

where ρ is the air density ($\sim 1.3\ kg\ m^{-3}$), c_p is the specific heat at constant pressure for air, L is the latent heat of vaporisation, u_{10} is the 10-metre wind speed, SST is the sea surface temperature (from OSTIA), $T_{1.5m}$ is the air temperature at 1.5 metres above the surface, q_{sat} is the saturated specific humidity at the sea surface temperature, $q_{1.5m}$ is the specific humidity at 1.5 metres above the sea surface and C_H and C_q are the transfer coefficients. In the MetUM the transfer coefficients vary according to the roughness length of the ocean, at stronger wind speeds the roughness length increases and so does the transfer coefficient (e.g. see Cook and Renfrew, 2015). Over the marginal ice zone (and coastal polynyas) the transfer coefficients also depend on the roughness length for sea ice in the ice covered portion of a grid box.

The sea ice and SST fields are taken from OSTIA data at the start of each simulation. This means there can be changes in the sea ice concentration during a case study, due to the stitching together of two or more MetUM simulations. Aside from these changes at the boundary between model simulations the sea ice field is fixed i.e. there is no formation, melt or advection of sea ice.

3

AN EVALUATION OF FOUR GLOBAL REANALYSIS PRODUCTS USING IN SITU OBSERVATIONS IN THE AMUNDSEN SEA EMBAYMENT

The following chapter was published as a paper in the *Journal of Geophysical Research: Atmospheres* under the title 'Evaluation of four global reanalysis products using in situ observations in the Amundsen Sea Embayment, Antarctica', with co-authors Ian Renfrew, Andrew Orr, Ben Webber, David Holland and Matthew Lazzara. All writing and work was undertaken by R.W. Jones, with comments from co-authors. It is as published except for the addition of some supplementary figures which could not be included in the original paper due to space limitations. I also make minor changes to the motivation and introduction to avoid repetition with chapters 1 and 2 of this thesis.

3.1 MOTIVATION

The Amundsen Sea sector of Antarctica is remote and observational studies are rare, as such global reanalysis products become a very valuable tool. The average

accumulation over both Thwaites and Pine Island Glacier (PIG) have been calculated from radar observations and compared to precipitation data from the latest generation of reanalysis products (Medley et al., 2014). Further, ocean models used to investigate the transport of relatively warm circumpolar deep water (CDW) on to the continental shelf in the Amundsen Sea have been driven by surface atmospheric forcing from a variety of different reanalysis products (Thoma et al., 2008; Schodlok et al., 2012; Assmann et al., 2013; Nakayama et al., 2014). Such modelling studies combined with oceanographic observations have increased scientific understanding of the processes causing the rapid retreat and thinning of glaciers such as PIG (Jacobs et al., 2011; Assmann et al., 2013). Investigations of the links between atmospheric and oceanographic processes in the Amundsen Sea have also utilised meteorological reanalysis products. Both ocean models (Thoma et al., 2008) and observations (Dutrieux et al., 2014) have highlighted the link between regional zonal wind anomalies and the amount of relatively warm CDW transported towards ice shelves. Weather and climate studies have also used reanalysis data: for example to study seasonal cycles of the Amundsen Sea Low (Hosking et al., 2013; Turner et al., 2013), and atmospheric teleconnections between West Antarctic meteorological conditions and tropical ocean indices (Ding et al., 2011; Fogt et al., 2012; Li et al., 2014; Clem and Fogt, 2015), as well as forcing atmospheric models (Deb et al., 2016). Finally, climatological studies have used reanalysis data to examine changes in pressure patterns in the Amundsen Sea over the last 30 years (Bracegirdle, 2013).

Despite the frequent use of reanalysis products within the ASE, there has been, to our knowledge, no comprehensive effort to validate them in this data sparse region. Bracegirdle (2013) use a short time series of observations from three drifting buoys released in the neighbouring Bellingshausen Sea to evaluate mean-sea-level pressure fields from reanlaysis products. They found biases of less than 1 hPa in ERA-Interim, CFSR and MERRA; ERA-Interim had the the smallest bias of the products evaluated (Bracegirdle, 2013). It has been shown that there are relatively large surface temperature biases over Antarctica in five global meteorological reanalysis data sets when compared with AWS data both on the interior plateau and in outlying coastal regions — (see Bracegirdle and Marshall, 2012) and (ERA-I only Jones and Lister, 2015), further reanalysis temperature biases have been shown to be larger in Antarctica than anywhere else in the world (Jones and Harpham, 2013). However,

these studies do not include any observations from the coastal Amundsen Sea sector, nor from over the adjacent ocean.

3.2 METEOROLOGICAL REANALYSIS SKILL IN ANTARCTICA

Antarctica represents a unique challenge for global meteorological reanalysis products. The relatively coarse grid resolution of reanalysis products means that regions of steep topography, coastlines and the marginal ice zone (where sharp temperature gradients are common) remain difficult to accurately resolve. Over Antarctica the sparse surface observational network and complex orography cause difficulties for reanalysis products attempting to simulate near-surface variables (Jones and Lister, 2015; Bracegirdle and Marshall, 2012).

Two recent studies have compared near-surface temperatures recorded at Antarctic weather stations to 2-metre temperatures from meteorological reanalysis products (Bracegirdle and Marshall, 2012; Jones and Lister, 2015). Bracegirdle and Marshall (2012) evaluate CFSR, MERRA, ERA-Interim, and two older reanalysis products the Japenese 25 year reanalysis and ECMWF's 40 reanalysis. After applying an altitude correction the mean bias compared with East Antarctic weather stations is reduced to between +0.3 $^{\circ}C$ and −0.7 $^{\circ}C$. Similarly, the temperature biases compared to weather stations on the Antarctic Peninsula are relatively small, between +1.1 $^{\circ}C$ and −0.1 $^{\circ}C$ for the 1979 to 1998 period. The largest biases of between +4 $^{\circ}C$ and +10 $^{\circ}C$ are on the Antarctic plateau, where reanalysis products are warmer than observations. Bracegirdle and Marshall (2012) postulate that these large biases may be caused by problems with surface fluxes and the strong surface temperature inversion over the plateau.

Jones and Lister (2015) limit their comparison to a single reanalysis product, ERA-Interim, with their observational data coming from a combination of automatic weather stations (AWSs) and manned stations. In order to assess the impact of the increased number of both remote and in-situ observations on ERA-Interim their analysis is split into three 11-year periods. Their results show that at the majority of 40 observing stations the magnitude of biases decreases between the 1979-1990 period and the 2002-2013 period. Once again it is found that both the magnitude and sign of temperature biases varies between the different regions of Antarctica. At both Vostok

and Amundsen-Scott on the high East Antarctic plateau ERA-Interim near-surface temperatures are warmer than the observations by +4.7 $^{\circ}C$ and +3.0 $^{\circ}C$ respectively for the 2002-2013 period. In contrast, coastal regions, particularly in the Ross Sea sector and at the two southernmost stations on the Antarctic Peninsula, ERA-Interim temperatures are colder than those observed by between -1 $^{\circ}C$ and -5 $^{\circ}C$ for 2002-2013.

Bracegirdle and Marshall (2012) use radiosondes launched from Antarctic research bases and frequently transmitted to the global telecommunications system (GTS), to evaluate reanalysis products. The 500 hPa pressure level is chosen as it is above the surface and boundary layer even across the highest parts of the Antarctic plateau (Bracegirdle and Marshall, 2012). At this altitude variables such as temperature are easier for reanalysis products to reproduce as they are dependent on the large scale flow and satellite observations are more reliable. Their results show that all of the examined reanalysis products are within 1.0 $^{\circ}C$ of the average radiosonde observed 500 hPa temperature for the 1999-2008 period. For both 500 hPa temperature and geopotential height there was little difference in skill between MERRA, CFSR and ERA-Interim, however the results do show that the two older reanalysis products (Japenese 25 year reanalysis, and ECMWF's reanalysis 40), include spurious temperature trends (Bracegirdle and Marshall, 2012). Aside from this study very few attempts have been made to evaluate reanalysis products using Antarctic radiosonde data.

Here we aim to provide a comprehensive evaluation of reanalysis products in the Amundsen Sea region by comparing them to: four automatic weather stations (AWSs) in the vicinity of Pine Island Glacier, research vessel meteorological data and 38 radiosondes launched in the Amundsen Sea in early 2014. No meteorological observations from the coastal Amundsen Sea sector were included in the studies of either Bracegirdle and Marshall (2012) or Jones and Lister (2015).

3.3 OBSERVATIONS, REANALYSES AND METHODOLOGY

3.3.1 OBSERVATIONS

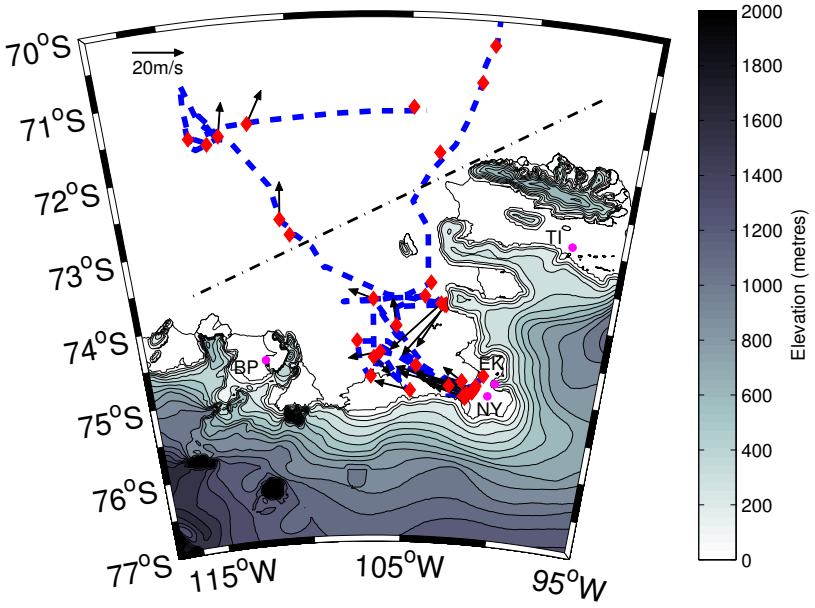

Figure 3.1: A map of the Amundsen Sea Embayment, with contour lines every 100m to show the surrounding topography. The dashed blue line shows the 2014 *JCR* ship track. The red diamonds show the locations of 38 radiosondes launched (from the *JCR*) and the magenta circles show the locations of the four AWSs used in this study. The diagonal dashed black line indicates the spatial divide between continental and shelf break radiosondes (used in Fig. 3.12), finally the vectors show the direction and relative strengths of LLJs where they were observed in radiosonde profiles. The topography data is grid cell average 2-minute elevation data is from the Etopo2 version 2 NOAA database, derived from the GLOBE digital elevation model.

AUTOMATIC WEATHER STATIONS

The AWS data for the Evans Knoll (EK), Thurston Island (TI) and Bear Peninsula (BP) sites has been downloaded from the AMRC website (http://amrc.ssec.wisc.edu). The fourth AWS used in this study is located on PIG and was installed by scientists from New York University (NYU). Table 3.1 gives a brief overview of the location, height and mean temperature at each of the AWSs. The BP, TI and NYU AWS are co-located with GPS stations and as such we have some confidence in their listed elevation. However, if the AWS altitudes are incorrectly recorded by e.g. 50 metres, the temperature biases

described later would change by ~ 0.5 $^{\circ}C$, the error in the listed elevation is unlikely to be larger than this.

Each of the AWSs records atmospheric pressure, temperature, relative humidity, wind speed and wind direction at a height of 3 metres above the surface. All of these variables are used in this comparison with the exception of AWS pressure. To compare station pressure with reanalysis pressure for a coarse grid cell is difficult in areas of steep and complex orography. It also requires an assumption about the adjustment to mean sea level, for these reasons we do not evaluate reanalysis mean sea level pressure using AWS observed pressure. Therefore the AWS comparison focusses on temperature, wind speed, wind direction, relative humidity and specific humidity, which can be calculated from the observed variables.

Table 3.1: Site details for Evans Knoll (EK), Thurston Island (TI), Bear Peninsula (BP) and New York University (NYU) AWSs, the mean temperature and pressure for NYU only cover the period February 2013 to February 2014, for other sites it is February 2011 to February 2014.

Site details	EK	TI	BP	NYU
Longitude (°W)	100.40	97.55	111.89	100.71
Latitude (°S)	74.85	72.93	74.55	75.01
Altitude (m)	188	145	312	70
Mean temp (°C)	-13.01	-11.21	-13.60	-15.39
Mean pressure (hPa)	962.7	954.4	930.4	975.28

RESEARCH VESSEL OBSERVATIONS

The research vessel meteorological data used in the evaluation are taken from instruments on board *RRS James Clark Ross (JCR)*, *RV Polarstern* and *Nathaniel B. Palmer*. On the *JCR* the temperature, humidity and pressure sensors are located above the bridge deck, 19 metres above the water surface and within a Stevenson screen, while the anemometer is located on the front mast 21 metres above the water surface. On the *RV Polarstern* temperature and humidity are measured by sensors 27 metres above the water surface, wind measurements are recorded by anemometers on both the port and starboard sides 37 metres above the water surface. On the *Nathaniel B. Palmer* wind speed and direction are measured at a height of 34 metres above the water surface and all other relevant meteorological variables at 19 metres. These observations are adjusted to the standard height for reanalysis products (10-m for

wind speed and direction, 2-m for temperature and humidity). In order to do this the observed sea surface temperature is used to calculate atmospheric stability and then a height adjustment based on Monin-Obukhov similarity theory is made (e.g. following Smith, 1988). For all of the data sets the pressure field is already adjusted to mean sea level pressure and so no correction is necessary. Across the three research vessel cruises there are a total of 357 data points (at 6 hourly resolution), or approximately 3 months of data.

RADIOSONDES

The map in Fig. 3.1 shows the locations of radiosondes launched during the *JCR* cruise to the Amundsen Sea in early 2014. There was usually one radiosonde launched each day (as close as possible to 1100 UTC) for comparison with 1200 UTC reanalysis data, the radiosondes recorded data well into the stratosphere providing profiles from the surface to approximately the 50 hPa pressure level. On three days 13th, 18th and 23rd February, multiple sondes were launched to investigate interesting weather events, on a few days we were unable to launch radiosondes due to wind gusts exceeding 45 knots. These radiosonde observations were withheld from the GTS in order to provide an independent atmospheric profile to compare against meteorological reanalyses.

3.3.2 REANALYSES

The most recently released global reanalysis products are evaluated in this study: ERA-Interim (Dee et al., 2011), JRA-55 (Kobayashi et al., 2015), CFSR (Saha et al., 2010) and MERRA (Rienecker et al., 2011). The reanalysis data sets for ERA-Interim, CFSR, and JRA-55 were downloaded from the Computational and Information Systems Laboratory research data archive website (http://rda.ucar.edu). Where possible the analysis fields were downloaded and concatenated for comparison with observational data. Some CFSR variables such as temperature are not analysed so the 6-hour forecast field is used. For data after 2010 CFSR is not brought forward so the CFSv2 is used for comparison. This is essentially the same model as CFSR and is being used to extend the CFSR data forward to the present day, from here on we refer to this product as CFSR. The MERRA data set is downloaded from NASA's web portal (http://disc.sci.gsfc.nasa.gov). It is noteworthy that the JRA-55 has a reduced horizontal resolution (1.5° by 1.5°) for its pressure level data and this is used in the

radiosonde comparison section.

3.3.3 COMPARISON METHODOLOGY

In the AWS comparison the nearest reanalysis land grid point is compared to the AWS data. For the purposes of this work it is necessary to adjust the reanalysis temperatures from the height of the nearest grid point to the height of the AWS. Here due to the cold, dry nature of the Antarctica atmosphere we use the dry adiabatic lapse rate of 9.8 $^{\circ}C\ km^{-1}$. As this value is uncertain we add error bars to the temperature corrections listed in Table 3.2 allowing the lapse rate to vary from 5.8 $^{\circ}C\ km^{-1}$ to 13.8 $^{\circ}C\ km^{-1}$. Previously, lapse rates of 6 $^{\circ}C\ km^{-1}$ (Jones and Lister, 2015) and 9.8 $^{\circ}C\ km^{-1}$ (Bracegirdle and Marshall, 2012) have been used.

Table 3.2: Temperature corrections applied to the reanalysis 2-m temperature field at each of the AWS sites, to account for the altitude difference between the reanalysis grid point and the altitude of each AWS (as listed in Table 3.1). These corrections assume the dry adiabatic lapse rate (9.8 $^{\circ}C\ km^{-1}$), with error bars to show how different the correction would be if the lapse rate is adjusted between 5.8 $^{\circ}C\ km^{-1}$ and 13.8 $^{\circ}C\ km^{-1}$.

	Temperature correction at AWS Site ($^{\circ}C$)			
	EK	TI	BP	NYU
ERA-I	+0.71 ± 0.29	+0.21 ± 0.09	+0.32 ± 0.13	+1.89 ± 0.77
JRA-55	-0.30 ± 0.13	-0.61 ± 0.25	-0.73 ± 0.30	+0.30 ± 0.13
CFSR	-1.45 ± 0.59	-0.67 ± 0.28	-1.02 ± 0.42	-0.23 ± 0.10
MERRA	-1.72 ± 0.70	-1.09 ± 0.55	-2.10 ± 0.86	-0.65 ± 0.27

It is known that unmanned AWSs in polar regions are prone to overestimate temperatures in low wind speed conditions due to a lack of ventilation. This is a particular problem in austral summer when there is near 24 hour daylight (e.g. Lazzara et al., 2012). For this reason low wind speed events (less than 2 $m\ s^{-1}$) are removed from the summertime *temperature* comparison, in all cases this reduces the magnitude of the temperature bias. At the BP AWS the anemometer stopped working during 2013 so the wind comparison here is based on only two years worth of data. The AWS instruments are at a nominal height of the 3-metres above the surface but this is likely to vary due to snow cover. The reanalysis variables at 2-metres (temperature, specific and relative humidity) are assumed to be comparable to the instrument height and no adjustment is applied. Renalysis wind speed and

direction are available at 10-metres above the surface, therefore a simple neutral adjustment is applied to adjust the reanalysis wind speed to 3-metres above the surface, assuming a logarithmic wind profile and with a roughness length of 0.1 mm for a snow covered surface. This simple adjustment is justified, firstly, as the exact instrument heights vary with time (due to snow cover), and secondly, the atmospheric stability is unknown - making a stability-based adjustment difficult.

For the research vessel and radiosonde data the closest reanalysis grid point to each observation is used. Due to the smoothed topography of the reanalyses resulting in a seaward extension of the land sea mask in the ASE, a comparison with the nearest marine grid point is troublesome as this can be 100 km distant. Further, some of the research vessel observations and radiosonde launches are from south of 75°S, and here linear interpolation of the four closest grid point would result in both four land grid points being used and more southerly, colder, continental grid points being incorporated. Therefore as the land sea masks are not consistent between reanalysis products, and due to significant variations in meteorological variables over length scales of 100 km or more, the methodology chosen was to use the closest grid point. This does mean that on some occasions land grid points are used in the comparison to radiosonde and research vessel observations but the frequency of this is relatively consistent between the reanalyses.

The ECMWF website suggests that both sea level pressure and wind speed from research vessels such as those used here may be assimilated through the GTS. Therefore these observations may not be independent of the reanalyses. The radiosonde observations are independent of the reanalysis products as they were deliberately withheld from the GTS. For comparison to the reanalysis pressure level data the radiosonde observations are interpolated on to a 5 hPa vertical grid from the surface to 50 hPa. Similarly the reanalysis pressure level data is linearly interpolated from each product's pressure levels on to the same vertical grid.

A variety of statistics are used throughout this comparison. Bias corresponds to (for example) the difference between the mean reanalysis 2-metre temperature and the AWS observed temperature. When the reanalysis mean temperature is colder than the observations the bias will be negative. The root mean square error (RMSE) is the mean difference between the observed value (e.g. temperature) and the simultaneous temperature value given by the reanalysis product. The standard deviation ratio is the

standard deviation of the reanalysis field divided by the observed standard deviation. If this value is greater (less) than 1 then this indicates that the reanalysis product has a larger (smaller) spread of values than seen in the observations. The R^2 value is used to show the correlation between the reanalysis fields and observations. Finally, the slope value is the gradient of the linear regression line that best fits the relationship between the reanalyses and observations.

3.4 AWS COMPARISON

3.4.1 SEASONAL TEMPERATURE COMPARISON

The representation of 2-m temperature is evaluated by season due to the large differences between summer and winter insolation in Antarctica, which result in significant seasonal temperature variations. During winter the absence of insolation allows radiative cooling of the surface to dominate, generally resulting in the formation of a strongly stable, cold boundary layer (King, 1990). In summer the boundary layer is warmer and tends to be weakly stably-stratified or even slightly unstable (Mastrantonio et al., 1999).

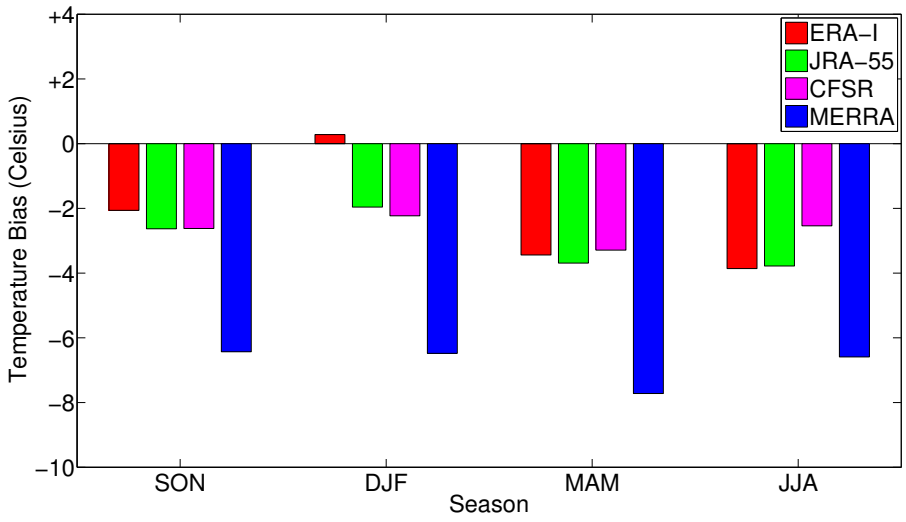

Figure 3.2: The magnitude of seasonal temperature biases for each of the reanalysis products at the Bear Peninsula AWS.

As an example the seasonal temperature biases from BP AWS are shown in Fig. 3.2. At BP (and across the other AMRC sites) ERA-I records its smallest bias in the austral summer and its largest bias in the austral winter (Fig. 3.2). Table 3.3 shows that across the AMRC sites both ERA-I and JRA-55 show a marked improvement in reproducing 2-m temperatures in summertime. Summer biases for ERA-I and JRA-55 respectively are $-0.23\ ^{\circ}C$ and $-1.91\ ^{\circ}C$ compared with $-3.70\ ^{\circ}C$ and $-3.89\ ^{\circ}C$ wintertime biases. This suggests ERA-I and JRA-55 have more skill capturing the weakly stable or even unstable summer boundary layer, whereas CFSR and MERRA temperature biases show little seasonal variability (e.g. see Fig. 3.2).

Table 3.3: Statistical comparison of reanalysis near-surface temperatures to observed seasonal temperatures. A negative bias indicates that the reanalysis product is colder than the observations. SON, DJF, MAM and JJA indicate the season with DJF corresponding to austral summer. The unit for bias and RMSE is $^{\circ}C$. * The NYU data set only covers a 13-month period.

Product	Stats	AMRC 3 site average				NYU*			
		SON	DJF	MAM	JJA	SON	DJF	MAM	JJA
ERA-I	Bias	-2.27	-0.23	-2.66	-3.70	1.35	0.36	3.02	2.83
	SD ratio	1.17	1.09	1.29	1.25	0.88	0.90	0.97	0.95
	R^2	0.79	0.72	0.74	0.73	0.93	0.83	0.88	0.86
	RMSE	4.37	2.22	5.16	6.34	2.83	2.06	4.44	4.32
	Slope	1.04	0.93	1.12	1.07	0.85	0.82	0.91	0.89
JRA-55	Bias	-2.82	-1.91	-3.40	-3.89	0.07	-0.18	1.74	1.55
	SD ratio	1.01	1.14	1.03	0.92	0.81	0.84	0.82	0.74
	R^2	0.82	0.74	0.80	0.80	0.83	0.69	0.84	0.76
	RMSE	4.17	2.88	4.68	5.29	3.74	2.70	4.24	4.77
	Slope	0.91	0.98	0.92	0.82	0.74	0.70	0.75	0.64
CFSR	Bias	-2.88	-2.63	-2.96	-2.68	-0.48	-2.50	1.52	1.79
	SD ratio	1.20	1.37	1.26	1.18	1.04	1.29	1.00	1.06
	R^2	0.75	0.62	0.75	0.73	0.78	0.59	0.84	0.79
	RMSE	5.02	4.02	5.19	5.45	4.31	4.75	4.13	4.71
	Slope	1.04	1.08	1.09	1.01	0.92	0.99	0.92	0.94
MERRA	Bias	-6.62	-6.86	-7.87	-6.89	-4.57	-6.00	-4.21	-3.11
	SD ratio	1.06	1.28	1.12	0.99	0.95	1.04	1.01	0.98
	R^2	0.82	0.73	0.79	0.80	0.85	0.75	0.83	0.81
	RMSE	7.31	7.29	8.57	7.72	5.69	6.52	5.78	4.94
	Slope	0.96	1.09	1.00	0.89	0.88	0.90	0.92	0.88

The results in Table 3.3 show that the AMRC mean biases (across EK, TI and BP) are negative for all four reanalysis products. Reanalysis 2-m temperatures are lower than those observed. The weighted (by length of time series) mean temperature bias for all four sites shows that ERA-I has the smallest bias($-1.81\ ^{\circ}C$), compared with CFSR ($-2.50\ ^{\circ}C$), JRA-55 ($-2.62\ ^{\circ}C$) and MERRA ($-6.80\ ^{\circ}C$). For MERRA the bias is significantly larger than the $-1.6\ ^{\circ}C$ average bias found at coastal East Antarctic stations by Bracegirdle and Marshall (2012), suggesting MERRA may have a very strong regional bias in West Antarctica.

The all-season bias for ERA-Interim at each site is: $-1.40\ ^{\circ}C$ at EK, $-2.98\ ^{\circ}C$ at TI, $-2.27\ ^{\circ}C$ at BP and $+1.89\ ^{\circ}C$ at NYU. These figures can be directly compared to the biases found at coastal AWS sites around Antarctica by Jones and Lister (2015), where a group of AWSs on the Ross Sea coastline showed a similar pattern. At Marble Point,

Manuela and Scott AWSs, ERA-Interim showed temperature biases of $-2.4\,^{\circ}C$, $-1.4\,^{\circ}C$ and $-1.4\,^{\circ}C$ respectively. These were some of the largest biases at coastal AWSs they examined and are of comparable magnitude to the ERA-I biases found at three of the sites used in the present study. Furthermore, a manned coastal station at McMurdo recorded a larger cold bias ($-4.8\,^{\circ}C$) than those seen at the three AMRC AWSs (Jones and Lister, 2015). Similarly to the NYU AWS in our results there were also two AWSs on the Ross Sea coastline where ERA-Interim displayed a warm bias for the 2002-2013 period, at Arelis and Cape Ross. The results presented here combined with those from Jones and Lister (2015) suggest a systematic cold bias in ERA-I 2-m temperatures (of approximately $-1.5\,^{\circ}C$) extending around West Antarctica from the Ross Sea to the western side of the Antarctic Peninsula, there are of course a few AWS stations where ERA-I shows a warm bias within this sector.

The NYU AWS — located on PIG and at a relatively low altitude — is notably different with positive biases in the comparison with ERA-I, JRA-55 and CFSR reanalyses (Table 3.3). The linear regression slope values are all less than 1 due to a warm bias at low temperatures. The NYU AWS is the only site located on an ice shelf and so cold-air drainage during katabatic flows may be more prevalent — a phenomena that is difficult to accurately model (Renfrew, 2004), perhaps leading to the warm bias. MERRA remains colder than NYU AWS observations, although the magnitude of the bias is smaller than that at the other sites.

The R^2 values show little variation between the four reanalysis products. R^2 values are typically between 0.7 and 0.85 (see Figs. 3.3 and 3.4), comparable with correlation coefficients at AWSs used in the Antarctic wide evaluation by Jones and Lister (2015). In the summer season there are occasions where the R^2 value drops below 0.7. The CFSR scatter plot in Fig. 3.3c indicates that the reduced correlation coefficient is primarily caused by large RMSEs when observed summertime temperatures fall below $-10\,^{\circ}C$. Larger biases and RMSEs are seen in the wintertime scatter plots (Fig. 3.4) than the summertime (Fig. 3.3), as discussed previously this seasonal difference is markedly larger for ERA-I and JRA.

The standard deviation ratios show that both CFSR and ERA-I produce larger standard deviations than observed across all seasons at TI and BP (see Table A.2, Figs. 3.3a, 3.3c, 3.4a and 3.4c). For example, Fig. 3.3c shows that CFSR produces temperatures up to $10\,^{\circ}C$ cooler than those observed. ERA-I also produces

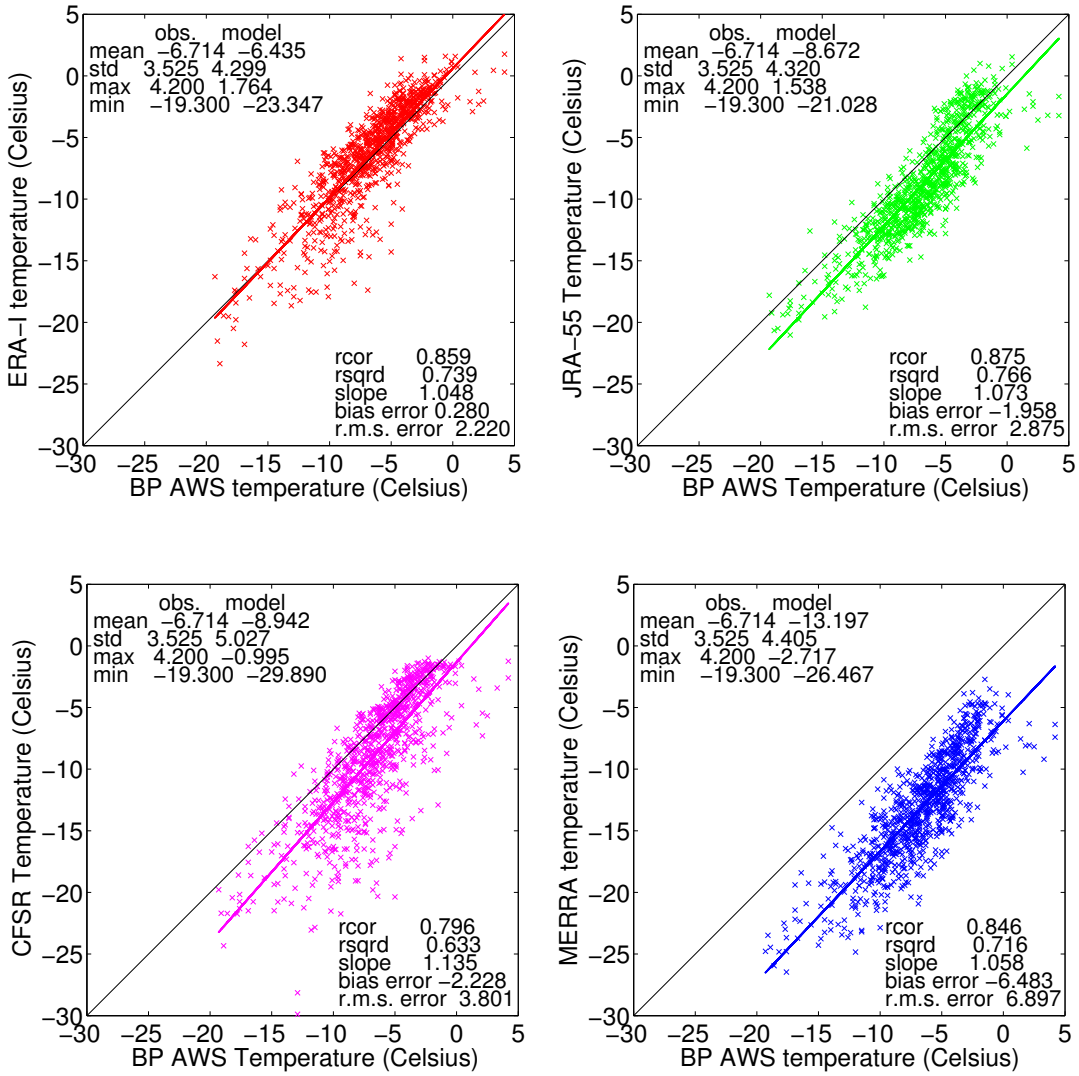

Figure 3.3: Summertime temperatures at BP AWS compared to 2-m temperature from reanalyses, with statistics shown in text. Top left (a) ERA-I; top right (b) JRA-55, bottom left (c) CFSR; and bottom right (d) MERRA.

anomalously cold temperatures and this causes the larger than observed standard deviations seen in Figs. 3.3a and 3.4a. MERRA has a large SD ratio in the summer months, as shown in Fig. 3.3d, in summer MERRA displays more variability around the mean than was observed.

- All four reanalyses produce temperatures that are colder than observed, the magnitude of this bias varies between $\sim 2\,^{\circ}C$ (ERA-I) and $\sim 6\,^{\circ}C$ (MERRA).
- ERA-I and JRA-55 show larger cold biases in the austral winter, suggesting the products are struggling to simulate the strong surface based inversion that is

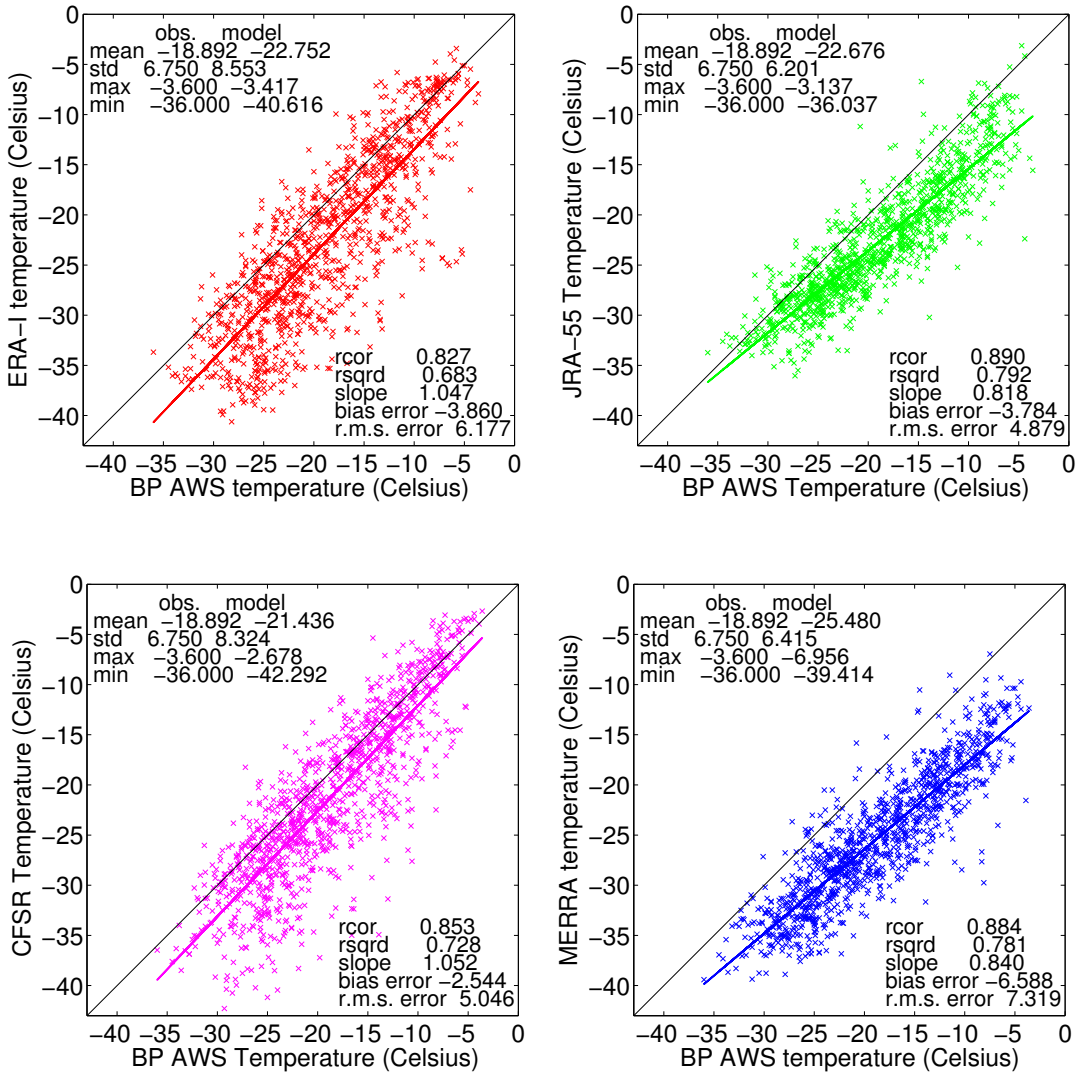

Figure 3.4: Wintertime temperatures at BP AWS compared to 2-m temperature from reanalyses, with statistics shown in text. Top left (a) ERA-I; top right (b) JRA-55; bottom left (c) CFSR; and bottom right (d) MERRA.

characteristic of Antarctic winter.

- ERA-I temperature biases and correlation coefficients are comparable with those found in the Antarctic wide study of Jones and Lister (2015). However MERRA contains a much larger temperature bias than was found by Bracegirdle and Marshall (2012) when compared with East Antarctic AWS.

3.4.2 WIND SPEED AND HUMIDITY COMPARISON

Wind speed and humidity comparison statistics are shown in Table 3.4. For brevity we show annual averages of these variables rather than splitting them seasonally as the seasonal differences are negligible.

Table 3.4: Statistical comparison of the four reanalysis products across the four AWS sites for wind speed, Relative Humidity and Specific Humidity. The statistics are the same as those in Table 3.3. Note humidity is not available at NYU site.

Product	Stats	Wind speed ($m\ s^{-1}$)		Rel. Hum. (%)	Spec. Hum. ($g\ kg^{-1}$)
		AMRC	NYU	AMRC	AMRC
ERA-I	Bias	-1.32	-0.80	-5.20	-0.20
	SD ratio	0.53	0.72	0.87	1.06
	R^2	0.43	0.63	0.25	0.87
	RMSE	5.73	3.22	14.12	0.39
	Slope	0.34	0.57	0.43	0.99
JRA-55	Bias	-0.58	-0.63	5.46	-0.25
	SD ratio	0.61	0.81	0.66	1.03
	R^2	0.46	0.75	0.36	0.81
	RMSE	5.31	2.66	12.99	0.47
	Slope	0.42	0.70	0.37	0.92
CFSR	Bias	-1.85	-2.27	12.33	-0.05
	SD ratio	0.54	0.57	0.47	1.12
	R^2	0.45	0.71	0.27	0.85
	RMSE	5.46	3.83	17.22	0.38
	Slope	0.36	0.48	0.23	1.04
MERRA	Bias	-0.40	-1.55		-0.63
	SD ratio	0.43	0.68		0.74
	R^2	0.37	0.60		0.79
	RMSE	5.62	3.61		0.76
	Slope	0.32	0.53		0.65

In both the AMRC 3 site average and at NYU AWS all of the reanalysis products have lower wind speeds than observed and struggle to reproduce the observed spread of wind speeds (see Table 3.4). Fig. 3.5 shows an example scatter plot from TI AWS, this site is chosen as it is representative of the biases observed at the other sites (see Table A.3). It should be noted that there are fewer strong wind events at EK AWS and so the wind speed bias is positive for three of the reanalysis products, this is largely due to an overestimations when the observed wind speed is below 5 $m\ s^{-1}$, the reanalyses still fail to capture the observed spread of wind speeds. As shown in Fig. 3.5 the

reanalyses tend to over-estimate the strength of the wind when the observed wind speed is low, and severely underestimate the strength of the wind when the observed wind speed is high. Across the AMRC sites the combination of these errors also causes the linear regression lines to have mean slopes between 0.3 and 0.45 for all reanalysis products (see Table 3.4 and Fig. 3.5). At the NYU AWS site the pattern is similar with all products displaying a negative bias, but the reanalysis products do a better job at low wind speeds at this site so the slope and correlation values are higher than at the AMRC sites.

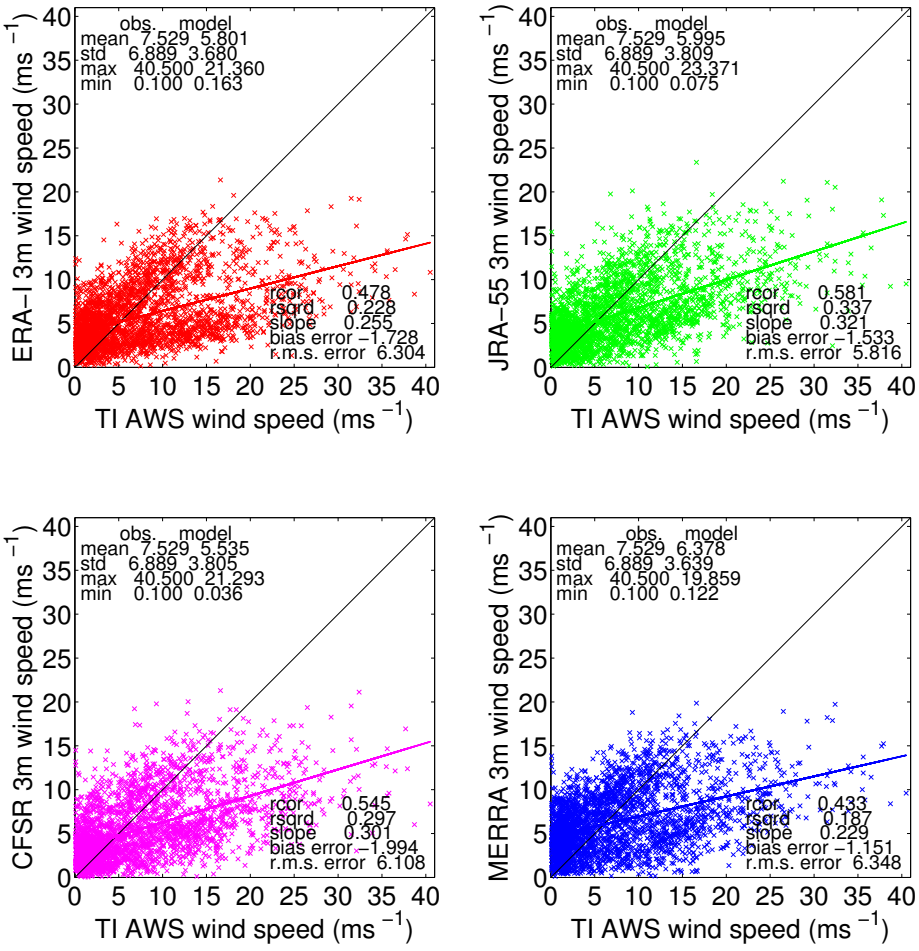

Figure 3.5: Scatter plots showing the TI AWS observed windspeed compared to the neutrally adjusted 3m windspeed in the four reanalysis products. Top left (a) ERA-I; top right (b) JRA-55; bottom left (c) CFSR; and bottom right (d) MERRA.

Interestingly, the biases at low and high observed wind speeds largely offset each other and the mean bias is relatively small (between $-0.4\ m\ s^{-1}$ and $-2.5\ m\ s^{-1}$) for all reanalysis products (see Fig. 3.5 for example at TI AWS). The sites with the largest

biases are TI and BP (see Table A.3), where large negative biases show the reanalysis winds are weaker than observed. At EK the reanalysis products tend to overestimate mean wind speed compared to observations (see Table A.3), however the scatter plots (not shown) reveal that even here reanalysis products struggle to reproduce observed wind speeds greater than 15 $m\ s^{-1}$.

Analysis of strong wind events (> 15 $m\ s^{-1}$) at BP and TI AWS revealed that at both sites the wind direction is a north or north-easterly during > 75% of these events. This suggests there may be an enhancement of the observed winds due to flow distortion, particularly at Thurston Island with mountainous terrain to the north (see Fig. 3.1). Such flow distortion is poorly represented in models with insufficient resolution (e.g. Renfrew et al., 2009; Elvidge and Renfrew, 2016). The northerly wind direction suggests that such winds are associated with offshore synoptic-scale cyclones. Reanalysis products and models with a coarser horizontal resolution have been shown to contain larger wind speed biases during Antarctic strong wind events where a cyclone and topographic effects combine to produce the strongest winds (Turner et al., 2009; Orr et al., 2014).

The bias in the 2-m relative humidity (RH) field varies greatly across the reanalysis products from -5.2% for ERA-I to 17% for CFSR (see Table 3.4). In Fig. 3.6 we chose to display the EK AWS RH scatter plots as the biases at this site are representative of those recorded at the three AMRC AWS sites (see Table A.3). RMSEs are large for all reanalysis products, up to 17% for CFSR at the AMRC sites. It is however notoriously difficult to measure RH particularly in the harsh environment in which these AWS are located, and problems with the observations may contribute to RH biases and RMSE (e.g. Renfrew and Anderson, 2002). Due to the low observed temperatures the specific humidity is low, averaged across the AMRC sites the mean value is 1.42 $g\ kg^{-1}$. CFSR has the smallest dry bias in the specific humidity filed of 0.05 $g\ kg^{-1}$. MERRA is a lot drier than observed with a bias of 0.63 $g\ kg^{-1}$, this is unsurprising given its cold temperature bias. ERA-I and JRA-55 both produce dry biases of $\sim$ 0.2 $g\ kg^{-1}$.

- All reanalysis products underestimate the observed spread of the wind speed at the AWS sites, they tend to overestimate at low wind speeds and underestimate at high wind speeds. This leads to the slope of linear regression lines to be between 0.25 and 0.7.

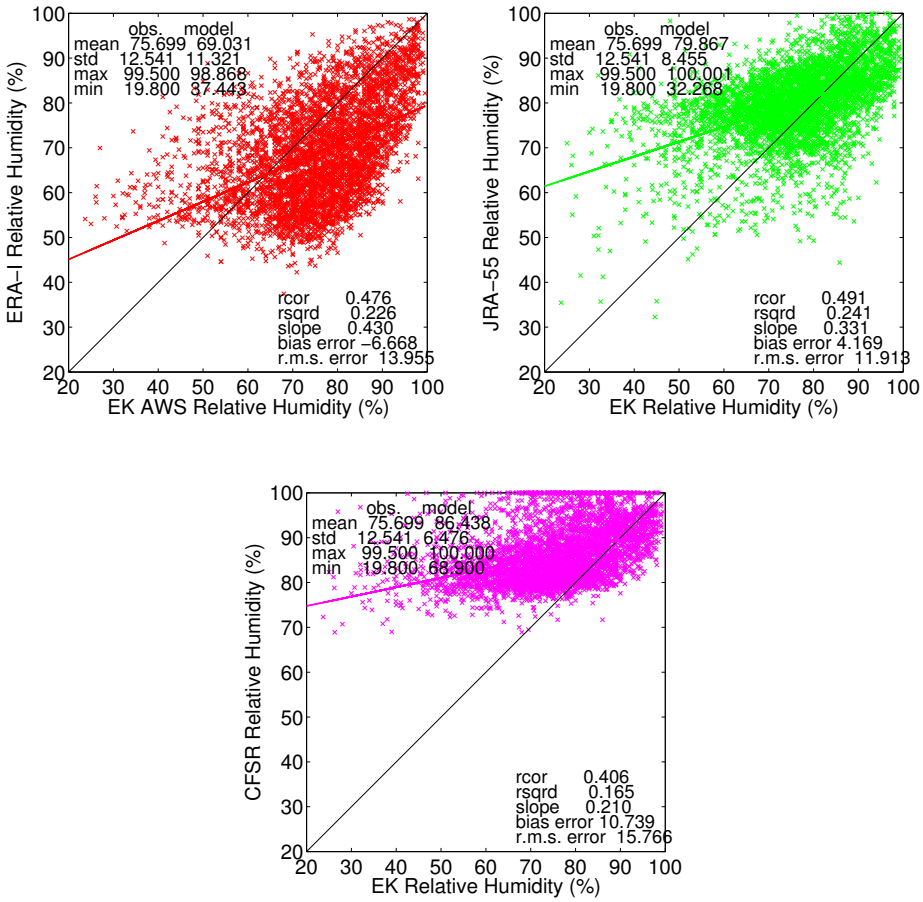

Figure 3.6: Scatter plots showing the EK AWS observed relative humidity compared to the 2 metre relative humidity from four reanalysis products. Top left (a) ERA-I; top right (b) JRA-55; bottom (c) CFSR.

- Orographic and katabatic effects, particularly at the BP and TI AWSs seem to enhance the wind speed, with strong wind events primarily coming from a northerly direction. This may explain why the reanalysis products are struggling to capture these events.

- There is a tendency for the reanalysis products to be drier than observed in the specific humidity field, particularly so in MERRA. In the relative humidity field RMSE errors are particularly large and there is a tendency for CFSR to have higher relative humidity values than were observed.

3.5 COMPARISON TO RESEARCH VESSEL METEOROLOGICAL DATA

Summertime research vessel cruises to the Amundsen Sea have become more frequent in recent years with at least five visits to the Amundsen Sea Embayment since 2007 (Dutrieux et al., 2014). Here we utilise research vessel meteorological data from three separate research cruises.

Table 3.5: Statistical comparison of the four reanalysis products to meteorological data from three research vessel cruises to the Amundsen Sea; *JCR* Feb 2014, *RV Polarstern* March 2010 and the *Nathaniel B. Palmer* Jan-Feb 2009. MSLP is the mean sea level pressure, Temp is temperature, Wsp is wind speed, q is specific humidity and RH is relative humidity. Observational data are corrected from sensor height to reanalysis output height.

		Ship meteorological observations				
Product	Stats	MSLP (hPa)	Temp ($°C$)	Wsp ($m\ s^{-1}$)	q ($g\ kg^{-1}$)	RH (%)
ERA-I	Bias	0.00	-0.62	-0.82	-0.20	-3.73
	SD ratio	1.00	1.20	0.97	1.08	1.03
	R^2	0.99	0.77	0.48	0.84	0.54
	RMSE	0.74	1.64	3.00	0.34	7.78
	Slope	1.00	1.04	0.67	0.99	0.77
JRA-55	Bias	-0.05	-0.39	-0.32	-0.03	2.03
	SD ratio	1.01	1.22	0.96	1.11	0.84
	R^2	0.99	0.76	0.71	0.79	0.48
	RMSE	1.26	1.58	1.96	0.32	7.53
	Slope	1.00	1.04	0.81	0.97	0.59
CFSR	Bias	-0.22	-1.63	-0.83	-0.22	2.32
	SD ratio	1.01	1.55	0.81	1.15	0.65
	R^2	0.97	0.72	0.46	0.83	0.34
	RMSE	1.85	2.88	2.88	0.39	8.66
	Slope	0.99	1.28	0.55	1.04	0.37
MERRA	Bias	0.46	-2.08	-1.02	-0.30	1.02
	SD ratio	1.01	1.50	0.81	1.11	0.80
	R^2	0.98	0.60	0.62	0.71	0.26
	RMSE	1.46	3.38	2.46	0.51	9.10
	Slope	1.00	1.13	0.64	0.93	0.39

Pressure is extermely well represented by all the reanalyses; the magnitude of biases in mean sea level pressure is less than 0.5 hPa and the R^2 values are greater than 0.95 (Table 3.5). Bracegirdle (2013) found pressure biases of similar magnitude using drifting buoy observations in the neighbouring Bellingshausen Sea. The ship board

instrumental error for pressure measurements is likely to be of a similar magnitude to the biases seen in Table 3.5.

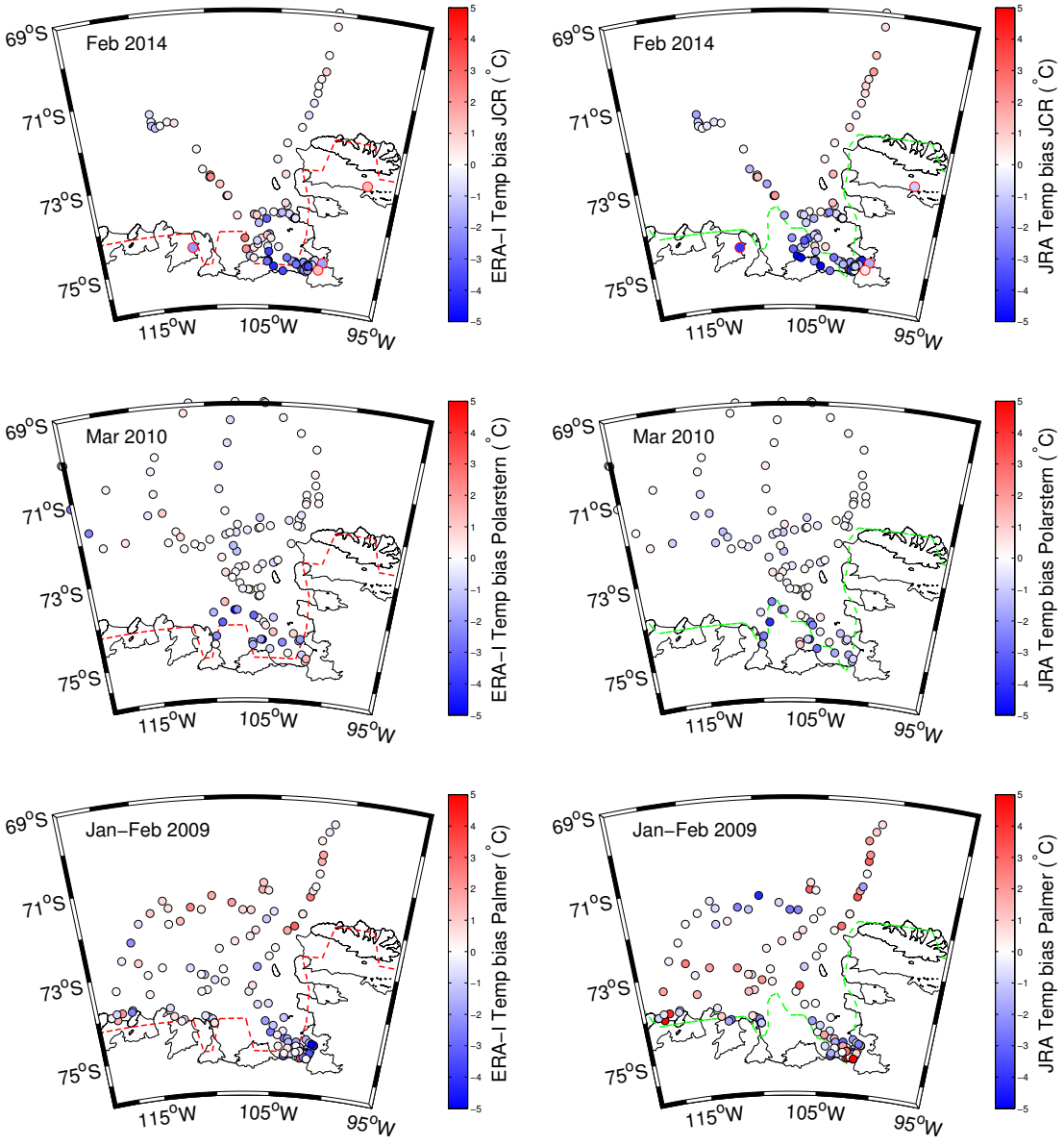

Figure 3.7: Spatial variability of reanalysis temperature biases (ERA-I left column, JRA right column) in comparison to research vessel meteorological data from: *JCR* (top row), *RV Polarstern* (middle row), and *Nathaniel B. Palmer* (bottom row). In the *JCR* figures the mean temperature bias from the AWSs for the month of Feb 2014 are shown in the larger circles with red edge colour. The dashed lines show the land sea mask (here the 0.95 contour is shown for ERA-I and 0.5 contour for JRA).

As seen in the AWS comparison, all four products are colder than the observed near-surface temperatures, with MERRA showing the largest bias of ($-2.08\ ^{\circ}C$). Similarly to the AWS comparison ERA-Interim and JRA-55 display a smaller

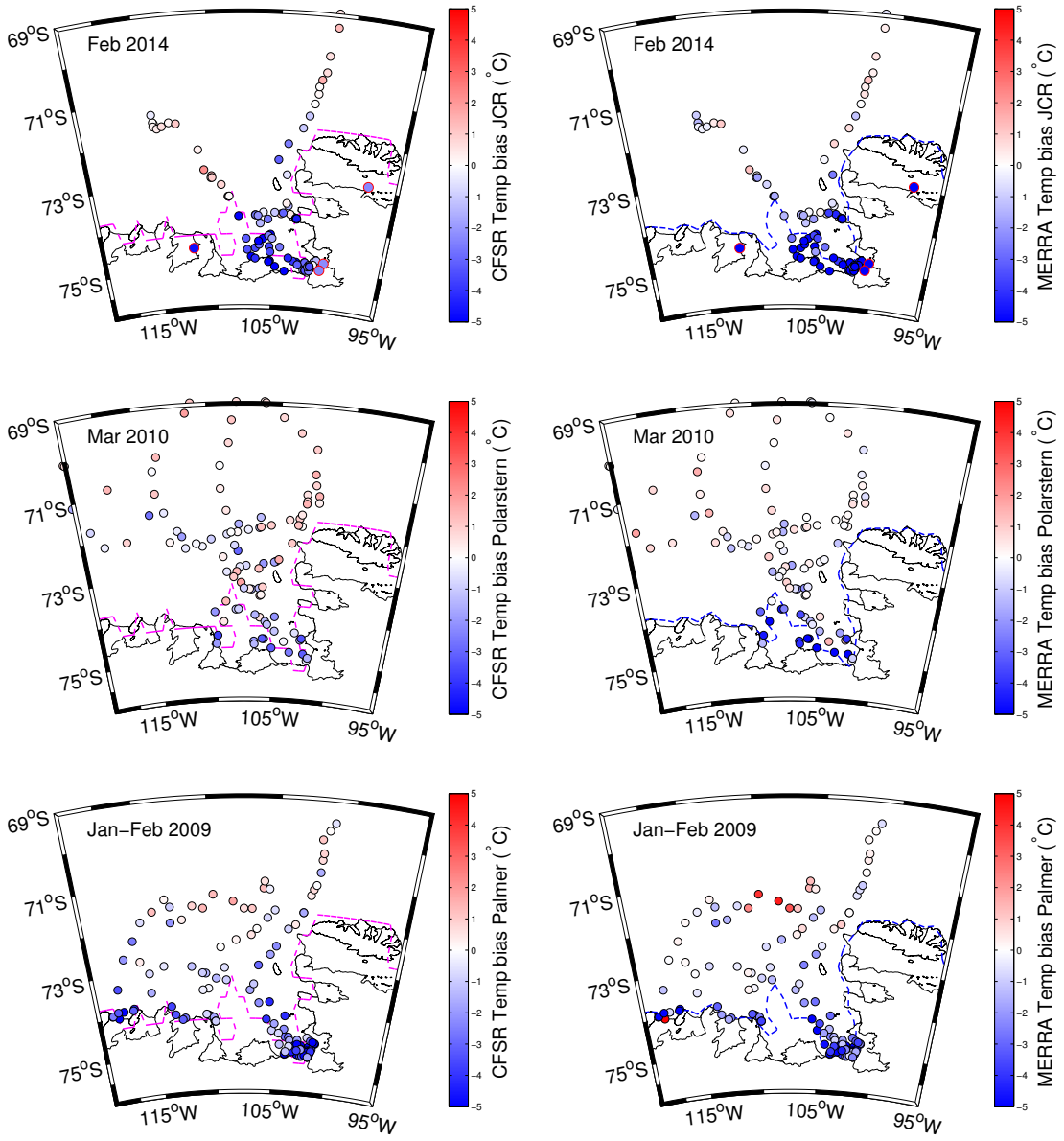

Figure 3.8: Spatial variability of reanalysis temperature biases (CFSR left column, MERRA right column) in comparison to research vessel meteorological data from: *JCR* (top row), *RV Polarstern* (middle row), and *Nathaniel B. Palmer* (bottom row). In the *JCR* figures the mean temperature bias from the AWSs for the month of Feb 2014 are shown in the larger circles with red edge colour. The dashed lines show land sea mask (here the 0.5 contour is shown for CFSR and MERRA).

(summertime) temperature bias than CFSR (Table 3.5). The map plots in Figs. 3.7 and 3.8 reveal the spatial distribution of temperature biases for the four reanalysis products. In all of the reanalysis products there is a tendency for temperature biases to be most negative when the vessel is located closer to the coastline, with the largest biases approaching $-6\ ^{\circ}C$. For MERRA and CFSR the negative temperature bias is

particularly large in the *JCR* and *Nathaniel B Palmer* comparisons as these ships spent more time closer to the PIG ice shelf. In the ERA-I and JRA plots there is a negative temperature bias apparent close to PIG in the *JCR* comparison (albeit weaker than that seen in MERRA) but the spatial pattern is less distinct in the *Palmer* comparison, hence these two products have smaller overall mean temperature biases. The reanalysis temperature biases compared to AWS observations in February 2014 are also included in the *JCR* map plots, these biases corroborate the nearby research vessel comparison points.

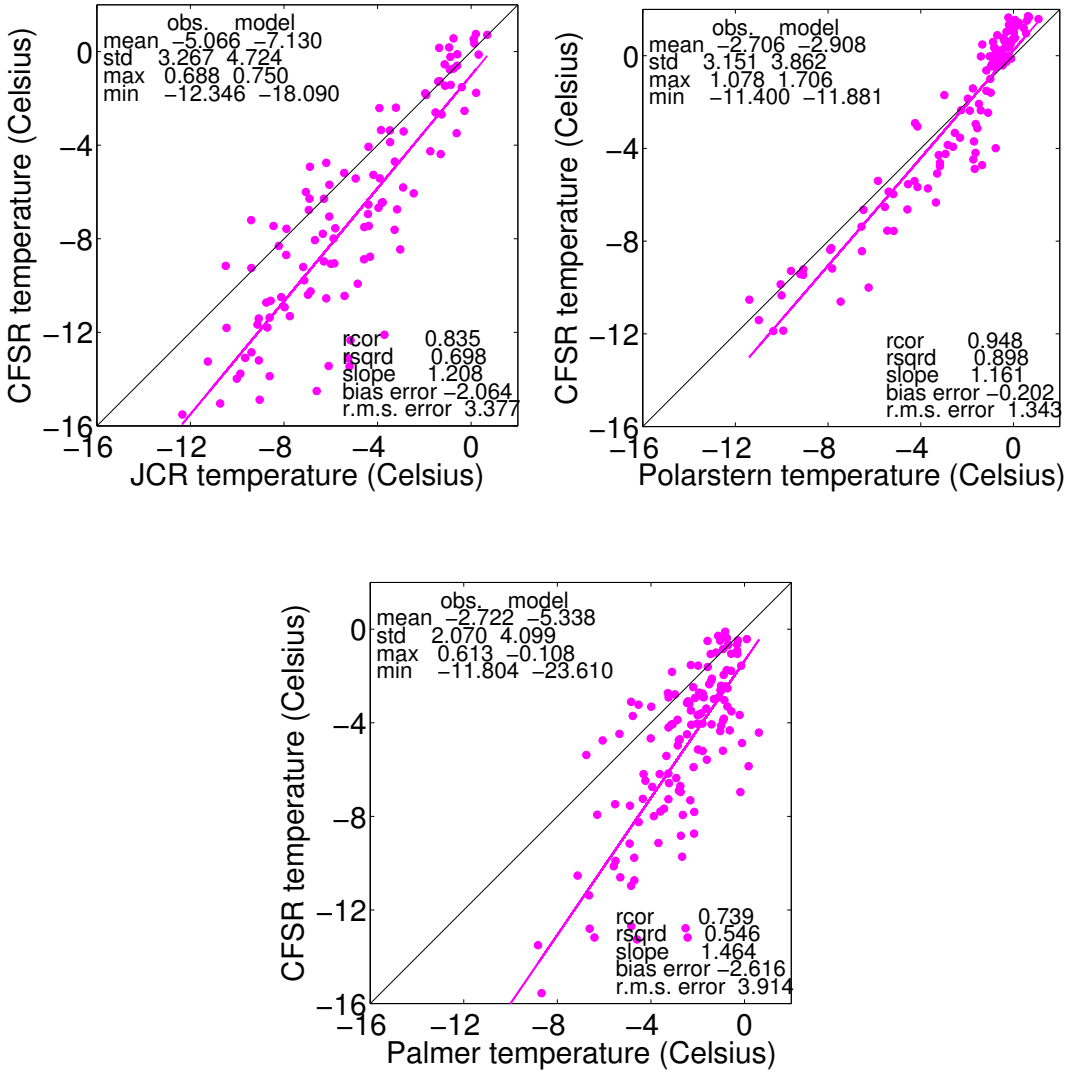

Figure 3.9: Temperature scatter plots comparing CFSR 2 metre temperatures to height adjusted research vessel observations: Top left (a) *JCR*; top right (b) *RV Polarstern*; bottom (c) *Nathaniel B Palmer*.

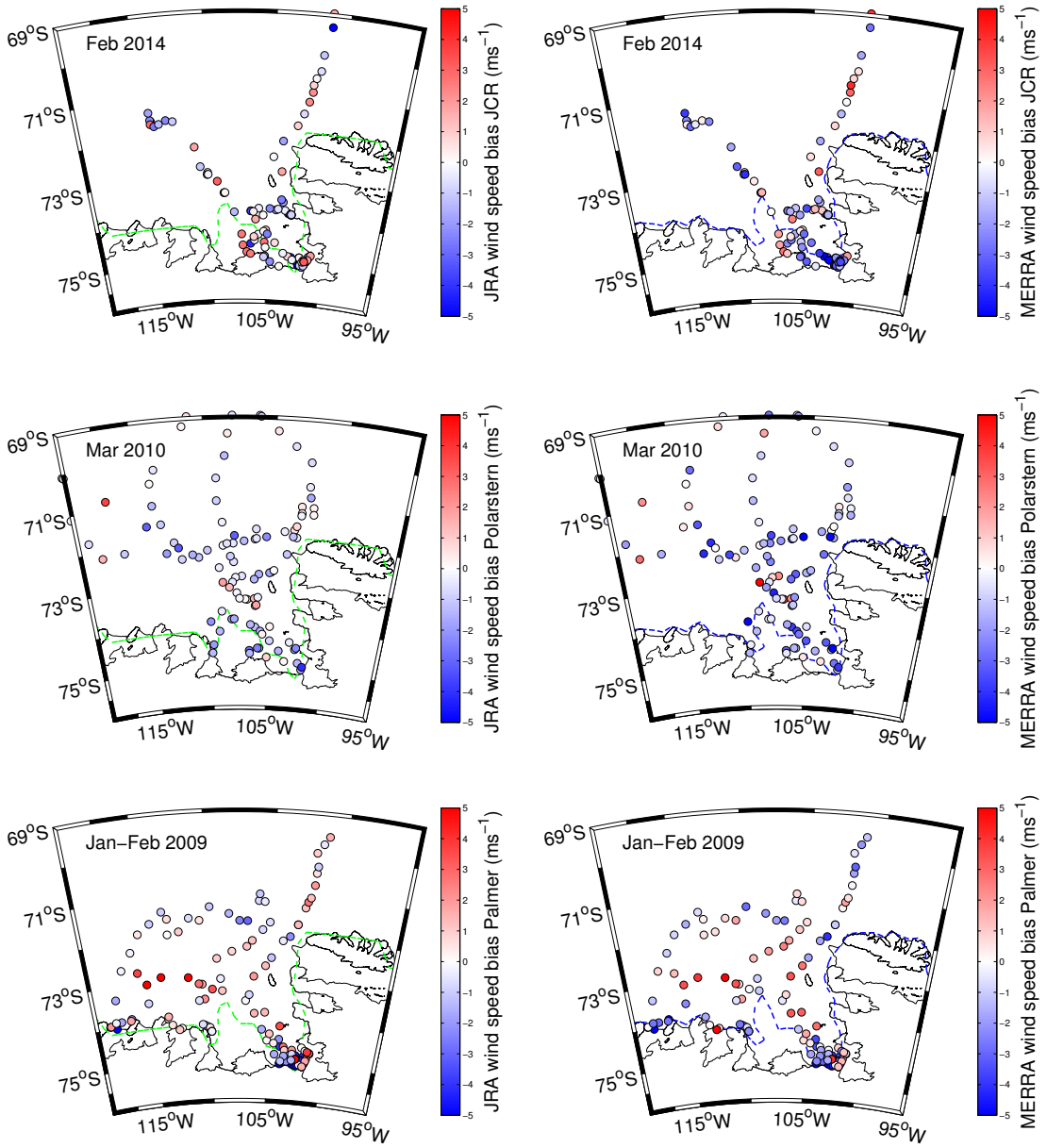

Figure 3.10: Spatial variability of reanalysis wind speed biases (JRA left column, MERRA right column) in comparison to research vessel meteorological data from: *JCR* (top row), *RV Polarstern* (middle row), and *Nathaniel B. Palmer* (bottom row). The dashed lines show land sea mask in each of the products (here the 0.5 contour is shown for both JRA and MERRA).

The scatter plots in Fig. 3.9 reveal that along with the spatial variability in the magnitude of temperature biases there is also a temperature dependence. For CFSR and MERRA (not shown) there is a tendency for smaller bias and RMSE values when the observed temperature is close to freezing. At colder temperatures CFSR and MERRA have less skill, temperatures below $-10\,^{\circ}C$ are more frequently observed close to the ice shelves. The temperature dependence of the bias is shown by the large

standard deviation ratio and slope values for CFSR and MERRA in Table 3.5, both products have larger standard deviations and slopes due to the cold temperature bias being bigger at colder temperatures (e.g. Fig. 3.9). This temperature dependence of the bias is not seen in ERA-I and JRA-55. It is noteworthy that the CFSR summertime cool biases compared to AWS observations displayed similar characteristics with larger biases at colder observed temperatures (see Fig. 3.3c).

The reanalysis products underestimate the mean wind speed compared to the research vessel observations by between $-0.32\ m\ s^{-1}$ (JRA-55) and $-1.02\ m\ s^{-1}$ (MERRA) (see Table 3.5). There is no clear pattern of spatial variability in the wind speed bias for any of the reanalysis products, as illustrated for JRA-55 and MERRA in Fig. 3.10. Scatter plots for all three cruises show an improved representation of high wind speeds than was seen in the AWS comparison (not shown). The biases at wind speeds between 15 $m\ s^{-1}$ and 19 $m\ s^{-1}$ (the highest observed research vessel wind speeds) are small. Pressure and wind speed observations from the research vessels are made available for assimilation into the GTS and they may explain the reduced bias. In contrast to the results seen here, Li et al. (2013) have shown that ERA-I contains biases at low and high wind speeds compared with Southern Ocean ship observations, overestimating low winds and underestimating high winds. Here we see little evidence of such systematic biases but note that our sample is limited and there are few strong wind observations from research vessels in the Amundsen Sea.

Biases in the specific and relative humidity fields are generally slightly smaller those seen in a comparison with summertime AWS observations, but all of the products are drier than observed for specific humidity (Table 3.5). The spatial distribution of biases (not shown), reveal there is a tendency for larger dry biases in the specific humidity field of MERRA and CFSR close to the coastline. This is spatially coherent with low temperature biases in the same region (see Fig. 3.8). As MERRA and CFSR both give temperatures that are colder than observed they are also likely to have less moisture. In the other reanalysis products there are no clear spatial patterns in the humidity biases; large biases are seen in many different locations, for relative humidity in particular.

- Overall reanalysis cold temperature biases are much smaller than those seen in the AWS comparison. However, cold temperature biases show large spatial

variability with much bigger cold biases when research vessel are located close to the continent.

- Reanalysis mean wind speeds tend to be slightly lower than observed, but there is no evidence of the same biases at high and low observed wind speeds that were seen in the AWS comparison. The magnitude of wind speed biases is variable across the region with no clear region where larger wind speed biases are observed.

- MERRA, CFSR and ERA-I all contain fairly large dry biases in the specific humidity field, spatially these biases tend to be larger close to the coastline particularly for CFSR. For relative humidity mean biases are smaller than were seen in the AWS comparison but RMSE remain fairly large.

3.6 RADIOSONDE PROFILE COMPARISON

A set of 38 radiosondes were launched from the *JCR* in the Amundsen Sea during February and March 2014. Having been deliberately withheld from the GTS they provide a unique observational data set for validating reanalysis products in this region. Here we focus on a comparison between 975 and 800 hPa, as the lower troposphere is most important for the underlying ocean and glaciers.

3.6.1 MEAN PROFILE BIASES

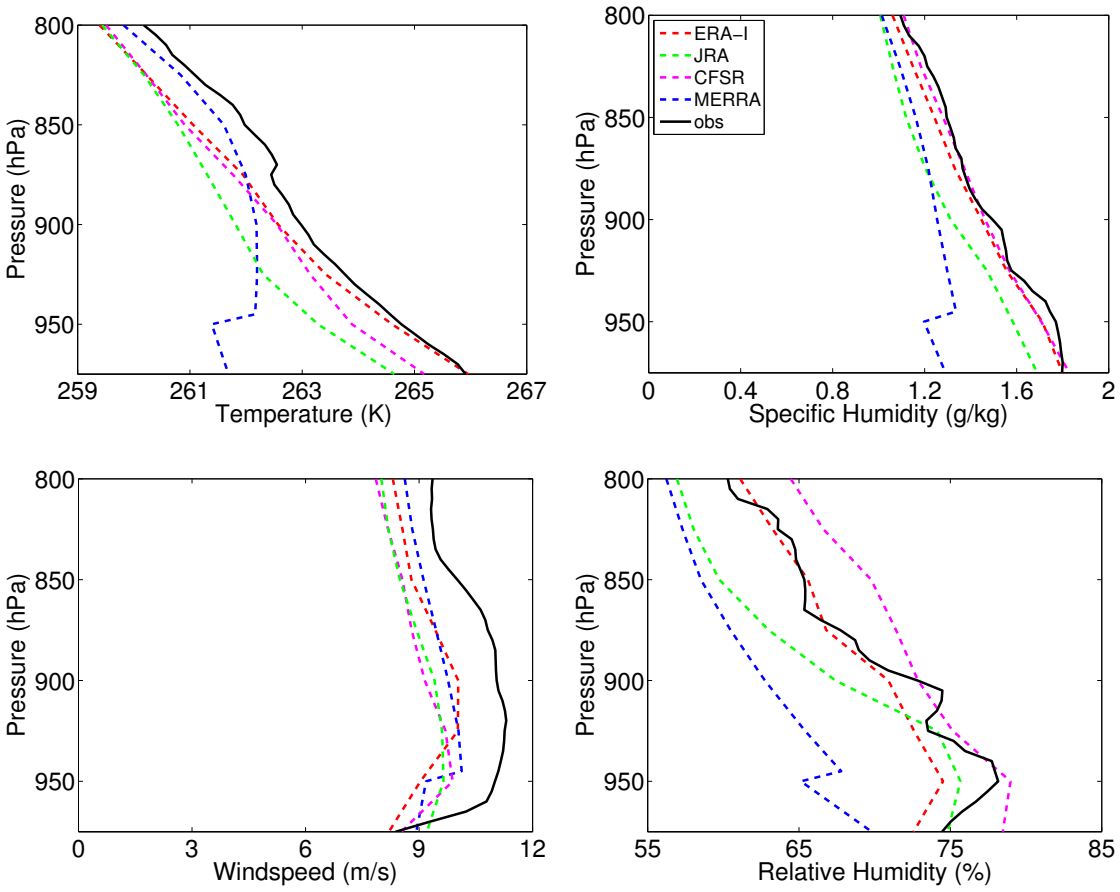

Figure 3.11: Mean atmospheric profiles from the radiosondes and reanalyses; Top left (a) Temperature; top right (b) Specific Humidity; bottom left (c) Wind speed; and bottom right (d) Relative Humidity. The coloured lines represent the same reanalysis products as in Fig. 3.2: red ERA-I, green JRA-55, magenta CFSR and blue MERRA.

All of the reanalysis products have a mean temperature profile that is colder than the radiosondes. The 975-800 hPa mean temperature bias varies between $-0.54\ ^{\circ}C$

for ERA-I and $-1.22\ ^{\circ}C$ for JRA-55 (Table 3.6). This cold bias is consistent in sign with the research vessel near-surface temperature biases. The mean temperature profiles in Fig. 3.11a reveal that CFSR and ERA-I are accurate to within $\sim 1\ ^{\circ}C$ of the average radiosonde temperature from 975 hPa to 800 hPa. JRA-55 also produces a similar shaped mean profile to the observations, but has a larger bias of between $-1\ ^{\circ}C$ and $-2\ ^{\circ}C$. Close to the surface MERRA has a large cold bias: at 975 hPa the average MERRA temperature is $4\ ^{\circ}C$ colder than observed, consistent with the large near-surface temperature biases seen during the *JCR* cruise (Table 3.5, Fig. 3.8).

All four of the reanalyses produce similar average wind speed profiles (see Fig. 3.11c). At 975hPa all four products accurately predict the near-surface wind speed to within 1 $m\ s^{-1}$. Above this the observations show a distinct low-level jet (discussed later) which is not captured by the reanalyses. As such there is a negative bias for all of the products, with average wind speeds $\sim 2\ m\ s^{-1}$ lower than the radiosonde observations between 950 hPa and 850 hPa.

The specific (Fig. 3.11b) and relative humidity (Fig. 3.11d) mean profiles reveal that ERA-I and CFSR provide accurate profiles of atmospheric moisture, ERA-I is perhaps the most accurate, particularly in the relative humidity profile. MERRA and JRA-55 are both drier than the observations, although JRA-55 accurately produces the relative humidity profile between 975 and 920 hPa with larger biases above this. The specific humidity profile shows a significant dry bias of 0.5 $g\ kg^{-1}$ for MERRA between 975 and 925 hPa, which reduces with increasing height. This is linked to the MERRA cold bias, colder air can hold less moisture, and as such there is a dry bias in the same part of the profile as the cold bias. Jakobson et al. (2013) also find that over Arctic sea ice MERRA is drier than observations of both specific and relative humidity, this suggests that MERRA may have difficulties with moisture budgets or transport, near Arctic sea ice and in continental shelf regions of Antarctica.

3.6.2 TEMPERATURE BIASES

By splitting the radiosondes into two groups by location (see Fig. 3.1) it becomes clear that the temperature biases seen in Fig. 3.11 are, in the main, caused by the group of radiosondes launched closer to the Antarctic continent (Fig. 3.12). All of the reanalysis products have a larger mean temperature bias for the 'continental' profiles

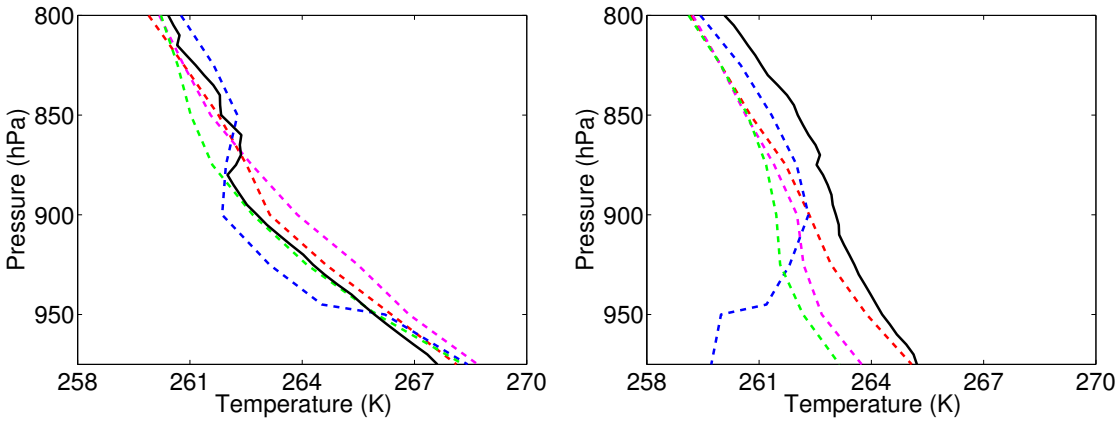

Figure 3.12: Radiosonde temperature profile comparison split into two groups; Left (a) shelf break radiosondes (11 profiles); Right (b) continental radiosondes (27 profiles). The map in Fig. 3.1 shows the spatial split. The coloured lines represent the same reanalysis products as in Fig. 3.11.

than for the 'shelf break' radiosondes. In the 'continental' group JRA-55 and MERRA produce the largest mean (975-800 hPa) biases of $-1.60\,^{\circ}C$ and $-1.50\,^{\circ}C$ respectively. For MERRA the negative temperature bias between 975 and 900 hPa only occurs in the 'continental' profiles, consistent with the distribution of temperature biases in comparison with research vessel observations (Fig. 3.8). In the layer between 975 hPa and 940 hPa, the lowest few hundred metres of the atmosphere, the MERRA mean temperature in the continental group is $4.23\,^{\circ}C$ colder than the radiosondes.

The larger biases in the continental radiosondes are consistent with the cold biases seen at three of the four AWSs. The near-surface cold bias in the continental radiosondes is greatest for MERRA, and is smallest in ERA-I, as was seen in the AWS comparison (see Table 3.3). In the research vessel comparison larger cold biases were also seen close to the continent with smaller biases towards the open ocean (Figs. 3.7 and 3.8). By combining these three observational data sets it becomes clear that all of the reanalysis products (but particularly MERRA) struggle to reproduce near-surface temperatures close to ice shelves and in coastal continental regions of the Amundsen Sea Embayment they all contain cold biases.

3.6.3 WIND SPEED BIASES

The wind speed profiles have also been split into two distinct groups: those containing a low-level jet (LLJ) and those without (Fig. 3.13). A LLJ in its most

simplistic form is a wind speed maxima in the lower part of the atmosphere. In order to identify LLJs the definition from Stull (1988), and later modified by Andreas et al. (2000), is used. Namely, to be classified as an LLJ a wind speed maxima must occur in the lowest 1.5 km of the atmosphere and must be at least 2 $m\ s^{-1}$ faster than both the wind speed minima above it and that recorded at the surface. LLJs were observed in 21 of the 38 radiosonde soundings (see Fig. 3.1 for locations).

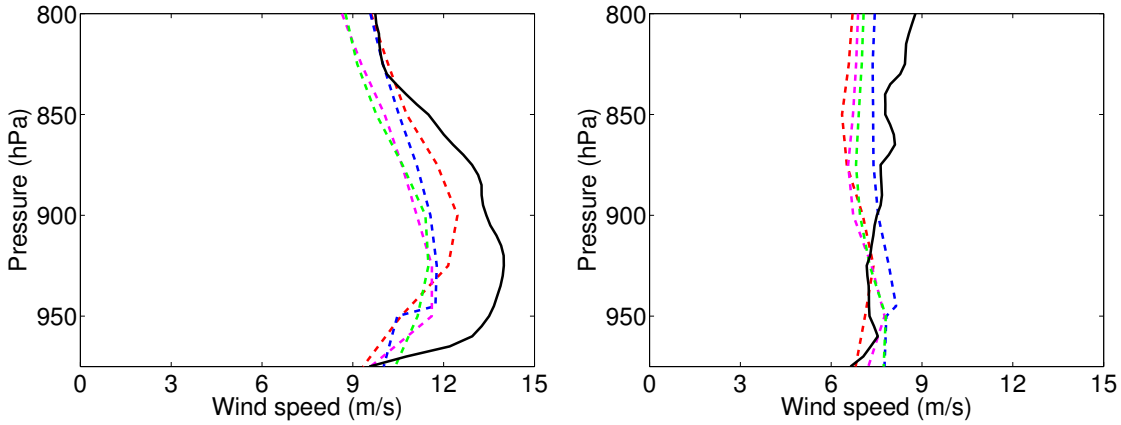

Figure 3.13: Average wind speed profiles split for two groups of radiosondes; Left (a) 21 profiles where a low level jet (LLJ) was recorded by the radiosonde; right (b) 17 profiles where a LLJ was not observed. The coloured lines represent the same reanalysis products as in Fig. 3.11.

Fig. 3.13 shows that in the group of soundings where an LLJ is not observed all of the reanalysis products accurately simulate the wind speed profile between 975 and 900 hPa. Above this they tend to underestimate the wind speed by between 1 $m\ s^{-1}$ and 2 $m\ s^{-1}$. When there is a LLJ, the reanalysis products (on average) show positive wind shear between 975 and 925 hPa, which indicates that at least some of the LLJs are being captured. However they all underestimate the mean jet wind speed by $\sim 2\ m\ s^{-1}$, which indicates they are either failing to produce the maximum wind speed within the LLJs or they underestimate the frequency of them; inspection of individual profiles reveals that both are factors. In comparison to Arctic dropsonde data it has been shown that ERA-I tends to produce LLJs that are both too broad and too weak (Liu et al., 2015). The mean profiles in Liu et al. (2015) are similar to those seen here, with ERA-I managing to reproduce the wind speed maxima at approximately the same altitude as the observations but unable to reproduce the observed magnitude. Here, normalised bias profiles (not shown) reveal that the bias relative to the mean

observed wind speed is greater in the LLJ group than in the no-LLJ group, i.e. the reanalyses perform worse when there is a LLJ.

3.6.4 BIASES IN PROFILES CONTAINING A TEMPERATURE INVERSION

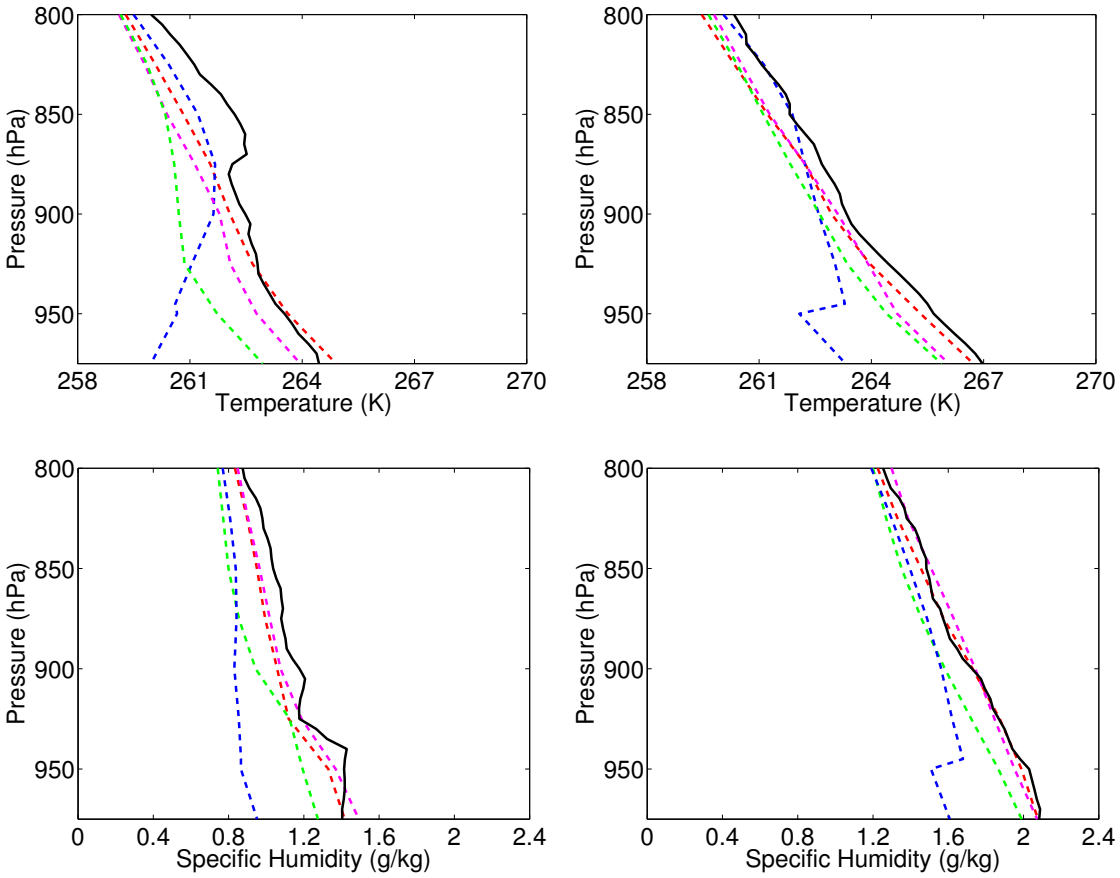

Figure 3.14: 975 to 800 hPa mean; Top left (a) temperature profiles when a temperature inversion was observed (16 profiles); top right (b) temperature profiles when a temperature inversion was not observed (22 profiles); bottom left (c) specific humidity profiles when a temperature inversion was observed (16); and bottom right (d) specific humidity profiles when a temperature inversion was not observed (22).

The profiles have also been split according to whether or not they contain a temperature inversion below the 800 hPa pressure level. Here a temperature inversion is defined as a temperature increase of $> 2\ ^{\circ}C$ (between the base and top of the inversion) between 975 hPa and 800 hPa, 16 of the 38 profiles contained an inversion. In Figs. 3.14 (a and b) the mean radiosonde and reanalysis temperature profiles are shown for both groups. JRA, CFSR and MERRA all have larger temperature biases for the group of radiosonde profiles which contain temperature inversions

(see Table 3.6). This larger bias is particularly apparent in the layer between 975 and 875 hPa where almost all of the temperature inversions were observed (not shown). Given that the vertical depth of temperature inversions in the observations is typically hundreds or even tens of metres, the coarse vertical resolution of reanalysis products will struggle to capture these features. ERA-I has a similar magnitude temperature bias in both groups, although larger RMSE in the inversion group.

Table 3.6: Mean profile statistics from 975 hPa to 800 hPa for each of the reanalysis products; Temperature (T), Relative Humidity (RH), Specific Humidity (q) and Wind speed (Ws). Along with the mean of all profiles (All), the profiles have been split into groups to see how the accuracy of reanalysis products varies depending on conditions. The splits are as follows: Shelf Break and Continental, Inversion (Inv) and Non-Inversion (No-Inv) and Low Level Jet (LLJ) and Non-Low Level Jet (No-LLJ).

		ERA-I		JRA-55		CFSR		MERRA	
		Bias	rmse	Bias	rmse	Bias	rmse	Bias	rmse
T	**All** (38)	**-0.54**	**1.42**	**-1.22**	**1.88**	**-0.79**	**1.96**	**-1.19**	**2.03**
	Shelf B. (11)	0.11	1.27	-0.28	1.21	0.47	1.68	-0.31	1.47
	Cont. (27)	-0.80	1.46	-1.60	2.06	-1.29	2.06	-1.50	2.13
	Inv. (16)	-0.54	1.64	-1.64	2.26	-1.02	2.19	-1.52	2.18
	No-inv (22)	-0.55	1.21	-0.92	1.54	-0.62	1.77	-0.93	1.88
RH	**All** (38)	**-1.22**	**12.47**	**-3.53**	**16.07**	**2.53**	**11.80**	**-7.67**	**17.59**
	Inv. (16)	-2.68	13.09	-3.96	15.48	2.03	11.59	-10.63	19.31
	No-Inv (22)	-0.16	11.82	-3.21	16.33	2.88	11.83	-5.48	15.98
q	**All** (38)	**-0.05**	**0.24**	**-0.16**	**0.33**	**-0.02**	**0.29**	**-0.23**	**0.38**
	Inv. (16)	-0.08	0.26	-0.19	0.36	-0.05	0.24	-0.31	0.43
	No-Inv (22)	-0.02	0.22	-0.13	0.31	0.00	0.32	-0.17	0.32
Ws	**All** (38)	**-0.95**	**3.48**	**-1.22**	**3.40**	**-1.16**	**3.27**	**-0.75**	**3.30**
	LLJ (21)	-1.17	3.65	-1.75	3.67	-1.75	3.40	-1.26	3.55
	No-LLJ (17)	-0.61	3.18	-0.43	2.89	-0.29	3.03	-0.01	2.85

In the Arctic multiple studies have found similar problems with the strength and depth of temperature inversions in reanalysis products (Lüpkes et al., 2010; Pavelsky et al., 2011; Harden et al., 2011; Jakobson et al., 2012). Lüpkes et al. (2010) show that ERA-I overestimates the altitude of the inversion base. Here individual profiles suggest that reanalysis inversions are vertically too broad and often too weak. Contributing to the larger temperature biases seen in JRA-55, CFSR and MERRA.

ERA-I and CFSR again produce remarkably accurate specific humidity profiles for both the inversion and non-inversion groups (Figs. 3.14c and 3.14d). However, neither of these products manages to capture the near constant specific humidity

between 975 and 940 hPa in the group containing inversions (Fig. 3.14c). In the inversion group both MERRA and JRA contain a larger mean specific humidity bias than the non-inversion group between 975 and 800 hPa. For MERRA it seems that the additional bias is driven by a larger dry bias in the surface layer, in JRA the increased bias is due to the layer between 900 and 800 hPa, typically above the height of temperature inversions.

3.6.5 EXAMPLES: 13TH AND 15TH FEB 2014

Comparing mean atmospheric profiles can hide deficiencies in the performance of reanalysis products. Here two examples are briefly discussed to illustrate profile biases at one instance in time and in differing synoptic situations.

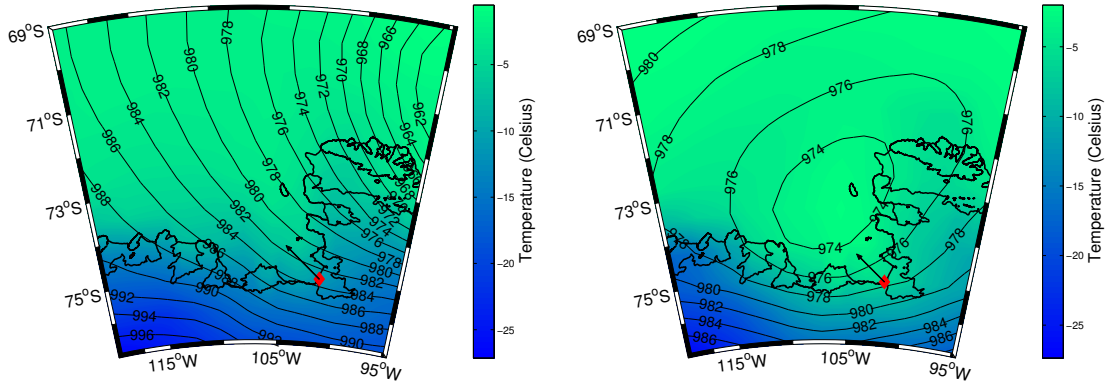

Figure 3.15: Mean sea level pressure and temperature over the Amundsen Sea Embayment at: Left (a) 1200UTC on 13th February; and right (b) 1200UTC on 15th February (both from ERA-I). The wind vector shows the wind direction recorded on the research vessel, the observed near-surface wind speed was 12 $m\ s^{-1}$ on the 13th and 10 $m\ s^{-1}$ on the 15th. The background colour contour shows the 2-m temperature (Celsius) with labelled isobars showing the mean sea level pressure (hPa).

On both the 13th and 15th February a radiosonde was launched from the *JCR* when it was located close to the ice shelf of PIG. On 13th February the implied wind direction from the isobars is slightly south of east, surface friction is the likely cause of south-easterly near-surface winds recorded on the *JCR*. A large, deep cyclone with centre to the north east of PIG is driving the synoptic weather pattern (see Fig. 3.15a), the isobars are close together, suggesting strong winds. The mean sea level pressure on board the *JCR* dropped through the day suggesting a westward movement of the cyclone, which is supported by ERA-I (not shown).

The synoptic conditions on 15th February show a weaker low pressure system centred north of the *JCR* with central pressure of 974 hPa (see Fig. 3.15b). Field notes reveal that light snow had fallen overnight but had stopped by 1120 UTC, the launch time. Low cloud associated with the cyclone was reported and the surface temperature recorded on the *JCR* was $-7.6\ ^{\circ}C$. Despite ERA-I pressure contours suggesting easterly near-surface flow, the wind direction recorded on the *JCR* was from the south east, blowing off PIG ice shelf.

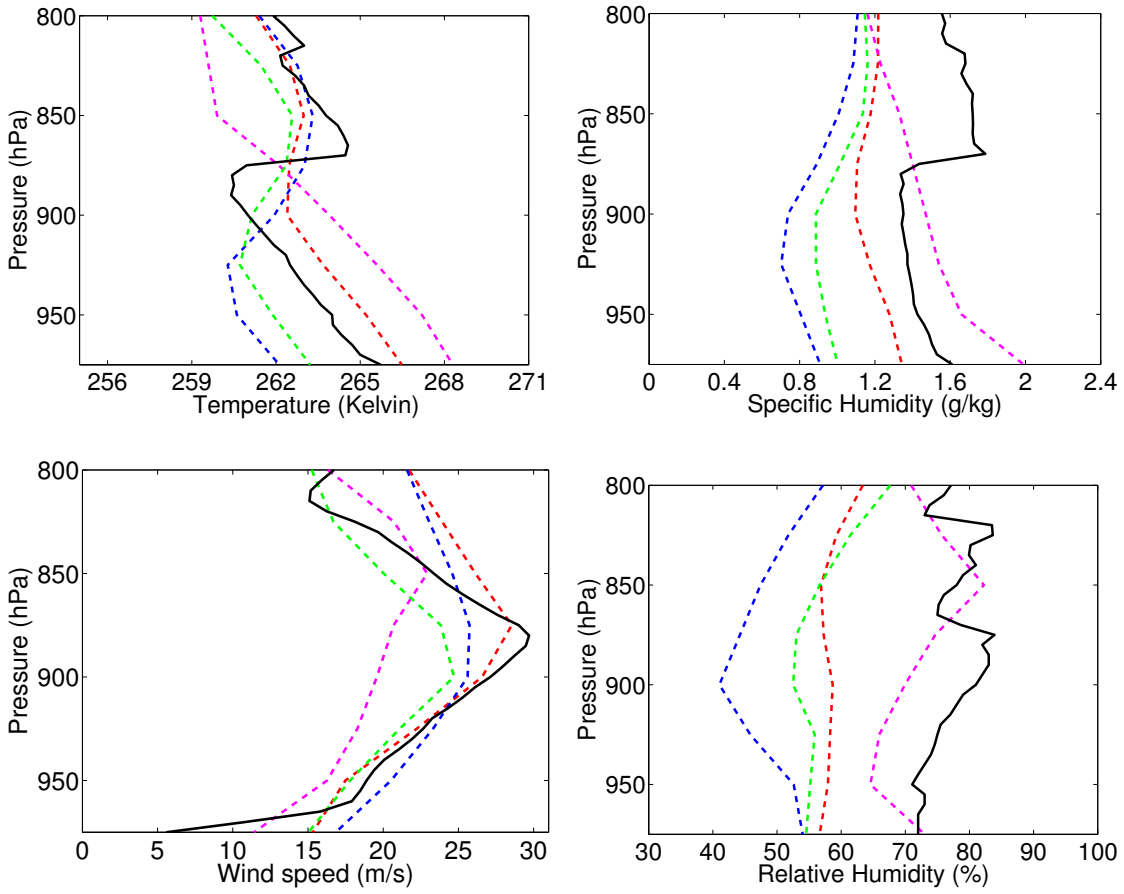

Figure 3.16: Radiosonde and reanalysis profiles from 1620UTC on 13th February 2014: Top left (a) Temperature; top right (b) Specific Humidity; bottom left (c) Wind speed; and bottom right (d) Relative Humidity.

The observed temperature profile from 13th Feb (Fig. 3.16a) shows a 5 $^{\circ}C$ temperature inversion at 880 hPa. JRA-55, ERA-I and MERRA all produce a temperature inversion that is both vertically broader and typically somewhat lower than observed; they all fail to reproduce the sharp temperature gradient over a few tens of metres - unsurprisingly given their coarse vertical resolution. All of the

reanalysis products struggle to reproduce a humidity inversion at the same altitude and are therefore too dry, particularly above the inversion (Fig. 3.16b). The wind speed profile from the radiosonde shows a strong LLJ at the same altitude as the base of the temperature inversion. The reanalysis products that contain a temperature inversion all produce a LLJ with peak wind speed at approximately the same altitude as observed. CFSR, which doesn't reproduce the inversion, does produce a LLJ but it is weaker and higher than in the other reanalysis products and the observations. Despite the shortcomings discussed here, it is clear that the reanalysis products are doing a relatively good job of reproducing the atmospheric profiles. In this case the temperature inversion and LLJ are likely linked to the synoptic-scale cyclone, perhaps a frontal system, and due to the larger scale of the forcing mechanism it appears the reanalysis products successfully identify features such as the inversion and LLJ.

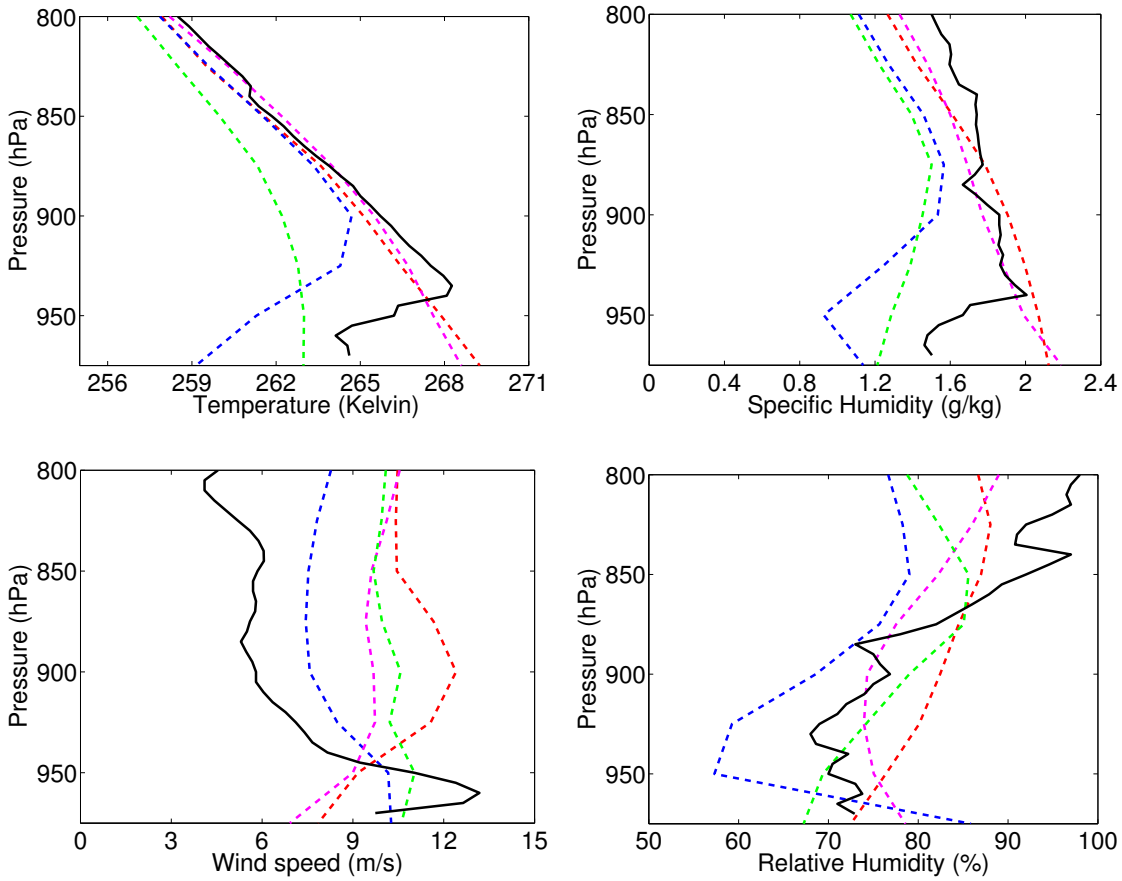

Figure 3.17: Radiosonde and reanalysis profiles from 1200UTC on 15th February 2014: Top left (a) Temperature; top right (b) Specific Humidity; bottom left (c) Wind speed; and bottom right (d) Relative Humidity. The coloured lines represent the same reanalysis products as in Fig. 3.11.

The radiosonde temperature profile from 15th Feb (Fig. 3.17) shows a low level temperature inversion with its base at 960 hPa, its top at 935 hPa and a temperature increase of approximately 4 $^{\circ}C$. Of the reanalysis products only MERRA produces an inversion of similar strength and depth, although in its case the inversion extends down to the surface. From the surface to 935 hPa MERRA is 4 $^{\circ}C$ colder than observed. ERA-I and CFSR both accurately reproduce temperatures above 900 hPa but fail to produce a near-surface inversion and hence over-estimate the surface temperature by 4 $^{\circ}C$.

Coincident with the base of the temperature inversion a LLJ is recorded in the observed wind speed profile (Fig.3.17c). Only ERA-I produces a feature that could be described as a LLJ and while this does match the maximum wind speed, it is more than 50 hPa (approx. 500 metres) above the observed jet and it is too broad. Above the jet the observed wind speed drops and all of the products over-estimate the wind speed between the 940 hPa and 800 hPa pressure levels. In this example the reanalysis products struggle to reproduce the temperature and wind speed profiles; with both the observed near-surface temperature inversion and low-level jet absent in three of the four reanalysis products. With the *JCR* located 2 km from PIG ice shelf and the wind blowing off the glacier it is possible that katabatic or orographic enhancement of the near-surface wind may have caused an acceleration of the jet and this may explain the inaccurate profiles from the reanalysis products.

- Mean atmospheric profiles show that ERA-I and CFSR are most accurate at reproducing temperature and humidity profiles (see Fig. 3.11). All products accurately reproduce the surface wind speed but underestimate the wind speed aloft (Fig. 3.11c).

- All products contain a cold temperature bias in the group of radiosondes which were launched close to the Antarctic continent (Fig. 3.12). The largest temperature bias is seen in MERRA with the product having a tendency to produce a strong near-surface inversion (Fig. 3.12).

- The wind speed bias between 950 and 850 hPa is caused by underestimations of the wind speed in profiles containing a LLJ, this indicates that the magnitude and frequency of LLJs are being under-represented in the reanalyses (Fig. 3.13).

- Evaluation of individual examples indicates that reanalyses have more skill at reproducing features such as temperature inversions and LLJs when there occurrence is linked to large-scale forcing mechanisms such as synoptic cyclones (compare Figs. 3.16 and 3.17).

3.7 OVERVIEW OF REANALYSIS PRODUCTS PERFORMANCE IN THE AMUNDSEN SEA

3.7.1 STRENGTHS AND WEAKNESSES COMMON TO ALL PRODUCTS

All four of the reanalysis products produce colder temperatures than those observed at three of the AWS sites (see Table 3.3 and Figs. 3.3 and 3.4). This cold bias is also seen (to a lesser extent) in comparison with summertime observations from research vessels and radiosondes (see Table 3.5 and Fig. 3.11). Over the ocean all of the products display greater cold biases near to the coastline compared with further out to sea, in agreement with temperature profile comparisons to the radiosondes. All the reanalyses are generally less accurate for temperature and humidity profiles closer to the continent and when there is a low-level inversion.

The AWS comparison revealed that all of the reanalysis products underestimate strong wind events ($> 15\ m\ s^{-1}$), suggesting they struggle to capture orographic and katabatic enhancement of the winds, and they overestimate low wind speeds. The reanalyses provide an improved representation of the wind speeds over the ocean, when compared with the summertime research vessel observations. They continue to show small negative biases in mean wind speed but the systematic biases at low and high wind speeds are not seen. The reanalyses are generally less accurate for wind speed profiles when a LLJ occurs; these are typically underestimated by $2\ m\ s^{-1}$ to $3\ m\ s^{-1}$, although some are not captured by the reanalyses at all. This is consistent with Liu et al. (2015) where ERA-I produced LLJs that were too weak and too vertically diffuse in comparison with Arctic dropsonde data.

3.7.2 ERA-INTERIM

Compared with observations at the three AMRC AWSs (with three year records), ERA-I shows the smallest cold biases of between $-1.4\ ^{\circ}C$ and $3.0\ ^{\circ}C$. These biases are similar to those found by Jones and Lister (2015) at AWS sites around the Ross Sea coastline but they are larger than ERA-I biases in coastal East Antarctica found by Bracegirdle and Marshall (2012). ERA-I has a much larger cold bias in austral winter than summer, possibly because it is not accurately reproducing the strong surface-based inversion

that is commonly observed during the polar night (King, 1990). Generally ERA-I has the smallest cold bias of the reanalyses examined here, although JRA-55 performs slightly better in the research-vessel comparison.

Relative and specific humidity biases in ERA-I are small compared with the other reanalysis products. Across the three comparisons specific humidity biases are between -0.05 and $-0.20\ g\ kg^{-1}$, while RH biases are between -1 and 6 %, although the RMSE for RH are generally between 5 and 15 %. The wind speed biases are between -0.80 and 1.40 $m\ s^{-1}$ (only JRA-55 has smaller wind speed biases) and the pattern of biases at high and low wind speeds compared with the AWS observations is the same as that seen in the other reanalyses. Overall, ERA-I contains the smallest temperature and humidity biases compared with observational data sets in the ASE, making it the most accurate product, based on this comparison.

3.7.3 JRA-55

JRA-55 cold biases are somewhat larger than those seen in ERA-I, similar to those seen in CFSR and smaller than those seen in MERRA. In the shelf break group of radiosonde profiles, and from the research vessel comparison, JRA-55 produces similar statistics to ERA-I for temperature over open water. JRA-55 contains the smallest biases in wind speed compared with AWS and research vessel observations. Generally, in the research vessel comparison JRA-55 is the most accurate of the reanalysis products, however in the radiosonde profile comparison it produces temperature and wind speed profiles with larger biases and RMSEs that ERA-I. This may be in part due to the reduced horizontal resolution of its pressure level data. Overall, JRA-55 is quite accurate when compared with the in-situ observations in the ASE but biases tend to be slightly larger than those for ERA-I.

3.7.4 CFSR

Compared with AWS observations the magnitude of CFSR cold biases are relatively constant across all four seasons but larger than those seen in ERA-I (e.g. Table 3.3; Fig. 3.2). Fig. 3.3c shows that in summertime the CFSR cold bias is larger when the observed temperature is lower. Generally, the CFSR cold biases in the ASE are larger than those found in coastal East Antarctica by Bracegirdle and Marshall (2012).

Radiosonde cold biases are slightly larger than ERA-I, but smaller than JRA-55 and MERRA. The CFSR humidity profiles are as accurate as ERA-I, producing the correct shape of both relative and specific humidity profiles. The specific humidity biases are also typically small between -0.02 and $-0.22\ g\ kg^{-1}$ across the AWS, research vessel and radiosonde comparisons, similar to the ERA-I values. The CFSR wind speed comparison against the AWS observations has the largest bias, although the performance over the ocean is comparable with the other reanalyses.

3.7.5 MERRA

MERRA has the largest temperature bias of the four reanalysis products evaluated. Near-surface temperatures are consistently colder than the AWS observations by $\sim 6\ ^{\circ}C$. This is significantly larger than the MERRA cold biases found by Bracegirdle and Marshall (2012) in coastal East Antarctica, which implies this large cold bias may be confined to West Antarctica. Fig. 3.8 demonstrates that MERRA temperature biases are much larger close to the continent — a spatial pattern that is enhanced compared with the other reanalysis products (Figs. 3.7 and 3.8). Profiles suggest MERRA predicts a surface-based temperature inversion that is both stronger and more frequent than the observations.

Specific humidity biases are also larger than in the other reanalysis products, with dry biases of $0.5\ g\ kg^{-1}$ for the radiosonde and AWS comparisons. Jakobson et al. (2012) find MERRA has a similar magnitude dry bias in the lower troposphere over the Arctic, but there the magnitude of the bias increased with height rather than decreased. Overall, large temperature and humidity biases make MERRA the least accurate of the four reanalysis products evaluated here over the Amundsen Sea.

3.7.6 IMPLICATIONS

Overall, the reanalyses assessed here provide a reasonable estimate of the state of the atmosphere over the ASE. However, while their accuracy at moderate wind speeds over open water is good, there should be some caution when wind speeds are high ($> 15\ m\ s^{-1}$), as these high wind speeds are likely to be underestimated, and near complex coastal topography where the reanalyses are unable to adequately capture the variability in winds. For example, the research vessel (and radiosonde) RMSE

are relatively large compared to other open-ocean locations (Li et al., 2013; Harden et al., 2015). These shortcomings would lead to underestimates in surface wind stress during high wind speed conditions and consequently alter the wind stress curl. Errors in the wind stress and its curl would lead to errors in the dynamics of an ocean model forced by these reanalyses, and will hamper the interpretation of observed ocean variability. They could also lead to an under-estimate of sea-ice divergence and the frequency of coastal polynyas.

The cold bias will affect both the surface sensible and latent heat fluxes, implying an overestimate in both heat fluxes (as the reanalyses are too cold and too dry). It has previously been shown that an older reanalysis product, the National Centre for Environmental Prediction Reanalysis 1, contained a cold temperature bias which changed the modelled melt rates of ice shelves and ice shelf cavities in the Amundsen Sea (Timmermann et al., 2012; Nakayama et al., 2014). However, the cold (and dry) bias combined with the potential underestimation of high wind speeds may partially offset one another for the heat fluxes (Renfrew et al., 2002). Nevertheless, such errors cannot entirely compensate across a range of values, so unknown errors will be introduced. In addition, the spatial distribution of these biases may lead to an underestimation of the importance of surface fluxes near the coast where the cold biases are particularly large.

3.8 CONCLUSIONS

In a validation study for the Amundsen Sea Embayment, the four most recently released global meteorological reanalysis products all produce cold biases of between approximately $-1.8\ ^{\circ}C$ (ERA-I) and $-6.8\ ^{\circ}C$ (MERRA) when compared with year-round AWS observations. Smaller cold biases were also found in comparisons with research vessel and radiosonde observations, although these comparisons are restricted to the summer lower-troposphere. ERA-I has the smallest temperature bias. The reanalysis cold bias in coastal regions of Antarctica is in agreement with previous studies (Bracegirdle and Marshall, 2012; Jones and Lister, 2015), although these did not cover coastal West Antarctica. A seasonal comparison of the biases shows that ERA-I has the smallest temperature bias in austral summer but all reanalysis products contain cold biases in austral winter. This implies parameterizations may perform

less well during the winter months. For all the reanalysis products the magnitude of temperature biases varies spatially. Close to the ice shelves that form large parts of the ASE coastline, the cold bias is much larger than in areas more distant from the coastline. Vertical profiles from the reanalyses generally correspond better away from the coastline and in the absence of temperature inversions or low-level jets.

In the comparison to AWS wind speeds, all four reanalysis products severely underestimate when observations are above 15 $m\ s^{-1}$ and overestimate when observations are below 5 $m\ s^{-1}$. Over the ocean, compared with research vessel observations, the reanalyses provide an improved representation of wind speed. This is in contrast with results from Li et al. (2013) who found ERA-I contained the same low and high wind biases in a comparison with Southern Ocean ship observations.

Overall, ERA-I has the smallest biases and errors in near-surface fields compared with meteorological observations within the ASE. This is consistent with the Antarctic-wide study of Bracegirdle and Marshall (2012). CFSR and JRA-55 have slightly larger cold biases but have a similar level of accuracy as ERA-I in the wind speed and humidity fields. MERRA contains the largest surface temperature bias and because of this also contains a large dry bias. The large MERRA temperature bias may be spatially limited to the ASE (c.f. Bracegirdle and Marshall, 2012). The biases at high and low observed wind speeds may be indicative of winds around other parts of coastal Antarctica.

Despite the use of a wide variety of meteorological data sets in this study there remains a lack of observations from West Antarctica. For example, the authors are not aware of any sustained wintertime meteorological observations over the sea ice or open water of the Amundsen Sea. Through fully utilising the existing observations and introducing a new data set this study provides a generally consistent evaluation of the reanalysis products in this area.

4

ASSESSING RECENT TRENDS IN ACCUMULATION ON PIG USING NEW ICE CORE OBSERVATIONS, GLOBAL REANALYSES AND RACMO

4.1 INTRODUCTION

The mass balance of any glacier is determined by the difference between the mass of snow that accumulates on top of the glacier and that lost through processes such as basal melt, iceberg calving, sublimation and surface melt. The storage of snow on the vast Antarctic continent is estimated to have a sea level equivalent of between 4.9 and 5.7 mm yr^{-1} (Lenaerts et al., 2012c). Given that annual average global sea level rise is approximately 3.2 mm yr^{-1} (Church et al., 2013), the 0.8 mm uncertainty in the Antarctic storage figure is large. As climate changes Antarctica is expected to warm, something which has already been observed in central West Antarctica (Bromwich et al., 2013a), and as warm air can hold more moisture, Antarctic accumulation is predicted to increase during the 21st century (e.g. Krinner et al., 2008). In order to predict where and by how much accumulation will change one can use complex global climate models (e.g. DeConto and Pollard, 2016). To understand if such

models have good predictive skill it is important to validate whether models and reanalysis products can accurately reproduce current and recent accumulation on West Antarctic glaciers.

Accumulation in low lying coastal regions of Antarctica can exceed 1 metre of water equivalent per year ($m.w.e\ yr^{-1}$) (Monaghan et al., 2006), the vast interior plateau is however very dry and often described as a 'polar desert' with less than 0.05 $m.w.e\ yr^{-1}$ of accumulation (Vaughan et al., 1999). Orographic uplift of maritime air at the coastline drives the enhanced precipitation (and accumulation) in coastal regions (Monaghan et al., 2006; Nicolas and Bromwich, 2011). On PIG and Thwaites glacier it has been shown using radar-derived observations that accumulation is a function of elevation with estimated accumulation of $\sim 0.7\ m.w.e\ yr^{-1}$ in coastal areas and $\sim 0.3\ m.w.e\ yr^{-1}$ in higher elevation portions of the basin (Medley et al., 2014).

4.2 MOTIVATION

In the Amundsen Sea region, the combined net mass loss from Pine Island and Thwaites glaciers is estimated to be $\sim 60\ Gt\ yr^{-1}$ (Rignot et al., 2008). The net mass loss of PIG alone is estimated to be $\sim 40\ Gt\ yr^{-1}$ (Medley et al., 2014). The combined rate of net mass loss has been increasing in recent years from $\sim 40\ Gt\ yr^{-1}$ in 1996 to $\sim 90\ Gt\ yr^{-1}$ in 2006 (Rignot et al., 2008). However estimates of accumulation on the two glaciers derived from both observations and models range from 129 $Gt\ yr^{-1}$ to 182 $Gt\ yr^{-1}$ (Arthern et al., 2006; Monaghan et al., 2006; Medley et al., 2013), so the range of these estimates is similar to the rate of net mass loss from PIG and Thwaites. This highlights that accumulation on to glaciers within the ASE is a key uncertainty in our ability to constrain the current rate of mass loss and therefore our estimates of the amount global sea level rise attributable to ice loss in this region.

There have been reports of differing trends in accumulation across West Antarctica. In inland regions of the Bellingshausen Sea sector it has been shown that accumulation has been increasing in recent decades (Thomas et al., 2015), partially offsetting accelerating ice loss at the coastline. In central West Antarctica at four relatively high elevation ice core sites (> 1600m), a statistically significant decrease in accumulation of $\sim 0.04\ m.w.e\ decade^{-1}$ has been observed between

1975 and 2010 (Burgener et al., 2013). In the vicinity of PIG and Thwaites glacier some ice core observations (Kaspari et al., 2004) have shown small increases in accumulation in recent decades. Such a trend is consistent with significant atmospheric warming in the region (Bromwich et al., 2013a), and a deepening of the Amundsen-Bellingshausen Sea low (Turner et al., 2015). However, a recent radar survey revealed no significant trend in accumulation on Thwaites glacier between 1980 and 2009 (Medley et al., 2013). Determining whether there is a statistically significant trend in either the modelled or observed accumulation data on PIG is a key objective of this chapter.

Only 40% of the Antarctic ice sheet lies below 2000 metres above sea level; despite this, 70% of the snow that falls on the continent each year accumulates below this height (Favier et al., 2013). Low elevation regions of West Antarctica have been identified as regions where there are very few reliable ice core observations, which creates large uncertainties in gridded estimates of accumulation in the region (Favier et al., 2013; Scambos et al., 2017; Turner et al., 2017). Medley et al. (2014) use ice core data from higher elevation sites (> 1200m) but note that no such records exist from lower elevation sites. Their results show that the largest discrepancy between the radar derived estimates and model values is found in low elevations regions (Medley et al., 2014). Here we present data from ten new ice cores on PIG and its tributaries. Nine of the ten sites are < 1200m above sea level (Fig. 4.1) and provide a valuable data set for validating reanalysis products and RACMO accumulation estimates in these low elevation, high accumulation regions.

4.3 AIMS

As highlighted above there are uncertainties surrounding both the recent trend in accumulation on PIG and the ability of atmospheric models to accurately reproduce the observed accumulation rate in this low elevation region of West Antarctica. Therefore the three main aims of this chapter are:

- To assess the accuracy of RACMO2.3 and the latest generation of global reanalysis in reproducing the ice core observed accumulation fields on PIG and its tributaries.

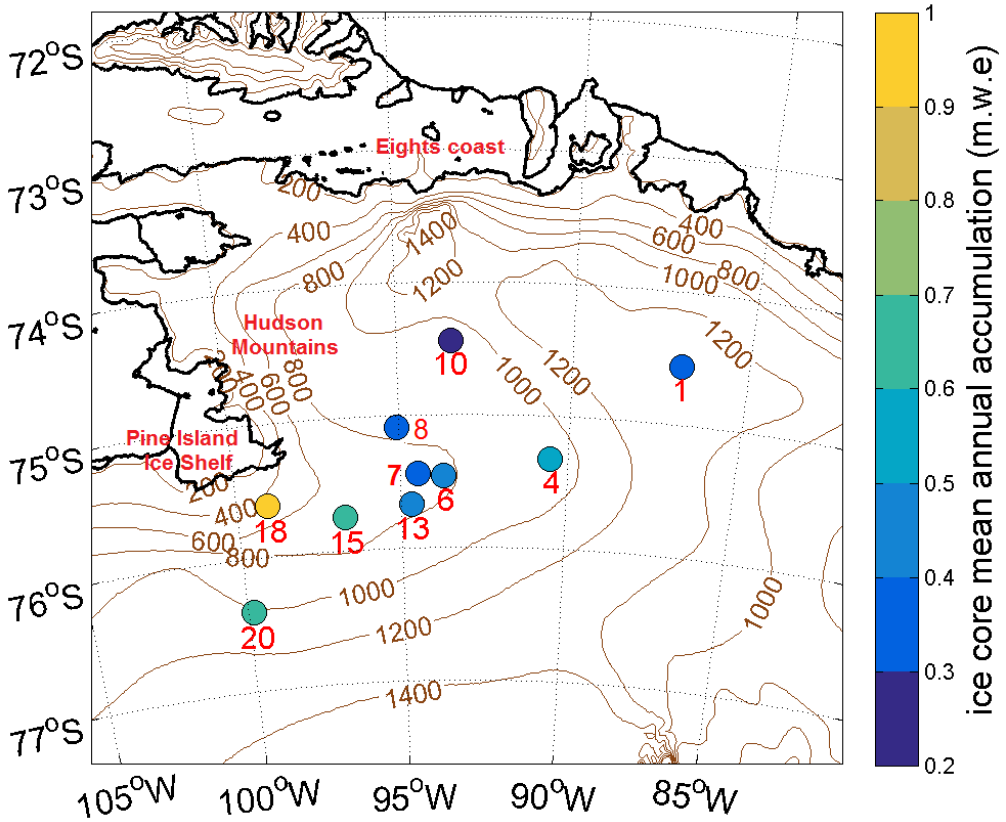

Figure 4.1: The location of each of the 10 ice core sites in the Pine Island Glacier region. The colour of the circle represents the 1979-2013 ice core observed mean annual accumulation.

- To investigate whether there are any trends in either the observed or modelled accumulation rate during the last 40 years.
- To assess the differences in atmospheric circulation between high and low accumulation years and the implications this has for future changes in accumulation on PIG during the 21st century.

4.4 METHODS

Accumulation in the Amundsen Sea region is largely controlled by precipitation; terms such as surface runoff, sublimation, and wind blown snow processes make up less than 10% of the total accumulation budget in the RACMO2.3 model (Lenaerts et al., 2012a; Medley et al., 2013). For ERA-I, JRA-55 and MERRA we therefore use precipitation minus evaporation as a proxy for accumulation. In the case of CFSR a sublimation field is available over Antarctica (but no evaporation field);

we therefore use precipitation minus sublimation as a proxy for accumulation. A similar methodology has been employed in multiple studies that compare reanalysis data with in-situ observations of accumulation (Agosta et al., 2012; Medley et al., 2014; Thomas and Bracegirdle, 2014; Wang et al., 2015). For RACMO2.3 the snow mass balance field is used, alongside precipitation and sublimation, this includes accumulation from processes such as wind blown snow and surface melt, which are absent in the reanalyses (see chapter 2 for a more detailed description of how RACMO2.3 calculates snow mass balance). For the reanalysis products (and RACMO2.3) the monthly mean precipitation minus evaporation or sublimation (surface mass balance) time series spans the period between 1979 and 2013 (1980-2013 for MERRA). The ice core accumulation records are of varying lengths (due to variations in the mean annual accumulation) but we focus on the period from 1979-2013 as this is the time period that overlaps with the reanalysis data. At site 18, where the mean annual accumulation is high, the ice core accumulation record only goes back to 1983.

For RACMO2.3 and all of the reanalysis products we interpolate from the gridded data set to the location of each site. Locally steep topography and rapid variation in mean annual accumulation over relatively short horizontal distances make this methodology appropriate. By averaging ice core data across multiple sites some of the small-scale variability that can be seen in individual cores is removed and there is an increase in fidelity between reanalyses and ice core records when more sites are included (Genthon et al., 2005; Banta et al., 2008). Therefore an average time series of 1979-2013 annual accumulation across the ten sites is calculated, this follows the methodology of other studies ice core studies in West Antarctica (Kaspari et al., 2004; Favier et al., 2013; Medley et al., 2014).

4.5 RESULTS

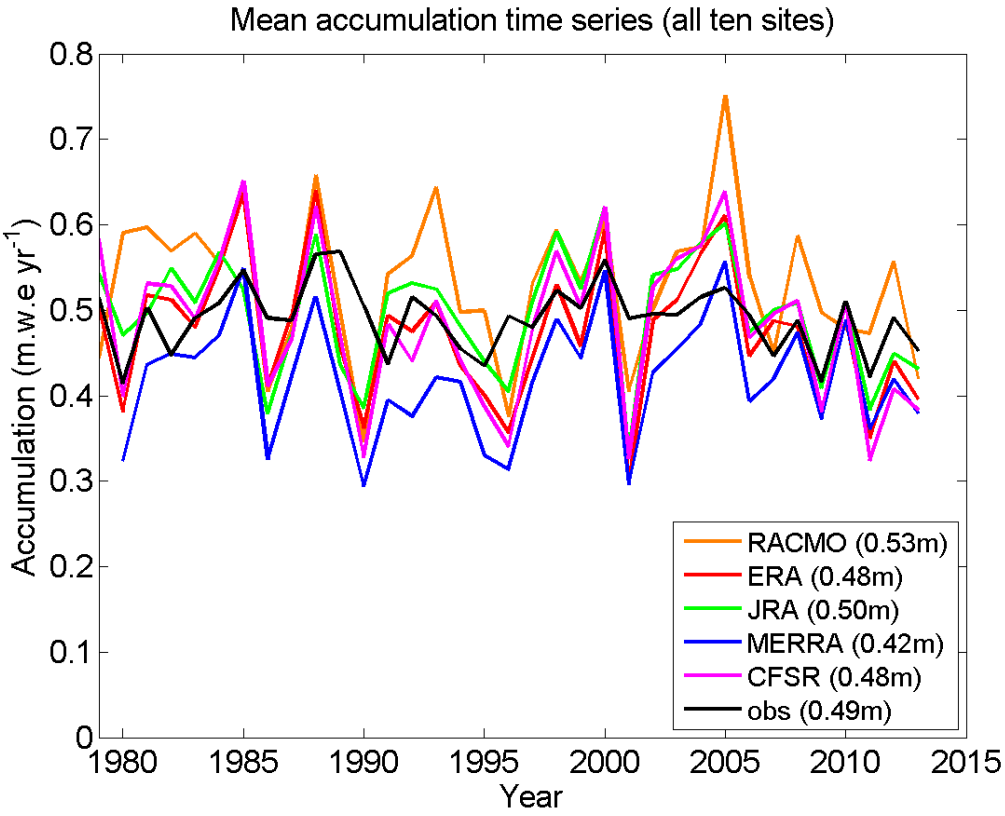

Figure 4.2: The time series of 1979-2013 annual accumulation averaged across all 10 ice core sites. The black line shows the ice core observations, other colours correspond to the models and reanalyses as shown in the legend with the corresponding mean accumulation in parentheses.

Fig. 4.2 shows the mean accumulation time series on PIG averaged across all 10 ice core sites. The ice core observed mean accumulation across these sites is 0.49 $m.w.e\ yr^{-1}$, this is consistent with the results of Medley et al. (2014) who estimate the catchment wide PIG accumulation to be 0.40 $m.w.e\ yr^{-1}$. The ice core sites in this study focus on the low elevation (high accumulation) portion of PIG so it is expected that our accumulation value is somewhat higher than that of Medley et al. (2014). ERA-I, CFSR and JRA-55 are all in good agreement with the observations, they produce mean annual accumulation rates within 0.01 $m.w.e\ yr^{-1}$ of the observed value. ERA-I, CFSR and MERRA have all shown good fidelity with low elevations accumulation observations around other regions of Antarctica (Favier et al., 2013; Medley et al., 2014; Wang et al., 2015). RACMO2.3 gives a slightly higher mean annual

accumulation rate of 0.53 $m.w.e\ yr^{-1}$. Morris et al. (2017) also show that RACMO2.3 slightly overestimates accumulation when compared with short records derived using a neutron density probe on PIG. The average MERRA mean annual accumulation is 0.42 $m.w.e\ yr^{-1}$, similarly Medley et al. (2013) find that MERRA underestimates the observed accumulation rate on the neighbouring Thwaites glacier.

Table 4.1: Accumulation time series statistics: mean, standard deviation and the correlation coefficients both between the ice cores and the models/reanalyses and between each reanalysis product and RACMO.

Time Series stats	**Ice cores**	**RACMO2.3**	**ERA-I**	**CFSR**	**JRA-55**	**MERRA**
Mean accum. (m)	0.49	0.53	0.48	0.48	0.50	0.42
Standard dev.	0.040	0.086	0.081	0.091	0.071	0.070
Correlation coefficients (R-values)						
Ice cores	–	0.31	0.61	0.60	0.44	0.56
RACMO2.3	–	–	0.75	0.72	0.74	0.76
ERA-I	–	–	–	0.96	0.88	0.92
CFSR	–	–	–	–	0.90	0.93
JRA-55	–	–	–	–	–	0.85

We also use the mean time series in Fig. 4.2 to examine the trend in annual accumulation on PIG. There is no statistically significant trend in any of the reanalyses, RACMO2.3, or the ice core observations between 1979 and 2013. ERA-I has the largest trend of $-0.017\ m.w.e\ decade^{-1}$ but this is not statistically significant at the 90% level. The observed time series, RACMO2.3, and the remaining reanalysis products all contain trends of $< 0.01\ m.w.e\ decade^{-1}$. The lack of a statistically significant trend in accumulation is consistent with the results of Medley et al. (2014); thus providing further evidence that there has not been a statistically significant trend in accumulation on PIG in recent decades. Some earlier ice core observations (e.g. Kaspari et al., 2004) did suggest an increase in accumulation in recent decades and this was incorporated into some glaciological model simulations (e.g. Wingham et al., 2009). In the present study just one individual ice core record (site 4) shows a significant increase in accumulation of $0.05\ m.w.e\ decade^{-1}$ (Fig. 4.3c). This shows the importance of averaging across multiple ice core sites rather than relying on an individual ice core (Genthon et al., 2005; Banta et al., 2008).

The standard deviations of the observed and modelled time series in Table 4.1 reveal that the models exaggerate the inter-annual variability of accumulation,

compared with the mean observed time series. This is also seen in the majority of the individual site time series (e.g., Figs. 4.3a and 4.3d). It is possible that, while the reanalyses and RACMO2.3 all produce large inter-annual variability that is driven by large-scale atmospheric processes, the individual point location nature of the ice core data means the observed time series also reflect very local changes such as sastrugi and topographic influences on accumulation within hollows and on ridges (Eisen et al., 2008). Banta et al. (2008) find that sastrugi and other forms of small scale variability can lead to changes of up to 15% in the observed accumulation rate in each year. Despite the observational uncertainties described above, the standard deviations from RACMO2.3 and the reanalysis products are approximately double that of the observed time series suggesting that they erroneously exaggerate the inter-annual variability on PIG.

The simulated accumulation time series from RACMO2.3 and the reanalysis products are all strongly correlated with one another, correlation coefficients are between 0.72 and 0.96 (see Table 4.1). Previous studies that have examined accumulation in West Antarctica from multiple reanalysis products have shown them to be highly correlated with one another (e.g. Burgener et al., 2013; Medley et al., 2014). RACMO2.3 and the reanalyses are in good agreeement with one another due to the precipitation events in this region being driven by large-scale atmospheric circulation with maritime air outbreaks and moist air being lifted as it travels up the continental slope (Nicolas and Bromwich, 2011).

The correlation coefficients with the ice core record range from 0.31 (RACMO2.3) to 0.61 (ERA-I). In all of the products except RACMO2.3 the correlation is statistically significant at the 95% level but it is weaker than some previous studies. For example, Medley et al. (2013) report correlation coefficients of 0.7 to 0.8 when comparing the reanalysis products to higher elevation ice core records. However, Burgener et al. (2013) also show somewhat reduced correlation coefficients between reanalysis products and ice core time series in central West Antarctica and suggest this is likely caused by small uncertainties in the dating and accumulation rates derived from the ice cores. Overall, the correlation coefficients in this study fall within the range of other similar studies in West Antarctica and the temporal variability of the reanalysis products are in good agreement with both one another and the observations.

Fig. 4.4 compares the modelled and observed mean annual accumulation at each

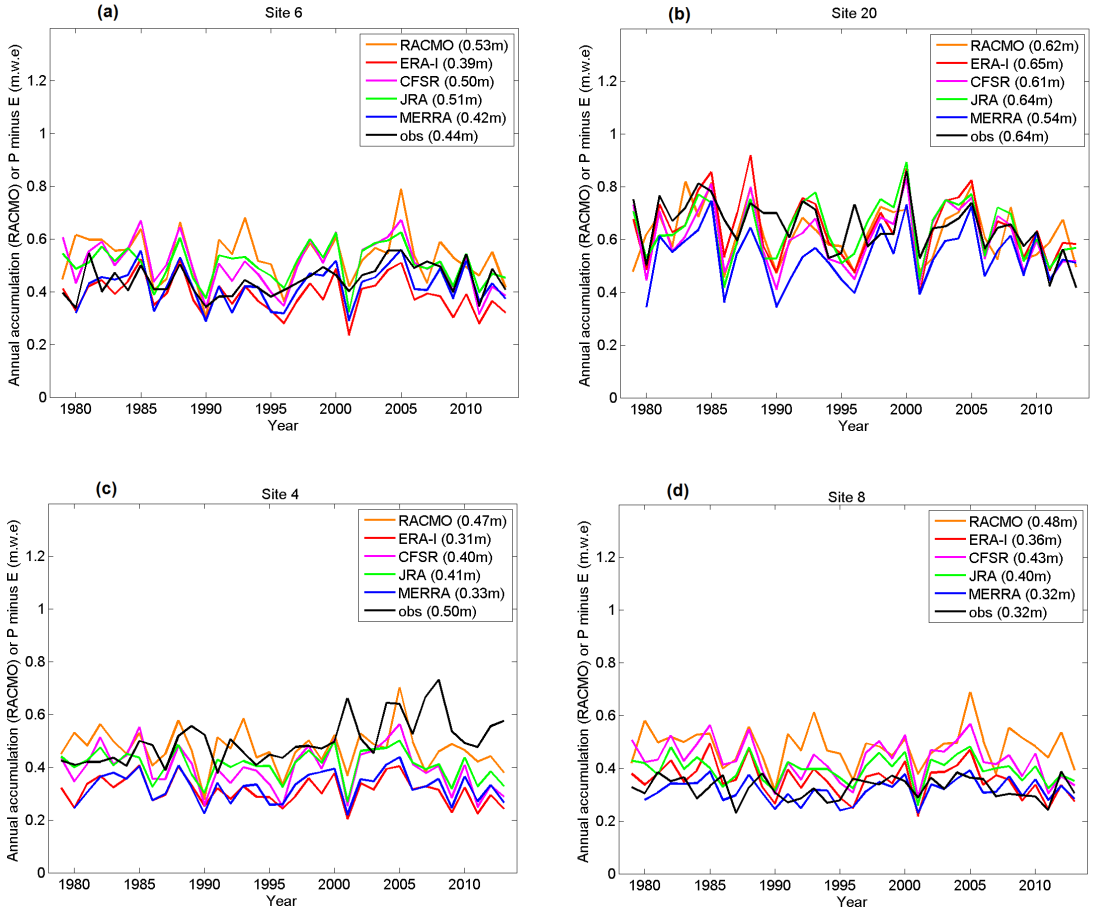

Figure 4.3: Time series plots showing the observed and modelled accumulation at individual sites between 1979 and 2013. a) site 6, b) site 20, c) site 4, and d) site 8. a) and b) are examples of sites with high correlation coefficients > 0.6, whereas at the sites shown in c) and d) the observations to model correlation coefficients are < 0.3.

of the ten sites. At the majority of the sites the observed accumulation rate lies within the range of values predicted by the reanalyses and RACMO2.3; site 18 and site 4 are the most obvious exceptions (highlighted in Fig. 4.4). When the ice core observed annual accumulation is less than 0.50 $m.w.e\ yr^{-1}$ all of the products except MERRA tend to overestimate accumulation by an average of between 0.05 $m.w.e\ yr^{-1}$ (ERA-I) and 0.09 $m.w.e\ yr^{-1}$ (RACMO2.3). Conversely, when the observed accumulation exceeds 0.50 $m.w.e\ yr^{-1}$, which occurs at the three western-most sites (Fig. 4.1), all of the products tend to underestimate accumulation by an average of between 0.08 $m.w.e\ yr^{-1}$ (RACMO2.3) and 0.16 $m.w.e\ yr^{-1}$ (ERA-I). This underestimation is primarily driven by large model underestimations at site 18, but across the three high accumulation sites there is only one occasion where a modelled value exceeds

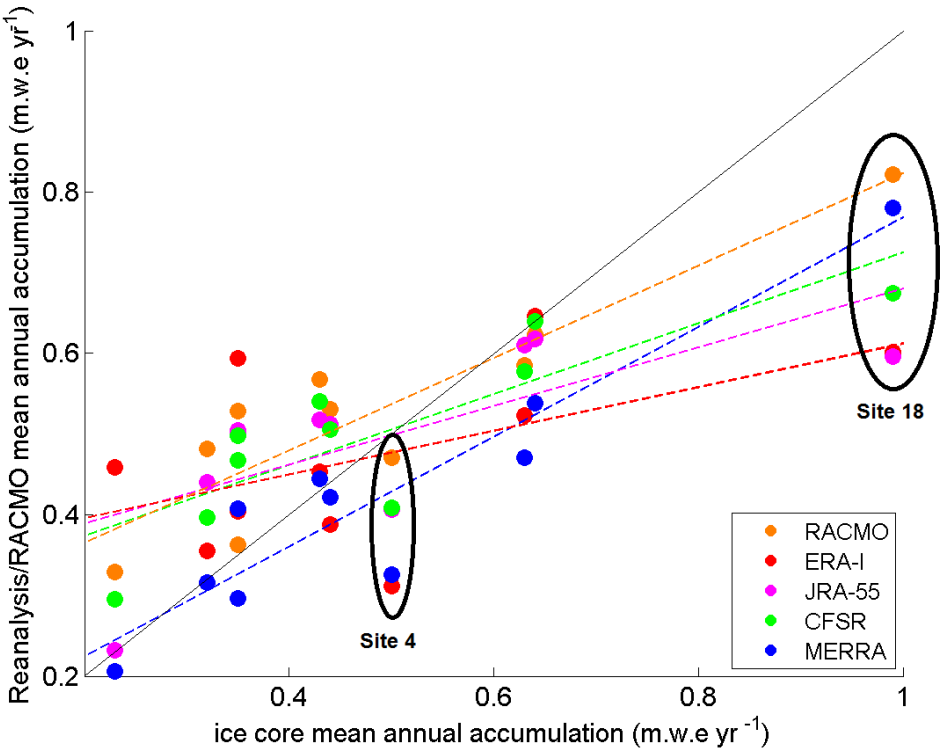

Figure 4.4: A scatter plot showing the observed and modelled mean annual accumulation across the ten sites. The black solid line shows where the observed value is equal to the model value. The dashed coloured lines show the least square regression lines for each product. Black ovals highlight site 18 and site 4 where the mean observed annual accumulation lies outside the modelled range.

the observation (ERA-I at site 20 by 0.01 m.w.e). At site 18 all of the products underestimate accumulation by at least 0.17 $m.w.e\ yr^{-1}$ (Fig. 4.4), aside from this site there are relatively few occasions where the modelled value differs from the observed value by such a large amount. 60% of the reanalysis/RACMO2.3 values are within 0.10 $m.w.e\ yr^{-1}$ of the observed accumulation rate across the ten sites (30 of the 50 RACMO2.3/reanalysis values).

4.5.1 THE SPATIAL DISTRIBUTION OF ACCUMULATION ON PIG

Fig. 4.5 shows the spatial distribution of accumulation in the vicinity of PIG from RACMO2.3 and three global reanalysis products. The coloured circles highlight that at the majority of sites the simulated accumulation rate in each of the products is in good agreement with the observations. MERRA is not shown in Fig. 4.5 for brevity, but all of the products give a similar pattern of accumulation across the region with the

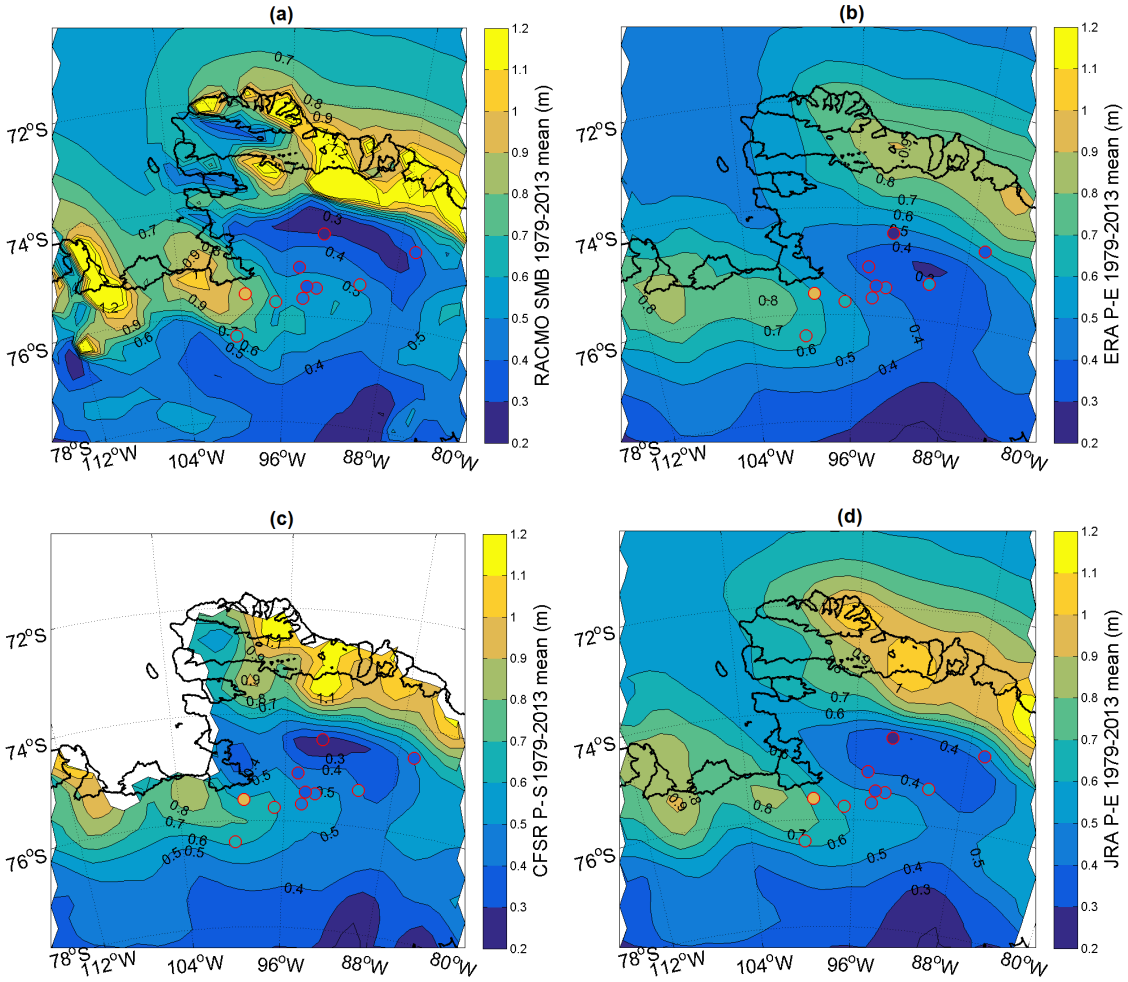

Figure 4.5: Map plots showing 1979-2013 mean annual accumulation (in metres) in the Amundsen Sea region: a) RACMO2.3, b) ERA-I, c) CFSR, d) JRA-55. The coloured circles show the ice core observed accumulation at each site, these are plotted using the same colour bar.

following common features:

1. An increase in accumulation moving down the trunk of Pine Island Glacier, from ~ 0.4 $m.w.e\ yr^{-1}$ at site 1 in the east to $\sim 0.6-0.8$ $m.w.e\ yr^{-1}$ at sites 18 and 20 in the west. This pattern is generally reproduced in all products.

2. Reduced accumulation on the northern tributaries of PIG which are in the precipitation shadow of the high ground of the Eights coastline to the north (see Fig. 4.1 for orographic contours). Most of the products agree that accumulation on these northern tributaries is approximately 0.30 $m.w.e\ yr^{-1}$. The ice core at site 10 is located within this precipitation shadow region and the observed annual accumulation is 0.23 $m.w.e\ yr^{-1}$, the lowest of the ten ice core derived

accumulation rates.

3. Evidence of enhanced accumulation rates in the low elevation region of PIG and over Pine Island ice shelf. In all of the products the accumulation rate approaches 0.80 $m.w.e\ yr^{-1}$ in these regions, and in RACMO2.3 the accumulation rate is even higher, approaching 1 $m.w.e\ yr^{-1}$ on the ice shelf.

The greatest differences between the reanalysis products and RACMO2.3 are seen at elevations below 800 m. This is in good agreement with the results of Medley et al. (2014) where it is shown that model spread increases significantly at elevations below 1000 m on PIG (see their Fig. 8). RACMO2.3 predicts accumulation rates of $>$ 1 $m.w.e\ yr^{-1}$ around many of the coastal regions of the ASE (Fig. 4.5a). CFSR, JRA-55 and MERRA produce accumulation rates that exceed $>$ 1 $m.w.e\ yr^{-1}$ at 73°S 92°W but not further south in the vicinity of Pine Island Bay (Fig. 4.5c and Fig. 4.5d). ERA-I has even lower accumulation estimates at low elevations, there is no area within the ASE where the ERA-I average annual accumulation exceeds 1 $m.w.e\ yr^{-1}$ (Fig. 4.5b). In general ERA-I tends to produce 0.20 to 0.30 $m.w.e\ yr^{-1}$ less accumulation than RACMO2.3 in the lower elevation regions of the ASE; for CFSR and JRA-55 the difference is slightly less, typically between 0.10 and 0.20 $m.w.e\ yr^{-1}$. The ice core at site 18 provides some evidence that average annual accumulation rates of $\sim$ 1 $m.w.e\ yr^{-1}$ are possible.

A further difference between the reanalysis products and RACMO2.3 is the position of the accumulation shadow on the northern tributaries of PIG. In ERA-I this is displaced to the southeast compared with RACMO2.3 (compare Fig. 4.5b to 4.5a), this is perhaps due to the comparatively coarse horizontal resolution of ERA-I ($\sim$ 70km compared to 27km RACMO2.3) and consequently poor representation of topography. Due to the differing placement of this low accumulation region, ERA-I overestimates the observed accumulation at site 10 by 0.25 $m.w.e\ yr^{-1}$ whereas RACMO2.3, CFSR, JRA-55, and MERRA are all in good agreement with the observation, with differences of $<$ 0.10 $m.w.e\ yr^{-1}$.

The spatial distribution of accumulation on PIG has previously been mapped using radar survey data (Medley et al., 2014) (Fig. 4.6). Comparing our spatial maps in Fig. 4.5 to that of Medley et al. (2014) (Fig. 4.6) reveals that across much of the PIG basin the models are in qualitatively good agreement with the radar survey. In Fig. 4.6

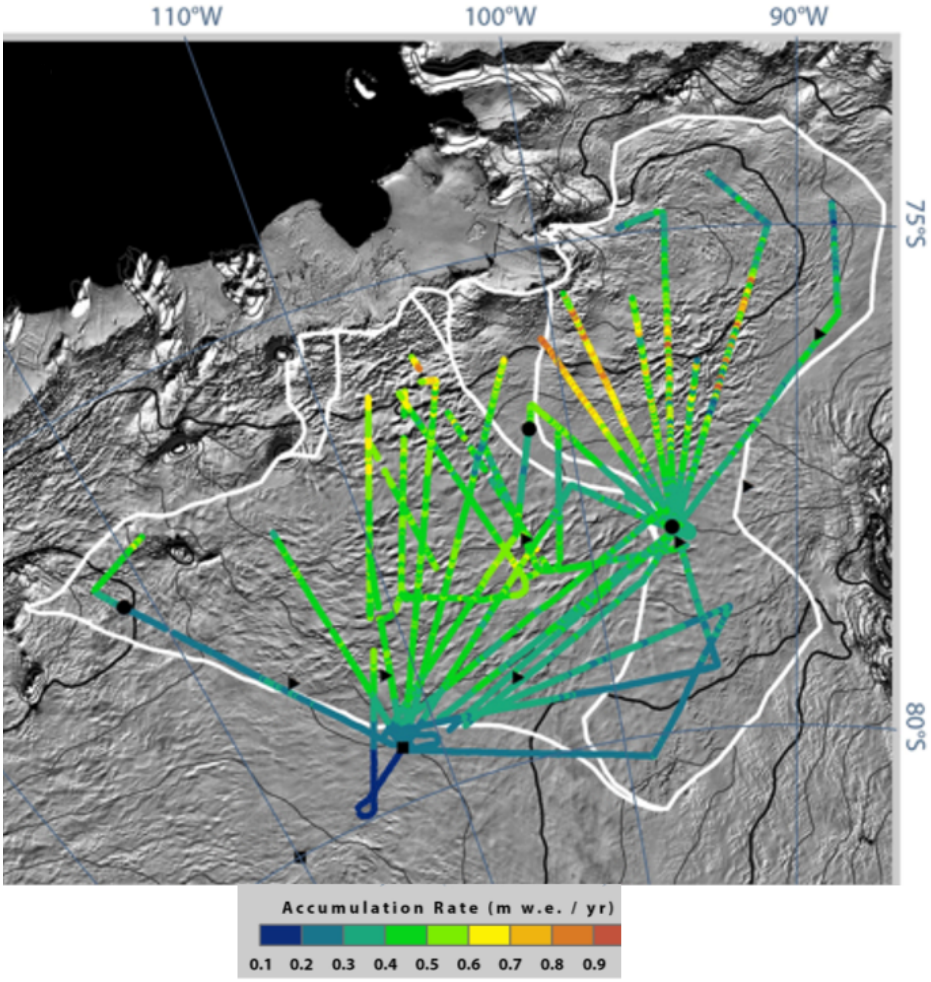

Figure 4.6: The radar derived accumulation rate on PIG and Thwaites glaciers. From Medley et al. (2014). The white line outlines different drainage basins, PIG basin is the eastern-most and Thwaites is the western-most. The thick black lines show the 1000 m and 2000 m elevation contours. Note the enhanced accumulation rates towards the western edge of PIG and the lower accumulation rates in the few radar lines that reach the northern part of PIG.

there is some evidence of an accumulation shadow on the northern tributaries of PIG (75°S, 95°W) in the radar data but our ice core data along with RACMO2.3 and the reanalysis products would suggest the accumulation is ~ 0.10 $m.w.e\ yr^{-1}$ lower than the radar derived values in this region. In the lower elevation western portion of PIG (76°S, 100°W) both the radar survey and the reanalysis products agree that the annual accumulation rate is approximately 0.80 $m.w.e\ yr^{-1}$. RACMO2.3 and the ice core data at site 18 suggest that accumulation rates could approach 1 $m.w.e\ yr^{-1}$ in this region. Interestingly, Medley et al. (2014) note the radar derived accumulation values do exceed 1 $m.w.e\ yr^{-1}$ in isolated sections of the low elevation portion of PIG.

This is perhaps the most likely explanation of the ice core derived accumulation rate at site 18, i.e. enhanced accumulation within a local surface depression or an area where drifting snow accumulates. Given the relatively coarse horizontal resolution of RACMO2.3 and the reanalyses we wouldn't expect them to capture such small scale features. Fig. 4.6 does also show that there is quite strong local variability in accumulation on the trunk of PIG when compared with that seen on the neighbouring Thwaites glacier. This local variability may be indicative of drifting snow depositional or erosional features such as sastrugi and snow-waves (e.g. Frezzotti et al., 2007).

4.5.2 WEST ANTARCTIC ATMOSPHERIC CIRCULATION IN LOW AND HIGH ACCUMULATION YEARS

In order to be able to predict future changes in accumulation on PIG it is first crucial to understand the relative importance of the mechanisms that currently control accumulation. Many different atmospheric phenomena/processes have been linked with West Antarctic accumulation including: mean annual air temperature (Krinner et al., 2008), the depth of the ASL (Thomas and Bracegirdle, 2014; Thomas et al., 2015), the longitudinal location of the ASL (Burgener et al., 2013), the meridional wind speed (Hosking et al., 2013; Thomas and Bracegirdle, 2014), and the El Niño Southern Oscillation index (Genthon et al., 2005). Here we examine how important each of these processes are in determining the accumulation on PIG. How and why each of these processes is thought to influence accumulation is explained at the start of the relevant section.

We use ERA-I to create composites of the atmospheric circulation for the five years with the highest accumulation on PIG and the five years with the lowest accumulation in the 1979-2013 period (Fig. 4.7). The mean accumulation in the five high accumulation years is 0.61 $m.w.e\ yr^{-1}$, while for the low accumulation years it is 0.35 $m.w.e\ yr^{-1}$ (Table 4.2). In high accumulation years there is a negative meridional wind anomaly across coastal parts of much of the Amundsen and Bellingshausen Sea sectors. This indicates more frequent, stronger or more persistent northerly winds that are linked to enhanced accumulation in West Antarctica due to their maritime source (e.g. Nicolas and Bromwich, 2011). In the low accumulation years the meridional wind anomaly is positive over much of West Antarctica showing that

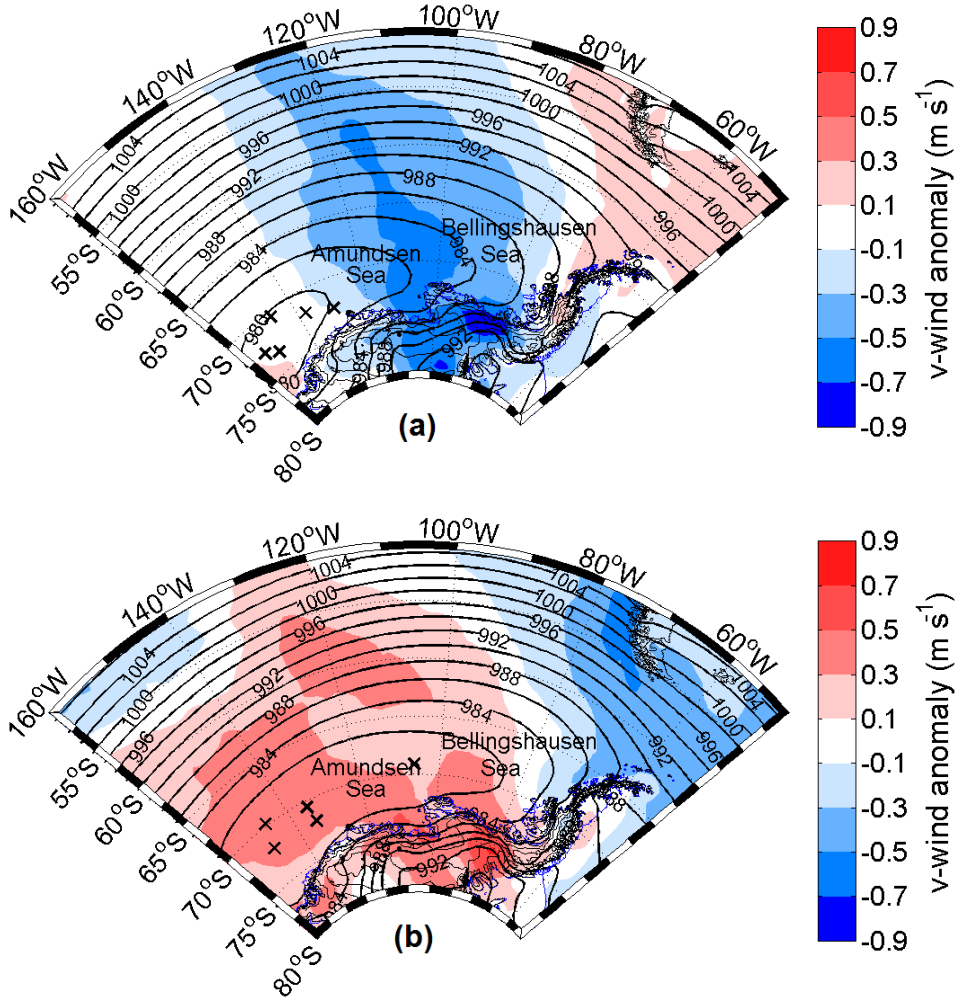

Figure 4.7: Composites of the meridional wind anomaly (colour contour), mean sea level pressure (black contours), with crosses marking the longitudinal location of the ASL in each year: (a) the five highest accumulation years; (b) the five low accumulation years.

dry, continentally sourced winds are more frequent, stronger or more persistent than is typical. While the regional mean sea level pressure is broadly similar in Figs. 4.7a and 4.7b there are some subtle differences. In the high accumulation years the mean depth of the ASL is approximately 1 hPa lower than in the low accumulation years. Further east in the Bellingshausen Sea close to the Antarctic Peninsula the mean sea level pressure is up to 4 hPa higher in the high accumulation years composite. In high accumulation years the ASL climatological trough is sharper, so the zonal pressure gradient is larger between the western Amundsen and the eastern Bellingshausen Seas. The position of the ASL in each year (shown by the crosses in Figs. 4.7a and 4.7b) is west of 130°W in nine of the ten years in the two composites, in one of the low

accumulation years it is further east at 107°W. Table 4.2 shows that on average the near-surface air temperature on PIG is 1.3 °C warmer in the five high accumulation years.

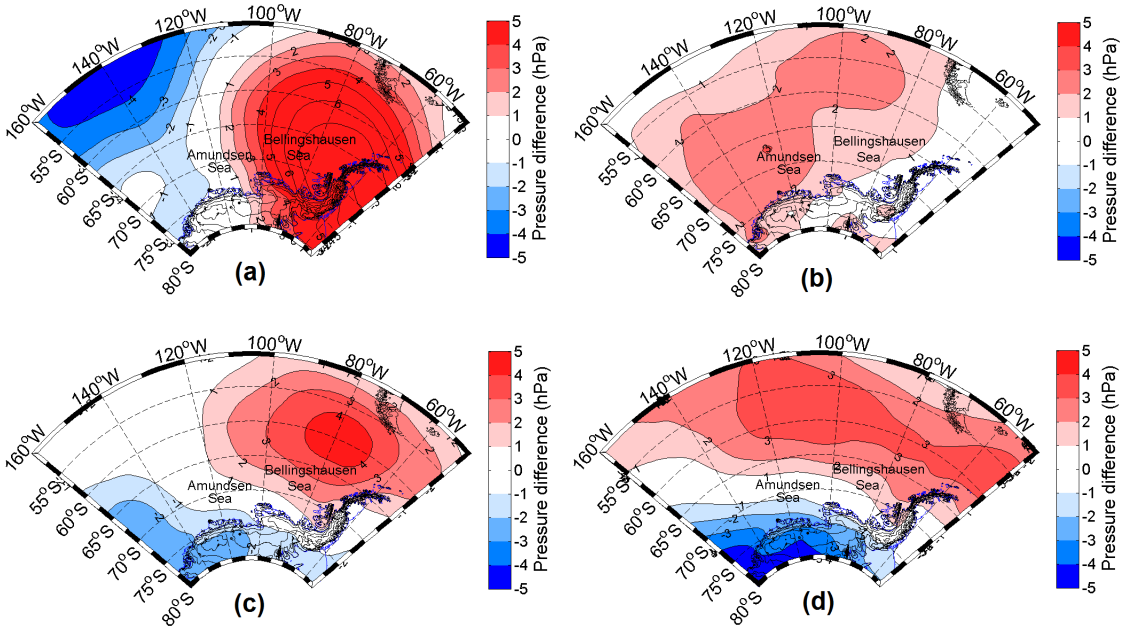

Figure 4.8: The ERA-I seasonal mean sea level pressure difference between high and low accumulation years. Where the pressure difference is positive (red) this indicates the mean sea level pressure is higher in high accumulation years: (a) spring (SON), (b) summer (DJF), (c) autumn (MAM), (d) winter (JJA).

Table 4.2: Seasonality of ERA-I accumulation and temperature on PIG in high and low accumulation years.

	High accumulation years		**Low accumulation years**	
	Mean seasonal accum. (m)	**Mean seasonal temp. (°C)**	**Mean seasonal accum.(m)**	**Mean seasonal temp. (°C)**
Spring (SON)	0.183	-18.6	0.078	-21.9
Summer (DJF)	0.069	-12.1	0.040	-12.0
Autumn (MAM)	0.169	-21.4	0.108	-22.1
Winter (JJA)	0.189	-24.9	0.125	-25.9
	Mean ann. accum. (m)	**Mean temp.** (°C)	**Mean ann. accum. (m)**	**Mean temp.** (°C)
	0.61	-19.2	0.35	-20.5

A seasonal break-down of accumulation reveals that in each of the four seasons accumulation is enhanced by at least 50% in the high accumulation years when

compared with the low accumulation years (Table 4.2). It is during the austral spring season that the greatest difference in accumulation is seen with the 0.183 *m.w.e* of high accumulation years, being more than double the 0.078 *m.w.e* of low accumulation years. This is also highlighted by the anomaly plot in Fig. 4.8a which shows that in spring there is a large enhancement of the zonal pressure gradient in high accumulation years. Higher mean sea level pressure is seen over the Antarctic Peninsula and slightly lower mean sea level pressure in the western Amundsen Sea — where the centre of the ASL typically sits in spring (see chapter 1). Table 4.2 shows that the temperature difference between high and low accumulation years is also greatest in the spring season (3.3 °C compared with a maximum of 1.0 °C in the other seasons). There is also an enhancement of the zonal pressure gradient during autumn and winter in high accumulation years (Figs. 4.8c and 4.8d).

4.5.3 WHAT ARE THE IMPORTANT METEOROLOGICAL PROCESSES AND ATMOSPHERIC PHENOMENA CONTROLLING THE ACCUMULATION ON PIG?

Here we conduct a statistical analysis to examine the relationship between the relevant atmospheric processes (outlined in section 4.5.2) and the observed accumulation on PIG. We examine how much of the observed variability in accumulation can be explained by these processes through analysing both how strongly correlated each process is with the observed accumulation and by using a multiple linear regression.

TEMPERATURE AND MERIDIONAL WIND

The mean annual temperature on PIG is predicted to be linked to the observed accumulation as warmer air is able to hold more moisture (Krinner et al., 2008). Years characterised by more northerly (negative) meridional winds on PIG are also thought to be associated with enhanced accumulation as there are more persistent or frequent maritime air outbreaks (Hosking et al., 2013; Thomas and Bracegirdle, 2014).

The scatter plots in Fig. 4.9 reveal that both the ERA-I meridional wind speed and ERA-I mean annual temperature on PIG are significantly correlated with the observed accumulation. The correlation coefficients for the meridional wind speed

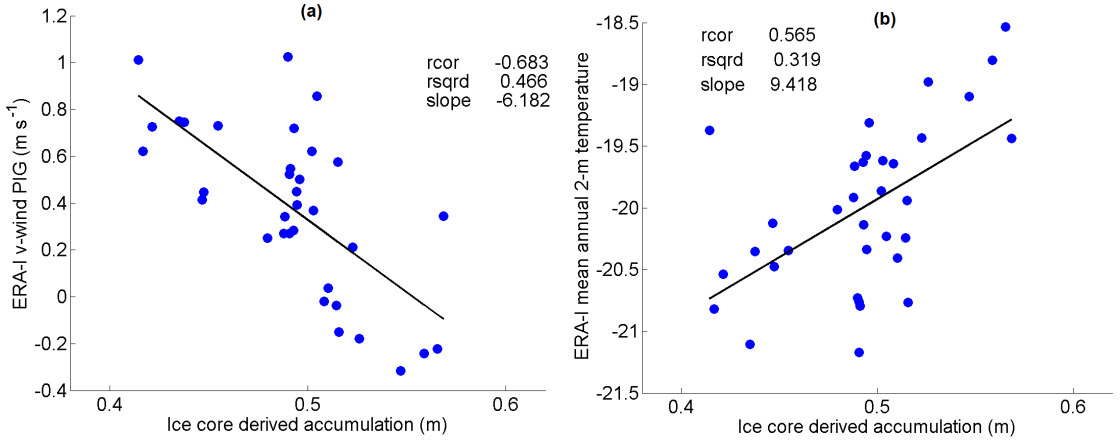

Figure 4.9: Scatter plots showing the relationship between ice core observed accumulation on PIG and: (a) ERA-I annual mean meridional wind on PIG (b) ERA-I annual mean near-surface temperature on PIG.

and mean annual temperature are −0.68 and 0.57 respectively. Warmer temperatures and/or stronger northerly winds are typically associated with higher ice core derived accumulation values. These R-values are higher than the correlation coefficient between near-surface temperature and meridional wind speed (R = 0.49). We also therefore use both mean annual temperature and meridional wind speed as predictors in a multiple linear regression, and here find that together they explain 53% of the observed variability in accumulation on PIG (i.e. $R^2 = 0.53$ which is higher than 0.47 and 0.32, the values for each individual predictor, see Fig. 4.9), both predictors are statistically significant at the 95% level.

THE AMUNDSEN SEA LOW

A deeper climatological ASL indicates there are either more frequent or deeper cyclones in West Antarctica. As such, years characterised by a deeper ASL are thought to be associated with higher accumulation on PIG due to the enhanced cyclone activity (Thomas and Bracegirdle, 2014; Thomas et al., 2015). The longitudinal location of the ASL drives the seasonal cycle of accumulation in West Antarctica (see chapter 1). It is also hypothesised that more westerly positions of the ASL will allow more frequent maritime air outbreaks and hence enhanced accumulation totals on PIG (Burgener et al., 2013).

The scatter plots in Fig. 4.10 show the correlation between the observed annual accumulation and both the depth of the ASL (Fig. 4.10a), and its longitudinal location

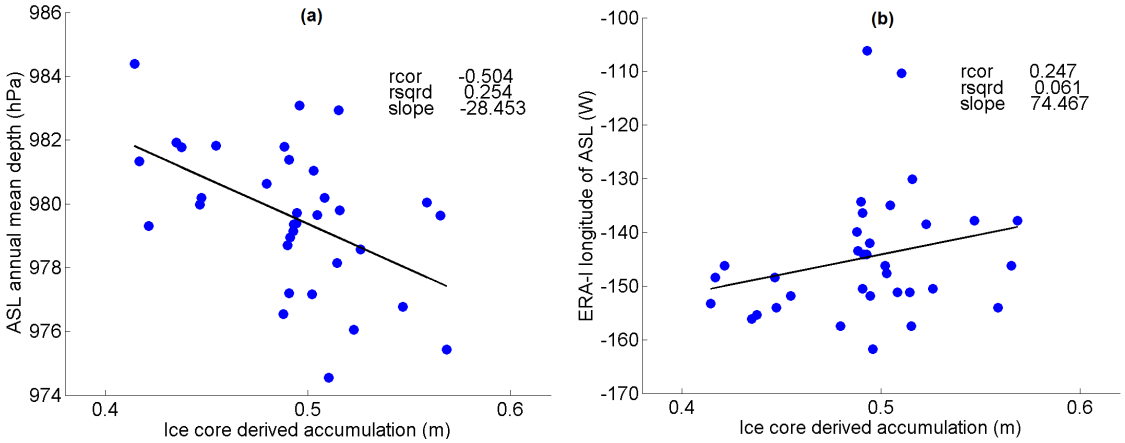

Figure 4.10: Scatter plots showing the relationship between ice core observed accumulation on PIG and: (a) ERA-I annual mean depth of the ASL and (b) ERA-I annual mean longitudinal location of the ASL.

(Fig. 4.10b). The correlation between the depth of the ASL and the observed accumulation (R = -0.50) is weaker than that of either temperature or meridional wind speed and accumulation, but remains statistically significant at the 95% level. The correlation coefficient between the longitudinal position of the ASL and observed accumulation is 0.25 and is not statistically significant at the 90% level. Despite the longitudinal cycle of the ASL controlling the seasonal cycle of precipitation on PIG, the observed accumulation is insensitive to its mean annual position.

Through adding the annual mean depth of the ASL as a third predictor of PIG accumulation in the multiple linear regression described above we can now explain 62% of the observed variability and all three predictors are statistically significant at the 95% level. If we add the longitudinal position of the ASL as a fourth predictor in the linear regression we do not see an increase in the R^2 value and the position of the ASL is not a statistically significant predictor at the 95% level. However, the longitudinal position and cycle of the ASL should still be considered when we discuss possible future changes in accumulation on PIG. As, for example, if the easterly location of the ASL in the Bellingshausen Sea currently observed during the summer months were to shift markedly westwards this would allow more frequent maritime air outbreaks. As summer is the currently the driest season, such a shift could result in increased annual accumulation on PIG.

ENSO AND SAM

ENSO affects the Amundsen Sea region through a Rossby wave train pattern that emanates from the central tropical Pacific (Turner et al., 2013; Raphael et al., 2016). This ENSO teleconnection has been shown to have a statistically significant impact on the mean sea level pressure in West Antarctica. During a La Niña event the ASL is significantly deeper than during an El Niño event (Raphael et al., 2016). This means that during an El Niño event there is less cyclone actively in the vicinity of PIG and therefore likely less precipitation/accumulation. The positive phase of the SAM is associated with lower mean sea level pressure at high latitudes and higher mean sea level pressure in mid-latitudes (Raphael et al., 2016). This results in a stronger polar jet, a deeper ASL, and a more southerly location of the ASL (i.e. closer to PIG) (Turner et al., 2013). This may lead to more accumulation on PIG.

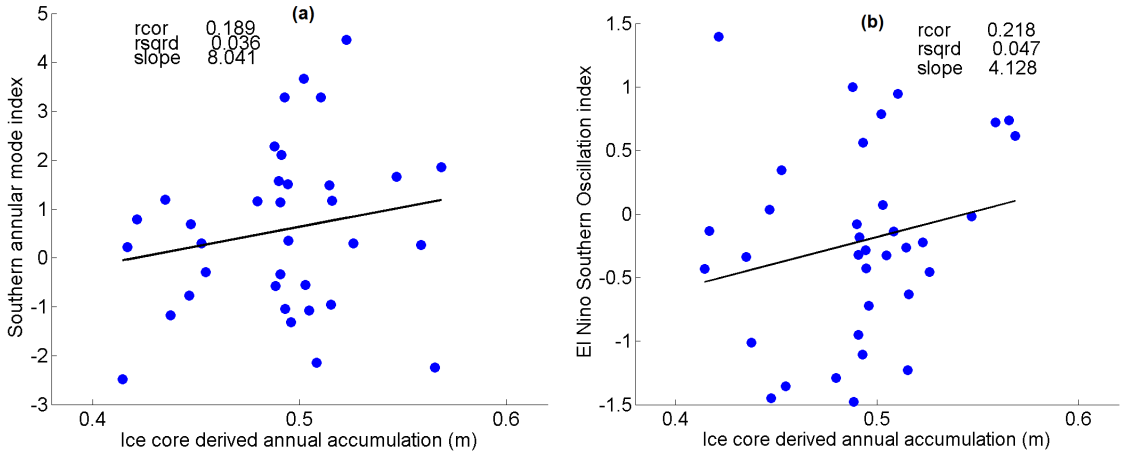

Figure 4.11: Scatter plots showing the relationship between ice core observed accumulation on PIG and: (a) Southern annular mode (SAM) index (data from (Marshall, 2003)) and, (b) El Niño Southern Oscillation index (data from (Wolter and Timlin, 2011)).

The scatter plot in Fig. 4.11a reveals that the SAM index is not significantly correlated with the observed mean annual accumulation on PIG. The SAM index measures the meridional pressure gradient between the mid-latitudes and Antarctica (Marshall, 2003), and as such we would not expect it to significantly alter the zonal pressure gradient, which we have found to be important in determining the observed accumulation (Fig. 4.8). Fig. 4.11b shows that the ENSO index also explains little of the observed variability of accumulation on PIG ($R^2 < 0.05$) and the relationship is statistically insignificant at the 90% level. The ENSO index is however significantly

correlated with the depth of the ASL in ERA-I (R=0.51). This correlation between the ENSO index and the depth of the ASL has also been shown in previous studies with a shallower ASL during the El Niño phase linked to an increase in blocking events in the south Pacific (Turner, 2004; Raphael et al., 2016). While the ENSO index will modulate the depth of the ASL and influence accumulation on PIG through this mechanism (see Fig. 4.10a), it is not directly linked to the observed accumulation on PIG and as such is not a significant predictor of accumulation. Previous studies such as Genthon et al. (2005) have observed a link between ENSO and West Antarctic accumulation but note that significant correlations are only seen in the western Amundsen Sea sector, while further east (closer to PIG) the correlation with ice core data becomes statistically insignificant.

Fogt et al. (2011) have suggested that the ENSO teleconnection only has a significant impact in high southern latitudes when either: a strong ENSO event occurs and the SAM phase is neutral, or when the ENSO index and SAM are in phase i.e. positive SAM and La Niña or negative SAM and El Niño. These are described as in phase because the positive phase of SAM and a La Niña event both act to reduce the mean sea level pressure in the West Antarctic region. To thoroughly test whether this is why we see no significant correlations between the observed accumulation and SAM/ENSO would require seasonally resolved ice core data or a much longer record of accumulation. There are 11 years in the 1979-2013 time series where the SAM phase is positive and a La Niña event is observed, the mean observed accumulation is 0.49 $m.w.e\ yr^{-1}$. There are 5 years in the time series where the SAM phase is negative and an El Niño event is observed, the mean accumulation is 0.50 $m.w.e\ yr^{-1}$. This suggests that there isn't a strong correlation between observed accumulation and SAM/ENSO indices even when the two occur in phase — but further research and observational data are needed here.

4.6 DISCUSSION

4.6.1 WHICH PRODUCTS MOST ACCURATELY REPRODUCE THE ICE CORE OBSERVED ACCUMULATION ON PIG?

We have examined the performance of four different reanalysis products and RACMO2.3 at a range of elevations in West Antarctica by comparing them to a new set of 10 ice cores collected from PIG in 2014 and 2015. Our results show that ERA-I, CFSR and JRA-55 all accurately reproduce the average observed annual accumulation across the ten sites to within 0.01 $m.w.e\ yr^{-1}$. There are some biases across the ten sites, which tend to average out (Fig. 4.4), but as was shown by Genthon et al. (2005) it is better practice to use the average observed accumulation across multiple sites. Their relatively coarse horizontal resolution means that none of these atmospheric products can be expected to accurately reproduce the local processes that dictate the amount of accumulation at an individual site.

RACMO2.3 produces an average annual accumulation rate across the ten sites of 0.53 $m.w.e\ yr^{-1}$, 0.04 $m.w.e\ yr^{-1}$ higher than obseved. At seven sites where the observed accumulation is less than 0.5 $m.w.e\ yr^{-1}$, RACMO2.3 overestimates annual accumulation by an average of 0.09 $m.w.e\ yr^{-1}$ at each site, more than any of the reanalysis products. RACMO2.3 has also been shown to overestimate accumulation compared with observations from regions below 2000 m elevation around Antarctica: both in coastal areas of East Antarctica (Agosta et al., 2012; Wang et al., 2015) and in low elevation regions of West Antarctica (Morris et al., 2017). MERRA underestimates annual accumulation by an average of 0.07 $m.w.e\ yr^{-1}$ when compared with the ice core data (Fig. 4.2). Our findings are in good agreement with the results of Medley et al. (2014) who show that MERRA produces a lower mean annual accumulation value than any other reanalysis product, and is lower than their observational estimates within both PIG and Thwaites basins. MERRA has also been shown to produce near-surface temperatures that are lower than observed in the vicinity of PIG (Jones et al., 2016), and this may partly explain why it underestimates accumulation.

The spatial distribution of accumulation on PIG is similar in all of the reanalysis products and RACMO2.3 (Fig. 4.5). The main differences between the products are

seen at low elevations. This is in keeping with multiple studies that show an increased spread of model estimates of accumulation at lower elevations in Antarctica (Favier et al., 2013; Medley et al., 2014; Wang et al., 2015, 2016). The spatial pattern of accumulation from ERA-I is different from that of the other reanalysis products with a much weaker gradient in accumulation from low to high elevation regions (Fig. 4.5b). This has also been seen in East Antarctica by Agosta et al. (2012), the coarse horizontal resolution of ERA-I is perhaps contributing to this. We know that orographic uplift over steep coastal terrain leads to most of the precipitation events observed in this region (e.g. Nicolas and Bromwich, 2011) and the smoothed orography of ERA-I could be causing this precipitation to occur over a wider area rather than being concentrated in the low elevation, near-coastal zone.

All of the reanalysis products and RACMO2.3 erroneously overestimate the observed inter-annual variability (see Table 4.1). While Medley et al. (2013) also show that reanalysis products, and more especially RACMO2.3, overestimate the ice core derived variability on Thwaites glacier, the difference between the observed and modelled variability is smaller than seen here. Small-scale drifting processes will not be adequately resolved by the reanalyses or RACMO2.3, but given the random nature of the variability induced by these processes it is unlikely that they alone can explain the enhanced variability in the models. Instead the models must be over estimating year-to-year variations in the amount of precipitation falling on PIG.

The correlation coefficients between the observed and modelled time series are relatively low in this study when compared with those found at higher elevation ice core sites in the vicinity of PIG (Medley et al., 2013). One potentially important phenomenon impacting the observed accumulation that is not adequately resolved by the reanalyses and RACMO2.3 is the presence of sastrugi. Sastrugi are ridges in snow that are common in low elevation regions of Antarctica, where near-surface winds are relatively strong (Bintanja, 1998). This is particularly important as the ice core sites in this study are all located on PIG itself, where sastrugi are likely to occur and have an impact on the ice core data (Venteris and Whillans, 1998; Eisen et al., 2008). As outlined by Eisen et al. (2008), sastrugi create quasi-stochastic variability in ice core records, with accumulation rates increasing or decreasing as sastrugi move through an ice core site. Sastrugi may explain why the time series correlation coefficients vary greatly between the ice core locations. The sites that are

highly influenced by sastrugi may be those where the correlation coefficients with the reanalyses and RACMO2.3 are not statistically significant (e.g. Fig. 4.3c and Fig. 4.3d), whereas those where the correlation coefficients are higher (Fig. 4.3a and Fig. 4.3b) may be locations where sastrugi are not as large or absent.

Fig. 4.12 shows the correlation coefficient at each site and contours of the mean wind speed from ERA-I. The sites with lowest correlation coefficient values (sites 4 and 10) are not characterised by particularly strong winds or steep orography (see orographic contours in Fig. 4.1) and as such there is no reason to suggest they are likely to be more greatly influenced by sastrugi than other sites. The mean wind speed does exceed 7 $m\ s^{-1}$ at all sites (generally 7 $m\ s^{-1}$ is identified as the critical threshold for sastrugi formation (Bintanja, 1998)), and as such sastrugi are likely to be influencing the ice core derived accumulation time series. Note also that the radar derived accumulation observations in Fig. 4.6 show enhanced variability over PIG compared to over neighbouring Thwaites glacier.

Overall, JRA-55 and CFSR most accurately capture both the observed mean annual accumulation rate on PIG and have sufficient horizontal resolution to capture the higher accumulation regions close to the coastline. ERA-I has the highest correlation coefficient compared with the observed accumulation record (R = 0.61) but due to its weak gradient in accumulation between high and low elevation regions and the displacement of the accumulation shadow region too far southeastwards (Fig. 4.5b), we do not believe it is performing as well as JRA-55 and CFSR. CFSR was also found to be in good agreement with the radar-derived accumulation rate on both PIG and Thwaites glaciers (Medley et al., 2014). JRA-55 was found to contain smaller biases than other reanalysis products (and RACMO) when compared with coastal (< 2000 metres elevation) stake line observations in East Antarctica (Wang et al., 2015). All of the products exaggerate the inter-annual variability of accumulation when compared with the ice core derived time series.

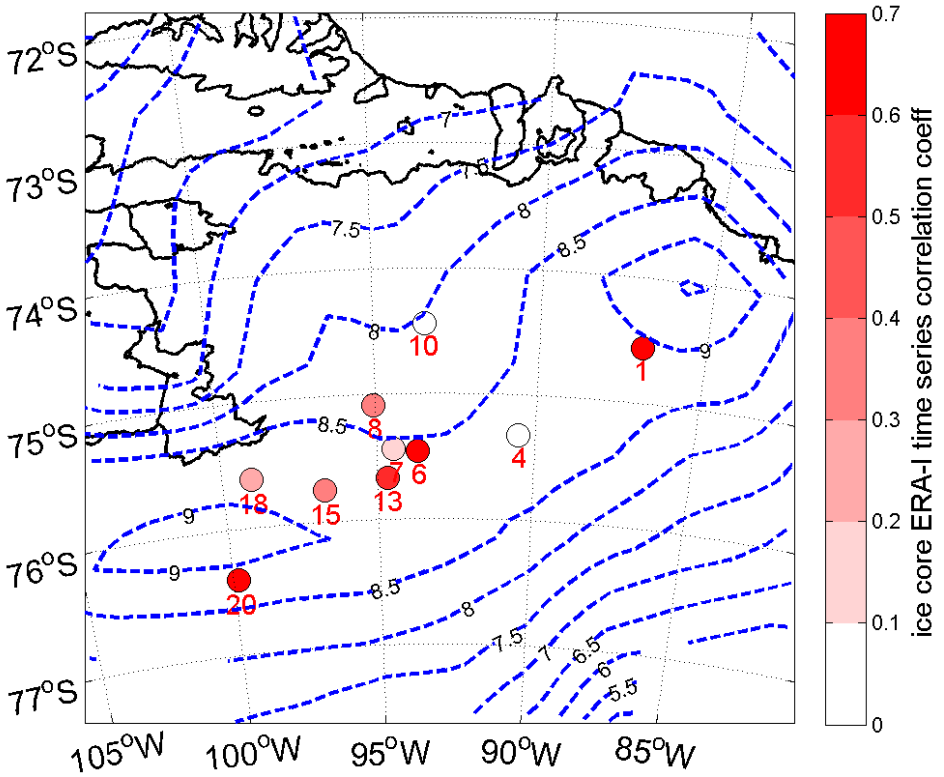

Figure 4.12: The correlation coefficient between the ice core observed time series of accumulation and ERA-I precipitation minus evaporation at each site (coloured circles). The blue dashed lines show the ERA-I 1979-2013 mean wind speed. Regions with a higher mean wind speed are more likely to be strongly influenced by snow erosional or depositional features.

4.6.2 ATMOSPHERIC CIRCULATION IN HIGH AND LOW ACCUMULATION YEARS AND IMPLICATIONS FOR 21ST CENTURY ACCUMULATION CHANGES

In both the observational and simulated records there is no statistically significant trend in the mean annual accumulation on PIG between 1979 and 2013. The reanalysis products also show there is no significant trend in either the near-surface air temperature or meridional wind speeds on PIG over the same time period (not shown). Given that our multiple linear regression shows that temperature and meridional winds control ~53% of the observed variability of accumulation it is unsurprising there is no trend in the accumulation. Some studies investigating the mass balance of PIG have implied a trend towards increasing accumulation on the glacier in recent decades (e.g. Wingham et al., 2009), our results show this trend is

absent in the ice core observations, reanalysis products, and RACMO2.3.

The plots showing the atmospheric circulation in high and low accumulation years (Fig. 4.7) reveal that high accumulation years are characterised by an enhanced zonal pressure gradient at approximately 70°S. Associated with this are anomalously northerly meridional winds in the Amundsen Sea sector. Hosking et al. (2016) examine how the ASL will change due to anthropogenic climate change and find that the seasonal cycle of the ASL is largely unchanged by the end of the 21st century. There is a slight poleward shift of its position in summer and autumn and a slight eastward shift in autumn and winter (Hosking et al., 2016), but given our result in Fig. 4.10b these changes are unlikely to have a significant impact on the amount of accumulation on PIG. Furthermore, Hosking et al. (2016) show that in the CMIP5 models there is little evidence of any significant changes in the meridional wind speed in the vicinity of PIG by the end of the 21st century. This implies that it is unlikely that changes in the ASL and meridional winds will have a significant impact on the amount of accumulation on PIG by the end of the 21st century.

Temperature is the other variable that is a significant predictor of the observed accumulation on PIG. When the near-surface annual average air temperature on PIG is higher there is more accumulation observed on PIG (Fig. 4.9b). Multiple studies have examined how temperature changes in Antarctica during the 21st century are likely to affect accumulation (Ligtenberg et al., 2013; Frieler et al., 2015; Lenaerts et al., 2016). Warmer air is capable of holding more moisture and this affect is amplified in regions where temperatures are cold (Pall et al., 2007). Consequently, over the continent as a whole there is likely to be an increase in accumulation as temperatures increase (e.g. Ligtenberg et al., 2013; Frieler et al., 2015; Lenaerts et al., 2016). The magnitude of the projected increase varies in different parts of Antarctica, with larger absolute increases in precipitation in coastal areas (Frieler et al., 2015). In the vicinity of PIG, projections suggest that during this century mean annual temperatures will increase by 2 °C to 3 °C (Bracegirdle et al., 2008; Ligtenberg et al., 2013). Most studies agree that for each degree of a warming a 4 to 6% increase in accumulation is likely to be observed (Monaghan et al., 2008; Ligtenberg et al., 2013; Frieler et al., 2015). The change in accumulation is further complicated by the increased frequency of surface melt events (Nicolas et al., 2017) and larger sublimation (Lenaerts et al., 2016) predicted to occur during the latter part of the 21st century. Overall though,

given the projected warming trend, we would anticipate a 10 to 20% increase in accumulation on PIG by the end of the century. In order to monitor when trends in near-surface temperature or accumulation become statistically significant on PIG we must continue to monitor these variables.

4.7 CONCLUSIONS

This work compares low elevation ice cores from coastal West Antarctica to accumulation fields derived from global reanalysis products and the regional climate model RACMO2.3. Our results show that there has been no significant trend in the observed or modelled accumulation rate on PIG between 1979 and 2013. This is a significant result and shows that increased mass losses from PIG in recent decades have not been partially offset by increased accumulation on to the glacier.

Despite the coarse resolution of the global reanalysis products JRA-55, CFSR and ERA-I are all able to accurately reproduce the ten site average observed mean annual accumulation on PIG of 0.49 $m.w.e\ yr^{-1}$. RACMO2.3 tends to slightly overestimate the accumulation rate by 0.04 $m.w.e\ yr^{-1}$, and MERRA underestimates by 0.07 $m.w.e\ yr^{-1}$. Spatially, the observations and models agree that the highest accumulation rates of 0.7 to 1.0 $m.w.e\ yr^{-1}$ are in the low elevation portion of PIG, on the western end of the trunk of the glacier and on Pine Island ice shelf. Higher up the glacier (further east) the accumulation rate is lower at 0.4 to 0.6 $m.w.e\ yr^{-1}$. JRA-55 and CFSR are most accurately capturing both the mean annual accumulation rate on PIG and the change from low accumulation rates on the eastern end of PIG to high accumulation rates further west.

It is shown that high accumulation years on PIG are characterised by both higher near-surface air temperatures on PIG and a strong zonal pressure gradient at approximately 70°S that drives more frequent (or persistent) northerly winds in the vicinity of PIG. The strength of the meridional winds, mean annual air temperature and the annual mean depth of the ASL can together explain 62% of the observed variability of accumulation on PIG. All three of these predictors are statistically significant at the 95% level in a multiple linear regression.

Future changes in the meridional winds on PIG are unlikely to be significant by the end of the 21st century and changes in the ASL over the same time period are fairly subtle (Hosking et al., 2016). We therefore expect temperature changes to be the main driver of accumulation change on PIG during this century. A warming of 2 to 3 °C is expected in the vicinity of PIG by the end of the 21st century and accumulation rates will increase in response to this change. Estimates from a range of future mass balance modelling studies suggest that accumulation in these coastal regions will

increase by 4-6% per °C of warming (Monaghan et al., 2008; Ligtenberg et al., 2013; Frieler et al., 2015). So the overall change in accumulation may be 10-20% by the end of the century. Given that Medley et al. (2014) estimate the annual accumulation on PIG is currently ~ 67 $Gt\ yr^{-1}$, the increase in accumulation by the end of the century will likely be 7 to 14 $Gt\ yr^{-1}$. Favier et al. (2014) predict that the net mass loss on PIG will increase to between 60 and 120 $Gt\ yr^{-1}$ by the end of the century, so changes in accumulation are likely to be relatively small in comparison with accelerating mass losses.

5

MODELLING THE METEOROLOGICAL CONDITIONS DURING HIGH HEAT FLUX EVENTS OVER THE AMUNDSEN SEA EMBAYMENT

5.1 INTRODUCTION

In the Amundsen Sea region there has been a focus on understanding the melt rate variability of glaciers such as Pine Island. Research has mainly focussed on variability of the inflow of relatively warm circumpolar deep water transported along oceanic troughs towards ice shelves (Thoma et al., 2008; Assmann et al., 2013; Dutrieux et al., 2014; Nakayama et al., 2014) and changes in the mass balance of glaciers in the region (Shepherd, 2001; Wingham et al., 2009; Favier et al., 2014). The rate of circumpolar deep water inflow is thought to be influenced by processes such as large-scale atmospheric circulation and remotely by pressure patterns in the tropical Pacific Ocean (Thoma et al., 2008; Dutrieux et al., 2014). Recently both ocean models and observations have suggested melt rate variability may also be linked to local processes closer to the glacier (St-Laurent et al., 2015; Christianson et al., 2016; Webber et al., 2017).

St-Laurent et al. (2015) use the Regional Ocean Model System to show that cold water generated in coastal polynyas in the eastern Amundsen Sea is transported towards Pine Island ice shelf and cools the water within the ice shelf cavity, reducing the rate of basal melt. This process is similar to that described at Totten glacier in East Antarctica by Gwyther et al. (2014), where a larger or more persistent polynya is thought to reduce the melt rate of the glacier. Webber et al. (2017) show a unique 5 year time series of observations from an ocean mooring close to Pine Island ice shelf. Local atmospheric forcing and associated sea ice formation (alongside changes in the local ocean circulation) are shown to be contributing to large interannual variability in ocean temperature in the vicinity of Pine Island ice shelf (Webber et al., 2017). A large local cooling event between October 2011 and March 2013 significantly reduced the ocean temperature within the water column to a depth of 400-700m below the surface. Mooring observations at the continental shelf break show no evidence of a decrease in on-shelf transport of circumpolar deep water corroborating the local nature of this event (Webber et al., 2017). This local cooling of the ocean is thought to have contributed to a slight decrease in the flow speed of Pine Island ice shelf between 2012 and 2014 (Christianson et al., 2016).

Mesoscale coastal polynyas and their associated high surface heat fluxes and sea ice formation are thought to have an impact on the oceanic conditions close to PIG. Therefore it is important we investigate the typical meteorological conditions associated with these high heat flux events and what horizontal resolution of atmospheric model is required to accurately capture them.

5.2 AIMS

Recent research suggests that coastal polynyas and local atmospheric processes may have an influence on the melt rate of PIG ice shelf. Here we look to investigate the atmospheric conditions associated with large ocean to atmosphere heat flux events in the ASE. Given that many ocean modelling and analysis studies in this region still use coarse resolution atmospheric data such as reanalyses (e.g. Thoma et al., 2008; Holland et al., 2010; Assmann et al., 2013; Webber et al., 2017) we will also investigate whether high horizontal resolution is required to accurately capture these events. This chapter has two distinct aims:

- To characterise the meteorological conditions associated with large heat flux events in the Amundsen Sea Embayment.
- To investigate several typical high heat flux case studies and establish whether coarse resolution atmospheric models can adequately capture their characteristics. In particular determining any systematic biases or deficiencies that appear related to model resolution.

Three high heat flux case studies have been chosen through an analysis of OSTIA sea ice concentration data and MODIS visible satellite imagery. We examined winter and spring OSTIA sea ice concentration data from 2011-2016 looking for areas of low sea-ice concentration, alongside this we viewed MODIS visible satellite imagery from 2012 onwards. Following this work we identified three areas of focus where coastal polynyas tend to form. These are outlined in Fig. 5.1 and are named according to surrounding glaciers and ice shelves:

- Pope, Smith Kohler (PSK) box is the area between 74.1°S and 72.75°S and 110°W and 115°W (outlined in green in Fig. 5.1; see also Figs. 5.7, 5.14, 5.17).
- Pine Island Glacier (PIG) box is the area between 75°S and 73.9°S and 101.5°W and 105°W (outlined in blue).
- Thurston box is bounded by 73.5°S and 72.5°S and 103°W and 105.5°W (outlined in red).

Chapter 2 outlines the model settings we use in the MetUM, here we note that the high resolution simulation has a horizontal resolution of 2.2 km, while the coarse resolution model is 17 km. We chose 17 km as the MetUM is currently operational at this resolution for the UK Met Office's global forecast simulations. While this is a higher horizontal resolution than the global reanalysis products evaluated in chapter 3 it is comparable to the new generation of reanalysis products currently being released e.g. ERA-5.

Before we examine high heat flux events, we first investigate a 'control' case study to validate the model and establish whether there are differences between the two resolutions of the MetUM when synoptic pressure gradients are weak and wind speeds relatively light. This control case is during a period when we have a relative wealth of observational data.

5.3 CONTROL CASE STUDY: FEB 2014

5.3.1 SYNOPTIC OVERVIEW

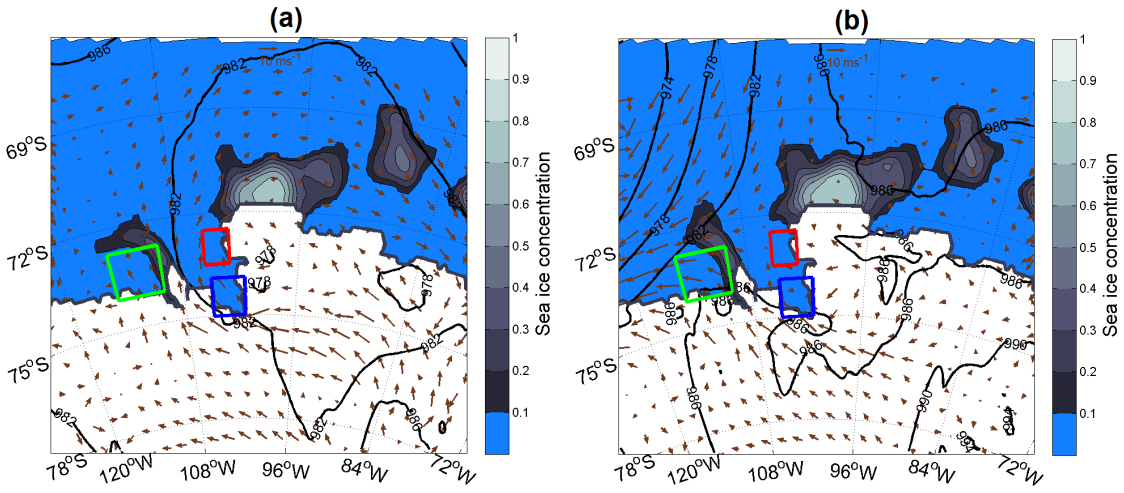

Figure 5.1: Mean sea level pressure (black contours), 10-m wind vectors and sea ice concentration (colour contours) from the MetUM 17 km resolution simulation at: (a) 1200 UTC 17th Feb 2014; (b) 1200 UTC 18th Feb 2014. Coastal polynya boxes are outlined: PIG polynya (blue), PSK polynya (green), Thurston polynya (red).

The 17th and 18th February 2014 are selected as a control case study. At this time there were four AWS stations operating in the ASE along with additional observations from *RRS James Clark Ross* (JCR) and data from five radiosondes launched as part of this project (see chapter 2), making this period one of the best observed during the iSTAR cruise. Fig. 5.1 shows that the pressure gradient during this case study is relatively weak. On 17th February there are light southeasterly winds over much of the ASE, later on 18th February a cyclone moves in from the northwest bringing milder northerly winds. There are large areas of open water with sea ice concentrations of less than 10% over most of the area of interest. Near-surface air temperatures are 2 to 3 °C below average for the time of the year, with mean values of -6 °C to -10 °C over open water within the ASE (not shown). Inland the modelled near-surface air temperatures are significantly colder ranging from mean values of -12 °C near the coast to -25 °C further inland and at higher elevations. Mean modelled wind speeds are light in the eastern side of the ASE ($4-6\ m\ s^{-1}$) but it was windier in the west where the influence of the cyclone pushed 48-hour mean wind speeds up to $\sim 10\ m\ s^{-1}$.

5.3.2 VALIDATION USING AWS OBSERVATIONS

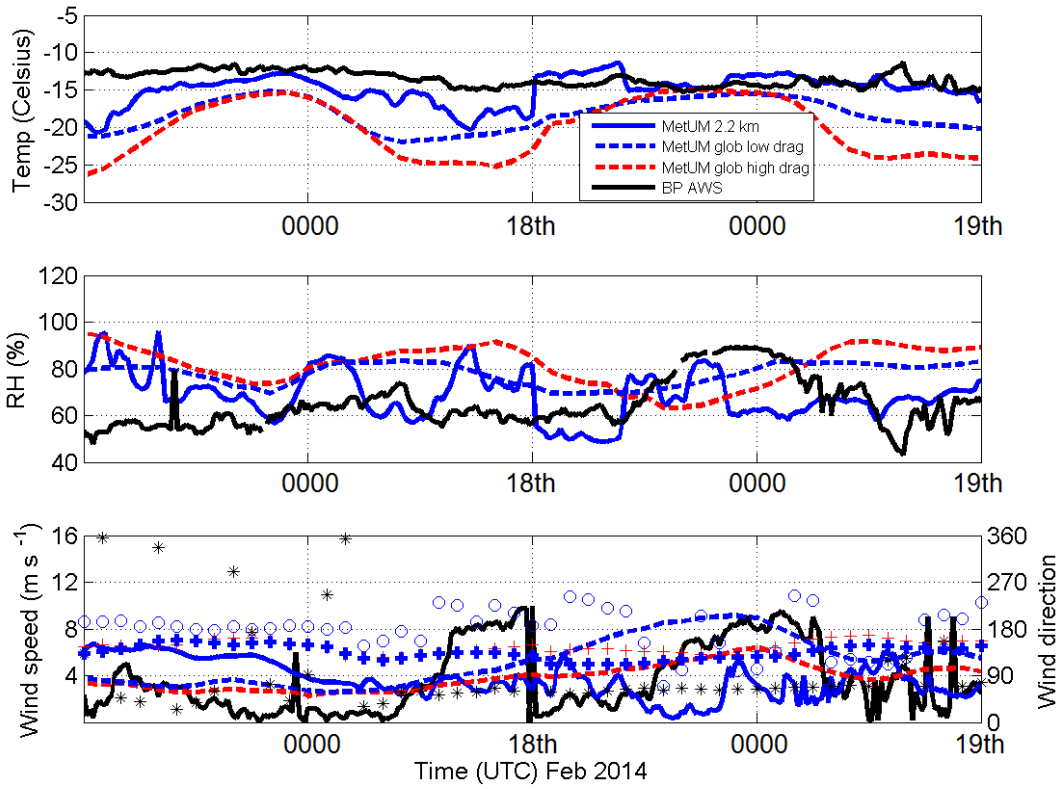

Figure 5.2: A time series comparing both resolutions of the MetUM to observations from Bear Peninsula AWS: 2-m temperature (top), Relative Humidity w.r.t water (middle), Wind speed and direction (bottom). In the wind direction plot the symbols represent the following: black stars = AWS observations, blue circles = MetUM high resolution simulation, blue crosses = MetUM coarse resolution simulation with low flow blocking drag coefficient, red crosses = MetUM coarse resolution simulation with default flow blocking drag coefficient (high).

There are two coarse resolution MetUM runs shown in Fig. 5.2 — the red dashed line shows the coarse resolution simulation with the high flow blocking drag coefficient whereas the blue dashed line shows the simulation with the updated (lower) flow blocking drag coefficient value (see chapter 2 for details). The difference between the MetUM global simulations with 'high' and 'low' drag coefficients shows that by updating the flow blocking drag coefficient in the coarse resolution model the mean temperature bias at Bear Peninsula (BP) AWS decreases from -6.5 °C ('high drag') to -4.7 °C ('low drag'). However, it does remain larger than the temperature bias in the high resolution model (-1.4 °C). The coarse resolution model temperature bias is greatest between 0300 and 1100 UTC each day which corresponds to the 'overnight' period (i.e. the sun is close to or below the horizon) in the ASE at this time of year.

Analysis of the radiation budget at Evans Knoll (EK) AWS (not shown) revealed that the net upwelling longwave radiation term was larger in the coarse resolution simulation during these 'overnight' time periods and hence the near-surface air temperature was colder. There is also a difference between the observed and modelled wind direction which may be contributing to the temperature bias. For much of the case study the observed winds at BP AWS come from the northeasterly direction (bringing relatively mild conditions) whereas both resolutions of the model show cooler southerly or southeasterly winds at this location (Fig. 5.2). Such wind direction biases are often linked to model temperature biases in simulations over the Amundsen Sea region (Deb et al., 2016).

The wind speed time series in Fig. 5.2 shows that both resolutions of the MetUM are in reasonable agreement with the observations. While wind speeds were generally quite light at BP AWS both resolutions of the model struggle to capture stronger winds that were observed at 0800-1200 UTC 18th February. Both resolutions of the model have higher values of relative humidity than observed for much of the time series (Fig. 5.2). The high resolution model relative humidity is on average 4% higher than observed, while the coarse resolution model is 13% higher than observed (in the updated 'low drag' simulation). While this bias can be greater than 20% at times, it is not overly concerning as observations of relative humidity in Antarctica are known to contain inaccuracies, particularly when air temperatures are low, so there could be observational bias as well as model bias (Renfrew and Anderson, 2002).

Fig. 5.3 compares the observations from New York University (NYU) AWS on PIG to both resolutions of the MetUM. Note that during this period the AWS humidity sensor was not operational so the humidity panel of Fig. 5.3 shows only model values. The high resolution model accurately reproduces the observed temperatures with mean modelled 2-m temperatures only 0.3 °C colder than observed. The coarse resolution model contains a persistent cold bias and is on average 2.8 °C colder than the observations. In the wind speed and direction comparison in Fig. 5.3 both resolutions of the model do a reasonable job of reproducing the observed conditions with light to moderate south to southeasterly winds.

Figs. 5.2 and 5.3 are generally representative of the other AWS sites too. The magnitude of the coarse resolution model temperature bias varies at different sites, ranging between -1.6 °C and -6.9 °C, it is always larger than the high resolution model

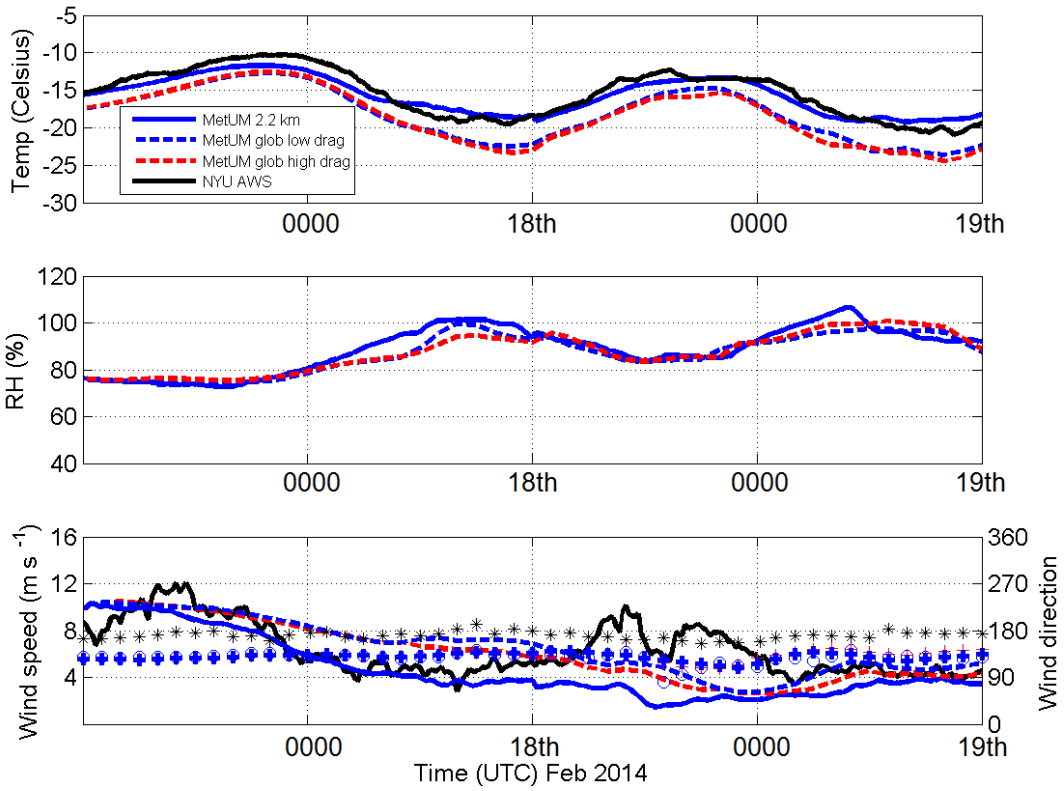

Figure 5.3: A time series comparing both resolutions of the MetUM to observations from New York University AWS: 2-m temperature (top), Relative Humidity w.r.t water (middle), Wind speed and direction (bottom). In the wind direction plot the symbols represent the following: black stars = AWS observations, blue circles = MetUM high resolution simulation, blue crosses = MetUM coarse resolution simulation with low flow blocking drag coefficient, red crosses = MetUM coarse resolution simulation with default flow blocking drag coefficient (high).

temperature bias. In the high resolution model the range of temperature biases is -0.2 °C to -2.9 °C. The temperature comparison in Fig. 5.2 is representative of those seen at EK and TI AWS where the coarse resolution model shows an overly large drop in temperature during the overnight period when observed wind speeds are light. Modelled wind speed and direction at all four AWS are generally in reasonable agreement with the observations, typically wind speed biases compared with AWS observations are less than 2 $m\ s^{-1}$. The models do however tend to miss short term increases in the wind speed such as those seen at BP AWS at 1000 UTC 18th February (Fig. 5.2) and that at ~ 1700 UTC 18th February at NYU AWS (Fig. 5.3).

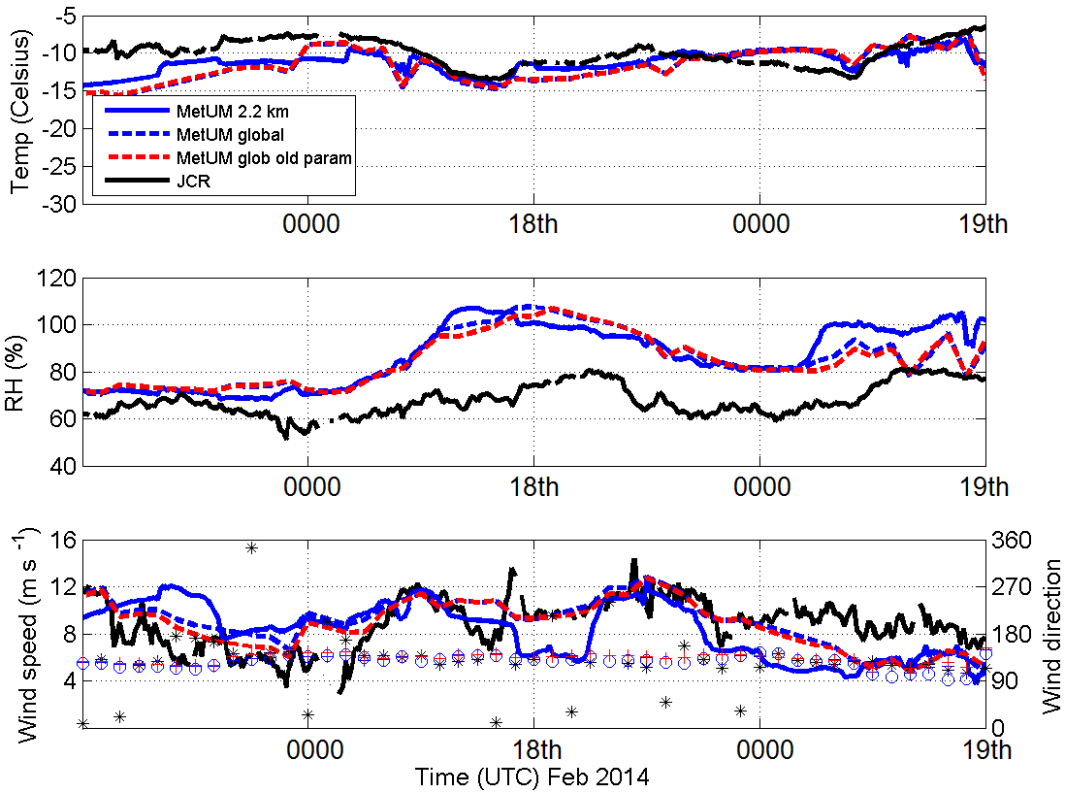

Figure 5.4: A time series comparing the MetUM to meteorological observations collected onboard RRS James Clarke Ross: Temperature (top), Relative Humidity w.r.t water (middle), Wind speed and direction (bottom). In the wind direction plot the symbols represent the following: black stars = AWS observations, blue circles = MetUM high resolution simulation, blue crosses = MetUM coarse resolution simulation with low flow blocking drag coefficient, red crosses = MetUM coarse resolution simulation with default flow blocking drag coefficient (high).

5.3.3 VALIDATION USING JCR OBSERVATIONS

Fig. 5.4 shows that, over the ocean, the two resolutions of the MetUM both have very similar near-surface temperature values. They are also both in good agreement with the *JCR* observations. The mean temperature bias is -1.2 °C for the high resolution model and -1.6 °C for the coarser resolution simulation, these are mainly caused by a cold bias in the first 12 hours of the case study. These temperature biases, particularly for the coarse resolution model, are smaller than were seen over land at the AWSs. Over the open water of the ocean there is a shallow neutral layer near the surface due to upward heat fluxes from the ocean to the atmosphere (see Fig. 5.5). Over land the boundary layer profile is more stable, such stable boundary layers are known to be a major challenge for both weather and climate models (e.g. Holtslag et al., 2013; Mahrt,

2013).

Both resolutions of the model accurately reproduce the observed wind speed time series in Fig. 5.4, and while there are some fluctuations in the observed wind direction the models and observations are in agreement that the wind is predominantly coming from the southeasterly quadrant. Once again the modelled relative humidity tends to be higher than observed but the same uncertainty is attached to the *JCR* humidity observations as in the AWS comparison. The modelled mean sea level pressure has been compared to the *JCR* observations and found to be in quite good agreement, although on 18th February both models underestimate the observed pressure by ~2 hPa (see Fig. A.1). The MetUM sea-surface-temperature values (derived from OSTIA) have also been compared to those observed on the JCR and there is good agreement that the observed sea-surface-temperature is close to the in-situ freezing temperature throughout the case study (not shown).

5.3.4 VALIDATION USING RADIOSONDE OBSERVATIONS

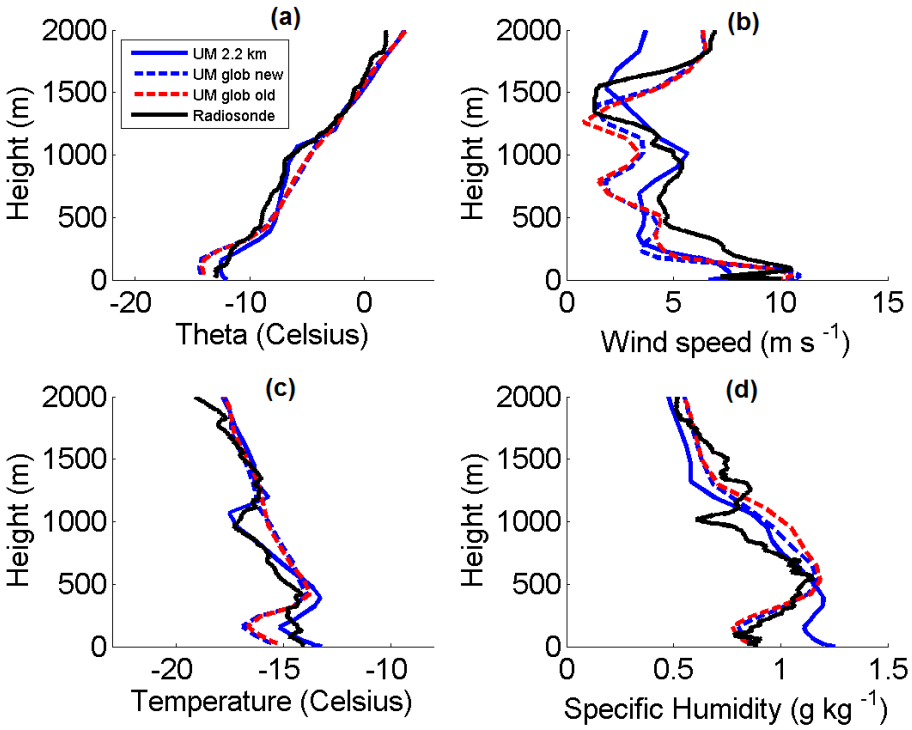

Figure 5.5: Vertical profiles from the MetUM compared to radiosonde observations at 0800 UTC on 18th February 2014: (a) Potential temperature; (b) wind speed; (c) Temperature; (d) Specific Humidity.

Fig. 5.5 compares vertical profiles from the MetUM to radiosonde profile observations in order to evaluate model performance above the surface. This radiosonde was launched from 75.0°S, 101.8°W, around 15 km north of Pine Island ice shelf, at the time the near-surface air temperature was -13.2 °C. The observed radiosonde profile shows a shallow (~100m deep) neutral layer capped by a stable layer. In general, the MetUM accurately reproduces the observed temperature profile with biases of less than 2 °C from the surface up to 2000 m. However, both resolutions of the MetUM show a temperature inversion at 100m altitude, whereas the observations show a layer (100-300m above the surface) in which the temperature is relatively constant with height.

In both the observations and the model there is a near-surface wind speed maxima. In the observations and coarser resolution model this is ~ 10 $m\ s^{-1}$ but it is weaker in the high resolution model (7 $m\ s^{-1}$). Above this, both resolutions of the MetUM accurately reproduce the observed wind speed profile in Fig. 5.5 despite some sharp changes between the surface and 2000m altitude. The MetUM also accurately reproduces the observed specific humidity profile, although the high resolution model is ~ 0.25 $g\ kg^{-1}$ too moist in the lowest 400m.

There were a further four radiosondes launched on 18th February, all within ~20 km of one another. The modelled and observed profiles from these launches are shown in the appendix (Figs. A.2 to A.5). The two profiles that follow the 0800 UTC launch at 1145 UTC and 1445 UTC show similar profiles and biases to those seen in Fig. 5.5. The coarse resolution model does though show a slight cold bias in the lowest 150 metres of the profile. The moist bias in the high resolution model in Fig. 5.5 decreases by 1445 UTC. Both resolutions of the model show slightly weaker winds than observed at 1145 UTC and 1445 UTC but model-observation agreement is reasonable. Later in the 1715 UTC and 2130 UTC profiles the observed depth of the neutral layer increases to ~500 metres and the observed wind speed strengthens. Both resolutions of the MetUM struggle to capture this change, the wind speed in particular is underestimated by the MetUM. The high resolution model does show a deepening of the neutral layer and is in good agreement with the observed temperatures over the lowest 200 metres of the profile but the neutral layer is not as deep as observed. At 1715 UTC the coarse resolution model shows a particularly large cold bias (approximately 4 °C) between the surface and ~250 m and an associated

0.4 $g\ kg^{-1}$ dry bias.

5.3.5 SUMMARY OF VALIDATION

Overall, in comparison with both the radiosonde and *JCR* observations the MetUM accurately reproduced the observed conditions, and both resolutions of the model are in reasonable agreement with one another. The high resolution model had a slightly smaller temperature bias compared to the *JCR* observations and in the radiosonde comparison it more accurately reproduced the observed increase in the depth of the neutral layer. However, the coarse resolution model more accurately captures a low-level jet in the wind speed profile. Over land, in the AWS comparison, there is a discrepancy between the two models with overly cold overnight temperatures in the coarse resolution simulation. The high resolution model had smaller temperature biases at all sites when compared with the AWS observations.

5.3.6 MODELLED TURBULENT HEAT FLUXES

In this summertime control case study there are low sea ice concentrations across much of the ASE. There was also very limited sea ice formation observed in the region, as such the boxes outlined in Fig. 5.6 are not true coastal polynyas during this control case study. Instead there are large sensible and latent heat fluxes from ocean to atmosphere widely throughout the ASE — the magnitude of the mean fluxes decreases with increasing fetch as the air warms over the ocean (Fig. 5.6a). The mean turbulent heat fluxes are up to ~200 W m^{-2} in southern coastal areas (Fig. 5.6a). The two resolutions of the MetUM are in good agreement on the magnitude of turbulent heat fluxes. Fig. 5.6b shows that across much of the region of interest the two models are within 20 W m^{-2} of each other. Fig. 5.6f shows that over a large area the wind speed difference between the two resolutions of the model is less than 1 $m\ s^{-1}$. However, there are some larger differences inland, particularly around complex orography. In Fig. 5.6d, over land the high resolution simulation is clearly warmer than the coarser resolution simulation by 1 to 5 °C. This is due to the overly large overnight cooling in the coarse resolution MetUM discussed in section 5.3.2.

In this control case study, where winds are relatively light the two resolutions of the MetUM are in good agreement on the magnitude of ocean to atmosphere heat

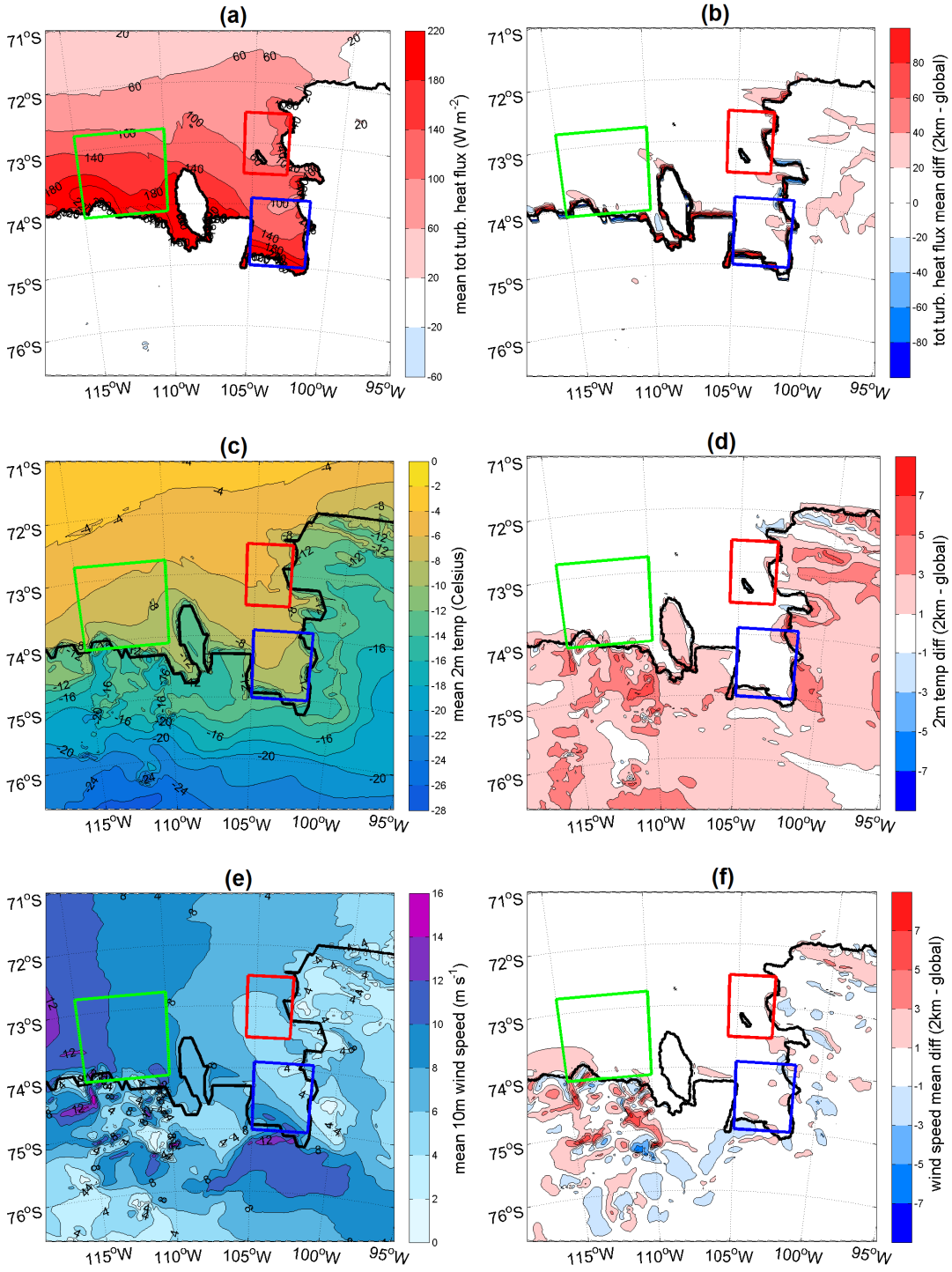

Figure 5.6: Modelled heat fluxes and near-surface variables for the high resolution model (left) and the difference between the high and coarse resolution models (right) for: a),b) total turbulent heat flux, c),d) 2-m temperature e),f) 10-m wind speed. All panels show the mean over the 48 hours of the case study.

fluxes. In coastal areas there are no large discrepancies in modelled near-surface winds and temperatures. Within the PIG polynya (outlined in blue in Fig. 5.6) the mean total turbulent heat flux is 7 W m^{-2} (6%) larger in the high resolution model. For all three of the 'coastal polynyas' the mean difference is less than 10 W m^{-2}.

5.3.7 FEBRUARY 2014 CONTROL CASE STUDY SUMMARY

- Both resolutions of the model are colder than AWS observed temperatures over land. The magnitude of this bias is larger in the coarse resolution model at all sites (ranging from 1.6 °C to 6.9 °C). Wind speed biases are comparable for the two resolutions of the model; the high resolution model ranging from $-1.7\ m\ s^{-1}$ to $+0.1\ m\ s^{-1}$ and the coarse resolution model between $-0.4\ m\ s^{-1}$ and $+1.6\ m\ s^{-1}$.

- Comparison with AWS data revealed the coarse resolution model was cooling near-surface temperatures too much during the overnight period. To reduce this problem we decreased the model value of the flow blocking drag coefficient which increased the mixing and thus reduced the vertical temperature gradient.

- When compared with observations from the *JCR* temperature biases for the high and coarse resolution model were -1.2 and -1.6 °C respectively and wind speed biases were $-0.5\ m\ s^{-1}$ and $-0.1\ m\ s^{-1}$ respectively.

- Both resolutions of the model showed quite good agreement with the observed radiosonde profiles. The high resolution model had smaller boundary layer temperature biases but the coarse resolution model more accurately captures the strength of the low-level-jet.

- In these light wind conditions the two resolutions of the MetUM are in good agreement on the magnitude of turbulent heat fluxes within the ASE. Differences between the two resolutions of the MetUM are also small for near-surface temperature and wind speeds, even in coastal areas.

5.4 HIGH HEAT FLUX CASE STUDY: OCT 2011

The previous section showed that in the case study of a weak synoptic pressure gradient the two resolutions of the MetUM are in good agreement on both the magnitude of heat fluxes within the ASE and the near-surface conditions (although over land there is a larger cold bias in the coarse resolution model). Now we will examine a strong wind case study where evidence from MODIS satellite imagery and OSTIA data showed the development of coastal polynyas.

5.4.1 SYNOPTIC OVERVIEW

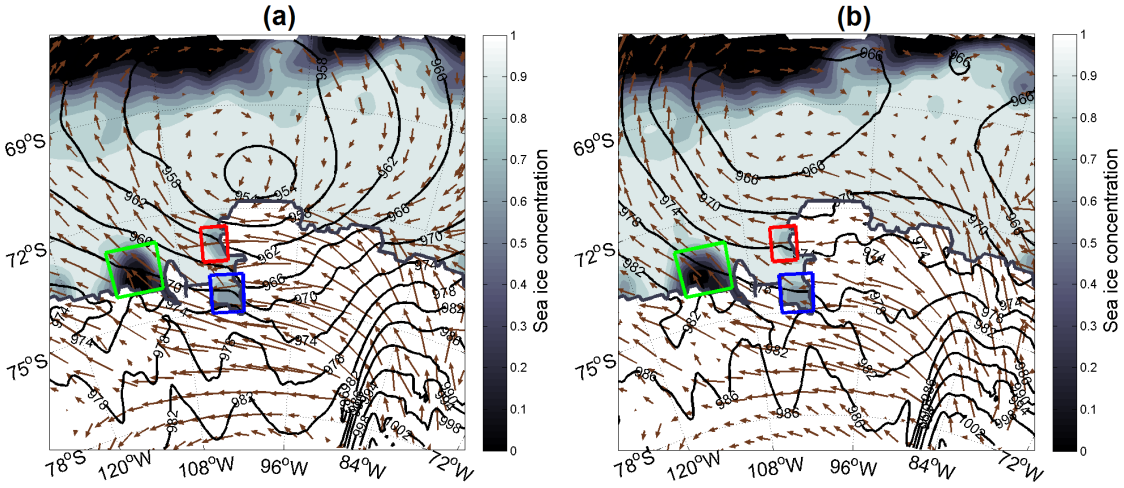

Figure 5.7: Mean sea level pressure, 10-m wind vectors and sea ice concentration from the MetUM 17 km resolution simulation at: (a) 0000 UTC 29th October 2011 and (b) 0000 UTC 30th October 2011. For reference wind vector see Fig. 5.1.

Fig. 5.7a shows a deep depression sitting to the north of Thurston Island with a central pressure of ~954 hPa. There are strong easterly winds on the southern flank of the cyclone that are reducing the sea ice concentration along the eastern shoreline of the ASE and within the PSK polynya further west. Gale force winds were recorded at three of the AWS sites with a peak wind speed of 26 $m\ s^{-1}$ (~58 mph) recorded at Evans Knoll at 0100 UTC 29th October 2011. During the 29th October the low pressure begins to fill and drift northwest, while fresh to strong south-easterly winds continue to affect much of the ASE (Fig. 5.7b). This is a springtime case study and air temperatures are relatively cold, with mean temperatures between −12 °C and −25 °C

over inland areas, rising to -6 °C to -12 °C over the coastal polynyas. Within the PIG and Thurston coastal polynyas the modelled sea ice concentration is reduced to a minimum of 0.5 to 0.6 at the coastline but gradually increases further west and north within the polynyas. In the PSK polynya the sea ice concentration is reduced to near 0 over quite a broad area particularly close to the southern shoreline, this site is known to be a recurring polynya location (e.g. Stammerjohn et al., 2015).

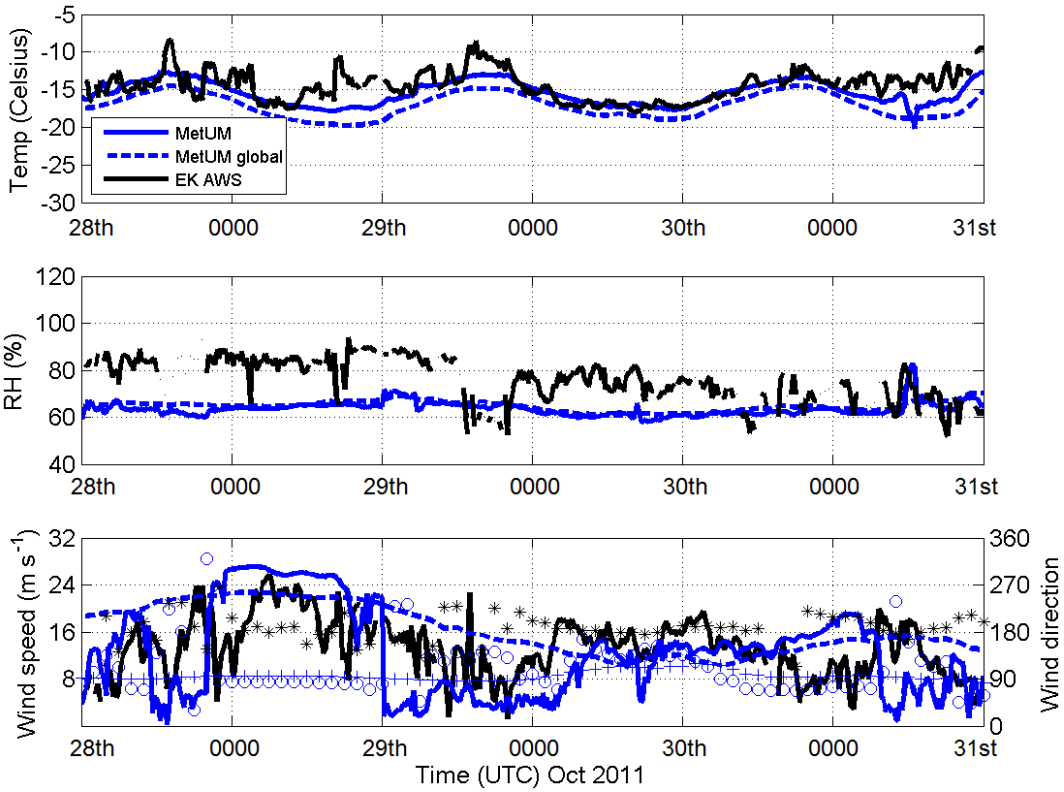

Figure 5.8: A time series comparing both resolutions of the MetUM to observations from Evans Knoll AWS: 2-m temperature (top), Relative Humidity w.r.t water (middle), Wind speed and direction (bottom). In the wind direction plot the symbols represent the following: black stars = AWS observations, blue circles = MetUM high resolution simulation, blue crosses = MetUM coarse resolution simulation.

Fig. 5.8 shows that the high resolution model near-surface temperatures have a smaller temperature bias (-1.0 °C) compared with the AWS observations at Evans Knoll than the coarse resolution model (-2.6 °C). Both resolutions of the MetUM accurately reproduce the peak wind speed at Evans Knoll AWS to within 2 $m\ s^{-1}$, the high resolution model does capture the amplitude of variability more accurately and appears qualitatively similar to the observations. The mean wind speed bias in the high resolution model is smaller at $-1.0\ m\ s^{-1}$ compared to $+3.0\ m\ s^{-1}$ in the coarser

resolution model. Both models give 2-m relative humidity values of approximately 60%, but this is drier than observed, by up to 20% during the first half of the case study.

Fig. 5.8 is representative of the biases at all three AWS sites available during this case study (see Fig. A.6 for a further example); the high resolution simulation is on average 0.19 °C colder than observed while the coarse resolution simulation is 0.64 °C colder than observed. The strong overnight cooling that was seen in the coarse resolution model during the February 2014 case study is absent in this case, probably due to the stronger winds and increased turbulent mixing. Wind speed biases during this case study range from $-1.0\ m\ s^{-1}$ to $+1.1\ m\ s^{-1}$ in the high resolution model and $+0.2\ m\ s^{-1}$ to $+3.0\ m\ s^{-1}$ in the coarse resolution model. Overall the high resolution model has slightly better fidelity.

5.4.2 MODELLED HEAT FLUXES WITHIN COASTAL POLYNYAS

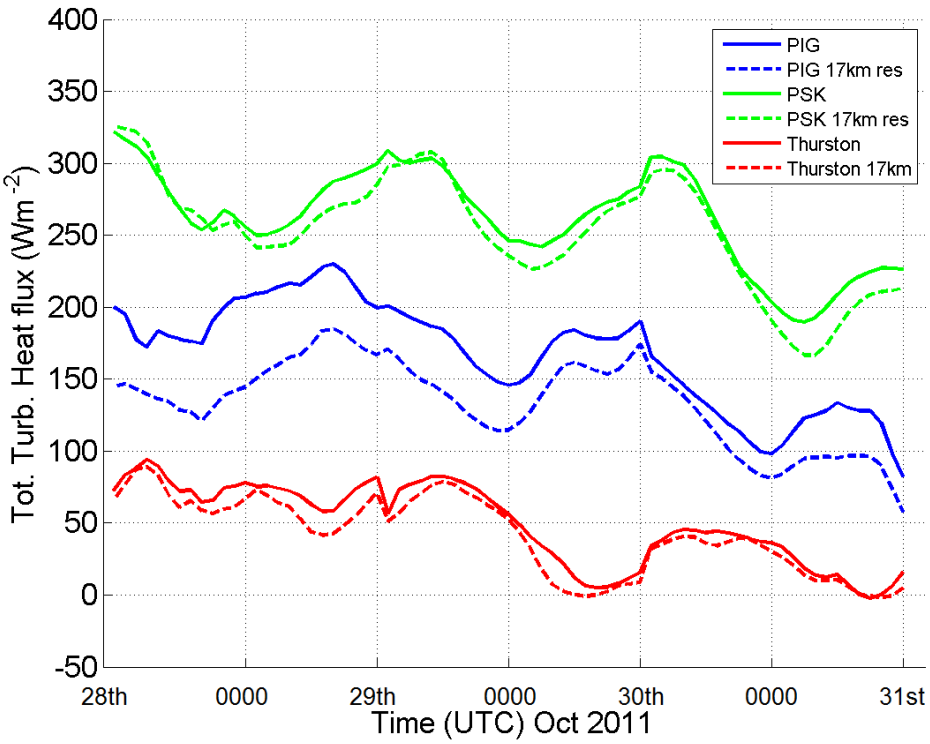

Figure 5.9: A time series of mean total turbulent heat flux within the coastal polynyas from 1200 UTC 28th October to 1200 UTC 31st October 2011. The dashed lines are the 17 km coarser resolution MetUM simulation, the solid lines are the high resolution MetUM simulation.

The time series of total turbulent heat flux in Fig. 5.9 shows that the largest heat

fluxes are observed over the PSK polynya, where sea ice concentration is lowest. In both the PSK and Thurston polynyas the two resolutions of the MetUM are in close agreement on the magnitude of the turbulent heat flux throughout the case study with relatively small differences of ~10-20 W m^{-2}. In the PIG polynya however, during the first half of the case study in particular, there is a difference of up to 60 W m^{-2}, with the higher resolution model giving larger heat fluxes. Over the 72 hours of the simulation the mean turbulent heat flux in the PIG polynya is 34 W m^{-2} (20%) larger in the high resolution simulation. This compares to mean differences of 9 W m^{-2} (4%) and 7 W m^{-2} (14%) within the PSK and Thurston polynyas respectively. When the turbulent heat flux is broken down into its latent and sensible heat components the difference between the two resolutions within the PIG polynya is largely driven by the sensible heat flux (not shown).

5.4.3 WHAT DRIVES THE HEAT FLUX DIFFERENCE IN PIG POLYNYA?

Here we investigate the significant difference in turbulent heat fluxes seen in the PIG polynya during the first half of the case study. As stated in chapter 2, model settings such as transfer coefficients and the surface roughness length are identical so it is likely that differences in near-surface meteorology are driving the difference in turbulent heat flux between the two resolutions of the model.

Fig. 5.10a shows the mean total turbulent heat flux from the high resolution model during the first half of the case study. In coastal regions of the PIG and PSK polynyas, where sea ice concentrations are lowest, the 36-hour mean total turbulent heat fluxes reach 300-400 W m^{-2}. These turbulent heat fluxes are comparable in magnitude to those seen over coastal polynyas in the Weddell Sea to the east of the Antarctic Peninsula (Renfrew et al., 2002; Fiedler et al., 2010). Fig. 5.10b reveals that over Thurston polynya the difference between the two resolutions is small, while in the PSK polynya there are some offsetting biases, with a region around 111°W where the high resolution MetUM has ~40 W m^{-2} larger heat fluxes. Within the PIG polynya, there is a consistent signal for larger heat fluxes in the high resolution simulation, particularly in the eastern and southern portion of the polynya. Mean total turbulent heat fluxes in these areas during the first half of the case study are 40-100 W m^{-2} larger in the high resolution simulation. Figs. 5.10d and 5.10f reveal that within

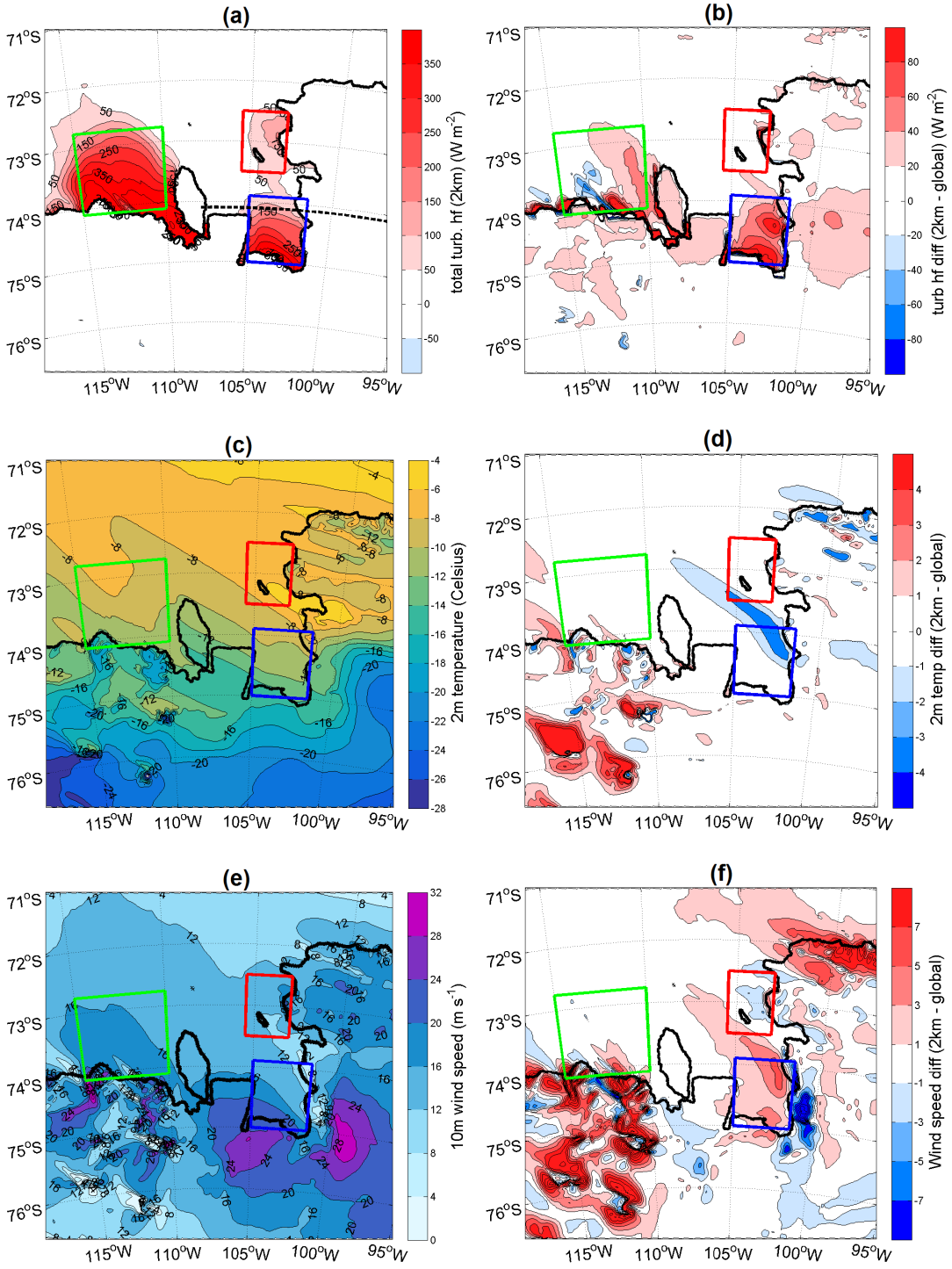

Figure 5.10: Modelled heat fluxes and near-surface variables for the high resolution model (left) and the difference between the high and coarse resolution models (right): a),b) total turbulent heat flux; c),d) 2-m temperature; e),f) 10-m wind speed. All panels show the mean over the first 36 hours of the case study. The black dashed line in Fig. 5.10a shows the location of the cross-section used in Figs. 5.11, 5.12, 5.13, 5.16 and 5.19.

the PIG polynya the high resolution simulation produces both cooler near-surface temperatures and stronger winds than the coarse resolution model. The 36-hour mean 2-m temperature in the northern part of the PIG polynya is 1 to 3°C cooler, in a northwest-southeast aligned band of colder air. The wind speed is widely $1-3\ m\ s^{-1}$ stronger, with an area close to the eastern shoreline where wind speeds are $5-9\ m\ s^{-1}$ higher in the high resolution simulation. The regions within the PIG polynya that have the largest temperature and wind speed differences match closely with areas where the difference in total turbulent heat flux is greatest, and are clearly responsible.

WHAT CAUSES THE STRONGER WINDS AND COLDER TEMPERATURES IN THE HIGH RESOLUTION SIMULATION?

Fig. 5.11 shows vertical cross-sections of the meridional component of the wind along 74.1°S (see black dashed line in Fig. 5.10a) from both the high (Fig. 5.11a) and coarse resolution simulations (Fig. 5.11b). Near the surface, over land, the meridional component of the wind is relatively light and slightly positive (southerly), with a reversal in direction aloft to give a light to moderate northerly component. At the coastline and over the PIG polynya there is a near-surface v-wind maximum approximately 50-200m above the surface. This southerly low-level jet is seen in both resolutions of the model however it is positioned slightly differently. In the coarser resolution model it is located on the western side of the PIG polynya with a maximum intensity of $\sim 16\ m\ s^{-1}$, in the high resolution model it is $\sim 1.5\ m\ s^{-1}$ weaker but it is broader, extending eastwards to the coastline along the eastern shoreline of the PIG polynya.

Fig. 5.12a shows the temperature difference between the two resolutions of the MetUM along the same cross-section and at the same time as in Fig. 5.11. The southerly jet that is located along the coastline in the high resolution simulation is advecting cold air northwards. Fig. 5.12a shows that the high resolution simulation has near-surface temperatures in the eastern half of the PIG polynya that are 3-5 °C colder than in the coarse resolution simulation. So along the eastern shoreline of the ASE the stronger southerly low-level jet is coincident with colder near-surface temperatures leading to larger turbulent heat fluxes in the high resolution simulation. At 0000 UTC 29th October (time of Fig. 5.11 and Fig. 5.12a) within the PIG polynya the high resolution simulation has a mean turbulent heat flux that is $62\ \mathrm{W\ m^{-2}}$ larger than

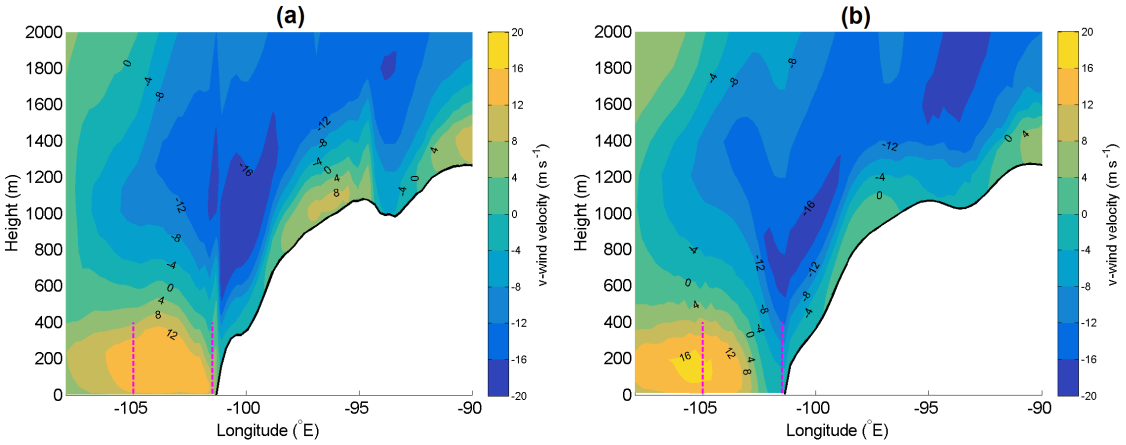

Figure 5.11: West to east cross sections of v-wind velocity along the latitude 74.1°S at 0000 UTC 29th October: a) high resolution, b) coarse resolution. The location of the cross-section is shown by the dashed black line in Fig. 5.10a. The dashed magenta lines mark the longitudinal extent of PIG polynya box.

the coarse resolution simulation.

The other panels of Fig. 5.12 show how the southerly low-level jet and temperature difference along the cross-section evolve over time. At 1200 UTC on 29th October (Fig. 5.12b) the jet is broader but remains in a similar position. The two resolutions of the MetUM are now in better agreement on the location of the jet, but the jet is 2 $m\ s^{-1}$ weaker in the high resolution model. The temperature difference between the two simulations is much reduced and confined to the very near coastal zone, and so the difference in total turbulent heat flux between the two resolutions has reduced to 32 W m^{-2}. Figs. 5.12c and 5.12d show the southerly jet has weakened below 11 $m\ s^{-1}$ and the near-surface temperature difference also weakens over time. By 1200 UTC 30th October (Fig. 5.12d) the mean turbulent heat flux within the PIG polynya is only 16 W m^{-2} larger in the high resolution model.

The wind speed cross-section in Fig. 5.13 shows that both of the MetUM simulations are picking up very strong, downslope winds upwind of the PIG polynya. These are predominantly easterly (downslope) winds. Then at the foot of the slope there is an abrupt hydraulic jump, a rapid deceleration of the wind speed coincident with strong vertical motion and upward tilting potential temperature isentropes (see Fig. A.7). This is consistent with other NWP studies of hydraulic jumps in Antarctica, which show vertical wind speeds of up to 1 $m\ s^{-1}$ and upward tilting isentropes, coincident with hydraulic jumps at or close to the base of a slope (Pettre and Andre,

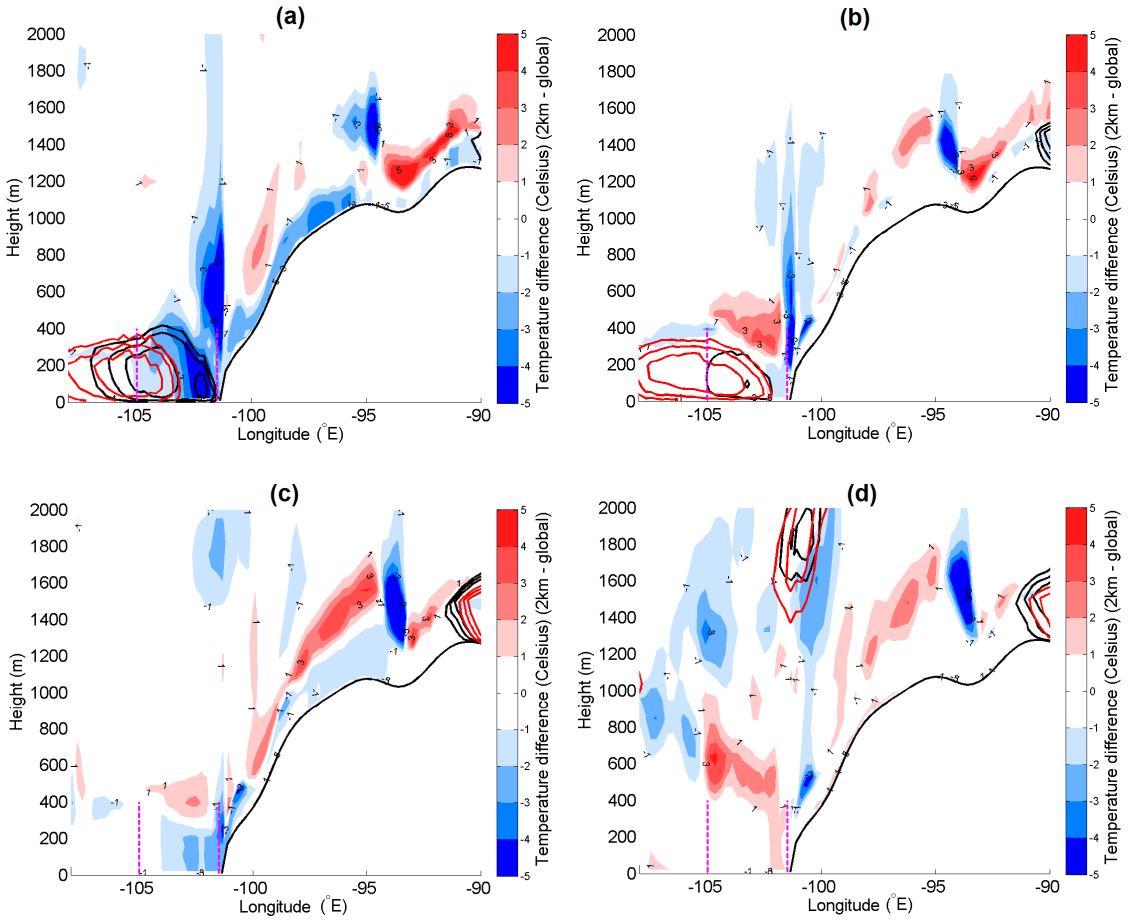

Figure 5.12: Cross-sections along 74.1°S showing the temperature difference between the two MetUM simulations (colour contours) at the following times: a) 0000 UTC 29th October; b) 1200 UTC 29th; c) 0000 UTC 30th; d) 1200 UTC 30th. The black lines are the 11, 13 and 15 m s^{-1} v-wind contours in the high resolution simulation, the red lines are the same contours in the coarser resolution simulation.

1991; Gallée and Pettré, 1998; Yu and Cai, 2006). In the high resolution simulation (Fig. 5.13a) the hydraulic jump is very sharp at the foot of the slope with a rapid deceleration of near-surface wind speed, which gradually increases again further west. In the coarser resolution simulation (Fig. 5.13b) the hydraulic jump is more diffuse and displaced to the west, perhaps due to the smoother model orography and lower grid resolution. This means that in the coarse resolution model the wind speed minimum downstream of the hydraulic jump is over the eastern half of the PIG polynya, with near-surface wind speeds of 12-16 $m\ s^{-1}$ compared to 16-20 $m\ s^{-1}$ in the higher resolution simulation. While Fig. 5.13 shows a single timestep this hydraulic jump was a coherent feature during the first 24-36 hours of the case study

and its representation is the root cause of the differing heat fluxes between the two resolutions of the MetUM. When the zonal wind speeds start to slacken during the second half of the case study (not shown) the hydraulic jump and southerly low-level jet are less pronounced in the cross-sections (Fig. A.8).

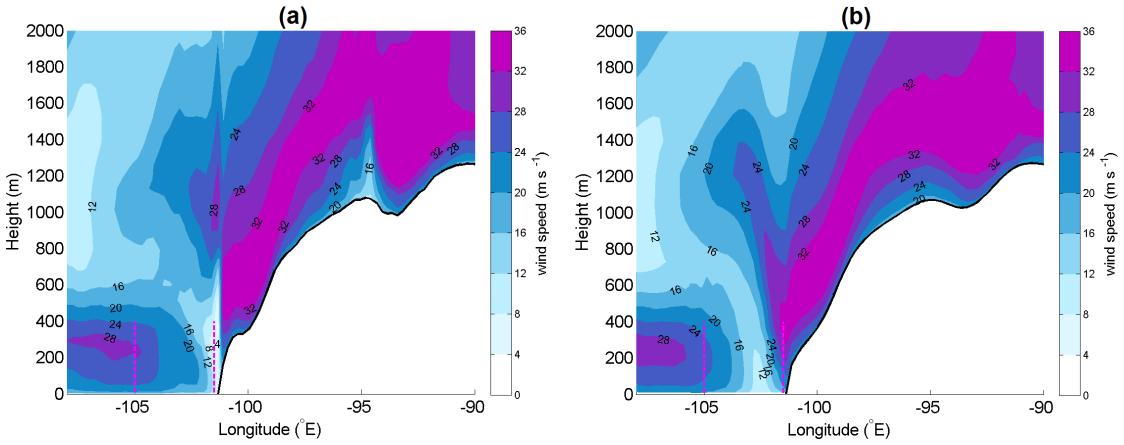

Figure 5.13: Wind speed cross-sections along the latitude 74.1°S at 0000 UTC 29th October: a) high resolution simulation; b) coarser resolution.

5.4.4 OCTOBER 2011 CASE STUDY SUMMARY

- Large sensible and latent heat fluxes are modelled in three coastal polynyas within the ASE. Mean total turbulent heat fluxes are up to 300-400 W m^{-2}, approximately an order of magnitude larger than the modelled turbulent heat fluxes in surrounding regions where the sea ice concentration is high.

- In two of the coastal polynyas (PSK and Thurston) the two resolutions of the MetUM are in good agreement on the magnitude of the turbulent heat fluxes, the coarse resolution mean turbulent heat fluxes were within 9 W m^{-2} (4%) (PSK) and 7 W m^{-2} (14%) (Thurston) of the high resolution simulation values.

- Over the PIG polynya box the high resolution simulation has colder air temperatures and higher wind speeds which drive larger turbulent heat fluxes. The mean turbulent heat flux within the PIG polynya is on average 34 W m^{-2} (20%) larger than in the coarse resolution simulation, with peak differences of over 60 W m^{-2}.

- The stronger winds and colder temperatures within the PIG polynya in the high resolution simulations are linked to a hydraulic jump at the foot of the slope and associated southerly low-level jet which are both located further east (at the foot of the slope), in the high resolution simulation. The coarse resolution simulation has a weaker and more diffuse hydraulic jump.

5.5 HIGH HEAT FLUX CASE STUDY 2: SEPT 2016

5.5.1 SYNOPTIC OVERVIEW

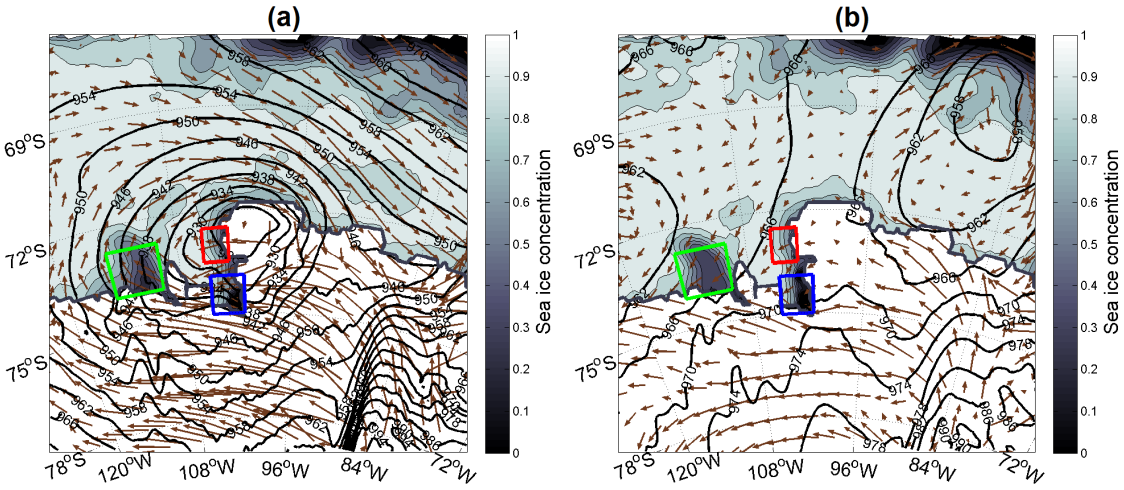

Figure 5.14: Mean sea level pressure, 10-m wind vectors and sea ice concentration from the MetUM 17km resolution simulation at: a) 0000 UTC 29th September 2016 and b) 0000 UTC 30th September 2016. For reference wind vector see Fig. 5.1.

At 0000 UTC 29th September 2016 (Fig. 5.14a) there was a deep depression with a central pressure of ~925 hPa located over Thurston Island. Associated with this simulation were gale or severe gale force winds, that affected the ASE during the period between 0600 UTC 28th September and 1500 UTC 29th September. The OSTIA data shows coastal polynyas opening along the eastern shoreline of the ASE with the sea ice concentration reduced to near zero within Pine Island Bay. There is also a significant reduction in sea ice further west in the PSK polynya. This is corroborated by MODIS visible satellite imagery which shows a large area of open water along the eastern shore of the ASE and within the PSK polynya on 30th September 2016 (see Fig. 1.9). By 0000 UTC 30th September (Fig. 5.14b) the depression has moved away to the west and the winds are significantly lighter over the region of interest, though the polynyas remain open. The maximum wind speed recorded during this case study was 45 $m\ s^{-1}$ (~101 mph) at Bear Peninsula AWS. Further east at Evans Knoll AWS winds are slightly less severe with a maximum speed of 37 $m\ s^{-1}$ (~83 mph).

The MetUM is validated against the available AWS data. At Evans Knoll both resolutions of the model accurately capture the magnitude of the peak wind speed,

although the model wind speed didn't peak until 3 to 4 hours after the observations. At Bear Peninsula both resolutions of the MetUM underestimate the peak wind speed by 15 $m\ s^{-1}$. The coarse resolution model in particular seems to struggle to reproduce the highest observed wind speeds (> 30 $m\ s^{-1}$) at Bear Peninsula. The near-surface temperature biases are similar to those seen in the October 2011 case study, with both resolutions of the model slightly colder than the observations. Overall the case verified reasonably well.

5.5.2 TURBULENT HEAT FLUXES

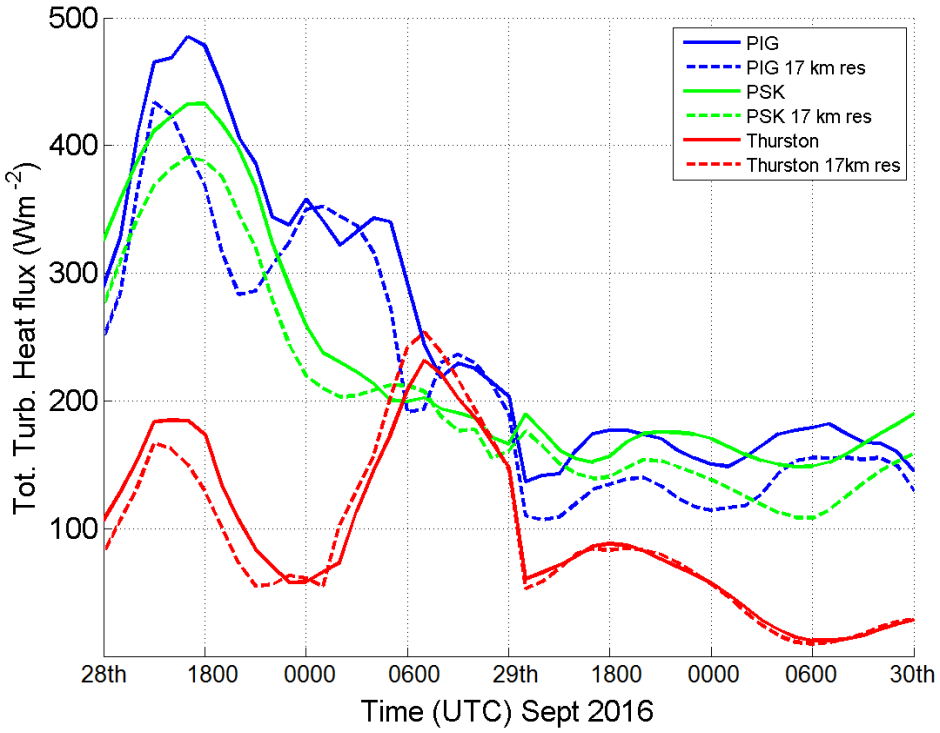

Figure 5.15: A time series of mean total turbulent heat flux within the coastal polynyas from 1200 UTC 28th September to 1200 UTC 30th September 2016. The dashed lines show the 17 km resolution MetUM simulation, the solid lines show the high resolution MetUM simulation.

The 48 hour mean total turbulent heat flux in coastal parts of the PIG polynya exceed 400 W m^{-2}, indeed 48 hour mean heat fluxes of 200-300 W m^{-2} were recorded quite widely within both the PIG and PSK polynyas. Within the regions of high sea ice concentration in the central Amundsen Sea (between the three polynyas) the mean turbulent heat flux was less than 40 W m^{-2}. The modelled mean wind speed values over the three coastal polynyas are ~10-14 $m\ s^{-1}$. In the same areas mean

2-m air temperatures are -10 to -14 °C, giving a large air-sea temperature deficit. The combination of the strong winds, open water, and large ocean-atmosphere temperature gradients are causing the very large turbulent heat fluxes in this case study.

Fig. 5.15 shows the time series of total turbulent heat flux within the three ASE coastal polynya boxes. In the PSK and PIG polynyas there are very large (up to 500 W m^{-2}) heat fluxes during the first 24 hours of the case study. these coincide with the strongest wind speeds. Later the cyclone moves westwards and the wind speed and turbulent heat fluxes reduce. In Thurston polynya there are two distinct peaks during the first half of the case study. The trough between them corresponds to the time period when the low pressure centre moved across the polynya bringing a spell of lighter winds and smaller turbulent heat fluxes (see Fig. 5.14a). The Thurston polynya mean wind speed dropped below 5 $m\ s^{-1}$ at 0000 UTC 29th September when the centre of the cyclone crossed the polynya.

In both the PSK and PIG polynyas, Fig. 5.15 shows that the high resolution simulation produces larger heat fluxes for the majority of the case study. In the PIG polynya this difference is particularly marked in the first 12 hours of the case study where differences of up to 100 W m^{-2} are simulated at 1800 UTC 28th September. In the PSK polynya the high resolution simulation produces turbulent heat fluxes that are 20-30 W m^{-2} larger than the coarse resolution model for much of the 48 hour case study. In the PIG and PSK polynyas the high resolution simulation produces 48 hour mean heat fluxes that are 35 W m^{-2} (14%) (PIG) and 27 W m^{-2} (12%) (PSK) larger than the coarse resolution model. In the Thurston polynya the two resolutions of the model are in good agreement on the magnitude of heat fluxes for much of the case study and as such the mean difference between the two resolutions of the model is just 3 W m^{-2} (3%).

5.5.3 PIG POLYNYA AND THE HYDRAULIC JUMP

Fig. 5.16 uses a combination of cross-sections and map plots to examine what is happening within the PIG polynya during the first 12 hours of the case study. We investigate why there is a sudden switch from much larger modelled turbulent fluxes in the high resolution simulation, to a situation where the two models produce

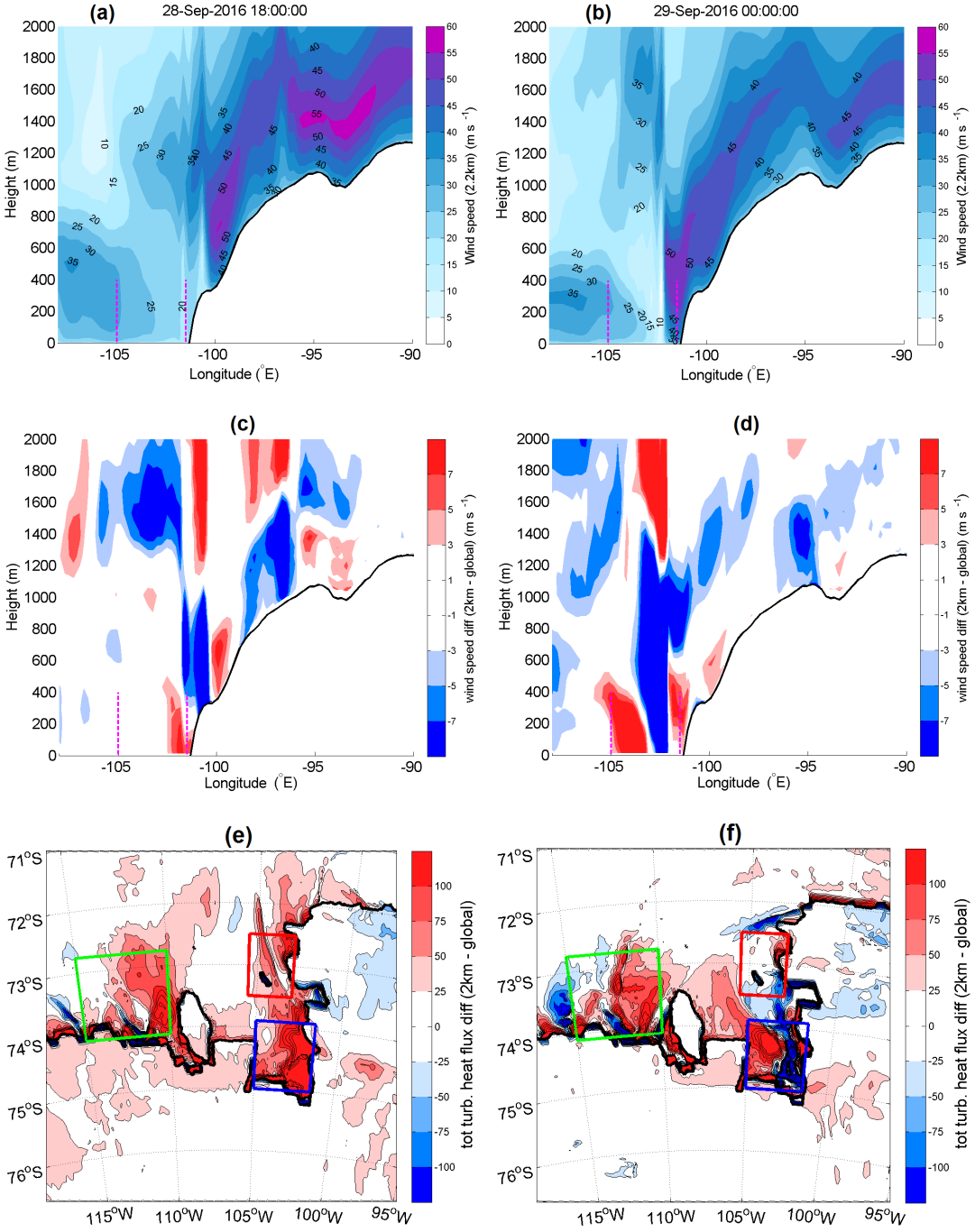

Figure 5.16: (a) high resolution wind speed cross-section along 74.1°S at 1800 UTC 28th September 2016; (b) high resolution wind speed cross-section along 74.1°S at 0000 UTC 29th September; (c) wind speed difference cross-section (2.2 km - 17 km) at 1800 UTC 28th; (d) wind speed difference cross-section at 0000 UTC 29th; (e) turbulent heat flux difference map plot at 1800 UTC 28th; (f) turbulent heat flux difference map plot at 0000 UTC 29th.

approximately the same PIG polynya mean fluxes (see Fig. 5.15). In Figs. 5.16a and 5.16b, it is clear that there is a hydraulic jump in the wind speed profile towards the foot of the slope of the Hudson Mountains. The wind accelerates as it travels

down the slope, broadly in a east to west direction, then towards the base of the slope it decelerates rapidly.

At 1800 UTC 28th September (Fig. 5.16a) the hydraulic jump is located slightly landward of the coastline at 100°W and the near-surface wind speed decelerates from 45 $m\ s^{-1}$ to 20 $m\ s^{-1}$ over a short horizontal distance. As in the October 2011 case study the coarse resolution simulation places the hydraulic jump slightly further westwards and it is less abrupt (not shown). This creates the wind speed difference pattern seen in Fig. 5.16c where the high resolution simulation has stronger winds in the peak downslope flow, then weaker winds where it places the hydraulic jump, but then stronger winds again further downstream (westwards) over the eastern part of the PIG polynya box, where the coarser resolution model is placing the hydraulic jump. At 1800 UTC 28th September Fig. 5.16e shows the impact that this has on the modelled heat fluxes. Downstream of the hydraulic jump at 1800 UTC 28th September is the eastern side of the ASE. Here there is a large reduction in sea ice cover, and the stronger winds in the high resolution simulation drive turbulent fluxes that are more than 100 W m^{-2} larger than in the coarser resolution simulation.

At 0000 UTC 29th September (6 hours later) the hydraulic jump is still seen in Fig. 5.16b, but crucially its location has shifted downslope to the seaward side of the coastline. The hydraulic jump is again more abrupt in the high resolution model. Fig. 5.16d shows that the pattern of the wind speed difference remains the same as previously. Where the high resolution model has the abrupt hydraulic jump and surface wind speed minima it has lower near-surface wind speed values than the coarse resolution model. Whereas further west, where the coarse resolution model is showing the surface wind speed minima the high resolution simulation has higher wind speeds. Fig. 5.16f shows the impact this shift in location has on the turbulent heat fluxes within PIG polynya. The high resolution model now has smaller turbulent heat fluxes along the eastern side of the PIG polynya but west of the hydraulic jump it has larger heat fluxes. Overall the positive and negative heat flux differences largely balance, and at 0000 UTC the high resolution PIG polynya mean turbulent heat flux is 8 W m^{-2} larger than the coarse resolution simulation. It is therefore the change in location of the hydraulic jump that causes the shift from larger heat fluxes in the high resolution simulation prior to 0000 UTC 29th September, to roughly equal PIG polynya mean heat fluxes (but with large differences on both the east and west side of

the hydraulic jump) between 0000 and 0600 UTC 29th September.

It is worth noting that later in the case study there are lighter winds over and upstream of the PIG polynya. The hydraulic jump is no longer present and the turbulent heat fluxes within the PIG polynya are more similar in the two resolutions of the MetUM. This increased agreement is not caused by large differences offsetting one another (e.g. see Fig. 5.16f) but rather through the differences being small across much of the PIG polynya.

5.5.4 PSK POLYNYA TURBULENT HEAT FLUX DIFFERENCES

Further west in PSK polynya there is no evidence of similar orographic features. Rather there is a tendency for the high resolution simulation to have slightly cooler near-surface temperatures and stronger wind speeds in the eastern half of PSK polynya and this drives the 27 W m^{-2} (12%) larger mean turbulent heat fluxes in the high resolution model (see Figs. 5.16e and 5.16f). The temperature and wind speed differences are particularly apparent during the first half of the case study when the wind speed was at its strongest. Map plots (not shown) indicate the high resolution simulation has modelled near-surface wind speeds in the eastern half of PSK polynya that exceed 20 $m\ s^{-1}$ at this time, i.e. this is another indication that the difference between the two model resolutions is most apparent when the wind speed is stronger.

5.5.5 SEPTEMBER 2016 CASE STUDY SUMMARY

- Within the PSK and PIG coastal polynyas the high resolution simulation is shown to have mean turbulent heat fluxes that are 27 W m^{-2} (12%) and 35 W m^{-2} (15%) larger than the coarser resolution simulation. Over Thurston polynya the two resolutions of the model show close agreement on near-surface winds, temperatures and the turbulent heat fluxes.

- In the PIG polynya the location of a hydraulic jump is shown to play an important role in determining the magnitude of the heat flux difference between the two simulations. In the early part of the case study the hydraulic jump is 400 m above sea level up the slope and the high resolution simulation has much larger turbulent heat fluxes over the polynya, similar to what was

seen in the October 2011 case study. However, when the hydraulic jump shifts downslope and offshore a pattern develops with the high resolution model having smaller turbulent heat fluxes at the location of the hydraulic jump in the eastern portion of the PIG polynya and larger fluxes west of the hydraulic jump. These differences largely balance to give a much smaller overall difference between the two model resolutions. Nevertheless, the difference in the location and magnitude of the heat fluxes could have a significant impact on the distribution of ocean mixed layer depth and salinity, thus potentially impacting the ocean circulation and basal melt rates.

- When the wind speeds become more moderate later in the case study the two resolutions of the model are in better agreement on the magnitude of the heat fluxes within the three coastal polynyas.

5.6 HIGH HEAT FLUX CASE STUDY 3: AUG 2012

5.6.1 SYNOPTIC OVERVIEW

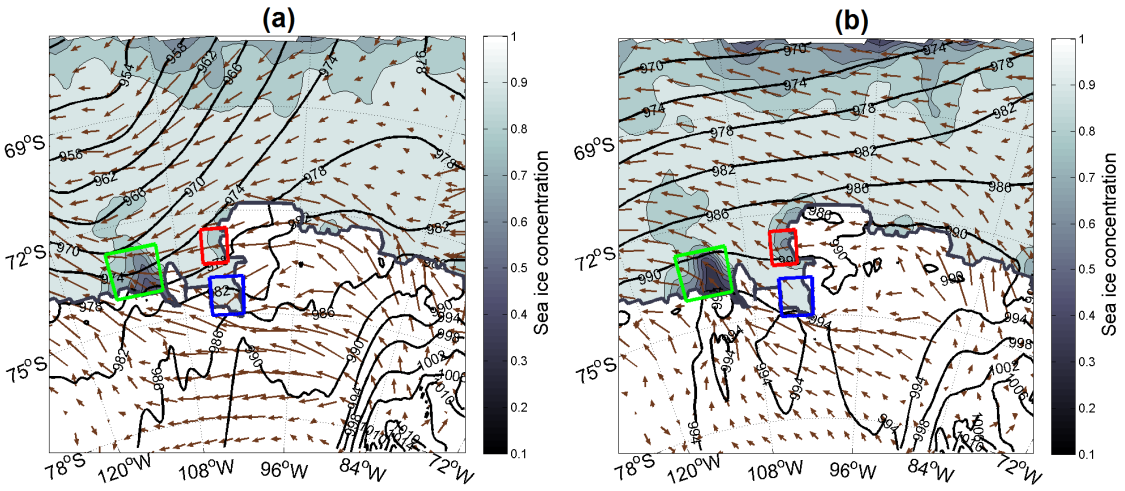

Figure 5.17: Mean sea level pressure, 10-m wind vectors and sea ice concentration from the MetUM 17 km resolution simulation at: a) 1200 UTC 28th August 2012 and b) 1200 UTC 29th August 2012. For reference wind vector see Fig. 5.1.

Fig. 5.17a shows a relatively strong pressure gradient across the ASE with easterly winds across the region. An area of low pressure to the northwest of the ASE is dominating the pressure pattern and as this starts to weaken the winds begin to drop and turn to being southeasterly across the coastal polynyas (Fig. 5.17b). This case study is slightly different to the previous high heat flux cases as there is no deep area of low pressure crossing the ASE, rather this is a sustained spell of moderate to strong easterly winds. As such the observed wind speeds are lower, with 15 $m\ s^{-1}$ maxima at Evans Knoll and Thurston Island AWS. Further west, at Bear Peninsula AWS, in the early part of the case study maximum wind speeds reach 28 $m\ s^{-1}$, but quickly drop to $10-15\ m\ s^{-1}$ and then drop away further in the second half of the case study. The sea ice data shows that while there is a reduction in sea ice within the three polynyas it is not as widespread or as dramatic as in the two previous case studies (compare Fig. 5.17 to Figs. 5.7 and 5.14) and as such the mean turbulent heat fluxes are not as large.

Comparison with the AWS observations reveals that both resolutions of the MetUM produce near-surface air temperatures that are colder than observed,

particularly when the wind speeds become lighter on the 29th and 30th August. The mean temperature bias compared to AWS observations is -2.3 °C in the high resolution model and -4.8 °C in the coarse resolution simulation, the high resolution MetUM has a smaller temperature bias at all three AWS sites. The high resolution simulation also does a good job of reproducing the observed wind speed time series but the coarse resolution simulation underestimates the observed wind speed by an average of $1.5 - 4.5\ m\ s^{-1}$ at the AWS sites (see Fig. A.9).

5.6.2 TURBULENT HEAT FLUXES

Within all three of the coastal polynya areas the turbulent heat fluxes are weaker than in the previous two case studies (Fig. 5.18). This is largely caused by the higher sea ice concentrations in the model but also due to the lighter winds. In this case study it is possible to see a large change in the polynya mean turbulent heat flux at the boundary between the two MetUM simulations; this is due to the use of the 29th August 2012 sea ice concentration field in the second MetUM simulation. Time series plots show this abrupt change is largely due to a reduction in the OSTIA mean sea ice concentration within the three polynyas rather than step changes in near-surface fields such as 10-m wind speed and 2-m temperature. The reduction in sea ice concentration is likely due to the strong easterly winds during the first half of the case study transporting more sea ice away from the coastline.

In Thurston polynya (red line) the coarser resolution model has larger turbulent heat fluxes for much of the case study, but generally the two resolutions of the MetUM are in good agreement (Fig. 5.18). In the PSK polynya (green line) the turbulent fluxes are much larger than in the other two polynyas, this is because there is a more widespread loss of sea ice here (see Fig. 5.17). The high resolution model has 10-30 W m^{-2} larger heat fluxes in the first 12 hours of the case study, when the wind speeds are strongest, but after this the two resolutions of the model are in good agreement. In the PIG polynya the story is different from that seen in the previous high heat flux case studies. While for the first ~12 hours of the case study the high resolution model does have larger turbulent heat fluxes by 20-40 W m^{-2}, for the remaining 36 hours of the case study the two resolutions of the model are in good agreement with only a 5-10 W m^{-2} difference between the two resolutions of the

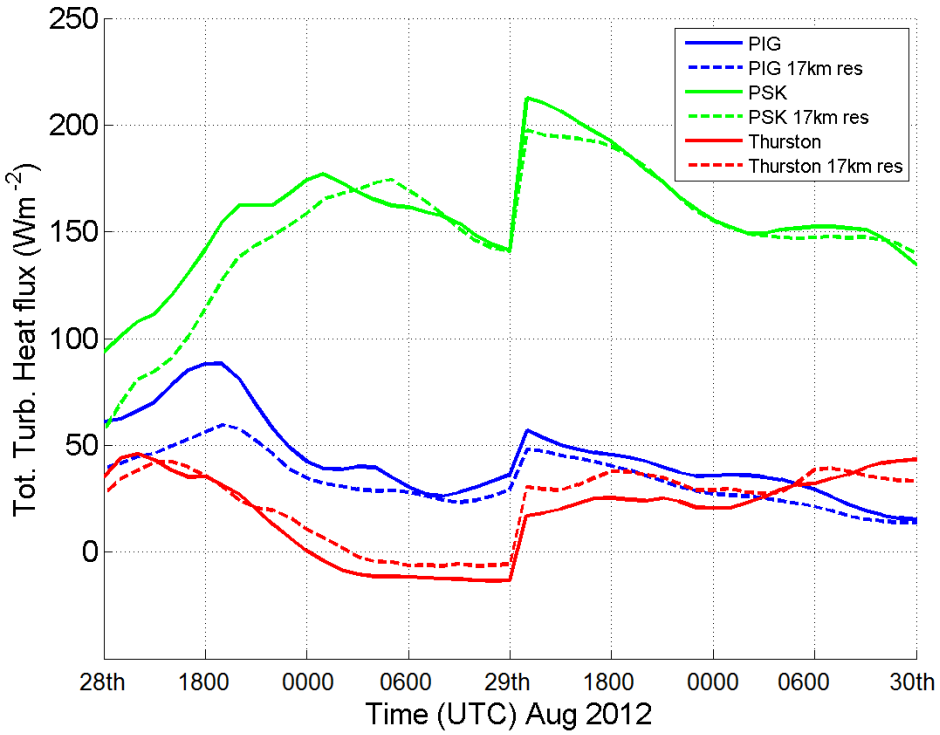

Figure 5.18: A time series of mean total turbulent heat flux within the coastal polynyas from 1200 UTC 28th August to 1200 UTC 30th August 2012. The dashed lines show the 17 km MetUM simulation, the solid lines show the high resolution MetUM simulation.

model. Within the PIG polynya the high resolution simulation has a mean turbulent heat flux that is 10 W m^{-2} (23%) larger than the coarse resolution simulation. Within the Thurston and PSK polynyas the mean turbulent heat flux differences are 4 W m^{-2} (20%) and 7 W m^{-2} (4%) respectively, in the case of Thurston polynya it is the coarse resolution simulation that has the larger total turbulent heat fluxes.

5.6.3 CROSS-SECTIONS

While for the majority of the case study the two resolutions of the model are in good agreement on the magnitude of turbulent heat fluxes within PIG polynya, it is important to understand what is occurring between 1200 UTC 28th August and 0000 UTC 29th August. The cross-section in Fig. 5.19a reveals that at 1500 UTC on 28th August there is a hydraulic jump at the base of the slope. Fig. 5.19b shows that there are stronger near-surface winds in the high resolution model in the western half of PIG polynya (but weaker winds very close to the coastline). The temperature cross-section in Fig. 5.19c shows the near-surface air warming as it travels downslope

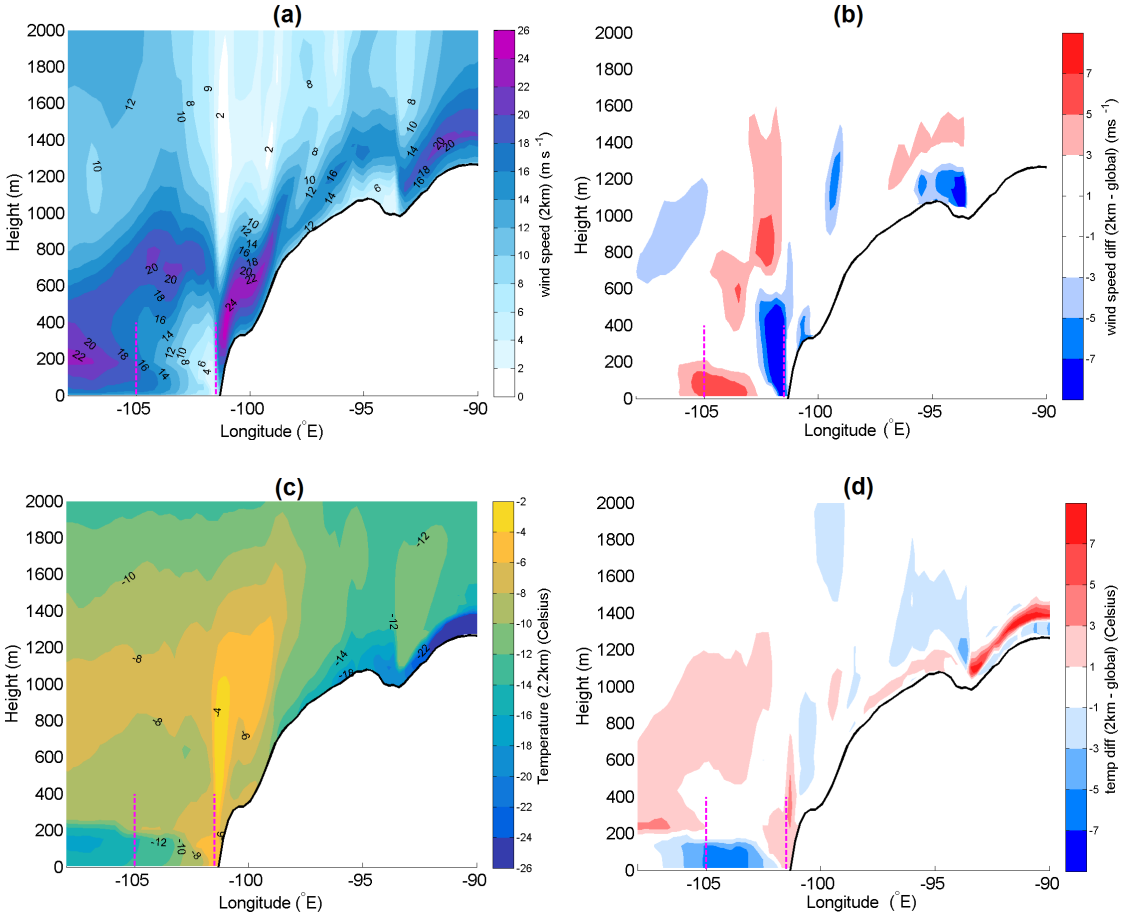

Figure 5.19: Cross-sections plots along 74.1°S at 1500 UTC on 28th August: (a) high resolution simulation wind speed, (b) wind speed difference (2.2 km - 17 km), (c) high res. temperature, (d) temperature difference (2.2 km - 17 km).

then cooling west of the coastline as it travels over broken sea ice. Fig. 5.19d reveals that along with the stronger wind speeds in the western half of PIG polynya the high resolution model also has cooler temperatures. This causes turbulent heat fluxes to be 40-60 W m^{-2} larger than in the coarse resolution model in the northwestern part of the polynya (not shown). Later in this case study the wind speeds become much lighter and the hydraulic jump at the foot of the slope is no longer seen in the models. Even by 0000 UTC on 29th August the near-surface wind speed difference over PIG polynya has reduced to only $1-3\ m\ s^{-1}$ (see Fig. A.10).

5.6.4 AUGUST 2012 CASE STUDY SUMMARY

- The heat fluxes in this case study are lower than in the previous two cases due to both lighter winds and there being less reduction of sea ice within the coastal polynyas.
- In this case study there is less of difference between the modelled heat fluxes in the two MetUM simulations. Largely there is good agreement within all three coastal polynya boxes
- Between 1200 UTC 28th August and 0000 UTC 29th August within PIG polynya there are larger heat fluxes in the high resolution model. Cross-sections reveal that once again it is how the MetUM simulates a hydraulic jump at the base of the slope that is driving the difference in heat fluxes. It must be noted that in this case study this feature only persists for a short time period.

5.7 DISCUSSION

5.7.1 IS A HIGH RESOLUTION ATMOSPHERIC MODEL REQUIRED TO ACCURATELY CAPTURE HIGH HEAT FLUX EVENTS IN THE ASE?

In the control case study when wind speeds were light, the two resolutions of the MetUM were in good agreement on the magnitude of turbulent heat fluxes within the ASE (see Fig. 5.6b). Furthermore, in the three high heat flux case studies, during lighter wind periods there is usually only a small difference between the heat fluxes produced by the two resolutions of the model (as illustrated in Fig. 5.20). However, particularly within PIG and to a lesser extent PSK polynas, during the three high heat flux case studies the high resolution MetUM produces turbulent fluxes that are 10-25% larger than the coarse resolution simulation. Fig. 5.20 shows that this difference between the two resolutions of the MetUM is linked to the strength of the wind. When the wind speed is stronger there is often a larger difference between the PIG polynya mean heat flux for the two resolutions of the MetUM. Fig. 5.20c shows that PIG polynya mean turbulent heat flux differences can exceed 100 W m^{-2}. Fig. 5.21 shows that in the other two coastal polynya boxes the same relationship between wind speed and turbulent heat flux difference is much less apparent, the stronger wind speeds do not seem to be associated with larger differences between the two resolutions of the MetUM.

While the heat fluxes are larger in the high resolution simulation, we cannot automatically assume that this model is more accurately capturing the event. There is evidence, via a comparison with the available meteorological observations, that suggests the high resolution model contains smaller temperature and wind speed biases. In comparison with AWS data it was shown that both resolutions of the MetUM are colder than observed for most of the case studies (e.g. Fig. 5.2). For example in the August 2012 case study the 2-m air temperatures were on average 2.34 °C and 5.83 °C colder than AWS observations for the high and coarse resolution simulations respectively. The high resolution model also does a better job of reproducing the AWS peak wind speeds associated with the case studies. This is in good agreement with the results of Orr et al. (2014), where it was shown that during a strong wind event in East Antarctica a higher horizontal resolution of the MetUM

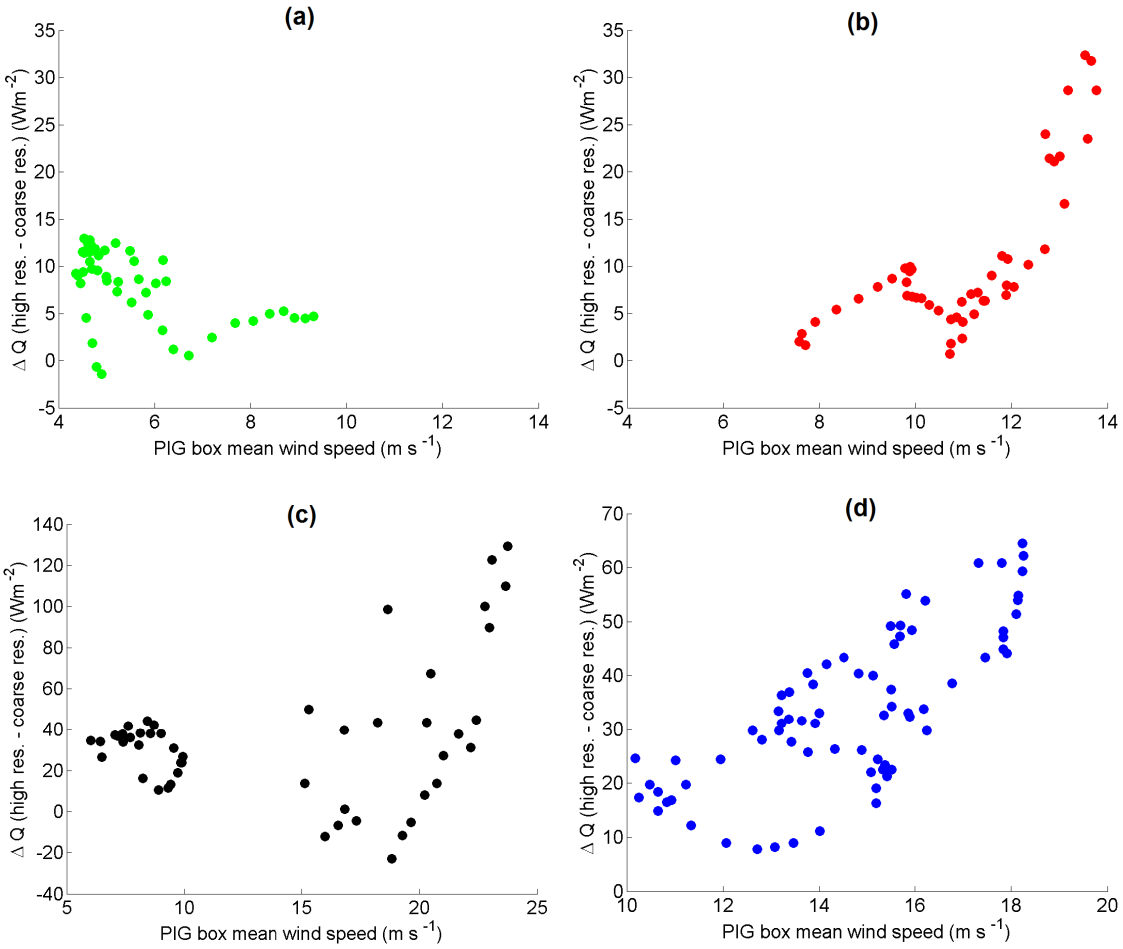

Figure 5.20: Scatter plots showing the relationship between the modelled high resolution MetUM wind speed within PIG polynya and the difference between the PIG polynya mean turbulent heat fluxes produced by the two resolutions of the MetUM: (a) 18th February 2014 case study, (b) 30th August 2012, (c) 28th September 2016, (d) 28th October 2011. Each point is one time. Note the change in axes for c) and d).

more accurately captured the peak wind speed (but still slightly underestimated it compared to observations).

Figs. 5.12 and 5.16 demonstrated that when features such as hydraulic jumps and low-level jets occur this often causes a divergence in the modelled heat fluxes over PIG polynya. These features are generated through interactions with the surrounding complex orography and the coastline. Both idealised models (Renfrew, 2004; Yu and Cai, 2006) and observations (Pettre and Andre, 1991; Renfrew and Anderson, 2006) have shown that a hydraulic jump at the foot of a slope such as the one seen in Fig. 5.16 can occur in coastal regions of Antarctica. The hydraulic jump at the base of a slope is sharp because there is a rapid transition from a supercritical to a sub-

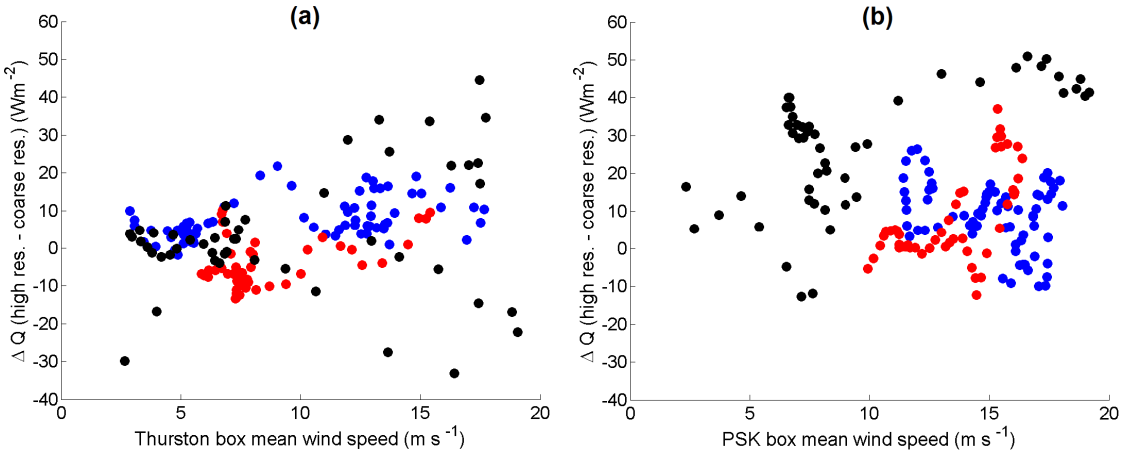

Figure 5.21: The relationship between the modelled wind speed and the difference between the turbulent heat fluxes in the two resolutions of the MetUM in a) Thurston polynya and b) PSK polynya. The red series shows the August 2012 case study, the black series September 2016 and the blue series October 2011.

critical flow at the base of the slope where cold air tends to pool (Renfrew, 2004). As the downslope flow decelerates there is a coincident increase in vertical motion, by continuity constraints, (Gallée and Pettré, 1998; Renfrew and Anderson, 2006; Yu and Cai, 2006), this was also seen in our MetUM case studies (see Fig. A.7). Previous work indicates that high resolution modelling is required to accurately position and capture these orographic features (Yu and Cai, 2006), which implies our coarse resolution model is not properly capturing these events.

Low-level jets have previously been observed in this region (see the work of chapter 3) and it was found they were often too weak or even absent in coarse resolution reanalysis products (Jones et al., 2016). Through moving to a higher resolution of Polar WRF (15km) it has been found that a better representation of Antarctic coastal winds is achieved (Bromwich et al., 2013b), suggesting that a high resolution model is needed to accurately capture the complex features we see in our case studies. Mathiot et al. (2012) also show that by using a downscaled, higher resolution atmospheric model the downslope winds around the Ross Sea are better represented. Using higher resolution atmospheric forcing produces a more accurate representation of coastal polynyas when coupled with sea ice models (Mathiot et al., 2012; Hollands et al., 2013). By moving from a coarse resolution reanalysis product to a higher resolution NWP product there is an increase in the mean wind speed in coastal parts of Antarctica (including the ASE), which is attributed to the high

resolution model more accurately predicting interactions with the underlying terrain (Dinniman et al., 2015).

For the MetUM it has been shown that when modelling a strong wind event in East Antarctica an increase in horizontal resolution from 12 km to 4 km or 1.5 km leads to more accurately capturing the interaction of strong winds with the coastline (Orr et al., 2014). For example, the high resolution simulations better represent barrier flows and downslope winds (Orr et al., 2014). Furthermore, work investigating foehn winds over the Antarctic Peninsular has shown that 1.5 km and 4 km resolution MetUM simulations have increased fidelity (over the 12 km and global simulations) with aircraft observations of these complex orographic flows (Elvidge et al., 2015, 2016; Elvidge and Renfrew, 2016).

The processes occurring close to coastlines represent a major challenge for weather and climate models given the high horizontal resolution required to capture them. However there is growing evidence to suggest that around Antarctica, near coastal processes local to glaciers and ice shelves may be important in determining ice shelf and glacier melt rate variability (Padman et al., 2012; Khazendar et al., 2013; Gwyther et al., 2014; St-Laurent et al., 2015). St-Laurent et al. (2015) have used a model to examine the impact of coastal polynyas in the eastern ASE (similar to those examined in our case studies) on the temperature of ocean water within the ice shelf cavity of PIG. Their results show that in years when the cooling within coastal polynyas is large the water temperature within the ice shelf cavity cools by up to 0.3 °C and is associated with a reduction in the modelled basal melt rate of the glacier (St-Laurent et al., 2015). Jenkins et al. (2016) provide support for this, showing that strong easterly winds close to PIG and the associated formation of coastal polynyas lead to cooler observed ocean temperatures. The ocean model in St-Laurent et al. (2015) was forced by winds from the Antarctic Mesoscale Prediction System model with a horizontal resolution of 10-20 km (St-Laurent et al., 2015). Our results indicate that by moving to a higher resolution atmospheric model the local cooling within the coastal polynyas would have been even larger and may have caused a greater reduction in the modelled ice shelf melt rate.

The evidence presented here suggests that the two resolutions of the MetUM are in good agreement during the control case study and more generally when wind speeds are relatively light. However, when the wind speed is stronger and we

see complex orographic flows and a hydraulic jump close to the base of the slope, evidence from both our comparison with available observations and research efforts around Antarctica suggest the high resolution model is more accurately capturing these features. Further, these atmospheric phenomena are important not only for determining the magnitude of heat fluxes within coastal polynyas but also for opening and maintaining the area of open water. In short, we present evidence that a high resolution atmospheric model is required to accurately capture these events.

5.7.2 WHAT IMPACT WILL USING A HIGHER RESOLUTION ATMOSPHERIC FORCING HAVE ON OCEAN MODELLING STUDIES IN THE ASE?

The heat fluxes within coastal polynyas are typically one to two orders of magnitude larger than through surrounding sea ice (Renfrew et al., 2002) (see Fig. 5.10a). The work of this chapter shows that when using a coarse resolution atmospheric model to force ocean models within the ASE it is likely the heat loss to the atmosphere will be underestimated. Table 5.1 shows that in the case studies we have investigated the heat fluxes close to Pine Island ice shelf may be up to between 10% and 25% larger when using a high resolution model. Webber et al. (2017) (their Fig. 5) show an example of how the observed ocean conditions in the ASE respond to increased atmospheric heat loss. There is deeper layer of colder, saltier water and a reduction in the ocean heat content to a depth of 400-700m.

Nakayama et al. (2014) show that when using an atmospheric model that drives larger ocean-atmosphere heat fluxes (due to lower surface air temperatures) there is an increase in the modelled ocean mixed layer depth (layer of cold, salty water). This deeper layer of cold, salty water reduces the volume of warm water transported on to the ASE continental shelf and as such, less warm water is transported towards the ice shelves and glaciers of the ASE (Nakayama et al., 2014). Dinniman et al. (2015) also show that higher resolution atmospheric forcing produces stronger winds in the ASE and a greater volume of cold water on the continental shelf. In their model however, the larger temperature contrast between the off-shelf and on-shelf water masses drives a larger advection of relatively warm circumpolar deep water on to the continental shelf and an associated increase in basal melt rate (Dinniman et al., 2015). Linking this to our results, the high resolution atmospheric model is both colder and

Table 5.1: The model mean and difference between the two resolutions of the MetUM for total turbulent heat flux (THF) in W m^{-2} within the coastal polynyas for each of the four case stuides.

	Mean THF (17 km)	Mean THF (2.2 km)	Diff. THF	**% Diff**
18th Feb 2014 control case study				
PIG	117	124	7	**6%**
PSK	158	157	-1	**-0.5%**
Thurston	87	95	8	**8%**
28th October 2011 high heat flux case study				
PIG	133	167	34	**20%**
PSK	253	262	9	**3.5%**
Thurston	42	49	7	**14%**
28th September 2016 high heat flux case study				
PIG	218	253	35	**14%**
PSK	202	229	27	**12%**
Thurston	94	97	3	**3%**
30th August 2012 high heat flux case study				
PIG	34	44	10	**23%**
PSK	150	157	7	**4%**
Thurston	23	19	-4	**-20%**

somewhat windier over coastal polynyas (see e.g. Figs. 5.10d, 5.10f) during high heat flux events. Using this high resolution atmosphere would drive a deepening of the cold winter water layer. Observational evidence from Christianson et al. (2016) would suggest the increased volume of cold water contributes to a slight decrease in basal melt rates of PIG. However modelling work suggests it is not yet clear whether this would result in an increase (Dinniman et al., 2015) or decrease (Timmermann et al., 2012; Nakayama et al., 2014) in the amount of warm circumpolar deep water being transported towards the ASE ice shelves

Another important difference between the two MetUM simulations is the wind speed and direction near the coastline. Fig. 5.11 highlighted the increased southerly component of the wind at the coastline in the high resolution model, altering the near-surface wind direction to a southeasterly (high resolution model) rather than an easterly (coarser resolution model), and increasing the wind speed. The surface wind stress in coastal regions will therefore be different in the two MetUM simulations. Webber et al. (2017) show there is a weak correlation between the surface wind stress and ocean currents in Pine Island Bay. Our results therefore indicate that

by using a high resolution atmospheric forcing product ocean models will have a different (and likely more accurate) simulation of the ocean circulation pattern close to PIG. Similarly, in the Ross Sea it has been shown that by using a higher resolution atmospheric forcing the wind stress pattern prescribed to an ocean model is changed and this gives a more realistic polynya extent and duration in Terra Nova Bay (Mathiot et al., 2012). Furthermore, Padman et al. (2012) conclude that in order to accurately resolve coastal ocean downwelling, an important process in determining the melt rate of Wilkins ice shelf, it is necessary to use high resolution atmospheric forcing that captures the wind stress variability that is induced by coastal topography.

5.8 CONCLUSIONS

This chapter has aimed to characterise the synoptic conditions associated with large heat flux events in the ASE and to investigate whether a high resolution atmospheric model is required to accurately capture such events. It is found that strong easterly and southeasterly winds associated with cyclones located to the north and northeast of the ASE are the typical conditions associated with high heat flux events. The continentally sourced winds are typically both cold and dry, leading to the large ocean to atmosphere heat fluxes.

Using the MetUM we investigated whether a move towards high resolution atmospheric models is required to adequately capture high heat flux events. A summertime control case study showed that when wind speeds are light the two MetUM simulations are in good agreement on the magnitude of ocean to atmosphere heat fluxes within the ASE (Fig. 5.6b). The three high heat flux events are characterised by deep areas of low pressure in the vicinity of the ASE with strong, downslope, easterly winds generating coastal polynyas. When the wind speeds are strongest and they interact with the steep orography there is a clear difference in the modelled heat fluxes, particularly within PIG polynya (Fig. 5.20). During these periods the high resolution model gives larger turbulent heat fluxes due to a combination of both stronger near-surface winds and lower temperatures. Within PIG polynya during the high heat flux events the high resolution MetUM gives turbulent heat fluxes that are 15-25% larger than the coarse resolution simulations (see Table 5.1). When the wind speeds are strongest this difference can increase to 25-30% (e.g first half of

Fig. 5.9 in PIG polynya). This difference is usually associated with the representation of a hydraulic jump in the flow at the base of the slope down from the Hudson Mountains. Our work and that of others, shows that around Antarctica higher resolution models more accurately capture coastal winds, particularly when there are interactions with the underlying terrain. Therefore, in order to accurately capture the magnitude of turbulent heat fluxes within coastal polynyas it is necessary to move towards a higher resolution atmospheric model (which better captures the coastal orography). Although not included in our study, the coarse horizontal resolution of global reanalysis products means they are also likely to be underestimating turbulent heat fluxes from coastal polynyas in the vicinity of PIG by at least 10-20%.

The results of this chapter also have important implications for ocean modelling studies within the ASE. The larger heat fluxes within coastal polynyas in the high resolution model will lead to a deeper and saltier mixed layer, and it is also important to capture the spatial distribution of these heat fluxes. The stronger winds and changing wind directions seen over coastal polynyas in the high resolution model will give a different wind stress field which may lead to changes in the modelled currents and circulation pattern close to PIG. This is particularly important because the area close to PIG was the region where the largest differences between the two model resolutions were seen.

Overall, we show that by using a high resolution atmospheric model (2.2 km) the heat fluxes in coastal polynyas and orographic flows within the ASE are more accurately captured. The divergence between the two resolutions of the model is greatest when the winds are at the strongest. If it is shown that local cooling within coastal polynyas is important in determining the basal melt rate of PIG then there should be a move towards forcing ocean and sea ice models using high resolution atmospheric products. This is particularly important close to PIG where the complex orography amplifies the importance of using a high resolution model. For studies investigating regions where the impact of complex coastal orography is less important then, given the broad similarities between the two model resolutions, an atmospheric resolution of the order 20 km is likely to suffice.

6

CONCLUSIONS

6.1 OVERVIEW

As part of the ice sheet stability research programme (iSTAR) this thesis has investigated aspects of the weather and climate within the Amundsen Sea Embayment that are important to both the underlying ocean and ice sheet. The atmosphere-ocean-ice interactions in this region are complex, and the glaciers within the ASE are amongst the most rapidly thinning and retreating in Antarctica. Ice losses from ASE glaciers contribute ~10% of current annual global sea level rise (Mouginot et al., 2014). The region is also very remote and meteorological observations sparse. We add valuable observations with a new set of 38 radiosondes from early 2014, the first radiosondes launched for research purposes within the ASE.

6.2 SUMMARY OF THE THESIS

Chapter 3 contains the most comprehensive evaluation of meteorological reanalysis products in West Antarctica to have been undertaken to date. There are many users of reanalysis products within the ASE and our work highlights both the strengths and limitations of global reanalysis products in this sparsely observed region. All of the current generation of global reanalysis products produce near-surface temperatures

that are between 1.8 (ERA-I) and 6.8 °C (MERRA) lower than observations from a network of four AWS within the ASE. The reanalysis products also underestimate the strength and frequency of strong wind events. The directional constancy of the AWS observations during strong wind events indicates they are likely to be orographic, e.g. katabatic, flows, and perhaps explains why the coarse resolution reanalyses are unable to accurately capture them. Compared with research vessel observations within the ASE the reanalysis temperature and wind speed biases are generally much reduced with mean temperature biases of less than 2.1 °C in all four reanalysis products. However, in the vicinity of PIG the cold bias persists due to the coarse resolution and smoothed orography of the reanalyses leading to a northward extension of the land-sea mask. Our unique radiosonde observations also show the same spatial variability of biases, with larger reanalysis temperature biases compared with radiosondes launched close to the ice shelves (smaller further offshore). The temperature bias is again larger in MERRA than in the other reanalysis products, with MERRA tending to produce a strong surface inversion that is not seen in the observations. The temperature biases tend to reduce in magnitude with increasing height above the surface and by the 900 hPa pressure level the reanalysis products are all within 1.5 °C of the observed mean temperature. The radiosondes also reveal frequent low-level jets in the lowest ~1 km of the atmosphere that the reanalysis products all struggle to accurately capture. We highlight the spatial variability of biases within the ASE to alert reanalysis users that these coarse resolution products may not always be an appropriate atmospheric forcing product for their application, particularly when looking at fine-scale processes in the vicinity of PIG. Jones and Harpham (2013) have previously highlighted that global reanalysis products contain larger near-surface temperature biases in Antarctica than anywhere else on the planet. As such this recommendation is likely applicable in many coastal Antarctic locations, particularly where the coastal orography is complex.

In chapter 4 we show that global reanalyses and RACMO2.3 are able to accurately reproduce the ice core observed time series of accumulation on PIG, though the different products contain varying biases. The 1979-2013 mean annual accumulation across the ten ice core sites is 0.49 $m.w.e\ yr^{-1}$. JRA-55, ERA-I and CFSR all accurately reproduce the observed value, with differences of only ± 0.01 $m.w.e\ yr^{-1}$ for each of the products. RACMO2.3 overestimates by 0.04 $m.w.e\ yr^{-1}$ and MERRA

underestimates by 0.07 $m.w.e\ yr^{-1}$. Our results show that there has been no statistically significant trend in either observed or modelled accumulation on PIG between 1979 and 2013. This in good agreement with a recent radar survey on PIG and Thwaites glaciers (Medley et al., 2013, 2014). This means that observed increases of mass loss from PIG in recent decades (e.g. Wingham et al., 2009) have not been offset by increased accumulation on to the glacier. High accumulation years are found to be characterised by a strong zonal pressure gradient in West Antarctica, which is associated with anomalously northerly meridional winds and warmer near-surface air temperatures. Near-surface air temperatures on PIG are predicted to increase during the 21st century (Bracegirdle et al., 2008; Monaghan et al., 2008) and there is likely to be an associated increase in accumulation of approximately 10 to 20% by the end of the century (Ligtenberg et al., 2013; Frieler et al., 2015). Changes in the depth and location of the ASL are predicted to be relatively limited during the 21st century (Hosking et al., 2016) and as such they will have a smaller impact on future changes in accumulation on PIG (Ligtenberg et al., 2013).

In chapter 5 we investigate high heat flux events within coastal polynyas in the ASE which are thought to impact the local ocean stratification and circulation in the vicinity of PIG (St-Laurent et al., 2015). Our findings show that strong easterly or southeasterly winds drive the formation of these polynyas, and, in our case studies, orographic flows are shown to occur during these strong wind events. For example, interactions with the underlying complex orography lead to the formation of a hydraulic jump in the vicinity of PIG; at or close to the foot of the slope down from the Hudson Mountains to the east. Coarse resolution simulations — likely due to their smoothed orography — produce a less abrupt and weaker hydraulic jump. Associated with this the high resolution simulations produce lower temperatures and stronger winds over a polynya in the vicinity of PIG and this causes ocean to atmosphere turbulent heat fluxes to be 10-20% larger than in the coarse resolution simulations. A move towards using higher resolution atmospheric models in this region will allow these orographic flows to be more adequately resolved. These results are likely applicable within many coastal polynyas around Antarctica. Previous work has shown that by using a higher resolution of NWP model a more accurate representation of coastal polynya size is achieved in coupled models (Mathiot et al., 2012; Hollands et al., 2013). Here we extend this by showing that, in regions of

Antarctica where polynyas are bounded by complex orography, coupled models that use a coarse atmospheric forcing product are also likely to underestimate the heat fluxes within the polynya.

In summary, this work has advanced our understanding of the skill of atmospheric models and reanalysis products in the ASE. We show that a move towards utilising higher horizontal resolution atmospheric products/models will: a) resolve issues surrounding the northward and westward extension of the land-sea mask that causes large temperature biases in coastal parts of the ASE and, b) more adequately resolve orographic flows that are not properly reproduced by reanalysis products or coarse resolution NWP simulations. Alongside this, chapter 4 shows that a regional climate model and most global reanalysis products are able to accurately reproduce the mean annual accumulation on PIG — a field which is dependent on large-scale atmospheric circulation rather than the fine-scale details discussed above. Chapter 4 utilises data from ten ice core sites on PIG and shows that there has been no statistically significant trend in either the observed or modelled accumulation on PIG in recent decades. Further, the reanalysis products show there is no statistically significant near-surface temperature trend on PIG between 1979 and 2013.

6.3 LIMITATIONS, FUTURE WORK AND PERSPECTIVES

Our evaluation of reanalysis products would have been enhanced by additional wintertime meteorological observations. Currently the only in-situ meteorological observations in the ASE during the winter come from the three AMRC AWSs, the NYU AWS on PIG is no longer operational. An upgrade of the present AWS network could provide useful additional observations. For example, if temperature sensors were fitted at multiple heights, we could test our hypothesis that the magnitude of reanalysis temperature biases increase when a strong near-surface temperature inversion is observed. Additionally, radiation sensors would allow insights into whether reanalysis skill changes on cloudy days compared with clear days. Scambos et al. (2017) layout plans to increase the AWS coverage on Thwaites Glacier in the near-future with the addition of six new stations, some of which will be equipped with the sensors described above. Our recommendation is that a similar network of AWS should be installed on PIG too and, if sensors to measure snow depth were added, this

would be highly beneficial for surface mass balance and accumulation studies.

There may also be opportunities in the future to collect wintertime observations within the sea-ice for example using modified drifting buoys that are currently being developed to survive the winter freeze-up (e.g. Inoue et al., 2009). This would have been a useful addition to our reanalysis evaluation as it would have allowed us to compare summertime near-surface biases from the research-vessel observations to wintertime biases when there is near total sea ice cover.

The next generation of global reanalysis products are currently in the process of being released, notably ECMWF's 5th generation reanalysis (ERA-5) and NASA's Modern-Era Retrospective Analysis version 2 (MERRA2). These products have a higher resolution than the four products evaluated in our study. A future study should investigate how their performance compares to the products evaluated in our study, both using the data we have already collated and any additional observations that become available.

To our knowledge there have been no ship-borne direct observations of surface turbulent heat fluxes in the Amundsen Sea region using the eddy-covariance methodology, though the bulk-formulae can be used to estimate heat fluxes during some research-vessel cruises. If, for example, the *JCR* had been making direct ocean-atmosphere heat flux observations, using a 3-d sonic/ultrasonic anemometer to measure the turbulent components of the wind speed, we could have used these to validate our 17th-19th February 2014 MetUM simulation. This would have allowed us to make more inferences about which resolution of the MetUM was closer to the 'observational truth' in terms of their turbulent heat fluxes within the polynyas. In the future there is the potential to use new technologies to observe the recurrent coastal polynyas that are known to form within the ASE. Despite the remote location of the ASE, future field campaigns that target the region could attempt to use unmanned aerial vehicles (drones) to investigate near-surface air temperatures, wind speeds and turbulent heat fluxes over coastal polynyas. These observations would provide valuable data with which to validate NWP simulations and provide insights on how the magnitude of turbulent fluxes vary spatially over the coastal polynyas of the ASE.

Our work validating the accumulation fields (or equivalent) from RACMO2.3 and reanalysis products involved a comparison with ten accumulation time series derived from low elevation ice cores. Given that the lack of reliable ice core data

from low elevation regions in West Antarctica has recently been highlighted in a number of studies (Favier et al., 2014; Medley et al., 2014; Scambos et al., 2017), our contribution here is vital. However, we do acknowledge that our study could have been further improved if we were able to seasonally resolve the ice core accumulation. This would have allowed us to examine the seasonal cycle of accumulation in both observations and atmospheric models. We could have investigated the link between the longitudinal location of the ASL and accumulation on PIG more thoroughly. Further, we could have examined whether there have been any significant trends in observed accumulation in any season. For example, warming in West Antarctica has been shown to be most pronounced in the spring season (SON) (Bromwich et al., 2013a). A future piece of research would be to investigate if there has been a coincident increase in the observed accumulation on PIG in springtime. High resolution (seasonally resolved), low elevation ice cores are also identified by Scambos et al. (2017) as vital for future observational campaigns on Thwaites Glacier. Again we would recommend widening this to include multiple ice core sites on PIG. Crucially, some of the cores should target regions where atmospheric models show accumulation rates that approach or exceed 1 $m.w.e\ yr^{-1}$. This will allow us to conclusively determine whether RACMO2.3 or global reanalysis products are in closer agreement with observations in these areas.

Following our investigation of the meteorological conditions associated with high heat flux events in the ASE an extension would be to study how higher heat fluxes within coastal polynyas affect the ocean stratification in a 1-dimensional model. This would allow analysis of the length of time for which changes in stratification persist following the closure of the polynya (i.e. a large reduction in the ocean to atmosphere heat flux in the model). Beyond this, there is also scope to use different resolutions of atmospheric forcing on a more complex ocean model. This would allow an investigation into what impact the updated forcing has on various aspects of the local ocean circulation — including the volume and temperature of warm CDW transported towards the ice shelf of PIG. Kimura et al. (2017) use two different atmospheric forcing products (RACMO2.3 and ERA-I) to force an ocean model of the Amundsen Sea, with significant differences between the simulations. There is however scope for such analysis to be widened to include more atmospheric models and reanalysis products, to analyse the range of ocean responses. It is

also now possible to produce a few years worth of output from a high resolution NWP model (such as the one we use in chapter 5) and this could also be used to force an ocean model in the ASE. With orographic flows in the vicinity of PIG more adequately captured it would allow thorough investigation of how these atmospheric phenomena affect the ocean circulation and stratification within the ASE.

A further interesting piece of future work would be to examine the likely future trends in either the frequency or extent of coastal polynyas within the ASE. There are a number of likely influences on this; warming temperatures in the ASE are likely to result in a shorter sea ice season (e.g. Bracegirdle et al., 2008) — this could lead to sea ice being more susceptible to being drawn away from the coastline during strong wind events in the winter and spring seasons. As we have shown these polynyas are typically generated during strong wind events when the near surface winds are from the easterly sector. Using CMIP5 (or CMIP6) simulations one could examine how the frequency and severity of these strong wind events is likely to change over the course of the 21st century. However, such features are unlikely to be adequately captured by the models, and so it may be more prudent to examine large-scale changes such as the meridional pressure gradient between West Antarctica and the southern mid-latitudes.

A limitation of all climate relevant studies in this region is the lack of long-term near-surface meteorological observations. The AWS we utilise throughout this thesis have only been operational since 2011 and there have already been some instrumentation failures. The maintenance and development of the sparse AWS network in years and decades to come will provide an invaluable data set with which to examine how West Antarctica is affected by anthropogenic climate change.

REFERENCES

Agosta, C., Favier, V., Genthon, C., Gallée, H., Krinner, G., Lenaerts, J. M., and van den Broeke, M. R. (2012). A 40-year accumulation dataset for Adelie Land, Antarctica and its application for model validation. *Climate Dynamics*, 38(1-2):75–86.

Alexander, S. P., Orr, A., Webster, S., and Murphy, D. J. (2017). Observations and fine-scale model simulations of gravity waves over Davis, East Antarctica (69 °S, 78 °E). *Journal of Geophysical Research: Atmospheres*, 112:1–16.

Anderson, P. (1994). A method for rescaling humidity sensors at temperatures well below freezing. *Journal of Atmospheric and Oceanic Technology*, 11(5):1388–1391.

Andreas, E. L., Claffey, K. J., and Makshtas, A. P. (2000). Low-level atmospheric jets and inversions over the western Weddell Sea. *Boundary-Layer Meteorology*, 97(3):459–486.

Arthern, R. J., Winebrenner, D. P., and Vaughan, D. G. (2006). Antarctic snow accumulation mapped using polarization of 4.3-cm wavelength microwave emission. *Journal of Geophysical Research Atmospheres*, 111(6):1–10.

Assmann, K. M., Jenkins, A., Shoosmith, D. R., Walker, D. P., Jacobs, S. S., and Nicholls, K. W. (2013). Variability of circumpolar deep water transport onto the Amundsen Sea Continental shelf through a shelf break trough. *Journal of Geophysical Research: Oceans*, 118(12):6603–6620.

Bamber, J. L., Riva, R. E. M., Vermeersen, B. L. A., and Lebrocq, A. M. (2009). Reassessment of the Potential of the West Antarctic Ice Sheet. *Science*, 324(May):901–904.

Banta, R. J., McConnell, J. R., Frey, M. M., Bales, R. C., and Taylor, K. (2008). Spatial and temporal variability in snow accumulation at the West Antarctic Ice Sheet Divide over recent centuries. *Journal of Geophysical Research*, 113(D23):D23102.

Biddle, L. C., Heywood, K. J., Kaiser, J., and Jenkins, A. (2017). Glacial meltwater identification in the Amundsen Sea. *Journal of Physical Oceanography*, 47(4):933–954.

Bintanja, R. (1998). The contribution of snowdrift sublimation to the surface mass balance of Antarctica. *Annals of Glaciology*, 27:251–259.

Bracegirdle, T. J. (2013). Climatology and recent increase of westerly winds over the Amundsen Sea derived from six reanalyses. *International Journal of Climatology*, 33(4):843–851.

Bracegirdle, T. J., Connolley, W. M., and Turner, J. (2008). Antarctic climate change over the twenty first century. *Journal of Geophysical Research Atmospheres*, 113(3):1–13.

Bracegirdle, T. J. and Marshall, G. J. (2012). The reliability of antarctic tropospheric pressure and temperature in the latest global reanalyses. *Journal of Climate*, 25(20):7138–7146.

Bromwich, D. H., Nicolas, J. P., and Monaghan, A. J. (2011). An Assessment of precipitation changes over antarctica and the southern ocean since 1989 in contemporary global reanalyses. *Journal of Climate*, 24(16):4189–4209.

Bromwich, D. H., Nicolas, J. P., Monaghan, A. J., Lazzara, M. A., Keller, L. M., Weidner, G. A., and Wilson, A. B. (2013a). Corrigendum: Central West Antarctica among the most rapidly warming regions on Earth. *Nature Geoscience*, 7(1):76–76.

Bromwich, D. H., Otieno, F. O., Hines, K. M., Manning, K. W., and Shilo, E. (2013b). Comprehensive evaluation of polar weather research and forecasting model performance in the antarctic. *Journal of Geophysical Research Atmospheres*, 118(2):274–292.

Burgener, L., Rupper, S., Koenig, L., Forster, R., Christensen, W. F., Williams, J., Koutnik, M., Miège, C., Steig, E. J., Tingey, D., Keeler, D., and Riley, L. (2013). An observed negative trend in West Antarctic accumulation rates from 1975 to 2010: Evidence from new observed and simulated records. *Journal of Geophysical Research Atmospheres*, 118(10):4205–4216.

Carrasco, J. F., Bromwich, D. H., and Monaghan, A. J. (2003). Distribution and Characteristics of Mesoscale Cyclones in the Antarctic: Ross Sea Eastward to the Weddell Sea*. *Monthly Weather Review*, 131:289–301.

Christianson, K., Bushuk, M., Dutrieux, P., Parizek, B. R., Joughin, I. R., Alley, R. B., Shean, D. E., Abrahamsen, E. P., Anandakrishnan, S., Heywood, K. J., Kim, T. W., Lee, S. H., Nicholls, K., Stanton, T., Truffer, M., Webber, B. G. M., Jenkins, A., Jacobs, S., Bindschadler, R., and Holland, D. M. (2016). Sensitivity of Pine Island Glacier to

observed ocean forcing. *Geophysical Research Letters*, 43(20):10,817–10,825.

Church, J. A., Clark, P. U., Cazenave, A., Gregory, J. M., Jevrejeva, S., Levermann, A., Merrifield, M. A., Milne, G. A., Nerem, R. S., Nunn, P. D., Payne, A. J., Pfeffer, W. T., Stammer, D., and Unnikrishnan, A. S. (2013). Sea Level Change. In Stocker, T. F., Qin, D., Plattner, G.-K., Tignor, M., Allen, S. K., Boschung, J., Nauels, A., Xia, Y., Bex, V., and Midgley, P. M., editors, *Climate Change 2013: The Physical Science Basis. Contribution of Working Group I to the Fifth Assessment Report of the Intergovernmental Panel on Climate Change.*, chapter 13, pages 1137–1216. Cambridge University Press, Cambridge, United Kingdom and New York, NY, USA.

Clem, K. R. and Fogt, R. L. (2015). South Pacific circulation changes and their connection to the tropics and regional Antarctic warming in austral spring, 1979-2012. *Journal of Geophysical Research: Atmospheres*, 120(7):2773–2792.

Connolley, W. M. (1997). Variability in annual mean circulation in southern high latitudes. *Climate Dynamics*, 13(10):745–756.

Cook, P. A. and Renfrew, I. A. (2015). Aircraft-based observations of air-sea turbulent fluxes around the british isles. *Quarterly Journal of the Royal Meteorological Society*, 141(686):139–152.

Deb, P., Orr, A., Hosking, J. S., Phillips, T., Turner, J., Bannister, D., Pope, J. O., and Colwell, S. (2016). An assessment of the Polar Weather Research and Forecasting (WRF) model representation of near-surface meteorological variables over West Antarctica. *Journal of Geophysical Research: Atmospheres*, 121:1532–1548.

DeConto, R. M. and Pollard, D. (2016). Contribution of Antarctica to past and future sea-level rise. *Nature*, 531(7596):591–597.

Dee, D. P., Uppala, S. M., Simmons, A. J., Berrisford, P., Poli, P., Kobayashi, S., Andrae, U., Balmaseda, M. A., Balsamo, G., Bauer, P., Bechtold, P., Beljaars, A. C. M., van de Berg, L., Bidlot, J., Bormann, N., Delsol, C., Dragani, R., Fuentes, M., Geer, A. J., Haimberger, L., Healy, S. B., Hersbach, H., Hólm, E. V., Isaksen, L., Kållberg, P., Köhler, M., Matricardi, M., Mcnally, A. P., Monge-Sanz, B. M., Morcrette, J. J., Park, B. K., Peubey, C., de Rosnay, P., Tavolato, C., Thépaut, J. N., and Vitart, F. (2011). The ERA-Interim reanalysis: Configuration and performance of the data assimilation system. *Quarterly Journal of the Royal Meteorological Society*, 137(656):553–597.

Ding, Q., Steig, E. J., Battisti, D. S., and Küttel, M. (2011). Winter warming in West Antarctica caused by central tropical Pacific warming. *Nature Geoscience*, 4(6):398–

403.

Dinniman, M. S., Klinck, J. M., Bai, L. S., Bromwich, D. H., Hines, K. M., and Holland, D. M. (2015). The effect of atmospheric forcing resolution on delivery of ocean heat to the antarctic floating ice shelves. *Journal of Climate*, 28(15):6067–6085.

Drucker, R., Martin, S., and Kwok, R. (2011). Sea ice production and export from coastal polynyas in the Weddell and Ross Seas. *Geophysical Research Letters*, 38(17):4–7.

Dutrieux, P., De Rydt, J., Jenkins, A., Holland, P. R., Ha, H. K., Lee, S. H., Steig, E. J., Ding, Q., Abrahamsen, E. P., and Schroder, M. (2014). Strong Sensitivity of Pine Island Ice-Shelf Melting to Climatic Variability. *Science*, 343(6167):174–178.

Eisen, O., Frezzotti, M., Genthon, C., Isaksson, E., Magand, O., Broeke, V. D., Michiel, R., Dixon, D. a., Ekaykin, A., Holmlund, P., Kameda, T., Karlöf, L., Kaspari, S., Lipenkov, V. Y., Oerter, H., Takahashi, S., and Vaughan, D. G. (2008). Ground-based measurements of spatial and temporal variability of snow accumulation in East Antarctica. *Reviews Of Geophysics*, 46(2006):RG2001.

Elvidge, A. D. and Renfrew, I. A. (2016). The causes of foehn warming in the lee of mountains. *Bulletin of the American Meteorological Society*, 97(3):455–466.

Elvidge, A. D., Renfrew, I. A., King, J. C., Orr, A., Lachlan-Cope, T. A., Weeks, M., and Gray, S. L. (2015). Foehn jets over the Larsen C Ice Shelf, Antarctica. *Quarterly Journal of the Royal Meteorological Society*, 141(688):698–713.

Elvidge, A. D., Renfrew, I. A., Weiss, A. I., Brooks, I. M., Lachlan-Cope, T. A., and King, J. C. (2016). Observations of surface momentum exchange over the marginal-ice-zone and recommendations for its parameterization. *Atmospheric Chemistry and Physics Discussions*, 15(19):26609–26660.

Favier, L., Durand, G., Cornford, S. L., Gudmundsson, G. H., Gagliardini, O., Gillet-Chaulet, F., Zwinger, T., Payne, A. J., and Le Brocq, A. M. (2014). Retreat of Pine Island Glacier controlled by marine ice-sheet instability. *Nature Climate Change*, 5(2):117–121.

Favier, V., Agosta, C., Parouty, S., Durand, G., Delaygue, G., Gallée, H., Drouet, A. S., Trouvilliez, A., and Krinner, G. (2013). An updated and quality controlled surface mass balance dataset for Antarctica. *Cryosphere*, 7(2):583–597.

Fiedler, E. K. (2010). Ocean-atmosphere heat fluxes at the Ronne Polynia, Antarctica. *Weather*, 65(1):16–21.

Fiedler, E. K., Lachlan-Cope, T. A., Renfrew, I. A., and King, J. C. (2010). Convective heat transfer over thin ice covered coastal polynyas. *Journal of Geophysical Research: Oceans*, 115(10):1–19.

Fogt, R. L., Bromwich, D. H., and Hines, K. M. (2011). Understanding the SAM influence on the South Pacific ENSO teleconnection. *Climate Dynamics*, 36(7):1555–1576.

Fogt, R. L., Wovrosh, A. J., Langen, R. A., and Simmonds, I. (2012). The characteristic variability and connection to the underlying synoptic activity of the Amundsen-Bellingshausen Seas Low. *Journal of Geophysical Research Atmospheres*, 117(7):1–22.

Frezzotti, M., Urbini, S., Proposito, M., Scarchilli, C., and Gandolfi, S. (2007). Spatial and temporal variability of surface mass balance near Talos Dome, East Antarctica. *Journal of Geophysical Research: Earth Surface*, 112(2).

Frieler, K., Clark, P. U., He, F., Buizert, C., Reese, R., Ligtenberg, S. R. M., van den Broeke, M. R., Winkelmann, R., and Levermann, A. (2015). Consistent evidence of increasing Antarctic accumulation with warming. *Nature Climate Change*, 5(4):348–352.

Gallée, H. and Pettré, P. (1998). Dynamical Constraints on Katabatic Wind Cessation in Adélie Land, Antarctica. *Journal of the Atmospheric Sciences*, 55(10):1755–1770.

Genthon, C., Kaspari, S., and Mayewski, P. A. (2005). Interannual variability of the surface mass balance of West Antarctica from ITASE cores and ERA40 reanalyses, 1958-2000. *Climate Dynamics*, 24(7-8):759–770.

Gillett, N. P., Kell, T. D., and Jones, P. D. (2006). Regional climate impacts of the Southern Annular Mode. *Geophysical Research Letters*, 33(23):1–4.

Gong, D. and Wang, S. (1999). Definition of Antarctic Oscillation index. *Geophysical Research Letters*, 26(4):459–462.

Greed, G. (2010). Unified Model Basic User Guide: Introduction (1-24). Retreived July 18th 2017, from https://code.metoffice.gov.uk/doc/um/vn10.2/papers/umdp_000.pdf.

Gwyther, D. E., Galton-Fenzi, B. K., Hunter, J. R., and Roberts, J. L. (2014). Simulated melt rates for the Totten and Dalton ice shelves. *Ocean Science*, 10(3):267–279.

Harden, B. E., Renfrew, I. A., and Petersen, G. N. (2011). A Climatology of wintertime barrier winds off southeast Greenland. *Journal of Climate*, 24(17):4701–4717.

Harden, B. E., Renfrew, I. A., and Petersen, G. N. (2015). Meteorological buoy observations from the central Iceland Sea. *Journal of Geophysical Research Atmospheres*, 120(8):3199–3208.

Holland, P. R., Jenkins, A., and Holland, D. M. (2010). Ice and ocean processes in the Bellingshausen sea, Antarctica. *Journal of Geophysical Research: Oceans*, 115(5):1–16.

Holland, P. R. and Kwok, R. (2012). Wind-driven trends in Antarctic sea-ice drift. *Nature Geoscience*, 5(12):872–875.

Hollands, T., Haid, V., Dierking, W., Timmermann, R., and Ebner, L. (2013). Sea ice motion and open water area at the Ronne Polynia, Antarctica: Synthetic aperture radar observations versus model results. *Journal of Geophysical Research: Oceans*, 118(4):1940–1954.

Holtslag, A. A., Svensson, G., Baas, P., Basu, S., Beare, B., Beljaars, A. C., Bosveld, F. C., Cuxart, J., Lindvall, J., Steeneveld, G. J., Tjernström, M., and Van De Wiel, B. J. (2013). Stable atmospheric boundary layers and diurnal cycles: Challenges for weather and climate models. *Bulletin of the American Meteorological Society*, 94(11):1691–1706.

Hosking, J. S., Orr, A., Bracegirdle, T. J., and Turner, J. (2016). Future circulation changes off West Antarctica: Sensitivity of the Amundsen Sea Low to projected anthropogenic forcing. *Geophysical Research Letters*, 43(1):367–376.

Hosking, J. S., Orr, A., Marshall, G. J., Turner, J., and Phillips, T. (2013). The influence of the amundsen-bellingshausen seas low on the climate of West Antarctica and its representation in coupled climate model simulations. *Journal of Climate*, 26(17):6633–6648.

Hughes, T. J. (1981). The weak underbelly of the West Antarctic Ice-sheet. *Journal of Glaciology*, 27(97):518–525.

Inoue, J., Enomoto, T., Miyoshi, T., and Yamane, S. (2009). Impact of observations from Arctic drifting buoys on the reanalysis of surface fields. *Geophysical Research Letters*, 36(8):1–5.

Jacobs, S. S. and Comiso, J. C. (1997). Climate variability in the Amundsen and Bellinghausen seas. *J. Climate*, 10(4):697–709.

Jacobs, S. S. and Hellmer, H. H. (1996). Freshening Could Come From Other Melting Ice in the. *Observatory*, 23(9):957–960.

Jacobs, S. S., Jenkins, A., Giulivi, C. F., and Dutrieux, P. (2011). Stronger ocean circulation and increased melting under Pine Island Glacier ice shelf. *Nature Geoscience*, 4(8):519–523.

Jakobson, E., Vihma, T., Palo, T., Jakobson, L., Keernik, H., and Jaagus, J. (2012). Validation of atmospheric reanalyses over the central Arctic Ocean. *Geophysical Research Letters*, 39(10):1–6.

Jakobson, L., Vihma, T., Jakobson, E., Palo, T., Männik, A., and Jaagus, J. (2013). Low-level jet characteristics over the Arctic Ocean in spring and summer. *Atmospheric Chemistry and Physics*, 13(21):11089–11099.

Jenkins, A., Dutrieux, P., Jacobs, S., Steig, E., Gudmundsson, H., Smith, J., and Heywood, K. (2016). Decadal Ocean Forcing and Antarctic Ice Sheet Response: Lessons from the Amundsen Sea. *Oceanography*, 29(4):106–117.

Jenkins, A., Dutrieux, P., Jacobs, S. S., McPhail, S. D., Perrett, J. R., Webb, A. T., and White, D. (2010). Observations beneath Pine Island Glacier in WestAntarctica and implications for its retreat. *Nature Geoscience*, 3(7):468–472.

Jones, P. D. and Harpham, C. (2013). Estimation of the absolute surface air temperature of the Earth. *Journal of Geophysical Research Atmospheres*, 118(8):3213–3217.

Jones, P. D. and Lister, D. H. (2015). Antarctic near-surface air temperatures compared with ERA-Interim values since 1979. *International Journal of Climatology*, 35(7):1354–1366.

Jones, R. W., Renfrew, I. A., Orr, A., Webber, B. G. M., Holland, D. M., and Lazzara, M. A. (2016). Evaluation of four global reanalysis products using in situ observations in the Amundsen Sea Embayment, Antarctica. *Journal of Geophysical Research: Atmospheres*, 121(11):6240–6257.

Joughin, I., Smith, B. E., and Medley, B. (2014). Marine Ice Sheet Collapse Potentially Underway for the Thwaites Glacier Basin, West Antarctica. *Science (New York, N.Y.)*, 344(May):735–738.

Kaspari, S., Mayewski, P. A., Dixon, D. A., Spikes, V. B., Sneed, S. B., Handley, M. J., and Hamilton, G. S. (2004). Climate variability in West Antarctica derived from annual accumulation-rate records from ITASE firn/ice cores. *Annals of Glaciology*, 39:585–594.

Khazendar, A., Schodlok, M., Fenty, I., Ligtenberg, S., Rignot, E., and van den

Broeke, M. (2013). Observed thinning of Totten Glacier is linked to coastal polynya variability. *Nature Communications*, 4(2857).

Kimura, S., Jenkins, A., Regan, H., Holland, P., Assmann, K., Whitt, D., van Wessem, M., van de Berg, W., Reijmer, C., and Dutrieux, P. (2017). Oceanographic controls on the variability of ice-shelf basal melting and circulation of glacial meltwater in the Amundsen Sea Embayment, Antarctica. *Journal of Geophysical Research: Oceans*, Accepted.

King, J. and Turner, J. (1997). *Antarctic Meteorology and Climatology*. Cambridge : Cambridge University Press.

King, J. C. (1990). Some measurements of turbulence over an antarctic ice shelf. *Quarterly Journal of the Royal Meteorological Society*, 116(492):379–400.

Kobayashi, S., Ota, Y., Harada, Y., Ebita, A., Moriya, M., Onoda, H., Onogi, K., Kamahori, H., Kobayashi, C., Endo, H., Miyaoka, K., and Takahashi, K. (2015). The JRA-55 Reanalysis: General Specifications and Basic Characteristics. *Journal of the Meteorological Society of Japan. Ser. II*, 93(1):5–48.

Krinner, G., Guicherd, B., Ox, K., Genthon, C., and Magand, O. (2008). Influence of oceanic boundary conditions in simulations of antarctic climate and surface mass balance change during the coming century. *Journal of Climate*, 21(5):938–962.

Kusahara, K., Hasumi, H., and Tamura, T. (2010). Modeling sea ice production and dense shelf water formation in coastal polynyas around East Antarctica. *Journal of Geophysical Research: Oceans*, 115(10):1–10.

Kwok, R. and Comiso, J. C. (2002). Southern Ocean climate and sea ice anomalies associated with the Southern Oscillation. *Journal of Climate*, 15(5):487–501.

Lachlan-Cope, T. A., Connolley, W. M., and Turner, J. (2001). The Role of the Non-Axisymmetric Antarctic Orography in forcing the observed pattern of variability of the Antarctic climate. *Geophysical Research Letters*, 28(21):4111–4114.

Lazzara, M. A., Weidner, G. A., Keller, L. M., Thom, J. E., and Cassano, J. J. (2012). Antarctic automatic weather station program: 30 years of polar observations. *Bulletin of the American Meteorological Society*, 93(10):1519–1537.

Lenaerts, J. T., Vizcaino, M., Fyke, J., van Kampenhout, L., and van den Broeke, M. R. (2016). Present-day and future Antarctic ice sheet climate and surface mass balance in the Community Earth System Model. *Climate Dynamics*, 47(5-6):1367–1381.

Lenaerts, J. T. M., van den Broeke, M. R., Déry, S. J., van Meijgaard, E., van de Berg,

W. J., Palm, S. P., and Sanz Rodrigo, J. (2012a). Modeling drifting snow in Antarctica with a regional climate model: 1. Methods and model evaluation. *Journal of Geophysical Research: Atmospheres*, 117(D5):D05108.

Lenaerts, J. T. M., van den Broeke, M. R., van Angelen, J. H., van Meijgaard, E., and Déry, S. J. (2012b). Drifting snow climate of the Greenland ice sheet: a study with a regional climate model. *The Cryosphere*, 6(4):891–899.

Lenaerts, J. T. M., Van Den Broeke, M. R., Van De Berg, W. J., Van Meijgaard, E., and Kuipers Munneke, P. (2012c). A new, high-resolution surface mass balance map of Antarctica (1979-2010) based on regional atmospheric climate modeling. *Geophysical Research Letters*, 39(4):1–5.

Li, M., Liu, J., Wang, Z., Wang, H., Zhang, Z., Zhang, L., and Yang, Q. (2013). Assessment of sea surface wind from NWP reanalyses and satellites in the Southern Ocean. *Journal of Atmospheric and Oceanic Technology*, 30(8):1842–1853.

Li, X., Holland, D. M., Gerber, E. P., and Yoo, C. (2014). Impacts of the north and tropical Atlantic Ocean on the Antarctic Peninsula and sea ice. *Nature*, 505(7484):538–542.

Ligtenberg, S. R. M., van de Berg, W. J., van den Broeke, M. R., Rae, J. G. L., and van Meijgaard, E. (2013). Future surface mass balance of the Antarctic ice sheet and its influence on sea level change, simulated by a regional atmospheric climate model. *Climate Dynamics*, 41(3-4):867–884.

Liu, Z., Schweiger, A., and Lindsay, R. (2015). Observations and Modeling of Atmospheric Profiles in the Arctic Seasonal Ice Zone. *Monthly Weather Review*, 143(1):39–53.

Lüpkes, C., Vihma, T., Jakobson, E., König-Langlo, G., and Tetzlaff, A. (2010). Meteorological observations from ship cruises during summer to the central Arctic: A comparison with reanalysis data. *Geophysical Research Letters*, 37(9):1–4.

Mahrt, L. (2013). Stably Stratified Atmospheric Boundary Layers. *Annual Review of Fluid Mechanics*, 46(July):23–45.

Mankoff, K. D., Jacobs, S. S., Tulaczyk, S. M., and Stammerjohn, S. E. (2012). The role of pine island glacier ice shelf basal channels in deep-water upwelling, polynyas and ocean circulation in pine island bay, antarctica. *Annals of Glaciology*, 53(60):123–128.

Marshall, G. J. (2003). Trends in the Southern Annular Mode from Observations and

Reanalyses. *J. Climate*, 16(1999):4134–4143.

Mastrantonio, G., Malvestuto, V., Argentini, S., Georgiadis, T., and Viola, A. (1999). Evidence of a Convective Boundary Layer Developing on the Antarctic Plateau during the Summer. *Meteorology and atmospheric Physics*, 71(1-2):127–132.

Mathiot, P., Jourdain, N. C., Barnier, B., Gallée, H., Molines, J. M., Le Sommer, J., and Penduff, T. (2012). Sensitivity of coastal polynyas and high-salinity shelf water production in the Ross Sea, Antarctica, to the atmospheric forcing. *Ocean Dynamics*, 62(5):701–723.

Medley, B., Joughin, I., Das, S. B., Steig, E. J., Conway, H., Gogineni, S., Criscitiello, A. S., McConnell, J. R., Smith, B. E., Van Den Broeke, M. R., Lenaerts, J. T. M., Bromwich, D. H., and Nicolas, J. P. (2013). Airborne-radar and ice-core observations of annual snow accumulation over Thwaites Glacier, West Antarctica confirm the spatiotemporal variability of global and regional atmospheric models. *Geophysical Research Letters*, 40(14):3649–3654.

Medley, B., Joughin, I., Smith, B. E., Das, S. B., Steig, E. J., Conway, H., Gogineni, S., Lewis, C., Criscitiello, A. S., McConnell, J. R., Van Den Broeke, M. R., Lenaerts, J. T. M., Bromwich, D. H., Nicolas, J. P., and Leuschen, C. (2014). Constraining the recent mass balance of pine island and thwaites glaciers, west antarctica, with airborne observations of snow accumulation. *Cryosphere*, 8(4):1375–1392.

Mercer, J. H. (1978). West Antarctic ice sheet and CO2 greenhouse effect: a threat of disaster. *Nature*, 271(5643):321–325.

Met Office (2017). 2016 one of the warmest two years on record. http://www.metoffice.gov.uk/news/releases/2017/2016-record-breaking-year-for-global-temperature. Date Accessed: 16th July 2017.

Monaghan, A. J., Bromwich, D. H., Chapman, W., and Comiso, J. C. (2008). Recent variability and trends of Antarctic near-surface temperature. *Journal of Geophysical Research Atmospheres*, 113(4).

Monaghan, A. J., Bromwich, D. H., and Wang, S.-H. (2006). Recent trends in Antarctic snow accumulation from Polar MM5 simulations. *Philosophical transactions. Series A, Mathematical, physical, and engineering sciences*, 364(1844):1683–1708.

Morales-Maqueda, M., Willmott, A., and Biggs, N. (2004). Polynya Dynamics: a Review of Observations and Modeling. *Reviews Of Geophysics*, 42(1):RG1004.

Morris, E. M., Mulvaney, R., Arthern, R. J., Davies, D., Gurney, R., Lambert, P., De Rydt,

J., Smith, A., Tuckwell, R., and Winstrup, M. (2017). Snow densification and recent accumulation along the iSTAR traverse, Pine Island Glacier, Antarctica. *Journal of Geophysical Research Earth Surfaces*, In review.

Mouginot, J., Rignot, E., and Scheuchl, B. (2014). Sustained increase in ice discharge from the Amundsen Sea Embayment, West Antarctica, from 1973 to 2013. *Geophysical Research Letters*, 41(5):1576–1584.

Nakayama, Y., Timmermann, R., Schröder, M., and Hellmer, H. H. (2014). On the difficulty of modeling Circumpolar Deep Water intrusions onto the Amundsen Sea continental shelf. *Ocean Modelling*, 84:26–34.

Nias, I. J., Cornford, S. L., and Payne, A. J. (2016). Contrasting the Modelled sensitivity of the Amundsen Sea Embayment ice streams. *Journal of Glaciology*, 62(233):552–562.

Nicolas, J. P. and Bromwich, D. H. (2011). Climate of West Antarctica and influence of marine air intrusions. *Journal of Climate*, 24(1):49–67.

Nicolas, J. P., Vogelmann, A. M., Scott, R. C., Wilson, A. B., Cadeddu, M. P., Bromwich, D. H., Verlinde, J., Lubin, D., Russell, L. M., Jenkinson, C., Powers, H. H., Ryczek, M., Stone, G., and Wille, J. D. (2017). January 2016 extensive summer melt in West Antarctica favoured by strong El Niño. *Nature Communications*, 8(15799):10p.

Noël, B., Van De Berg, W. J., Van Meijgaard, E., Kuipers Munneke, P., Van De Wal, R. S. W., and Van Den Broeke, M. R. (2015). Evaluation of the updated regional climate model RACMO2.3: Summer snowfall impact on the Greenland Ice Sheet. *Cryosphere*, 9(5):1831–1844.

Nye, J. F. (1963). Correction Factor for Accumulation Measured by the Thickness of the Annual Layers in an Ice Sheet. *Journal of Glaciology*, 4(36):785–788.

O'Donnell, R., Lewis, N., Mcintyre, S., and Condon, J. (2011). Improved methods for PCA-based reconstructions: Case study using the Steig et al. (2009) antarctic temperature reconstruction. *Journal of Climate*, 24(8):2099–2115.

Orr, A., Phillips, T., Webster, S., Elvidge, A., Weeks, M., Hosking, S., and Turner, J. (2014). Met Office Unified Model high-resolution simulations of a strong wind event in Antarctica. *Quarterly Journal of the Royal Meteorological Society*, 140(684):2287–2297.

Padman, L., Costa, D. P., Dinniman, M. S., Fricker, H. A., Goebel, M. E., Huckstadt, L. A., Humbert, A., Joughin, I., Lenaerts, J. T. M., Ligtenberg, S. R. M., Scambos, T.,

and Van Den Broeke, M. R. (2012). Oceanic controls on the mass balance of Wilkins Ice Shelf, Antarctica. *Journal of Geophysical Research: Oceans*, 117(1):1–17.

Pall, P., Allen, M. R., and Stone, D. A. (2007). Testing the Clausius-Clapeyron constraint on changes in extreme precipitation under CO2 warming. *Climate Dynamics*, 28(4):351–363.

Papritz, L., Pfahl, S., Sodemann, H., and Wernli, H. (2015). A climatology of cold air outbreaks and their impact on air-sea heat fluxes in the high-latitude South Pacific. *Journal of Climate*, 28(1):342–364.

Parish, T. and Bromwich, D. (1987). The surface windfield over the Antarctic ice sheets. *Nature*, 330(6125):51–54.

Pavelsky, T. M., Boé, J., Hall, A., and Fetzer, E. J. (2011). Atmospheric inversion strength over polar oceans in winter regulated by sea ice. *Climate Dynamics*, 36(5-6):945–955.

Pettre, P. and Andre, J. (1991). Surface-pressure change through Loewe's Phenomena and katabatic flow jumps: Study of two cases in Adelie Land, Antarctica. *Journal of Atmospheric Sciences*, 48(4):557–571.

Petty, A. A., Holland, P. R., and Feltham, D. L. (2014). Sea ice and the ocean mixed layer over the Antarctic shelf seas. *Cryosphere*, 8(2):761–783.

Pritchard, H. D., Ligtenberg, S. R. M., Fricker, H. A., Vaughan, D. G., van den Broeke, M. R., and Padman, L. (2012). Antarctic ice-sheet loss driven by basal melting of ice shelves. *Nature*, 484(7395):502–505.

Raphael, M. N., Marshall, G. J., Turner, J., Fogt, R. L., Schneider, D., Dixon, D. A., Hosking, J. S., Jones, J. M., and Hobbs, W. R. (2016). The Amundsen sea low: Variability, change, and impact on Antarctic climate. *Bulletin of the American Meteorological Society*, 97(1):111–121.

Renfrew, I. A. (2004). The dynamics of idealized katabatic flow over a moderate slope and ice shelf. *Quarterly Journal of the Royal Meteorological Society*, 130(598):1023–1045.

Renfrew, I. A. (2006). Polynyas and Leads in the Southern Ocean. In Riffenburgh, B., editor, *Encyclopedia of the Antarctic*. Abingdon: Routledge.

Renfrew, I. A. and Anderson, P. S. (2002). The surface climatology of an ordinary katabatic wind regime in Coats Land, Antarctica. *Tellus, Series A: Dynamic Meteorology and Oceanography*, 54(5):463–484.

Renfrew, I. A. and Anderson, P. S. (2006). Profiles of katabatic flow in summer and winter over Coats Land, Antarctica. *Quarterly Journal of the Royal Meteorological Society*, 132(616):779–802.

Renfrew, I. A. and King, J. C. (2000). A simple model of the convective internal boundary layer and its application to surface heat flux estimates within polynyas. *Boundary-Layer Meteorology*, 94(3):335–356.

Renfrew, I. A., King, J. C., and Markus, T. (2002). Coastal polynyas in the southern Weddell Sea: Variability of the surface energy budget. *Journal of Geophysical Research*, 107(C6):3063.

Renfrew, I. A., Petersen, G. N., Sproson, D. A. J., Moore, G. W. K., Adiwidjaja, H., Zhang, S., and North, R. (2009). A comparison of aircraft-based surface-layer observations over Denmark Strait and the Irminger Sea with meteorological analyses and QuikSCAT winds. *Quarterly Journal of the Royal Meteorological Society*, 135(645):2046–2066.

Rienecker, M. M., Suarez, M. J., Gelaro, R., Todling, R., Bacmeister, J., Liu, E., Bosilovich, M. G., Schubert, S. D., Takacs, L., Kim, G. K., Bloom, S., Chen, J., Collins, D., Conaty, A., Da Silva, A., Gu, W., Joiner, J., Koster, R. D., Lucchesi, R., Molod, A., Owens, T., Pawson, S., Pegion, P., Redder, C. R., Reichle, R., Robertson, F. R., Ruddick, A. G., Sienkiewicz, M., and Woollen, J. (2011). MERRA: NASA's modern-era retrospective analysis for research and applications. *Journal of Climate*, 24(14):3624–3648.

Rignot, E., Bamber, J. L., van den Broeke, M. R., Davis, C., Li, Y., van de Berg, W. J., and van Meijgaard, E. (2008). Recent Antarctic ice mass loss from radarinterferometry and regional climatemodelling. *Nature Geoscience*, 1(2):106–110.

Rignot, E., Jacobs, S., Mouginot, J., and Scheuchl, B. (2013). Ice-Shelf Melting Around Antarctica. *Science*, 341(6143):266–270.

Rignot, E., Mouginot, J., Morlighem, M., Seroussi, H., and Scheuchl, B. (2014). Widespread, rapid grounding line retreat of Pine Island, Thwaites, Smith, and Kohler glaciers, West Antarctica, from 1992 to 2011. *Geophysical Research Letters*, 41(10):3502–3509.

Saha, S., Moorthi, S., Pan, H. L., Wu, X., Wang, J., Nadiga, S., Tripp, P., Kistler, R., Woollen, J., Behringer, D., Liu, H., Stokes, D., Grumbine, R., Gayno, G., Wang, J., Hou, Y. T., Chuang, H. Y., Juang, H. M. H., Sela, J., Iredell, M., Treadon, R., Kleist,

D., Van Delst, P., Keyser, D., Derber, J., Ek, M., Meng, J., Wei, H., Yang, R., Lord, S., Van Den Dool, H., Kumar, A., Wang, W., Long, C., Chelliah, M., Xue, Y., Huang, B., Schemm, J. K., Ebisuzaki, W., Lin, R., Xie, P., Chen, M., Zhou, S., Higgins, W., Zou, C. Z., Liu, Q., Chen, Y., Han, Y., Cucurull, L., Reynolds, R. W., Rutledge, G., and Goldberg, M. (2010). The NCEP climate forecast system reanalysis. *Bulletin of the American Meteorological Society*, 91(8):1015–1057.

Scambos, T., Bell, R., Alley, R., Anandakrishnan, S., Bromwich, D., Brunt, K., Christianson, K., Creyts, T., Das, S., DeConto, R., Dutrieux, P., Fricker, H., Holland, D., MacGregor, J., Medley, B., Nicolas, J., Pollard, D., Siegfried, M., Smith, A., Steig, E., Trusel, L., Vaughan, D., and Yager, P. (2017). How much, how fast?: A science review and outlook for research on the instability of Antarctica's Thwaites Glacier in the 21st century. *Global and Planetary Change*, 153(April):16–34.

Scambos, T., Raup, B., and Bohlander, J. (2001). *Images of Antarctic Ice Shelves, Version 1 [2008-2015]*. NSIDC: National Snow and Ice Data Center, Boulder, Colorado USA.

Schodlok, M. P., Menemenlis, D., Rignot, E., and Studinger, M. (2012). Sensitivity of the ice-shelf/ocean system to the sub-ice-shelf cavity shape measured by nasa icebridge in pine island glacier, west antarctica. *Annals of Glaciology*, 53(60):156–162.

Shepherd, A. (2001). Inland Thinning of Pine Island Glacier, West Antarctica. *Science*, 291(5505):862–864.

Shepherd, A., Ivins, E. R., A, G., Barletta, V. R., Bentley, M. J., Bettadpur, S., Briggs, K. H., Bromwich, D. H., Forsberg, R., Galin, N., Horwath, M., Jacobs, S., Joughin, I., King, M. a., Lenaerts, J. T. M., Li, J., Ligtenberg, S. R. M., Luckman, A., Luthcke, S. B., McMillan, M., Meister, R., Milne, G., Mouginot, J., Muir, A., Nicolas, J. P., Paden, J., Payne, a. J., Pritchard, H., Rignot, E., Rott, H., Sorensen, L. S., Scambos, T. a., Scheuchl, B., Schrama, E. J. O., Smith, B., Sundal, a. V., van Angelen, J. H., van de Berg, W. J., van den Broeke, M. R., Vaughan, D. G., Velicogna, I., Wahr, J., Whitehouse, P. L., Wingham, D. J., Yi, D., Young, D., and Zwally, H. J. (2012). A Reconciled Estimate of Ice-Sheet Mass Balance. *Science*, 338(6111):1183–1189.

Smith, S. D. (1988). Coefficients for sea surface wind stress, heat flux, and wind profiles as a function of wind speed and temperature. *Journal of Geophysical Research: Oceans*, 93(C12):15467–15472.

Smith, S. D., Anderson, R. J., Hartog, G. D., Topham, D. R., and Perkin, R. G. (1983).

An investigation of a polynya in the Canadian Archipelago: 1. Introduction and oceanography. *Journal of Geophysical Research: Oceans*, 88(C5):2900.

Smith, S. D., Muench, R. D., and Pease, C. H. (1990). Polynyas and leads: An overview of physical processes and environment. *Journal of Geophysical Research*, 95(C6):9461–9479.

St-Laurent, P., Klinck, J. M., and Dinniman, M. S. (2015). Impact of local winter cooling on the melt of Pine Island Glacier, Antarctica. *Journal of Geophysical Research: Oceans*, 120(10):6718–6732.

Stammerjohn, S., Massom, R., Rind, D., and Martinson, D. (2012). Regions of rapid sea ice change: An inter-hemispheric seasonal comparison. *Geophysical Research Letters*, 39(6):1–8.

Stammerjohn, S. E., Maksym, T., Massom, R. A., Lowry, K. E., Arrigo, K. R., Yuan, X., Raphael, M., Randall-Goodwin, E., Sherrell, R. M., and Yager, P. L. (2015). Seasonal sea ice changes in the Amundsen Sea, Antarctica, over the period of 1979 to 2014. *Elementa: Science of the Anthropocene*, 3:000055.

Steig, E. J., Schneider, D. P., Rutherford, S. D., Mann, M. E., Comiso, J. C., and Shindell, D. T. (2009). Warming of the Antarctic ice-sheet surface since the 1957 International Geophysical Year. *Nature*, 457(7228):459–462.

Stull, R. (1988). *An Introduction to Boundary Layer Meteorology*. Dordretch; London: Kluwer Academic Publishers.

Suortti, T. M., Kats, A., Rivi, R., Kämpfer, N., Leiterer, U., Miloshevich, L. M., Neuber, R., Paukkunen, A., Ruppert, P., Vömel, H., and Yushkov, V. (2008). Tropospheric comparisons of Vaisala radiosondes and balloon-borne frost-Point and Lyman-α hygrometers during the LAUTLOS-WAVVAP experiment. *Journal of Atmospheric and Oceanic Technology*, 25(2):149–166.

Thoma, M., Jenkins, A., Holland, D., and Jacobs, S. (2008). Modelling Circumpolar Deep Water intrusions on the Amundsen Sea continental shelf, Antarctica. *Geophysical Research Letters*, 35(18):2–7.

Thomas, E. R. and Bracegirdle, T. J. (2014). Precipitation pathways for five new ice core sites in Ellsworth Land, West Antarctica. *Climate Dynamics*, 44(7-8):2067–2078.

Thomas, E. R., Hosking, J. S., Tuckwell, R. R., Warren, R. A., and Ludlow, E. C. (2015). Twentieth century increase in snowfall in coastal West Antarctica. *Geophysical Research Letters*, 42(21):9387–9393.

Thompson, D. W. J. and Wallace, J. M. (2000a). Annular Mode in the Extratropical Circulation. Part I : Month-to-Month Variability. *Journal of Climate*, 13(1999):1000–1016.

Thompson, D. W. J. and Wallace, J. M. (2000b). Annular Mode in the Extratropical Circulation. Part I I: Trends. *Journal of Climate*, 13(1999):1000–1016.

Timmermann, R., Wang, Q., and Hellmer, H. H. (2012). Ice shelf basal melting in a global finite-element sea ice – ice shelf – ocean model. *Annals of Glaciology*, 53(1):303–314.

Trenberth, K. E. (1997). The Definition of El Niño. *Bulletin of the American Meteorological Society*, 78(12):2771–2777.

Turner, J. (2004). The El Niño-Southern Oscillation and Antarctica. *International Journal of Climatology*, 24(1):1–31.

Turner, J., Chenoli, S. N., Abu Samah, A., Marshall, G., Phillips, T., and Orr, A. (2009). Strong wind events in the Antarctic. *Journal of Geophysical Research Atmospheres*, 114(18).

Turner, J., Hosking, J. S., Bracegirdle, T. J., Marshall, G. J., and Phillips, T. (2015). Recent changes in Antarctic Sea Ice. *Philosophical Transactions of the Royal Society of London A: Mathematical, Physical and Engineering Sciences*, 373(2045).

Turner, J., Orr, A., Gudmundsson, G. H., Jenkins, A., Bingham, R. G., Hillenbrand, C. D., and Bracegirdle, T. J. (2017). Atmosphere-ocean-ice interactions in the Amundsen Sea Embayment, West Antarctica. *Reviews of Geophysics*, 55(1):235–276.

Turner, J., Phillips, T., Hosking, J. S., Marshall, G. J., and Orr, A. (2013). The amundsen sea low. *International Journal of Climatology*, 33(7):1818–1829.

van De Berg, W. J. and Medley, B. (2016). Brief Communication: Upper-air relaxation in RACMO2 significantly improves modelled interannual surface mass balance variability in Antarctica. *Cryosphere*, 10(1):459–463.

van de Berg, W. J., van den Broeke, M. R., Reijmer, C. H., and van Meijgaard, E. (2006). Reassessment of the Antarctic surface mass balance using calibrated output of a regional atmospheric climate model. *Journal of Geophysical Research Atmospheres*, 111(11):1–15.

van den Broeke, M., van de Berg, W. J., and van Meijgaard, E. (2006). Snowfall in coastal West Antarctica much greater than previously assumed. *Geophysical Research Letters*, 33(2):2–5.

van den Broeke, M. R. and van Lipzig, N. P. M. (2003). Factors Controlling the Near-Surface Wind Field in Antarctica. *Monthly Weather Review*, 131(4):733–743.

van Loon, H. (1967). The Half-Yearly Oscillations in Middle and High Southern Latitudes and the Coreless Winter. *Journal of the Atmospheric Sciences*, 24:472–486.

van Wessem, J. M., Reijmer, C. H., Lenaerts, J. T. M., Van De Berg, W. J., Van Den Broeke, M. R., and Van Meijgaard, E. (2014a). Updated cloud physics in a regional atmospheric climate model improves the modelled surface energy balance of Antarctica. *Cryosphere*, 8(1):125–135.

van Wessem, J. M., Reijmer, C. H., Morlighem, M., Mouginot, J., Rignot, E., Medley, B., Joughin, I., Wouters, B., Depoorter, M. A., Bamber, J. L., Lenaerts, J. T. M., Van De Berg, W. J., Van Den Broeke, M. R., and Van Meijgaard, E. (2014b). Improved representation of East Antarctic surface mass balance in a regional atmospheric climate model. *Journal of Glaciology*, 60(222):761–770.

Vaughan, D. G., Bamber, J. L., Giovinetto, M., Russell, J., and Cooper, A. P. R. (1999). Reassessment of net surface mass balance in Antarctica. *Journal of Climate*, 12(4):933–946.

Venteris, E. R. and Whillans, I. M. (1998). Variability of accumulation rate in the catchments of Ice Streams B, C, D and E, Antarctica. *Annals of Glaciology*, 27:227–230.

Wåhlin, A. K., Kalén, O., Arneborg, L., Björk, G., Carvajal, G. K., Ha, H. K., Kim, T. W., Lee, S. H., Lee, J. H., and Stranne, C. (2013). Variability of Warm Deep Water Inflow in a Submarine Trough on the Amundsen Sea Shelf. *Journal of Physical Oceanography*, 43(10):2054–2070.

Wåhlin, A. K., Yuan, X., Björk, G., and Nohr, C. (2010). Inflow of Warm Circumpolar Deep Water in the Central Amundsen Shelf. *Journal of Physical Oceanography*, 40(6):1427–1434.

Walter, B. A. (1989). A study of the planetary boundary-layer over the polynya downwind of St-Lawrence Island in the Bering Sea using aircraft data. *Boundary-Layer Meteorology*, 48(3):255–282.

Walters, D., Boutle, I., Brooks, M., Melvin, T., Stratton, R., Vosper, S., Wells, H., Williams, K., Wood, N., Allen, T., Bushell, A., Copsey, D., Earnshaw, P., Edwards, J., Gross, M., Hardiman, S., Harris, C., Heming, J., Klingaman, N., Levine, R., Manners, J., Martin, G., Milton, S., Mittermaier, M., Morcrette, C., Riddick, T., Roberts,

M., Sanchez, C., Selwood, P., Stirling, A., Smith, C., Suri, D., Tennant, W., Luigi Vidale, P., Wilkinson, J., Willett, M., Woolnough, S., and Xavier, P. (2017). The Met Office Unified Model Global Atmosphere 6.0/6.1 and JULES Global Land 6.0/6.1 configurations. *Geoscientific Model Development*, 10(4):1487–1520.

Wamser, C. and Martinson, D. G. (1993). Drag coefficients for winter Antarctic pack ice. *Journal of Geophysical Research*, 98(C7):12431.

Wang, Y., Ding, M., van Wessem, J. M., Schlosser, E., Altnau, S., van den Broeke, M. R., Lenaerts, J. T. M., Thomas, E. R., Isaksson, E., Wang, J., and Sun, W. (2016). A comparison of Antarctic ice sheet surface mass balance from atmospheric climate models and in situ observations. *Journal of Climate*, 29(14):5317–5337.

Wang, Y., Hou, S., Sun, W., Lenaerts, J. T., van den Broeke, M. R., and van Wessem, J. M. (2015). Recent surface mass balance from Syowa Station to Dome F, East Antarctica: comparison of field observations, atmospheric reanalyses, and a regional atmospheric climate model. *Climate Dynamics*, 45(9-10):2885–2899.

Webber, B. G. M., Heywood, K. J., Stevens, D. P., Dutrieux, P., Abrahamsen, E. P., Jenkins, A., Jacobs, S. S., Ha, H. K., Lee, S. H., and Kim, T. W. (2017). Mechanisms driving variability in the ocean forcing of Pine Island Glacier. *Nature Communications*, 8:14507.

Weijer, W., Veneziani, M., Stossel, A., Hecht, M. W., Jeffery, N., Jonko, A., Hodos, T., and Wang, H. (2017). Local atmospheric response to an open-ocean polynya in a high-resolution climate model. *Journal of Climate*, 30(5):1629–1641.

Wingham, D. J., Ridout, A. J., Scharroo, R., Arthern, R. J., and Shum, C. K. (1998). Antarctic elevation change from 1992 to 1996. *Science*, 282(5388):456–458.

Wingham, D. J., Wallis, D. W., and Shepherd, A. (2009). Spatial and temporal evolution of Pine Island Glacier thinning, 1995-2006. *Geophysical Research Letters*, 36(17):5–9.

Wolter, K. and Timlin, M. S. (2011). El Niño/Southern Oscillation behaviour since 1871 as diagnosed in an extended multivariate ENSO index. *International Journal of Climatology*, 31(7):1074–1087.

Yu, Y. and Cai, X. M. (2006). Structure and dynamics of katabatic flow jumps: Idealised simulations. *Boundary-Layer Meteorology*, 118(3):527–555.

A

SUPPLEMENTARY FIGURES AND TABLES

Table A.1: A table showing details of the radiosonde launches and launch locations. Column headings abbreviated for space, (Lat) Latitude (°S), (Long) Longitude (°W), (Alt) Maximum Altitude (km).

Date	Time	Lat	Long	Alt	Notes
1st Feb	1130	67.41	100.54	19.5	8/8 low cloud, 15-20 knots NW winds. Temperature 0°C. Launched while on station for the test CTD
2nd Feb	1620	70.40	101.67	22.3	8/8 low cloud, foggy and poor visibility. 97% surface humidity. Temp. -1.26°C. Wind speed 5 knots. Launched while on station for CTD3, no wind obs.
3rd Feb	1115	70.91	102.13	23.3	8/8 low cloud. Surface obs. Temp -1°C, Humidity 98%, Wind speed 6 knots. Slow ascent rate only 2-3m/s
4th Feb	1135	71.85	103.7	11.2	7/8 cloud. Good vis. Thin layer of low cloud. Surface temp -2.1°C, Wind speed 5 knots NE.
5th Feb	1220	73.57	103.83	22.6	1/8 cloud, almost clear blue sky, good vis. Surface temp -4.8°C. Wind speed 10knots S
6th Feb	1130	73.81	106.53	20.8	1/8 cloud, some high cirrus. Wind 20 knots from the SE. Temp -4.7°C
7th Feb	1200	73.75	104.09	22.9	2/8 cloud cover, some low cumulus but more high cirrus. 15 knot wind from the NE. Temp -5°C.
8th Feb	1310	73.86	103.07	21.8	Clear blue sky with bits of high cirrus. 4 knots easterly. Temp -5.7°C. Location at Edwards Island for seal tagging.
9th Feb	1210	74.18	105.42	19.7	Blue sky, scattered low cloud and high cirrus 3/8. Close to B31 iceberg.
11th Feb	1700	74.96	101.44	21.5	Off ice flow, clear blue sky, temp -10°C . On station for CTD 41, first launch at PIG.
11th Feb	2330	74.78	101.02	22.5	2nd Launch of day, lighter off ice winds still blue sky. Launched while on station for CTD 45.

Date	Time	Lat	Long	Alt	Notes
12th Feb	1300	75.04	101.97	22	Layer of low cloud, SE wind- off ice flow. On station for the recovery of mooring.
13th Feb	1330	74.99	101.54	21.7	6/8 low cloud cover. Temperature -9.0 wind from SE, off ice flow. Launched during Toyo, while 1 mile from PIG.
13th Feb	1620	74.97	101.49	20.6	7/8 cloud cover, very close to ice front within 1km for toyo. Wind off ice and ship close to centre of low pres.
13th Feb	2045	74.94	101.41	20.0	Very strong winds and pressure decreased to 974mb, still toyo'ing along the ice front.
15th Feb	1115	75.07	101.87	20.3	Additional toyo section along ice front, 7/8 cloud with wind coming from SE at 20knots.
16th Feb	2230	75.03	101.75	20.1	On station for Autosub, clear skies and SE winds. Late launch time for comparison with 0000UTC reanalysis.
17th Feb	1130	75.01	104.68	22.1	Close to Thwaites. On station for CTD 54 wind stronger than forecast at 20-25knots.
18th Feb	0800	75.02	101.79	22.1	On station for Autosub recovery. Very cold surface temp- near -15°C, off ice flow.
18th Feb	1145	74.86	102.08	23.0	On station for mooring deployment- still -15°C and off-ice flow.
18th Feb	1445	74.86	102.09	21.7	Clear blue skies, now -12°C. Continuing time series while triangulating mooring.
18th Feb	1710	74.93	102.72	21.6	A few more clouds but still -11°C. On station for CTD 60. Much more distinct boundary layer.
18th Feb	2130	75.04	101.79	23.2	On station for Autosub deployment. Most cloud is high cirrus, temp remains -11°C.
19th Feb	1715	74.82	106.67	22.1	At Thwaites on station for CTD 62. Launch delayed due not being on station.
20th Feb	1145	74.36	107.33	20	Sunny but cold -13°C, 6/8 cloud cover. On station for CTD 68.

Date	Time	Lat	Long	Alt	Notes
21st Feb	1130	74.68	104.42	19.7	Temp. increased to -3.5°C with winds from NE. No wind obs.
21st Feb	1645	74.50	106.21	22.1	Investigating earlier loss of wind data. Total cloud cover with light ENE wind.
22nd Feb	1210	74.58	106.52	22.7	Launched while on station for CTD 72. 8/8 low cloud cover with l.snow, temp -2.5°C.
23rd Feb	1130	73.87	103.14	22.9	On station at Edwards Islands. Temp +0.06 with 20knot off ice winds from the NE. Very strong winds aloft.
23rd Feb	1750	73.87	103.07	21.9	Delayed 2nd launch due to 40knot gusts. 35knot winds from NE at the time of launch.
23rd Feb	2110	73.83	103.31	21.8	Moved 5miles off Edwards Islands due to high winds preventing small boat deployment, 30-35knot NE.
25th Feb	2245	72.93	110.31	22.1	Seal tagging north of Thwaites on fast ice. 100% sea ice cover 8/8 cloud with l.snow.
26th Feb	1330	72.72	110.72	-	Final morning of seal tagging, lots of sea ice and feeling very cold at -10C. 15-20 knot southerly winds.
27th Feb	1200	71.64	113.55	22.0	On station for CTD 78- iSTAR 2 mooring not recovered. Launch only just post dawn.
28th Feb	1130	71.54	114.29	17.6	Launched at dawn local time. On station for iStar 4 mooring recovery. 7/8 low cloud cover.
2nd Mar	1330	71.55	113.04	22.0	On station for mooring recovery. 5/8 cloud. Temp -7 with new pancake ice forming.
3rd Mar	1150	71.42	111.80	16.7	Steaming north with near 100% cover of new thin sea ice. 8/8 cover of low cloud.
4th Mar	1130	71.27	104.85	19.8	Final mooring deployment. Winds very light so launched while steaming.

Table A.2: Statistical comparison of reanalysis near-surface temperatures to observed seasonal temperatures from each AWS site. The unit for bias and RMSE is $°C$. Biases where the reanalysis products are warmer than observed biases are shown in *italics* while cool biases greater than $3°C$ are in **bold**. * The NYU data set only covers a 13-month period.

	Stats	EK				TI				BP				NYU*			
		SON	DJF	MAM	JJA	SON	DJF	MAM	JJA	SON	DJF	MAM	JJA	SON	DJF	MAM	JJA
ERA-I	Bias	-1.70	-1.12	-1.43	-1.33	-2.40	*0.81*	-2.44	**-5.25**	-2.06	*0.28*	**-3.44**	**-3.86**	*1.35*	*0.36*	*3.02*	*2.83*
	SD ratio	0.98	1.01	1.06	1.01	1.29	1.05	1.37	1.48	1.25	1.22	1.45	1.27	0.88	0.90	0.97	0.95
	R^2	0.83	0.77	0.77	0.80	0.74	0.66	0.76	0.71	0.80	0.74	0.70	0.68	0.93	0.83	0.88	0.86
	RMSE	3.62	2.38	4.18	4.19	4.96	2.21	5.09	8.22	4.17	2.22	5.86	6.18	2.83	2.06	4.44	4.32
	Slope	0.89	0.89	0.93	0.90	1.11	0.85	1.20	1.25	1.12	1.05	1.22	1.05	0.85	0.82	0.91	0.89
JRA-55	Bias	-2.13	-1.79	-2.27	-2.35	**-3.04**	-1.33	**-3.59**	**-4.88**	-2.63	-1.96	**-3.69**	**-3.78**	*0.07*	-0.18	*1.74*	*1.55*
	SD ratio	0.90	1.06	0.91	0.85	1.10	1.14	1.13	0.98	1.02	1.23	1.06	0.92	0.81	0.84	0.82	0.74
	R^2	0.83	0.74	0.81	0.80	0.79	0.71	0.80	0.80	0.84	0.77	0.78	0.79	0.83	0.69	0.84	0.76
	RMSE	3.84	2.92	4.01	4.47	4.48	2.42	4.82	5.98	3.71	2.88	4.69	4.88	3.74	2.70	4.24	4.77
	Slope	0.82	0.91	0.82	0.76	0.98	0.96	1.01	0.87	0.93	1.07	0.94	0.82	0.74	0.70	0.75	0.64
CFSR	Bias	-2.51	-2.65	-1.92	-1.43	-2.84	-2.34	**-3.01**	**-3.41**	-2.62	-2.23	**-3.29**	-2.54	-0.48	-2.50	*1.52*	*1.79*
	SD ratio	1.07	1.17	1.06	1.04	1.30	1.52	1.34	1.27	1.24	1.43	1.37	1.23	1.04	1.29	1.00	1.06
	R^2	0.77	0.66	0.74	0.73	0.71	0.57	0.76	0.74	0.78	0.63	0.74	0.73	0.78	0.59	0.84	0.79
	RMSE	4.68	3.91	4.63	4.88	5.43	4.04	5.28	6.03	4.59	3.80	5.26	5.05	4.31	4.75	4.13	4.71
	Slope	0.94	0.96	0.91	0.89	1.09	1.15	1.17	1.09	1.09	1.14	1.18	1.05	0.92	0.99	0.92	0.94
MERRA	Bias	**-6.27**	**-6.81**	**-7.19**	**-5.84**	**-6.50**	**-6.63**	**-8.03**	**-7.58**	**-6.43**	**-6.48**	**-7.72**	**-6.59**	**-4.57**	**-6.00**	**-4.21**	**-3.11**
	SD ratio	0.98	1.24	1.05	0.99	1.15	1.36	1.24	1.04	1.05	1.25	1.08	0.95	0.95	1.04	1.01	0.98
	R^2	0.84	0.78	0.81	0.84	0.81	0.68	0.80	0.78	0.82	0.72	0.75	0.78	0.85	0.75	0.83	0.81
	RMSE	7.00	7.25	7.98	6.79	7.28	7.10	8.80	8.47	7.06	6.90	8.32	7.32	5.69	6.52	5.78	4.94
	Slope	0.90	1.10	0.95	0.91	1.04	1.12	1.11	0.91	0.95	1.06	0.94	0.84	0.88	0.90	0.92	0.88

Table A.3: Statistical comparison of the four reanalysis products across the four AWS sites for Wind speed (Wsp) ($m\ s^{-1}$), Relative Humidity (RH) (%) and Specific Humidity ($g\ kg^{-1}$). Note humidity is not available at NYU site.

Product	Stats	Wind speed				Relative Humidity			Spec. Humidity		
		EK	TI	BP	NYU	EK	TI	BP	EK	TI	BP
ERA-I	Bias	1.28	-1.73	-3.52	-0.80	-6.67	-3.29	-5.64	-0.25	-0.14	-0.21
	SD ratio	0.74	0.53	0.31	0.72	0.90	0.91	0.80	0.94	1.17	1.08
	R^2	0.54	0.23	0.51	0.63	0.23	0.18	0.34	0.88	0.87	0.86
	RMSE	3.50	6.30	7.40	3.22	13.96	13.42	14.99	0.39	0.41	0.38
	Slope	0.54	0.26	0.22	0.57	0.43	0.39	0.46	0.88	1.09	1.00
JRA-55	Bias	1.51	-1.53	-1.71	-0.63	4.17	5.26	6.95	-0.23	-0.31	-0.22
	SD ratio	0.88	0.55	0.39	0.81	0.67	0.79	0.53	0.96	1.09	1.03
	R^2	0.54	0.34	0.49	0.75	0.24	0.31	0.53	0.86	0.74	0.82
	RMSE	3.64	5.82	6.48	2.66	11.91	12.22	14.83	0.40	0.59	0.42
	Slope	0.65	0.32	0.28	0.70	0.33	0.44	0.33	0.88	0.94	0.93
CFSR	Bias	-0.26	-1.99	-3.29	-2.27	10.74	11.57	14.67	-0.02	-0.11	-0.01
	SD ratio	0.67	0.51	0.43	0.57	0.52	0.45	0.43	1.07	1.12	1.18
	R^2	0.44	0.30	0.60	0.71	0.17	0.14	0.49	0.84	0.83	0.88
	RMSE	3.61	6.11	6.67	3.83	15.77	16.58	19.31	0.37	0.43	0.33
	Slope	0.44	0.30	0.33	0.48	0.21	0.17	0.30	0.98	1.03	1.11
MERRA	Bias	1.47	-1.15	-1.51	-1.55				-0.62	-0.71	-0.56
	SD ratio	0.75	0.53	0.31	0.68				0.67	0.80	0.74
	R^2	0.52	0.19	0.41	0.60				0.82	0.75	0.79
	RMSE	3.62	6.35	6.88	3.61				0.75	0.84	0.68
	Slope	0.54	0.23	0.20	0.53				0.60	0.69	0.65

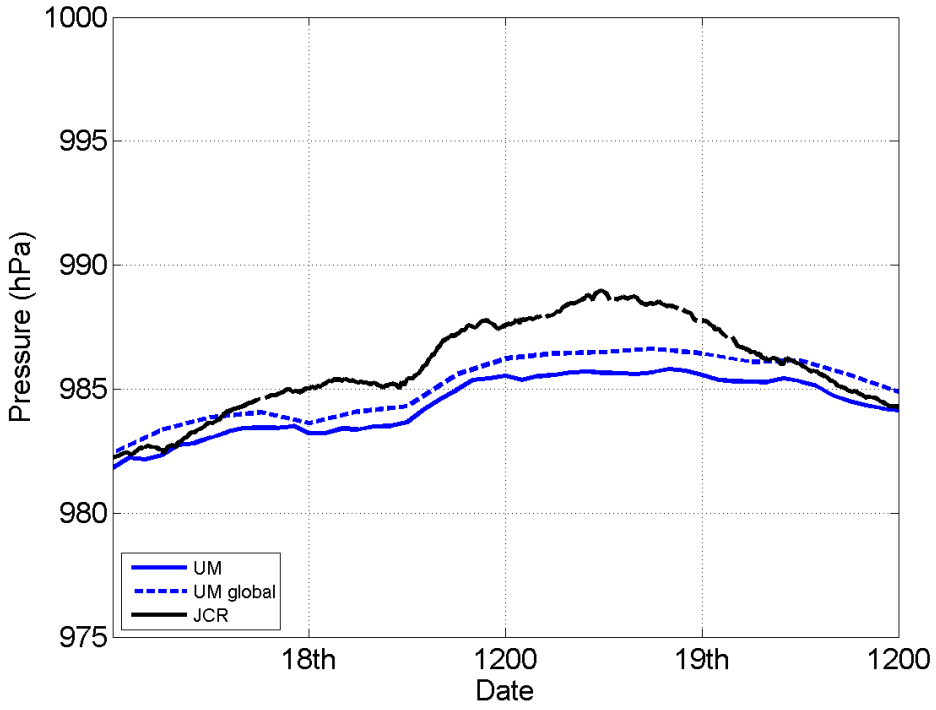

Figure A.1: A comparison of the observed mean sea level pressure onboard RRS James Clark Ross to the MetUM high resolution simulation (blue solid) and MetUM 17 km simulation (blue dashed) between 17th-19th February 2014.

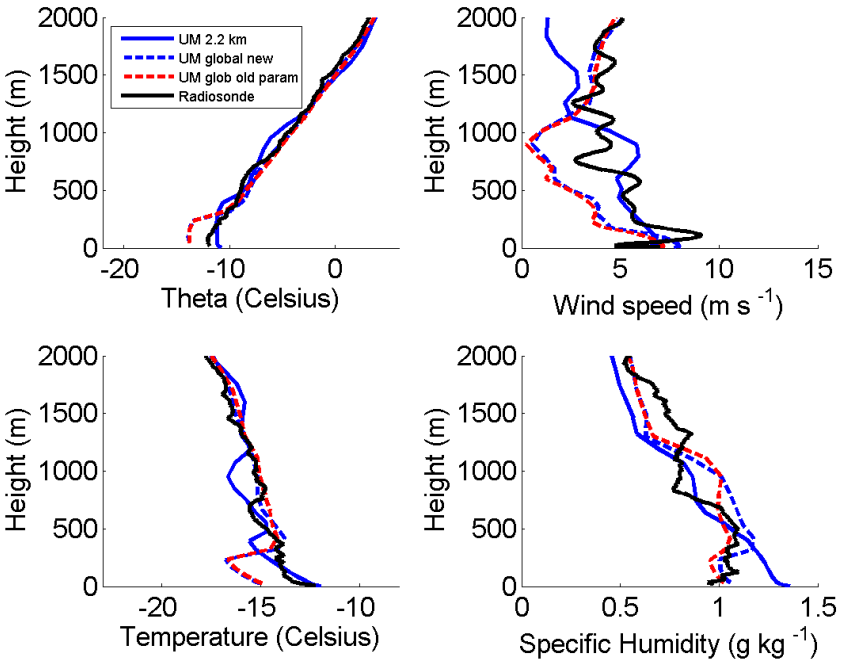

Figure A.2: Vertical profiles from the MetUM compared to radiosonde observations at 1145 UTC on 18th February 2014: Potential temperature (top left); wind speed (top right); Temperature (bottom left); Specific Humidity (bottom right).

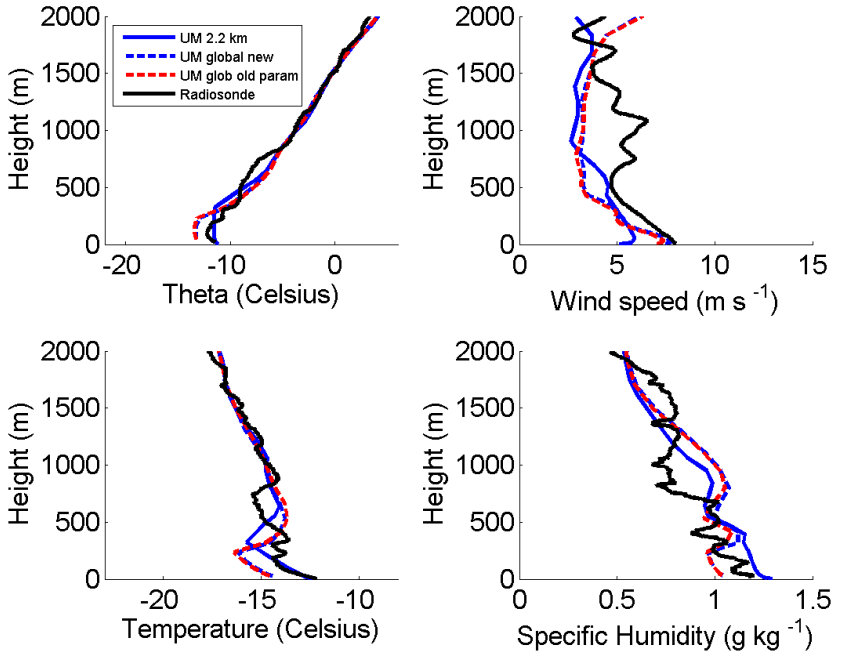

Figure A.3: Vertical profiles from the MetUM compared to radiosonde observations at 1445 UTC on 18th February 2014: Potential temperature (top left); wind speed (top right); Temperature (bottom left); Specific Humidity (bottom right).

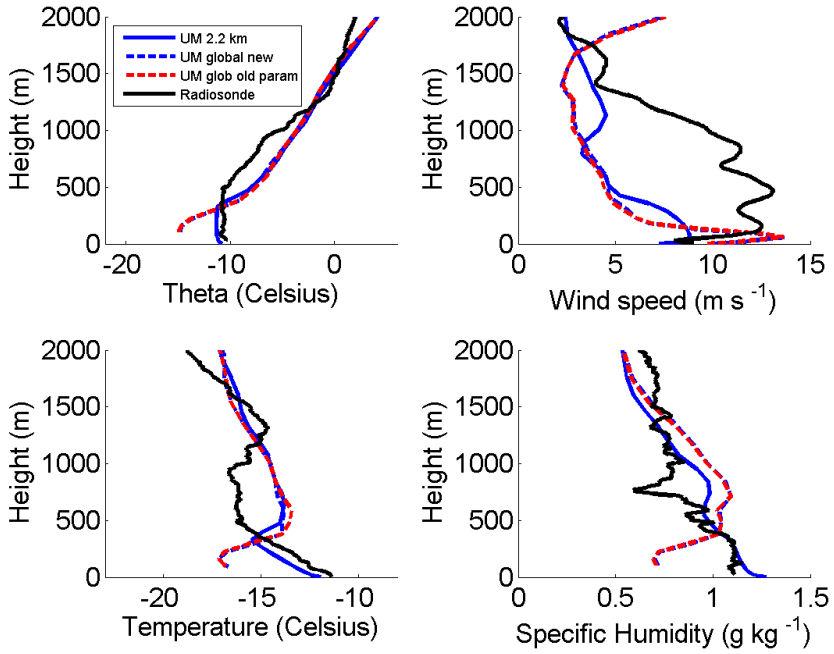

Figure A.4: Vertical profiles from the MetUM compared to radiosonde observations at 1715 UTC on 18th February 2014: Potential temperature (top left); wind speed (top right); Temperature (bottom left); Specific Humidity (bottom right).

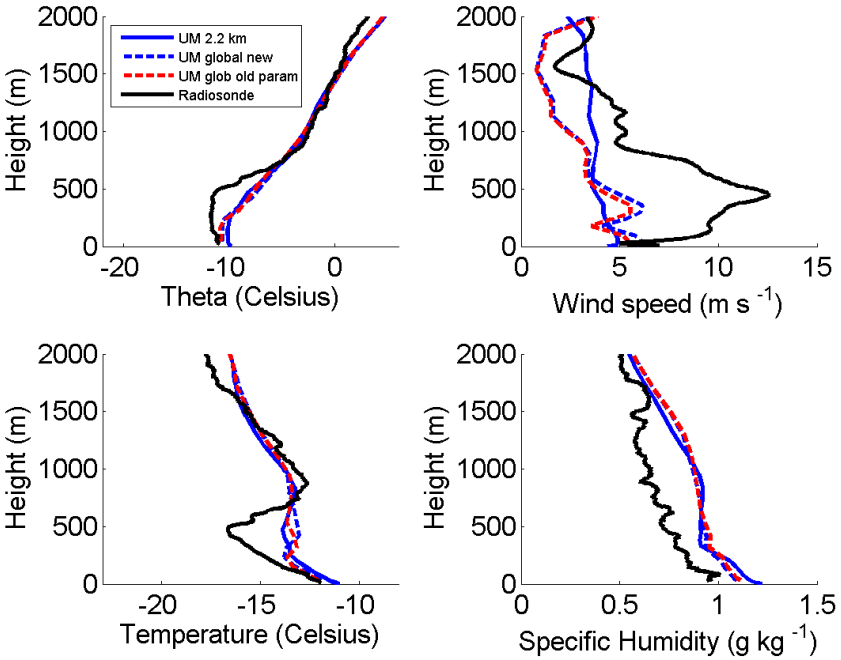

Figure A.5: Vertical profiles from the MetUM compared to radiosonde observations at 2130 UTC on 18th February 2014: Potential temperature (top left); wind speed (top right); Temperature (bottom left); Specific Humidity (bottom right).

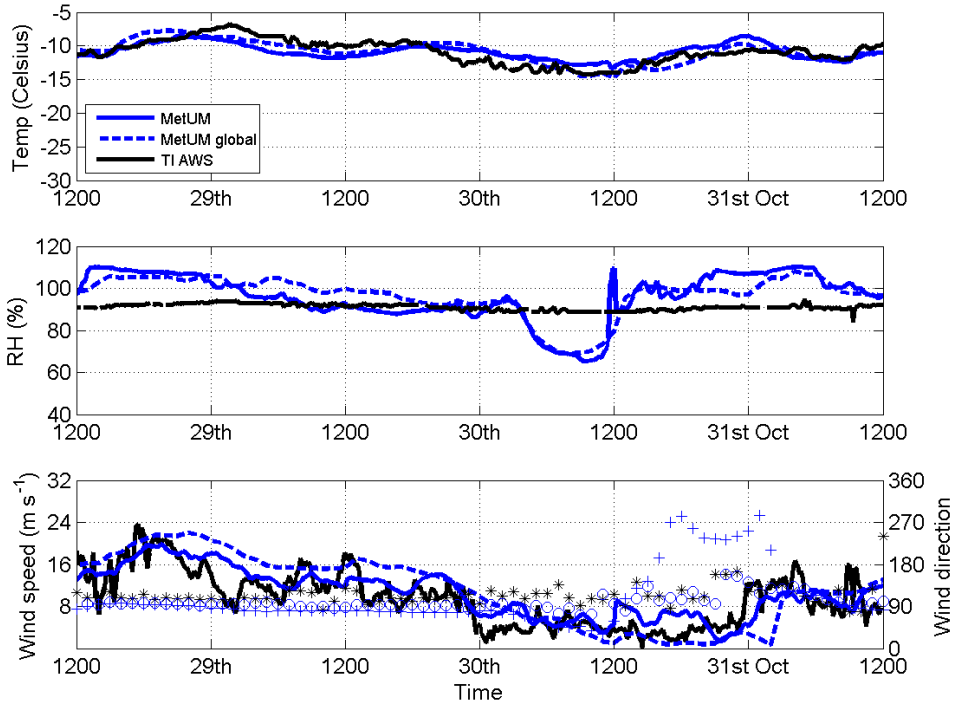

Figure A.6: A comparison of the modelled and observed: temperature (top), relative humidity (middle), and wind speed and direction (bottom), at Thurston Island AWS between 28th-31st October 2011.

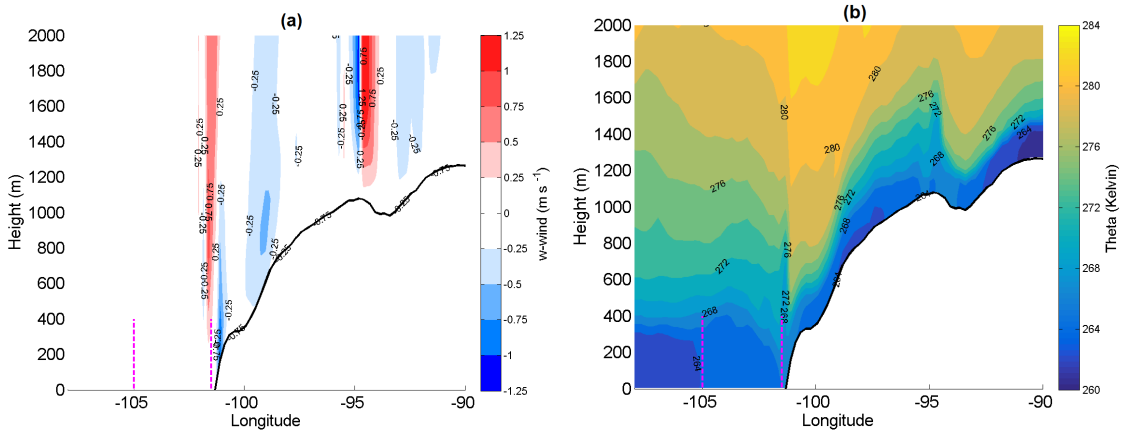

Figure A.7: (a) High resolution vertical wind speed cross-section along the latitude 74.1°S at 0000 UTC 29th October, note the vertical motion at the location of the hydraulic jump. (b) high resolution model potential temperature along the same cross-section at the same time, notice the upward tilting isentropes at the foot of the slope.

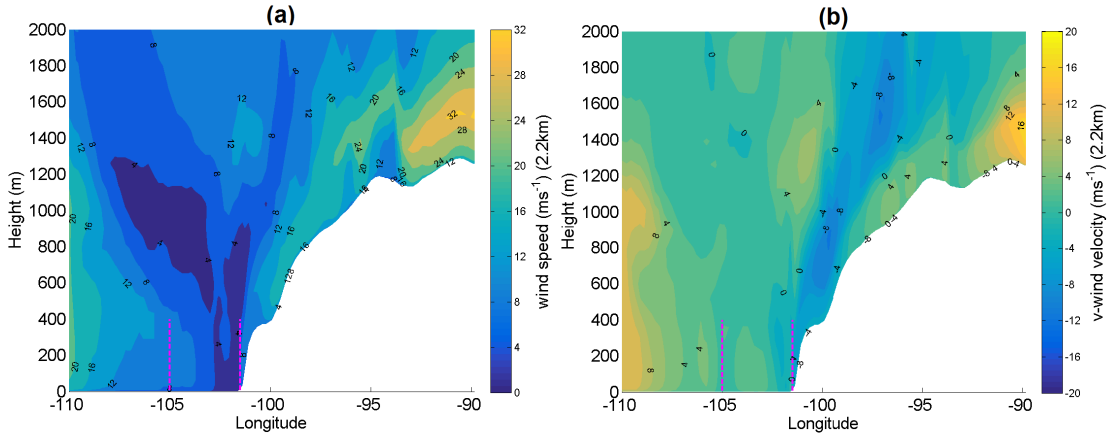

Figure A.8: (a) High resolution wind speed cross-section along the latitude 74.1°S at 1800 UTC 30th October, note the abscence of a distinct hydraulic jump. (b) high resolution model v-wind along the same cross-section at the same time, notice the absence of the southerly low-level jet.

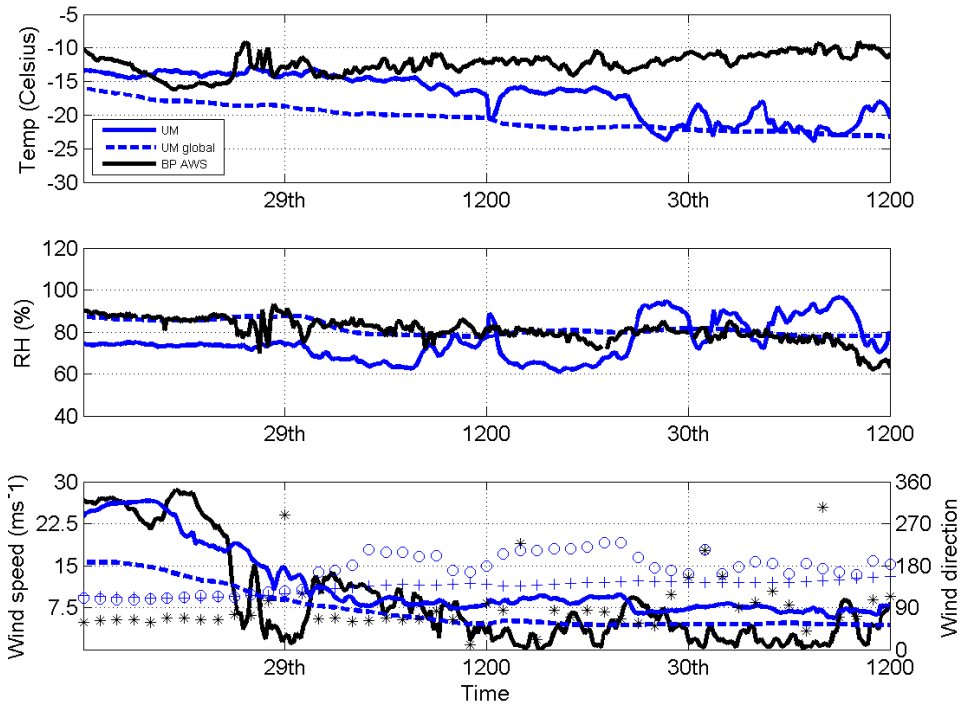

Figure A.9: A comparison of the modelled and observed: temperature (top), relative humidity (middle), and wind speed and direction (bottom), at Bear Peninsula AWS between 28th-30th August 2012.

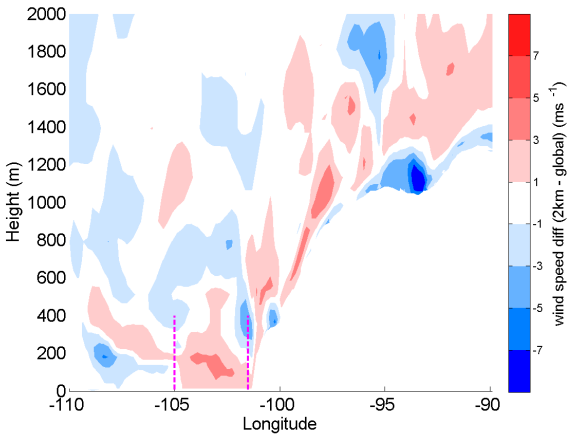

Figure A.10: Wind speed difference cross-section along 74.1°S at 0000 UTC 29th August 2012. Note there is now a much smaller difference between the two resolutions of the MetUM in the wind speed field over PIG polynya.